

ROBUST MEASUREMENT OF THE COSMIC DISTANCE SCALE USING
BARYON ACOUSTIC OSCILLATIONS

by
Xiaoying Xu

A Dissertation Submitted to the Faculty of the
DEPARTMENT OF ASTRONOMY
In Partial Fulfillment of the Requirements
For the Degree of
DOCTOR OF PHILOSOPHY
In the Graduate College
THE UNIVERSITY OF ARIZONA

2 0 1 2

THE UNIVERSITY OF ARIZONA
GRADUATE COLLEGE

As members of the Dissertation Committee, we certify that we have read the dissertation prepared by Xiaoying Xu entitled “Robust measurement of the cosmic distance scale using baryon acoustic oscillations” and recommend that it be accepted as fulfilling the dissertation requirement for the Degree of Doctor of Philosophy.

_____ Date: 5 June 2012
Christopher Walker

_____ Date: 5 June 2012
Daniel Eisenstein

_____ Date: 5 June 2012
Romeel Davé

_____ Date: 5 June 2012
Philip Pinto

_____ Date: 5 June 2012
Edward Olszewski

Final approval and acceptance of this dissertation is contingent upon the candidate’s submission of the final copies of the dissertation to the Graduate College.

I hereby certify that I have read this dissertation prepared under my direction and recommend that it be accepted as fulfilling the dissertation requirement.

_____ Date: 5 June 2012
Dissertation Director: Christopher Walker

STATEMENT BY AUTHOR

This dissertation has been submitted in partial fulfillment of requirements for an advanced degree at The University of Arizona and is deposited in the University Library to be made available to borrowers under rules of the Library.

Brief quotations from this dissertation are allowable without special permission, provided that accurate acknowledgment of source is made. Requests for permission for extended quotation from or reproduction of this manuscript in whole or in part may be granted by the head of the major department or the Dean of the Graduate College when in his or her judgment the proposed use of the material is in the interests of scholarship. In all other instances, however, permission must be obtained from the author.

SIGNED: Xiaoying Xu

ACKNOWLEDGMENTS

When I was little, I never dreamed of becoming an author, but here I sit writing this “book” that will constitute my thesis. One thing I have always dreamed of, however, was to earn a PhD, which upon completion of this “book” and some “answering and debating” (as a thesis defense is known in Chinese), I hope that one shall be conferred upon me.

So...one dream down (or pending...), $N - 1$ to go. But before I embark on further conquests, there are certainly a large number of people I am grateful to in getting this far.

First and foremost I must thank my mother, who this thesis is also dedicated to, for her unwavering belief in my ability to actually accomplish something with my life (har-har). She has always encouraged me to pursue my dreams and test the limits of my capabilities.

Then, of course, I thank my advisor, Daniel Eisenstein, for his patient mentorship and guidance. His kind support and tolerance towards my often-obtuse mind have been most encouraging. In Chinese culture, we are forever indebted to our teachers for the knowledge they have imparted to us. I will try my best to use this knowledge for good and not for evil, although I will make no guarantees in the matter...

I’m also incredibly grateful towards Chris Walker for all his help in chairing my committee after Daniel’s move to Harvard. Also for his willingness to assume the risks involved in letting someone who predominantly works in theory (such as myself) help assemble the optical system for a major radio telescope camera. I’d also like to thank Phil Pinto for all his help and advice, especially when I just moved to Boston. The multiple occasions where he has supplied food and shelter to this poor graduate student will forever be remembered. Also thanks to Romeel Davé for sitting on both my prelim and thesis committees and Edo for graciously agreeing to sit on my defense committee at the last minute!

Next I thank my friend Wenqian (Elizabeth) Wang, whom I have known for 13 years, for her continued words of encouragement during my graduate student days. Also, my long-time friends Zhongying (Zoey) Zhou, Kabkaisone (Katherine) Phromkharanourak, Christina Yung, Siyu Liu, Shanli Liu and Helen Fang for their support and kindness. I hope we remain good friends for many years to come!

Finally I thank my friends from Steward Observatory: Lei Bai, Vanessa Bailey, Fuyan Bian, Amanda Brady-Ford, Kate Brutlag, Jon Eckel, Pablo Espinoza, Dennis Just, Jenna Kloosterman, Erica McEvoy, Kushal Mehta (my academic brother), Marc Metchnik, Kyle Penner, Megan Reiter, Hee-Jong Seo (my academic sister), Suresh Sivanandam, Johanna Teske, Greg Walth, Ken Wong and Lei Xu, as well as Gongjie Li at the Harvard Center for Astrophysics for help with homework/prelim studying, insightful discussions and words of encouragement.

DEDICATION

This thesis is dedicated to my mother:

Jie Gu,

for her encouragement, patience and advice. I know she has always meant well and always believed in me. Without her, I certainly would not be where I am today.

And to my friend:

Wenqian (Elizabeth) Wang,

for suggesting over lunch on a fine winter's day during high-school that I should pursue astronomy.

TABLE OF CONTENTS

	LIST OF FIGURES	9
	LIST OF TABLES	12
	ABSTRACT	13
1	INTRODUCTION	15
	1.1 Astronomy, Cosmology and Dark Energy	15
	1.2 Cosmological Probes of Dark Energy	17
	1.2.1 Type Ia Supernovae	18
	1.2.2 Weak Gravitational Lensing	19
	1.2.3 Galaxy Clusters	20
	1.3 The BAO Method	20
	1.3.1 Introduction to BAO	21
	1.3.2 Physics	22
	1.3.3 Measurement	25
	1.3.4 Application to Cosmology	29
	1.3.5 Complications	32
2	A NEW STATISTIC FOR ANALYZING BARYON ACOUSTIC OSCILLATIONS	38
	2.1 Introduction	38
	2.2 The $\omega_\ell(r_s)$ Statistic	42
	2.2.1 Equations and Properties	42
	2.2.2 Computation	45
	2.2.3 Covariance Matrix	48
	2.2.4 Summary of Key Features	49
	2.3 Simulations and Analysis Methods	50
	2.3.1 Simulations	51
	2.3.2 Halo Occupation Distributions	52
	2.3.3 Fitting $\omega_0(r_s)$ to Measure the Peak Shift	53
	2.3.4 Resampling Methods	59
	2.4 Comparison to the Power Spectrum	60
	2.4.1 Comparison from Simulations	60
	2.4.2 Theory Constraints on σ_α	63
	2.5 Conclusions	67
3	A 2% DISTANCE TO $z = 0.35$ BY RECONSTRUCTION BARYON ACOUSTIC OSCILLATIONS	72
	3.1 Introduction	73
	3.2 Datasets	76
	3.2.1 Simulations	76

3.2.2	SDSS DR7	77
3.3	Methods	78
3.3.1	Reconstruction	78
3.3.2	Covariance Matrices	83
3.3.3	Fitting the Acoustic Feature	92
3.4	Reconstructing Simulations	101
3.5	LasDamas Redshift Space Fitting Results	107
3.5.1	Without Reconstruction	107
3.5.2	With Reconstruction	126
3.6	LasDamas Real Space Results	138
3.6.1	Covariance Matrices	138
3.6.2	Fitting Forms	140
3.6.3	Without Reconstruction Fitting Results	143
3.6.4	With Reconstruction Fitting Results	145
3.7	Measuring the BAO in SDSS DR7	147
3.7.1	Covariance Matrices	147
3.7.2	Fit Results	148
3.7.3	Comparison with LasDamas Cosmology	154
3.7.4	Significance of the BAO Detection	156
3.8	Conclusions	159
4	THE CLUSTERING OF GALAXIES IN THE SDSS-III BARYON OSCILLATION SPECTROSCOPIC SURVEY: BARYON ACOUSTIC OSCILLATIONS IN THE DATA RELEASE 9 SPECTROSCOPIC GALAXY SAMPLE	163
4.1	Introduction	164
4.2	The Data	166
4.3	Analysis Methods	169
4.3.1	Measuring the Correlation Function	169
4.3.2	Reconstruction	170
4.3.3	Fitting the Correlation Function	172
4.3.4	Mocks and Covariance Matrices	175
4.4	Results	176
4.4.1	Correlation Function Results	176
4.4.2	Robustness of Techniques	182
4.4.3	Consensus Results	193
4.5	Cosmological Implications	197
4.5.1	Comparison with Past Results	197
4.5.2	Cosmological Parameters	203
4.6	Conclusions	212

5	MAPPING THE COSMIC EXPANSION HISTORY USING THE ANISOTROPIC BARYON ACOUSTIC OSCILLATIONS SIGNAL IN SDSS DR7	216
5.1	Introduction	216
5.2	Theory	219
5.2.1	Background, Basics and Definitions	219
5.2.2	Formalism for the Correlation Function	222
5.2.3	The Anisotropic Signal	225
5.2.4	A Non-linear Model	228
5.2.5	Covariance Matrix Formalism	235
5.3	Analysis	239
5.3.1	Reconstruction	239
5.3.2	Computation	241
5.3.3	Fitting	243
5.4	Mock Catalogue Results	249
5.5	DR7 Results	272
5.5.1	Anisotropic Results	272
5.5.2	Comparison with Past Works	281
5.6	Cosmological Implications	287
5.7	Conclusions	291
6	CONCLUSIONS	294
7	EVALUATING $\widetilde{W}_\ell(k)$	300
8	FISHER MATRIX PREDICTIONS	301
	REFERENCES	303

LIST OF FIGURES

2.1	Filters for calculating $\omega_\ell(r_s)$	44
2.2	Monopole of the $\omega_\ell(r_s)$ statistic ($\omega_0(r_s)$).	46
2.3	Comparison of fits to $\omega_0(r_s)$ using various models.	58
2.4	Comparison of acoustic scales (α) measured from $\omega_\ell(r_s)$ versus $P(k)$	61
2.5	Comparison of expected errors on measured acoustic scale using $\omega_\ell(r_s)$, $P(k)$ and $\xi(r)$	64
2.6	Location of acoustic information in $\omega_\ell(r_s)$, $P(k)$ and $\xi(r)$	68
2.7	Optimal fitting range for extracting all the acoustic information using $\omega_\ell(r_s)$	69
3.1	Pictorial summary of reconstruction.	79
3.2	Sample and best-fit covariance matrix diagonal and off-diagonal terms.	91
3.3	Comparison of covariance matrices derived from different cosmologies.	93
3.4	α versus B_0^2 from fits to redshift-space LRG mocks before reconstruction.	97
3.5	Fits to average of redshift-space LRG mocks before reconstruction using different $A(r)$ marginalization terms.	99
3.6	Average pre- and post-reconstruction $\xi(\vec{r})$ from DR7 LRG mocks.	102
3.7	Average $\xi(r)$ of LRG mocks before and after reconstruction in redshift space.	104
3.8	Average $\xi(r)$ obtained using different smoothing lengths for reconstruction on redshift-space LRG mocks.	106
3.9	Sample fits to redshift-space LRG mocks before reconstruction.	109
3.10	α versus σ_α of redshift-space LRG mocks before reconstruction.	113
3.11	Validation of our fitting method in redshift space before reconstruction using LRG mocks: varying fiducial cosmology.	119
3.12	Validation of our fitting method in redshift space before reconstruction using LRG mocks: varying fitting parameters.	122
3.13	Sample fits to redshift-space LRG mocks after reconstruction.	127
3.14	Comparison of σ_α from LRG mocks before and after reconstruction in redshift space.	128
3.15	Signal-to-noise of α measurements from LRG mocks in redshift space after reconstruction.	130
3.16	Effects of fitting with a covariance matrix derived from the wrong cosmology.	132
3.17	Validation of our fitting method in redshift space after reconstruction using LRG mocks.	133
3.18	Detectability of the BAO in redshift-space LRG mocks.	138
3.19	α versus σ_α of real-space LRG mocks before reconstruction	144

3.20	Comparison of σ_α from LRG mocks before and after reconstruction in real space.	146
3.21	Fits to DR7 LRG sample before and after reconstruction.	150
3.22	Comparison of the $A(r)$ marginalization required in DR7 LRGs versus the LRG mocks.	155
3.23	Significance of BAO detection in DR7 LRG sample.	157
4.1	CMASS $\xi(r)$ before and after reconstruction.	177
4.2	Comparison of σ_α before and after reconstruction from DR9 CMASS mocks.	178
4.3	Significance of CMASS BAO detection.	179
4.4	Average $\xi(r)$ of CMASS mocks before and after reconstruction.	181
4.5	Signal-to-noise ratio of BAO measurements from CMASS mocks.	183
4.6	BAO significance in CMASS as a function of $A(r)$	192
4.7	Comparison of α and σ_α measured using $\xi(r)$ and $P(k)$ from the CMASS mocks.	194
4.9	Comparison of LRG and CMASS $\xi(r)$ after reconstruction.	198
4.10	Combined CMASS+LRG BAO detection significance.	199
4.11	BAO distance-redshift relation.	200
4.12	w_0 versus H_0 for a w CDM universe.	210
4.13	w_0 versus Ω_K for an ow CDM universe.	211
4.14	H_0 comparison between CMB+BAO+SN and direct HST measurement.	213
5.1	Variation of redshift-space linear theory monopole and quadrupole models with ϵ	226
5.2	Variation of redshift-space non-linear monopole and quadrupole models with ϵ	227
5.3	Variation of redshift-space non-linear monopole and quadrupole models with Σ_{nl}	230
5.4	Variation of redshift-space non-linear monopole and quadrupole models with Σ_s	231
5.5	Variation of redshift-space non-linear monopole and quadrupole models with β	232
5.6	Derivatives of redshift-space model quadrupole.	236
5.7	Average monopole and quadrupole of LasDamas mocks in redshift space before reconstruction.	250
5.8	Comparison between monopole and quadrupole of LasDamas mocks before and after reconstruction.	252
5.9	ϵ versus β fit from LasDamas mocks after reconstruction.	253
5.10	ϵ versus α and D_A versus H fit from LasDamas mocks after reconstruction.	254
5.11	σ_α versus σ_ϵ fit from LasDamas mocks after reconstruction.	255

5.12	ϵ versus σ_ϵ fit from LasDamas mocks before and after reconstruction.	256
5.13	ϵ before reconstruction versus ϵ after reconstruction measured from LasDamas mocks.	257
5.14	Validation of our fitting method on the LasDamas mocks: varying fiducial model parameters.	258
5.15	Validation of our fitting method on the LasDamas mocks: varying fiducial cosmology.	259
5.16	Average monopole and quadrupole of LasDamas mocks in real space before and after reconstruction.	264
5.17	Signal-to-noise of α and ϵ measurements from LasDamas mocks in redshift space after reconstruction.	271
5.18	DR7 anisotropic fit results.	273
5.19	σ_α versus σ_ϵ measured from the LasDamas mocks after reconstruction with DR7 point overplotted.	276
5.20	DR7 $\chi^2(\alpha, \epsilon)$ surfaces, and $p(\alpha)$ and $p(\epsilon)$ distributions.	277
5.21	Investigating the change in σ_α between the monopole+quadrupole fits and the monopole-only fits.	284
5.22	Predictions for α and ϵ as a function of z	287
5.23	Our ϵ measurement in the context of current cosmological constraints.	288

LIST OF TABLES

2.1	HOD properties used for $\omega_0(r_s)$ analysis.	54
2.2	$\omega_0(r_s)$ fit results for each HOD model.	56
2.3	Difference in mean α between fits to $\omega_0(r_s)$ and $P(k)$	60
3.1	Fit results to average of mock LRG correlation functions.	98
3.2	α measurements from redshift-space LRG mocks for different fitting parameters.	115
3.3	α measurements from redshift-space LRG mocks for different reconstruction smoothing lengths.	134
3.4	α measurements from redshift-space LRG mocks for different reconstruction parameters.	135
3.5	α measurements from real-space LRG mocks for different fitting parameters.	141
3.6	α measurements from LRG data for different fitting parameters.	149
3.7	α measurements from LRG data for different reconstruction parameters.	153
4.1	α measurements from CMASS mocks for different fitting and reconstruction parameters.	184
4.2	α measurements from CMASS data for different fitting and reconstruction parameters.	188
4.3	Cosmological constraints from CMASS, LRG and other datasets.	205
5.1	ϵ bias checks on the LasDamas mocks.	260
5.2	α and ϵ measurements from LasDamas mocks for different fitting and reconstruction parameters.	261
5.3	Summary of DR7 distance constraints.	274
5.4	α measurements from DR7 data for different fitting and reconstruction parameters.	279
5.5	Investigating the change in σ_α between the monopole+quadrupole fits and the monopole-only fits.	285

ABSTRACT

We present techniques for obtaining precision distance measurements using the baryon acoustic oscillations (BAO) through controlling systematics and reducing statistical uncertainties. Using the resulting distance-redshift relation, we can infer cosmological parameters such as w , the equation of state of dark energy.

We introduce a new statistic, $\omega_\ell(r_s)$, for BAO analysis that affords better control over systematics. It is computed by band-filtering the power spectrum $P(k)$ or the correlation function $\xi(r)$ to extract the BAO signal. This is conducive to several favourable outcomes. We compute $\omega_\ell(r_s)$ from 44 simulations and compare the results to $P(k)$ and $\xi(r)$. We find that the acoustic scales and theoretical errors we measure are consistent between all three statistics.

We demonstrate the first application of reconstruction to a galaxy redshift survey. Reconstruction is designed to partially undo the effects of non-linear structure growth on the BAO, allowing more precise measurements of the acoustic scale. We also present a new method for deriving a smooth covariance matrix based on a Gaussian model. In addition, we develop and perform detailed robustness tests on the $\xi(r)$ model we employ to extract the BAO scale from the data. Using these methods, we obtain spherically-averaged distances to $z = 0.35$ and $z = 0.57$ from SDSS DR7 and DR9 with 1.9% and 1.7% precision respectively. Combined with WMAP7 CMB observations, SNLS3 data and BAO measurements from 6dF, we measure $w = -1.08 \pm 0.08$ assuming a w CDM cosmology. This represents a $\sim 8\%$ measurement of w and is consistent with a cosmological constant.

The preceding does not capture the expansion history of the universe, $H(z)$, encoded in the line-of-sight distance scale. To disentangle $H(z)$, we exploit the anisotropic BAO signal that arises if we assume the wrong cosmology when calcu-

lating the clustering distribution. Since we expect the BAO signal to be isotropic, we can use the magnitude of the anisotropy to separately measure $H(z)$ and $D_A(z)$. We apply our simple models to SDSS DR7 data and obtain a $\sim 3.6\%$ measurement of $D_A(z = 0.35)$ and a $\sim 8.4\%$ measurement of $H(z = 0.35)$.

CHAPTER 1

INTRODUCTION

1.1 Astronomy, Cosmology and Dark Energy

Mankind has always been fascinated by the cosmos and what lies beyond the limits of our planet Earth. Indeed, entire civilizations have been built based on patterns dictated by astronomical phenomenon. The Mayan culture of Mesoamerica is especially notable, with the detail of their structures, i.e. number of steps, number and direction of doors, number of decorative elements, etc., all patterned on the natural phases observed in the moon, sun and stars. For millenia, humans have been observing the skies, seeking to understand the secrets of our universe: *How was it created? How did it become the way it is now?* However, it is only recently, with the flourishing of astronomy as a science, that we became equipped to answer these questions.

The sub-field of cosmology within astronomy is directly concerned with these issues. Data show that the universe was formed in an event known as the Big Bang which was accompanied by a period of rapid expansion. This allowed the originally hot and dense universe to cool and form subatomic particles. Over time, these coalesced into atoms, stars and galaxies.

In the early 1900s, the expansion of the universe in our present epoch was first posited both theoretically and through observations (Slipher, 1913; Lemaître, 1927; Hubble, 1929). However, it was not until the late 1990s that the most perplexing discovery of modern cosmology was made: that the expansion is in fact accelerating! The first conclusive evidence came by observing Type Ia supernovae, which should have appeared much brighter had the universe been static (Riess et al., 1998; Perlmutter et al., 1999). Then arose the question of what causes this accelerated ex-

pansion. Naively we would expect, that if the universe were dominated by matter, then gravity would eventually cause the universe to decelerate and perhaps even collapse back onto itself. However, the above evidence for the contrary suggests that our universe has an additional component that is dominating its behaviour, a component now known as “dark energy”.

General relativity provides some clues as to what dark energy is due to its apparent link to the cosmological constant Λ . This was first introduced by Einstein into his field equations to, ironically enough, make the universe static (Einstein, 1917). Since then, it has been found that a Λ -like term can arise from scalar fields parameterizing the potential energy of the vacuum. If the vacuum has a positive energy density, then its corresponding pressure is negative, which is precisely what is needed to counteract gravity and accelerate the expansion of the universe (Ratra & Peebles, 1988; Frieman et al., 1995).

Nonetheless, whether or not vacuum energy is in fact dark energy remains a point of contention. Although indirect observations of dark energy via cosmological probes indicate that it is very similar to a cosmological constant in the present epoch (e.g. the work presented in Chapter 4), the measured value of Λ is many orders of magnitude smaller than that predicted from vacuum energy arguments in standard particle physics. Introducing elements of supersymmetry (Golfand & Likhtman, 1971) may reconcile observation and theory, however, these methods require a large amount of “fine-tuning” (Cremmer et al., 1983). Other attempts to save vacuum energy as a candidate for dark energy evoke string theory (Kachru, Kumar & Silverstein, 1999) and even wormholes (Coleman, 1988). However, a much simpler yet still physically plausible model involves a vacuum energy that somehow redshifts away with time (Barnard et al., 2008). Such a process can result in the very small vacuum energy density observed today that resembles a cosmological

constant. In these models, dark energy has become known as quintessence.

The main concern of the cosmologist lies in testing and ruling out these models. Since dark energy does not appear to radiate and hence cannot be directly observed, cosmologists use a number of observations to indirectly probe the macroscopic properties of dark energy such as its equation of state w . This equation of state relates the energy density of dark energy ρ to its pressure p ,

$$p = w\rho. \tag{1.1}$$

The value of w varies with different models of dark energy, for example, if dark energy corresponds to a cosmological constant, then $w = -1$. To determine the time variability (if any) of dark energy, we need to know w in the local universe as well as in the higher redshift universe. Therefore, measuring w is currently the key goal in observational cosmology.

1.2 Cosmological Probes of Dark Energy

At the present, many experiments are in the process of taking data for the purposes of measuring w . In the low-redshift universe, the most popular cosmological probes of dark energy are Type Ia supernovae, weak gravitational lensing, galaxy clusters and the baryon acoustic oscillations (BAO). Higher redshift techniques such as extracting the BAO signal in Ly- α absorption lines from quasar spectra (e.g. Slosar et al. (2009)) and tracing the reionization history using neutral hydrogen 21cm emission (e.g. McQuinn et al. (2006)) are currently under development.

This thesis will focus on the low-redshift BAO method which will be detailed in §1.3. The following gives a brief overview of the other indirect probes of dark energy employed at low redshift. These techniques all benefit from having accurate redshift measurements such as those provided by spectroscopic observations (e.g. the Sloan Digital Sky Survey). However, improved photometric redshift techniques

are being explored in many upcoming large-scale surveys due to the relative ease in acquiring photometric data (e.g. the Dark Energy Survey and the Large Synoptic Survey Telescope).

1.2.1 Type Ia Supernovae

Type Ia supernovae occur when the cores of carbon-oxygen white dwarfs heat up and ignite a thermonuclear explosion as they approach the Chandrasekhar mass ($1.4M_{\odot}$). The heating is a result of the white dwarf accreting mass from a red giant companion (Whelan & Iben, 1973) or coalescing with another white dwarf (Iben & Tutukov, 1984; Webbink, 1984). The peak magnitude of the resulting explosion is related to how fast the supernova’s light declines from this peak (Phillips, 1993). Hence, by measuring the supernova light curve, we can predict its peak luminosity. This facilitates their use as “standard candles” (Colgate, 1979) for measuring cosmological distances.

The distance measured using Type Ia supernovae is known as the luminosity distance,

$$D_L = \sqrt{\frac{L}{4\pi F}}, \quad (1.2)$$

where L is the intrinsic luminosity of the supernovae and F is the flux observed on Earth. Since there are many Type Ia supernovae at various different redshifts z , we can measure D_L as a function of z . This relationship depends on the properties of dark energy because they affect the expansion rate of the Universe which sets the distance scales we measure. The value of w can then be determined by fitting model $D_L - z$ curves to the data. Such was the technique employed in the initial discovery of the accelerated expansion of our Universe discussed in §1.1.

The key observational challenges to the supernova method include uncertainties in the absolute magnitude of Type Ia’s as well as reddening by dust. It has been shown that Type Ia absolute magnitudes may evolve with redshift (Riess et al.,

1999; Drell, Loredó & Wasserman, 2000; Howell et al., 2007) which affects their calibration as standard candles. However, this appears to be a minor effect (Riess et al., 1998; Schmidt et al., 1998) and the cosmological parameters obtained by assuming a non-evolving model are mostly 1σ consistent with an evolving model (Linden, Virey & Tilquin, 2009). Reddening occurs when intergalactic dust alters the apparent magnitudes that we observe (Aguirre, 1999). This is also a small effect and can be corrected for using appropriate reddening models (Perlmutter et al., 1999; Reindl et al., 2005; Nobili & Goobar, 2008; Chotard et al., 2011).

1.2.2 Weak Gravitational Lensing

Gravitational lensing is the bending of light from distant sources due to massive objects such as galaxy clusters (known as lenses), that lie along the line-of-sight. Weak lensing arises when the source and the lens are not perfectly aligned, but are sufficiently close in the plane of the sky. The lens distorts the shape of the source and also magnifies its brightness. Since the same lens affects all sources that lie along the same line-of-sight, the distortion of the sources, known as the shear, is correlated at different redshifts. This correlation is related to how galaxies are distributed in the universe which in turn is regulated by cosmological parameters such as w (Kaiser, 1992, 1998; Hu, 1998).

The key observational challenges of the weak lensing approach lie in measuring the galaxy shapes to determine their shear. Uncertainties arise because it is difficult to disentangle the intrinsic galaxy shape, distortions caused by lensing and distortions caused by other factors such as telescope optics and atmospheric blurring (e.g. Kitching, Taylor & Heavens 2008). Galaxies that appear lensed but are in fact merely intrinsically aligned on the sky pose additional complications (e.g. Bridle & King 2000; Catelan, Kamionkowski & Blandford 2001).

1.2.3 Galaxy Clusters

Galaxy clusters are the largest gravitationally bound structures in the universe. They reside in the most massive dark matter halos which are thought to be formed through gravitational processes only, i.e. independent of gas physics, star formation and feedback (Haiman, Mohr & Holder, 2001). This implies that the abundance of clusters as a function of redshift depends only on a few factors such as the geometry of the universe. Since this geometry is linked to the expansion of the universe and hence dark energy, it is possible to measure w by counting the number of clusters at various different redshifts (e.g. Bahcall & Fan 1998; Blanchard & Bartlett 1998; Viana & Liddle 1999).

The prevailing challenge in this approach is that we do not observe all clusters that fall within a given survey area due to limited survey sensitivities. This effectively imposes a minimum mass on the detectable galaxy clusters which needs to be included in the models used to extract w . However, predicting this mass from observed quantities introduces a major source of systematic error. Current mass errors fall at the $\sim 10\%$ level for all mass estimation techniques (e.g. from X-ray gas measurements (Kravtsov, Vikhlinin & Nagai, 2006), Sunyaev-Zel'dovich effect measurements (Hallman et al., 2006) and weak lensing measurements (Becker & Kravtsov, 2011)).

1.3 The BAO Method

The baryon acoustic oscillations (BAO) method is one of the most powerful probes of dark energy and is the main focus of this thesis. The following serves as a general introduction to BAO and forms the basis for understanding the contents of this thesis.

1.3.1 Introduction to BAO

The interactions between matter and photons in the early universe give rise to the BAO (see §1.3.2) which are essentially sound waves propagating through the primordial plasma. Signatures of these waves are left on the photon and baryon distributions, which can still be observed today. The existence of the BAO was first theorized by Sakharov (1966); Peebles & Yu (1970) and Sunyaev & Zeldovich (1970) as an observable effect in the cosmic microwave background (CMB), the relic photons from the primordial universe. It has since been detected with high fidelity in the Wilkinson Microwave Anisotropy Probe (WMAP; Bennett et al. 2003) observations of the CMB (Hinshaw et al., 2003, 2007; Nolta et al., 2007; Larson et al., 2011).

In terms of the baryons, the BAO phenomenon gives rise to a characteristic scale in their distribution. This is known as the acoustic scale which has a magnitude of ~ 150 comoving Mpc. In the low redshift universe, the BAO can be detected in the clustering signal of galaxies (formed from the baryons), which can be measured from large galaxy surveys as described in §1.3.3. This characteristic scale can be used as a “standard ruler” for measuring the distance to the median redshift of a galaxy sample (Eisenstein, 2002, 2003; Blake & Glazebrook, 2003; Hu & Haiman, 2003; Linder, 2003; Seo & Eisenstein, 2003; Matsubara, 2004; Amendola, Quercellini & Giallongo, 2005). Again, since the distances we measure are related to the expansion history of our universe and hence the properties of dark energy, we can fit models to measured distance-redshift relations and infer quantities such as w . Further elaboration on this method can be found in §1.3.4.

The BAO scale was first proposed as a standard ruler for measuring the properties of dark energy by Eisenstein (2002); Blake & Glazebrook (2003); Hu & Haiman (2003); Linder (2003) and Seo & Eisenstein (2003). The first detections came in 2005 by Eisenstein et al. (2005) using the luminous red galaxy sample (Eisenstein

et al., 2001) from the third data release (DR3) of the Sloan Digital Sky Survey (SDSS) and by Cole et al. (2005) using the 2 Degree Field Galaxy Survey (2dF). Since then, numerous BAO studies have been performed on successive SDSS data releases (Tegmark et al., 2006; Hütsi, 2006; Padmanabhan, White & Eisenstein, 2007; Percival et al., 2010) as well as galaxy surveys such as the 6 Degree Field Galaxy Survey (Beutler et al., 2011) and WiggleZ (Blake et al., 2011a,b,c). In particular, Chapters 3 and 4 of this thesis present BAO results based on the SDSS data release 7 (DR7) luminous red galaxy (LRG) sample and the latest SDSS data release 9 (DR9) constant-mass (CMASS) galaxy sample.

Spectroscopic surveys allowing the accurate measurement of redshifts greatly increases the power of this method, as the radial distances inferred from these redshifts provides an extra dimension along which the BAO scale can be measured.

Since the BAO method makes use of a standard ruler and is therefore purely based in geometry, it is argued to have the least systematic error of all the available dark energy probes. However, small complications resulting from non-linear structure growth, galaxy bias and redshift-space distortions do arise. These will be described in more detail in §1.3.5.

To fully harness the potential of the BAO technique in obtaining precision measurements of the properties of dark energy, robust distance measurements are integral. This thesis details practical techniques for achieving high-precision distance measures using the BAO.

1.3.2 Physics

The following description of BAO physics is adapted from Eisenstein, Seo & White (2007) and the review articles Eisenstein & Bennett (2008) and Weinberg et al. (2012).

The baryon acoustic oscillations are a relic of early universe physics beginning

with tiny density perturbations seeded by inflation (Sakharov , 1966; Peebles & Yu, 1970; Sunyaev & Zeldovich, 1970). These perturbations consist of dark matter, baryons, photons and neutrinos. The neutrinos decouple and stream off early on and are thus not a major concern for BAO. The temperatures in the early universe are very high so all the gas is completely ionized. As a result, there are many free electrons which serve as a large source of opacity to the photons due to Thompson scattering. This effectively traps the photons inside the baryons and locks them together into a single fluid.

The perturbation continues to grow through accruing the surrounding mass and contracts further due to self-gravity. This further increases the temperature inside the overdensity which subsequently increases the amount of radiation pressure from the photons. Eventually this pressure becomes so large, that the photons can push the photon-baryon fluid outwards from the center of the perturbation in a spherical pressure wave. As pressure waves are essentially sound waves, this pulse travels through the surrounding medium at the sound speed, c_s , defined as

$$c_s^2 = \frac{\partial p / \partial T}{\partial \rho / \partial T} = \frac{c^2}{3} \frac{4\rho_r}{4\rho_r + 3\rho_b} \quad (1.3)$$

where T is the temperature, p is the pressure and ρ is the density. The subscript r denotes radiation and the subscript b denotes baryons.

The dark matter only interacts gravitationally and hence remains near the center of the initial perturbation. It exerts a restoring force on the photon-baryon fluid due to its gravitational attraction to the baryons. The competition between this inward pulling gravitational force and the outward pushing radiation pressure determines how far the sound wave propagates through the plasma. At recombination, the universe has expanded and cooled sufficiently for protons to begin capturing electrons. This removes the source of opacity locking together the photon-baryon fluid, causing the photons to decouple and stream away forming the CMB. Losing the radiation

pressure propagating them forward, the baryons are left behind in spherical shells centered on the initial overdensity. The radius of these shells is a characteristic scale known as the sound horizon or the acoustic scale and can be calculated as

$$r_s = \int_0^{t_*} \frac{c_s(t)}{1+z} dt = \int_{z_*}^{\infty} \frac{c_s(z)}{H(z)} dz \quad (1.4)$$

where t_* and z_* are the time and redshift of recombination respectively and $H(z)$ is the Hubble parameter. Using reasonable values for these parameters, we find that $r_s \sim 150$ comoving Mpc. The fact that this scale is characteristic and unvarying is essential for its utility as a cosmological standard ruler (see §1.3.4).

With time, most of the baryons in the shells are drawn towards the overdensities of dark matter which have largely remained at their original positions. However, some dark matter is also drawn towards the baryons that were deposited in these spherical shells. This results in small ($\sim 1\%$) baryon and dark matter excesses, known as acoustic peaks, at separations corresponding to the acoustic scale. These regions where the dark matter and baryons are relatively concentrated act as seeds for the subsequent formation of dark matter halos through gravitational accretion. As the universe continues to evolve, galaxies begin forming in these dark matter halos. Hence, we would expect to see slight excesses in the clustering distribution of galaxies at separations corresponding to the acoustic scale.

The acoustic scale corresponds to a harmonic sequence of oscillations in Fourier space, where an analogous story can be told. The name baryon acoustic oscillations stems from this phenomenon. In Fourier space, the spherical sound wave is akin to a plane wave perturbation (Bond & Efstathiou, 1984; Holtzman, 1989; Hu & Sugiyama, 1996; Hu & White, 1996; Eisenstein & Hu, 1998). If, at the time of recombination, the sound wave travels a distance such that the baryons are deposited on the crest of another wave, then constructive interference occurs. Conversely, if the baryons are deposited at the trough of another wave, destructive interference occurs.

Hence we can think of the sound horizon as the wavelength of the fundamental mode for a series of harmonics corresponding to these oscillatory interference patterns.

In this simple picture, these harmonics could continue to arbitrarily small wavelengths (or high wavenumbers, k). However, a process known as Silk damping (Silk, 1968) prevents this from occurring. This process arises due to the non-zero mean free path of photons undergoing Thompson scattering which allows photons to diffuse through the baryons for small distances or large k . The diffusion scale is around $8h^{-1}\text{Mpc}$ and is determined by the plasma composition which dictates how far a photon can typically travel before being scattered. This diffusion of photons effectively smooths out the baryon distribution at small scales, inhibiting any characteristic patterns in baryon deposition. As a result, the higher harmonics are damped out, and analogously, the acoustic peak is broadened. This is what sets the $\sim 8h^{-1}\text{Mpc}$ intrinsic width of the acoustic peak.

1.3.3 Measurement

As mentioned in the preceding section, the acoustic signal is imprinted on the clustering distribution of galaxies which traces the underlying dark matter. Therefore, before we can use BAO for cosmology, there are two essential measurements we must make. The first is a statistical measure of galaxy clustering which can be made from large galaxy surveys in the low redshift universe. The second is a distance measure to the median redshift of the galaxy sample from the galaxy clustering statistic using the BAO. This section is intended as a simple introduction to these measurements. Complications are discussed in §1.3.5. Due to the difficulty in observing galaxies at high redshift, measuring the BAO at high- z is more difficult. BAO techniques such as using the Ly- α forest in quasar spectra (e.g. Slosar et al. 2009) and neutral hydrogen 21cm emission (e.g. McQuinn et al. 2006) to trace dark matter are currently under investigation.

To measure the clustering distribution of galaxies in an ensemble sense, we typically use the correlation function, $\xi(\vec{r})$, or power spectrum, $P(\vec{k})$, statistics. These are Fourier transform pairs with $\xi(r)$ in configuration space and $P(k)$ in Fourier space. We mainly concern ourselves with $\xi(\vec{r})$ in this thesis. $\xi(\vec{r})$ measures the excess probability of finding two galaxies with a certain separation \vec{r} relative to a random distribution. The BAO phenomenon results in an excess of baryons and dark matter, and hence galaxies, at characteristic separations corresponding to the acoustic scale ($r_s \sim 150$ comoving Mpc). Therefore, if we measure the galaxy correlation function, we expect to see a small excess in the clustering distribution known as the acoustic peak at $|\vec{r}| \sim r_s$.

The formal definition of the galaxy (or matter) correlation function is

$$\xi(\vec{r}) = \langle \delta(\vec{r}') \delta(\vec{r}' + \vec{r}) \rangle, \quad (1.5)$$

where $\delta(\vec{r}') = (\rho - \bar{\rho})/\bar{\rho}$ is the fractional overdensity at location \vec{r}' . In practice, to calculate the correlation function, we begin with a measurement of galaxy positions from a large galaxy survey. Note that since the BAO scale is very large, it is necessary to use data from galaxy surveys that cover a very large volume such as the SDSS. With these positions, we can calculate the distance from each galaxy to every other galaxy. Spectroscopic surveys are best because they provide distance information in the line-of-sight direction, however, it is possible to do purely angular BAO analyses (in the plane of the sky) with a penalty in precision (see §1.3.4). We then specify bins in r and $\mu = \cos(\theta)$, where θ is the line-of-sight angle between two galaxies, and count the number of galaxy pairs with separations that fall within each bin. We must also generate a reference set of particles with random positions in the same survey geometry since the correlation function compares data sets to

random distributions. We then estimate the correlation function as

$$\xi(r, \mu) = \frac{DD - 2DR + RR}{RR} - 1, \quad (1.6)$$

where DD is the number of data-data pairs, DR is the number of data-random pairs and RR is the number of random-random pairs. This is more commonly known as the Landy-Szalay estimator (Landy & Szalay, 1993) and is analyzed in detail by Bernstein (1994). Other estimators such as that proposed in Hamilton (1993) are viable as well.

Recently, we also introduced a new clustering statistic for analyzing BAO known as $\omega_\ell(r_s)$. This new statistic preserves the favourable properties of the traditional $\xi(\vec{r})$ and $P(\vec{k})$ statistics but also eliminates some of their associated systematics. This is detailed in Chapter 2.

The extraction of the acoustic scale (which subsequently leads to a distance measure) from the data is typically achieved by assuming a model for a chosen clustering statistic that includes the acoustic scale as a parameter. We can then fit this model to the data to obtain the best-fit value of the acoustic scale. If we take a χ^2 approach in finding the best-fit, then by calculating χ^2 at various values of the acoustic scale, we also map out its associated error distribution $p \propto \exp(-\chi^2/2)$. In configuration space, this effectively centroids the acoustic peak in the correlation function. This value of the acoustic scale and its probability distribution are the key measurements needed for inferring cosmological parameters. However, in order to perform these measurements, one must accurately model the covariance matrix between the various scales where the clustering statistic is measured as well as develop an unbiased model template for the fitting. This covariance matrix is a measure of the statistical uncertainty in the clustering statistic which propagates into the statistical uncertainty of the measured distance scale. It has 2 principle components, sample variance and shot-noise. In Chapter 3, we present a new method

for estimating covariances as well as a robust BAO model for measuring the acoustic scale from the correlation function.

In Fourier space, the covariance is simple in the limit that the density field is Gaussian. This simply means that the amplitudes of the initial density fluctuations $\delta(\vec{k})$ are drawn from Gaussian distributions with standard deviations equal to $\sqrt{P(\vec{k})}$. Since $P(\vec{k}) \propto \delta^2(\vec{k})$, the standard deviation in $P(\vec{k})$ is $\sigma_P \sim P(\vec{k})$. The finite size of the survey truncates the number of modes measured, which amounts to dividing σ_P by the square root of the number of independent modes. This is $\propto V/2$, where V is the survey volume. The sample variance resulting from this truncation can be quite high at large scales near where the BAO is found. The BAO signal itself however, is fairly weak, making galaxy surveys that cover very large volumes necessary to obtain a robust BAO detection. This constitutes the sample variance component of the statistical uncertainty.

Due to the finite number of galaxies in the survey, shot-noise also contributes to the error with a magnitude equal to $1/n$, where n is the number density of galaxies (Kaiser, 1986). This brings the total variance in the power spectrum to

$$\sigma_P^2 \propto \frac{2}{V} \left(P(\vec{k}) + 1/n \right)^2 \quad (1.7)$$

in the Gaussian limit. Since the correlation function and the power spectrum are Fourier transform pairs, we can also transform this variance into configuration space to give the variance in the correlation function as in Equation (3.9) in Chapter 3.

Lastly we note that in the following chapters, $\xi(r)$ will be used to refer to the angle-averaged correlation function (i.e. the monopole of $\xi(\vec{r})$). If the clustering distribution of galaxies is truly isotropic (as it is thought to be on large scales), then the monopole contains all possible clustering information. However, certain observational effects (see §1.3.5) and cosmology-dependent assumptions may introduce some anisotropy into the clustering. Hence, the location of the acoustic peak may

appear at slightly different positions along the line-of-sight and transverse directions. The effects of this anisotropic BAO signal bleeds into the higher order multipoles and can be used to put further constraints on cosmology as detailed in Chapter 5. This is a manifestation of the Alcock-Paczynski test (Alcock & Paczynski, 1979) which uses the measured anisotropy of an object that is known to be isotropic to infer the true cosmology of the universe.

1.3.4 Application to Cosmology

The measured acoustic scale and its error/probability distribution are the essential ingredients for BAO cosmology. This section outlines how the BAO can be used as a standard ruler and how the measured acoustic scale (BAO size) can be transformed into a distance measure.

The size of an object such as the characteristic scale of the BAO can be measured in two primary directions. The first is in the transverse direction where the angular size ($\Delta\theta$) of the BAO in the plane of the sky can be measured. The second is in the line-of-sight direction where its size (Δz) along the redshift axis can be measured. The true size of an object (r_{\perp}) and its measured transverse angular size are related to the angular diameter distance to redshift z ($D_A(z)$) by

$$D_A(z) = \frac{r_{\perp}}{1+z} \Delta\theta, \quad (1.8)$$

where z is the redshift of the object, or in the case of BAO, z is the median redshift of the galaxy sample. The true (r_{\parallel}) and measured sizes in the line-of-sight direction are related to the Hubble parameter $H(z)$ by

$$H(z) = \frac{c\Delta z}{r_{\parallel}} \quad (1.9)$$

Spectroscopic measurements are needed in order to obtain distance information in this direction. In theory, the BAO should lie at the same location along the line-of-sight and transverse directions, so $r_s = r_{\parallel} = r_{\perp}$.

Since we know what r_s should be (this has been measured to 1.1% accuracy by WMAP in Jarosik et al. (2011)), we can infer $D_A(z)$ and $H(z)$ from the measured BAO sizes, $\Delta\theta$ and Δz , along the transverse and line-of-sight directions respectively. However, typically the signal-to-noise in the line-of-sight direction is poor due to the size limits on surveys, so we instead measure the spherically averaged correlation function or power spectrum (the monopole), which in turn leads to the measurement of a spherically averaged acoustic scale. From this we can infer the spherically averaged distance to redshift z which is defined as

$$D_V(z) \propto \sqrt[3]{\frac{D_A^2(z)}{H(z)}}. \quad (1.10)$$

One can see that $D_V(z)$ contains 2 powers of the transverse distance scale $D_A(z)$ along the 2 orthogonal directions in the plane of the sky and 1 power of the radial distance scale which is dependent on $H(z)$. We develop and test the necessary tools for obtaining a robust measurement of D_V in Chapter 3. We then apply these tools to the SDSS DR7 data in Chapter 3 and the SDSS DR9 data in Chapter 4.

The problem with measuring D_V is that it does not allow us to separately constrain $D_A(z)$ and $H(z)$, the latter of which is especially important because it defines the expansion history of the universe. Padmanabhan & White (2008) propose a method for breaking this degeneracy between D_A and H by using information from the higher order multipoles which reflect any anisotropies in the clustering. Anisotropic clustering arises due to observational effects, but it may also arise if one assumes the wrong cosmology when calculating the correlation function. These incorrect assumptions result in incongruent distance measures which make the BAO appear at different locations along the line-of-sight and transverse directions. The resulting anisotropic BAO signal can be used as an Alcock-Paczynski test to separately and directly measure D_A and H . Chapter 5 extends the toolkit developed in Chapter 3 to anisotropic BAO analysis and applies it to the SDSS DR7 data using

the multipole technique of Padmanabhan & White (2008).

The error distribution of the measured acoustic scale can be propagated into the error distributions of D_A , H or D_V . These can then be fed into a Markov Chain Monte Carlo (MCMC) algorithm, such as CosmoMC (Lewis & Bridle, 2002), which measures the values of the cosmological parameters. The dependence of the expansion rate of the universe on its energy content (i.e. matter, dark energy, curvature and radiation) implies that $H(z)$, which measures the expansion rate, and the distances we measure such as $D_A(z)$ are functions of the properties of these constituents. Specifically,

$$D_A(z) = \frac{c}{1+z} \int_0^z \frac{dz}{H(z)} \quad (1.11)$$

$$H(z) = H_0 \sqrt{\Omega_m(1+z)^3 + \Omega_\kappa(1+z)^2 + \Omega_X \exp \left[3 \int_0^z \frac{1+w(z)}{1+z} dz \right]}, \quad (1.12)$$

where Ω_m , Ω_κ and Ω_X are respectively the density ratios of matter, curvature and dark energy at the present day to the critical density of the universe. The fractional density of radiation Ω_r is on the order of 10^{-5} at the present day, a value so small that it is negligible and hence not included in the equations here. $w(z)$ is the equation of state parameter for dark energy discussed in §1.1. Here, Ω_X corresponds to an arbitrary dark energy model. Dark energy evolves with time as

$$\Omega_X(z) = \Omega_X \exp \left[3 \int_0^z \frac{1+w(z)}{1+z} dz \right]. \quad (1.13)$$

If dark energy is due to a cosmological constant Λ , then Ω_X becomes Ω_Λ and $w(z) = -1$. The integral in Equation (1.13) then goes to a constant implying the dark energy density parameter $\Omega_X = \Omega_\Lambda$ does not evolve with time.

MCMC codes start with an initial guess for the cosmological parameters such as Ω_X or w and calculate the expected observables (such as $D_V(z)$) in this cosmology. The probability distribution of $D_V(z)$ measured from the data is used to determine

the likelihood of the calculated value and hence, the likelihood of the input cosmology. Through a series of rejections and acceptances, the code converges on the cosmological parameters that match the data best. By measuring $D_V(z)$ at various redshifts, we better constrain the distance-redshift relation which results in tighter measures of the cosmological parameters. In addition, distance measures from the CMB (high redshift) and supernovae methods can be combined with BAO measurements to further improve the precision of the measured cosmology. This has been demonstrated numerous times in the literature, e.g. Efstathiou et al. (2002); Percival et al. (2002); Spergel et al. (2003); Tegmark et al. (2004); Komatsu et al. (2009); Percival et al. (2010); Reid et al. (2010); Blake et al. (2011a,b,c) and Beutler et al. (2011). We perform a similar analysis in Chapter 4 for the latest SDSS DR9 data.

1.3.5 Complications

Owing to the simple, geometric nature of the BAO method and the fact that it manifests at large spatial scales which are mostly linear (see §1.3.5.1), it is fairly devoid of systematic error and is therefore limited by the statistical uncertainties described in §1.3.3. This is in contrast to the other major dark energy probes discussed in §1.2. The major goal of this thesis is to discuss methods of limiting the impact of systematics and also improving the statistical precision of BAO measurements. Hence, this section gives a brief introduction to the major sources of uncertainty in BAO measurements. In addition to the 3 dominant complications listed in this section, other complications such as the effects of binning and the uncertainty in the cosmic number density of galaxies (the integral constraint) have some minor influence on the measurement of the BAO as well. The new clustering statistic we introduce in Chapter 2 addresses these minor complications.

1.3.5.1 Non-linear Structure Growth

The first major source of uncertainty in the measurement of the acoustic scale is due to non-linear structure growth. The amplitudes of the initial overdensities are very small. During the early stages of their growth, they merely accrete matter from their surroundings by gravitational attraction and have little interaction with each other. As a result, the various modes of the density perturbation grow independently. This is the regime of linear structure growth. However, as these overdensities become more massive, they begin exerting gravitational pulls on each other. The modes no longer grow independently, but rather develop complicated couplings with each other, giving rise to non-linear structure growth (e.g. Jain & Bertschinger (1994); Meiksin et al. (1999); Meiksin & White (1999); Scoccimarro et al. (1999)). Fortunately this occurs predominantly on small scales where the gravitational interaction between structures is non-negligible. The BAO remains largely unaffected, but in order to obtain the percent-level precision measurements required for cosmology, we must consider the consequences of this non-linear evolution.

Non-linear structure growth has 2 main effects on the BAO (Seo & Eisenstein, 2005; Amendola, Quercellini & Giallongo, 2005; Springel et al., 2005; Jeong & Komatsu, 2006; Huff et al., 2007; Ma, 2007; Eisenstein, Seo & White, 2007; Angulo et al., 2008; Wagner, Müller & Steinmetz, 2008; Crocce & Scoccimarro, 2008; Sanchez et al., 2008; Seo et al., 2008; Smith et al., 2008; Padmanabhan & White, 2009; Seo et al., 2010; Mehta et al., 2011). The first is a smearing of the acoustic peak which results from the movement of the overdensities. This makes centroiding the peak more difficult and leads to a statistically less precise measurement of the BAO scale. The second is a small shifting in the position of the acoustic peak from its predicted linear theory position. This can distort the acoustic scale we wish to use as a standard ruler. Analogously in Fourier space, the acoustic oscillations become

increasingly more damped at high k and the wiggles shift slightly in position.

Many studies have aimed at quantifying the significance of the BAO shift using perturbation theory and simulation methods. For example, Padmanabhan & White (2009) compute a value for the shift using 2^{nd} order perturbation theory. Crocce & Scoccimarro (2008) perform a similar calculation using renormalized perturbation theory. Seo et al. (2010) use N-body simulations to quantify the shift for dark matter only, while Mehta et al. (2011) perform a similar analysis on mock galaxy catalogues. All of these studies find shifts of $\sim 0.3\%$ at $z = 0$, which is far below the statistical precision expected from BAO analyses (about $\sim 5\%$ for a $1h^{-1}$ Gpc survey; Weinberg et al. 2012).

Furthermore, the effects of non-linear evolution on the BAO can be partially removed by applying a procedure known as reconstruction (Eisenstein et al., 2007). This procedure can be thought of as running gravity backwards: shifting dark matter or galaxies back along their displacement vectors to their expected linear theory positions. Through performing this procedure, we can remove some of the smearing of the acoustic peak which subsequently allows us to centroid it more precisely. While it is impossible to remove all the effects of non-linear structure growth using the simple 1^{st} order technique presented by (Eisenstein et al., 2007), it certainly gains us a considerable amount of precision (about a factor of 2). Any residual acoustic peak smearing can be modeled by applying a Gaussian smoothing of the acoustic oscillations in Fourier space using the prescription in Eisenstein, Seo & White (2007). A detailed description of reconstruction is given in Chapter 3, where we demonstrate, for the first time, its utility on an actual galaxy survey. We show that the statistical precision of our BAO scale measurement improves by almost a factor of 2 when we apply reconstruction to SDSS DR7 data. In the past, this procedure has been studied on N-body simulations such as Seo et al. (2008); Noh et

al. (2009); Seo et al. (2010) and Mehta et al. (2011), which serve as solid foundations for our analysis.

1.3.5.2 Redshift-space Distortions

Another source of uncertainty in BAO measurements is due to redshift-space distortions. These are observational effects that distort our measurements of redshift and our subsequent measure of clustering along the line-of-sight direction. The origin of these distortions is the peculiar velocity of galaxies on small scales and the coherent infall of galaxies on large scales. These motions add additional red or blue-shifts to the true cosmological redshifts of the galaxies which translate into the galaxies appearing slightly further or closer along the line-of-sight than they actually are. On small scales, the distribution of galaxies appears slightly elongated along the line of sight. This is known as the Finger of God (FoG) effect. On large scales, the clustering of galaxies appears squashed along the line-of-sight, an effect that has been studied and parameterized by Kaiser (1987).

Both of these effects alter the shape of the monopole clustering statistics coherently at all scales (including the BAO scale), which may slightly broaden the peak further. Hence, they must be accounted for with some degree of fidelity in our fitting templates so as to not confuse these broadband effects with the BAO information. Numerous analytic models have been proposed for modeling redshift-space distortions (Kaiser, 1987; Peacock & Dodds, 1994; Cole, Fisher & Weinberg, 1995; White, 2001), but it is unclear how well these fare at the precision levels required for BAO. Fortunately, since broadband effects are smoothly varying with scale and present regardless of whether the BAO exists or not, they are mostly separable from the acoustic information. This means that we can introduce additional marginalization (or nuisance) terms into the template to remove the unwanted broadband power without having to accurately model these effects.

In Chapter 5, we find that using simple redshift-space distortion models when we attempt to analyze the anisotropic BAO signal can lead to small biases in the measured anisotropy and inferred errors. This suggests that the simple models plus the additional marginalization is not enough to completely separate out redshift-space distortions from Alcock-Paczynski information (i.e. the “fake” anisotropy we introduce by assuming the wrong cosmology when calculating the correlation function). At our current levels of statistical precision, these biases are not detectable. This does however suggest that when the quality of data improves in the future, we will need to go to more accurate models such as discussed in Reid & White (2011).

1.3.5.3 Galaxy Bias

Lastly, a discussion of how galaxy bias may complicate BAO measurements is given here. Since we cannot directly observe dark matter, we use galaxies as tracers of the underlying dark matter distribution. However, galaxies only form in the most massive dark matter halos, so they are inherently biased tracers. This bias shows up as a multiplicative offset between $\xi(r)$ or $P(k)$ of the galaxies and the matter. At large scales, this bias is well-approximated by a constant; however, in truth there is some slight variation with scale due to non-linear structure growth. This variation may cause the acoustic peak to experience a small shift. Padmanabhan & White (2008) use perturbation theory to measure the approximate magnitude of this shift while Mehta et al. (2011) accomplishes similar aims using N-body simulations. Both studies find shifts $\sim 0.5\%$ at $z = 1$, with slightly higher shifts for more biased tracers. This is, again, much smaller than the statistical uncertainties in BAO measurements.

As with redshift-space distortions, galaxy bias is a broadband effect which we can attempt to marginalize out using nuisance parameters. Since we are only interested in the BAO information, this approach is much simpler than trying to derive complicated models of galaxy bias (e.g. Bernardeau et al. 2002 and Jeong & Komatsu

2009). We perform detailed tests of a fitting template that uses marginalization parameters for the broadband (i.e. redshift-space distortions and scale-dependent bias) in Chapter 3 and apply it to SDSS DR7 and DR9 data in Chapters 3 and 4 to measure the acoustic scale and the spherically averaged distance D_V . In Chapter 5 we use an extension of this fitting model to measure the anisotropic BAO signal in SDSS DR7 which gives us separate constraints on the transverse and line-of-sight distance scales defined by D_A and H respectively.

CHAPTER 2

A NEW STATISTIC FOR ANALYZING BARYON ACOUSTIC OSCILLATIONS

We introduce a new statistic $\omega_\ell(r_s)$ for measuring and analyzing large-scale structure and particularly the baryon acoustic oscillations. $\omega_\ell(r_s)$ is a band-filtered, configuration space statistic that is easily implemented and has advantages over the traditional power spectrum and correlation function estimators. Unlike these estimators, $\omega_\ell(r_s)$ can localize most of the acoustic information into a single dip at the acoustic scale while also avoiding sensitivity to the poorly constrained large scale power (i.e., the integral constraint) through the use of a localized and compensated filter. It is also sensitive to anisotropic clustering through pair counting and does not require any binning of data. We measure the shift in the acoustic peak due to nonlinear effects using the monopole $\omega_0(r_s)$ derived from subsampled dark matter catalogues as well as from mock galaxy catalogues created via halo occupation distribution (HOD) modeling. All of these are drawn from 44 realizations of 1024^3 particle dark matter simulations in a $1h^{-1}$ Gpc box at $z=1$. We compare these shifts with those obtained from the power spectrum and conclude that the results agree. We therefore expect that distance measurements obtained from $\omega_0(r_s)$ and $P(k)$ will be consistent with each other. We also show that it is possible to extract the same amount of acoustic information by fitting over a finite range using either $\omega_0(r_s)$ or $P(k)$ derived from equal volume surveys.

2.1 Introduction

Previous analysis of the baryon acoustic oscillations (BAO) have been conducted using the traditional power spectrum and correlation function statistics. Although analytically they are both perfectly adequate, the estimators used to derive them

from simulations and observational data are subject to numerous difficulties.

The largest survey scales are always poorly constrained due to effects such as the integral constraint making it a challenge to estimate the correlation function $\xi(r)$ accurately at these scales. The integral constraint arises due to the fact that we do not know the cosmic number density of any population of mass tracers (de Lapparent et al., 1988; Baumgart & Fry, 1991; Peacock & Nicholson, 1991; Hamilton, 1993). Many techniques used to estimate $\xi(r)$ (Peebles, 1973; Sharp, 1979; Hewett, 1982; Blanchard & Alimini, 1988; Landy & Szalay, 1993; Hamilton, 1993) take the number density of tracers in the survey volume to be the true number density. This assumption effectively ignores all power at scales larger than the survey size while simultaneously increasing the correlation between scales smaller than the survey size which causes the off-diagonal covariance matrix terms to be larger than they would be otherwise.

Limited survey volume and awkward survey boundaries are the major concerns when trying to estimate the power spectrum $P(k)$. Typically, the measured power spectrum is a convolution of the window function, the Fourier transform of the selection function of the survey, and the underlying true power spectrum (Feldman et al., 1994; Park et al., 1992; Baumgart & Fry, 1991; Peacock & Nicholson, 1991; Kaiser & Peacock, 1991). Therefore, these $P(k)$ estimators are biased. In the limit of infinite volume, the window function should be a delta function. However, real surveys have finite volume and hence the window function has a finite albeit very small width. This induces an artificial smoothing at small separations in k when attempting to deconvolve the window function from the observed density field. Pair counting estimators, like those for $\xi(r)$, avoid this issue because the relative positions of all tracer particles and hence the true distribution is recorded.

Estimating $\xi(r)$ and $P(k)$ also requires the binning of data. When any binning

process is invoked, one must carefully define any averaging used to derive the value in each bin. To reduce these errors, bin sizes are made smaller which increases the dimensionality of the covariance matrix, making it even more difficult to estimate. Also, survey boundaries need to be addressed with special care.

In the study of large scale structure, we are also interested in any anisotropies in the distribution of objects. These can result from the bulk motions of objects (Peebles, 1980; Davis & Peebles, 1983; Kaiser, 1987) as well as assumed models for the Hubble parameter $H(z)$ and the angular diameter distance $D_A(z)$ while calculating object separations along the line of sight (LOS) and transverse directions respectively. Since, at large scales we would expect the distribution to be isotropic, any anisotropy can be deconstructed into velocity field information which in turn provides us with constraints on Ω_m , the derivative of the growth function $f = d\ln D/d\ln a$ and the anisotropic parameter $\beta = f/b$, where b is the galaxy bias (Kaiser, 1987; Hamilton, 1998; Peacock et al., 2001; Hawkins et al., 2003; Tegmark, Hamilton & Xu, 2002; Zehavi et al., 2002; Song & Percival, 2008; Percival & White, 2009; White et al., 2009). After modeling these anisotropies, any residual anisotropies can be used to constrain $D_A(z)H(z)$ (Alcock & Paczynski, 1979). If our assumed $H(z)$ or $D_A(z)$ models are incorrect then the distribution of objects will still appear anisotropic after the bulk motion effects are removed. The magnitude of this residual anisotropy can be used to infer the true underlying cosmology (Padmanabhan & White, 2008; Okumura et al., 2008).

Anisotropic information can be extracted from the redshift-space correlation function and to a lesser extent from the redshift space power spectrum (Szalay et al., 1998). If one imagines a wide angle survey, $P(k)$ estimators that rely on a Fourier transform from a Cartesian grid will suffer because an arbitrary wave vector (\vec{k}) will not necessarily be parallel to the LOS (Cole, Fisher & Weinberg, 1994, 1995; Zaroubi

et al., 1995; Szapudi, 2004). This means that each \vec{k} mode will contain information about both the LOS and transverse distributions. After averaging to obtain the spherically averaged power spectrum, any anisotropies in the distribution of survey objects will have been erased. Instead of taking a spherical average, one can also analyze the full 3D $P(\vec{k})$ through Legendre decomposition into radial and angular components. However, an infinite sum is required and applicability is limited to the linear regime (Heavens & Taylor, 1995; Percival et al., 2004). Pair count estimators for $\xi(r)$, on the other hand, record the distribution of tracers accurately because they record each pair’s angle to the LOS as well as their separation. This means that any anisotropies in the distribution of galaxies will become obvious. Statistics sensitive to anisotropic clustering are desirable as they offer us a means to probe the underlying cosmology.

It is also aesthetically pleasing, to localize the acoustic information into a single feature at the acoustic scale. This is true for $\xi(r)$ but not for $P(k)$, which has oscillatory acoustic features.

Although all of the above mentioned disadvantages of $\xi(r)$ and $P(k)$ are minor, it is still beneficial to derive a new statistic that does away with as many of the above setbacks as possible. $\omega_\ell(r_s)$ is an example of such an alternative.

The organization of this chapter will be as follows. In §2.2, we introduce $\omega_\ell(r_s)$, including its properties and computation. In §2.3, we describe the simulations, halo occupation models and analysis methods we use to derive acoustic peak shifts through implementation of the monopole $\omega_0(r_s)$. We demonstrate the mutual consistency between the peak shifts measured from the same simulations using $\omega_0(r_s)$ and $P(k)$ in §2.4. This is indicative of the agreement we expect between distance measures from $\omega_0(r_s)$ and $P(k)$. We also show that with a reasonable finite fitting range and our current choice of filter for computing $\omega_\ell(r_s)$, we can extract the

same amount of acoustic information using either $\omega_0(r_s)$ or $P(k)$ from equal volume surveys. Finally, we state the main results of this chapter in §2.5. Details of the matter and galaxy model $P(k)$ results discussed in this chapter can be found in Seo et al. (2010) and Mehta et al. (2011) respectively (hereafter referred to as S&M collectively).

2.2 The $\omega_\ell(r_s)$ Statistic

2.2.1 Equations and Properties

We expand the angle dependence of the power spectrum and correlation function out as a series of Legendre polynomials in $\mu = \hat{r} \cdot \hat{z} = \cos(\theta)$, where θ is the LOS angle:

$$\xi(r, \mu) \equiv \sum_{\ell} \xi_{\ell}(r) L_{\ell}(\mu) \quad (2.1)$$

$$\Delta^2(k, \mu) \equiv \frac{k^3 P(k, \mu)}{2\pi^2} = \sum_{\ell} \Delta_{\ell}^2(k) L_{\ell}(\mu) \quad (2.2)$$

so that

$$\xi_{\ell}(r) = i^{\ell} \int \frac{dk}{k} \Delta_{\ell}^2(k) j_{\ell}(kr) \quad (2.3)$$

where j_{ℓ} is the spherical Bessel function of order ℓ and L_{ℓ} is the Legendre polynomial of order ℓ .

Imagine we have a filter, $W_{\ell}(r, \mu, r_s) = W_{\ell}(r, r_s) L_{\ell}(\mu)$, which we take to be compact and compensated ($\int r^2 dr W_{\ell}(r, r_s) = 0$) with a characteristic scale r_s . We define our statistic as the redshift-space correlation function, $\xi_s(r, \mu)$, convolved with the filter as a function of filtering scale r_s .

$$\omega_{\ell}(r_s) \equiv i^{\ell} \int d^3r \xi_s(r, \mu) W_{\ell}(r, r_s) L_{\ell}(\mu) \quad (2.4)$$

$$= \frac{4\pi i^{\ell}}{2\ell + 1} \int r^2 dr \xi_{\ell}(r) W_{\ell}(r, r_s) \quad (2.5)$$

$$= \int \frac{dk}{k} \Delta_{\ell}^2(k) \widetilde{W}_{\ell}(k, r_s) \quad (2.6)$$

with

$$\widetilde{W}_\ell(k, r_s) \equiv (-1)^\ell \frac{4\pi}{2\ell + 1} \int r^2 dr W_\ell(r, r_s) j_\ell(kr) \quad (2.7)$$

where the i^ℓ has been inserted for later convenience. By making the filter compensated, we reduce the sensitivity to the poorly constrained power at large scales and the dependence on the uncertain mean density in the sample. The correlation function is defined such that $\xi(r, \mu) + 1 \propto n^{-2}$ (Peebles, 1980). Integrating the left-hand side of this equation against $W_\ell(r, r_s) L_\ell(\mu) d^3r$ results in $\omega_\ell(r_s)$ scaling directly with n^{-2} following equation (2.4). The constant term integrates to 0 as the filter is compensated. Hence, any uncertainty in n enters as a pure multiplicative offset in $\omega_\ell(r_s)$, which is less likely to overwhelm the acoustic signature at large scales. This in essence, eliminates sensitivity to the integral constraint, which is a small effect to begin with. This feature of the filter also makes the statistic measured in different subvolumes of a survey more independent. We expect that this will make internal error estimates from methods such as bootstrap or jackknife more robust (Padmanabhan et al., 2009). Some useful expressions for evaluating the filter are given in Appendix 7.

Following Padmanabhan, White & Eisenstein (2007) we consider a low order, smooth compensated filter. For simplicity we assume W_ℓ is independent of ℓ , though we could of course choose different weights for each multipole¹. In terms of $x \equiv (r/r_s)^3$, the filter

$$W(x) = (2x)^2(1-x)^2 \left(\frac{1}{2} - x \right) \frac{1}{r_s^3} \quad (2.8)$$

satisfies $W(0) = W'(0) = W(1) = W'(1) = 0$ and $\int dx W(x) = 0$. The suggested form in configuration space (top panel of Figure 2.1) has a broad hump peaking

¹For example, we could make the k -weight for $\ell = 0$ and $\ell = 2$ equal. Doing so facilitates the computation of $Q(r) = \frac{\xi_2(r)}{3/r^2 \int_0^r \xi(r') r'^2 dr' - \xi_0(r)} = \frac{4/3\beta + 4/7\beta^2}{1 + 2/3\beta + (1/5)\beta^2}$ (Hamilton, 1992), when transformed to r_s space, since it involves both the monopole and the quadrupole. This ratio is useful for estimating the anisotropic parameter β , however, it has limited applicability outside linear theory.

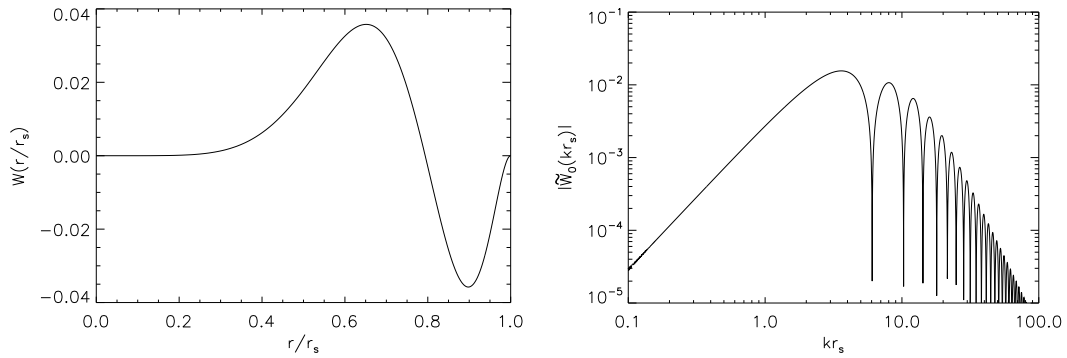


Figure 2.1: (left) The filter $W_\ell(r/r_s)$ in configuration space. There is a broad hump matching the width of the acoustic peak in $\xi(r)$ which peaks at $r \simeq 0.65 r_s$ and a sharp (negative) spike at $0.9 r_s$ with a width on the order of 10%. A filter of this shape will smear a feature, such as the acoustic peak in $\xi(r)$, by only a small amount which means that the acoustic information will be well localized in $\omega_\ell(r_s)$. Its compensated nature implies that $\omega_\ell(r_s)$ is not sensitive to the integral constraint. (right) The filter $\widetilde{W}_\ell(kr_s)$ for $\ell = 0$. The insensitivity of this filter to large scales is reflected in the fact that it is singly compensated and $\widetilde{W}_\ell \sim k^2$ as $k \rightarrow 0$. At small scales $\widetilde{W}_\ell(kr_s) \rightarrow \cos(kr_s)/(kr_s)^4$. This is a much more rapid drop-off than observed in the kernel for $\xi(r)$, which scales as $(kr)^{-1}$. These properties of the filter imply that $\omega_\ell(r_s)$ only probes a narrow range of scales in Fourier space, and that it is insensitive to large scale fluctuations or poorly constrained small-scale structure.

at $r \simeq 0.65 r_s$ that matches the width of the acoustic peak in $\xi(r)$ and a sharp (negative) spike at $0.9 r_s$ of width $\mathcal{O}(10\%)$. This filter will smear a feature, such as the acoustic peak in $\xi(r)$, by very little which means that the acoustic information will be localized in $\omega_\ell(r_s)$, however, not as localized as in $\xi(r)$. Obviously, given sufficient signal-to-noise, measuring $\omega_\ell(r_s)$ for many r_s values would allow resolution in $\xi(r)$ even below the intrinsic width of $W(r/r_s)$ (see §2.2.3).

With this choice of W_ℓ the window function \widetilde{W}_ℓ can be computed analytically (see Appendix for numerical details) or numerically via fast Hankel transforms. We show $\widetilde{W}_\ell(kr_s)$ for $\ell = 0$, in the bottom panel of Figure 2.1. Since the filter is singly compensated, $\widetilde{W}_\ell \sim k^2$ as $k \rightarrow 0$, reflecting insensitivity to large scales. At small scales $\widetilde{W}_\ell(kr_s) \rightarrow \cos(kr_s)/(kr_s)^4$, a much more rapid convergence than evinced by the kernel for $\xi(r)$, which scales as $(kr)^{-1}$. Thus ω_ℓ probes a narrow range of scales in Fourier space and is insensitive to fluctuations on large scales or poorly measured or modeled small-scale structure. One can choose the range of k to be sampled by appropriate choice of r_s : more information from high k modes can be included by using smaller r_s .

As an example, the linear theory monopole statistic $\omega_0(r_s)$ is plotted in Figure 2.2. Plotting $r_s^2 \omega_0$ versus r_s gives a convenient vertical range. The acoustic information is mostly localized into a single dip around the acoustic scale (see §2.4.2.1).

2.2.2 Computation

It is possible to adapt $\omega_\ell(r_s)$ into a sum over unbinned pair counts for any sample of mass tracers following the methods described in Padmanabhan, White & Eisenstein (2007); there is no need to first compute $\xi(r, \mu)$ via binning of data. Pair counting allows us to record each galaxy's angle to the LOS (μ) accurately. Hence, like $\xi(r)$, $\omega_\ell(r_s)$ is sensitive to any anisotropies of the tracer distribution in clusters (discussed in §2.1).

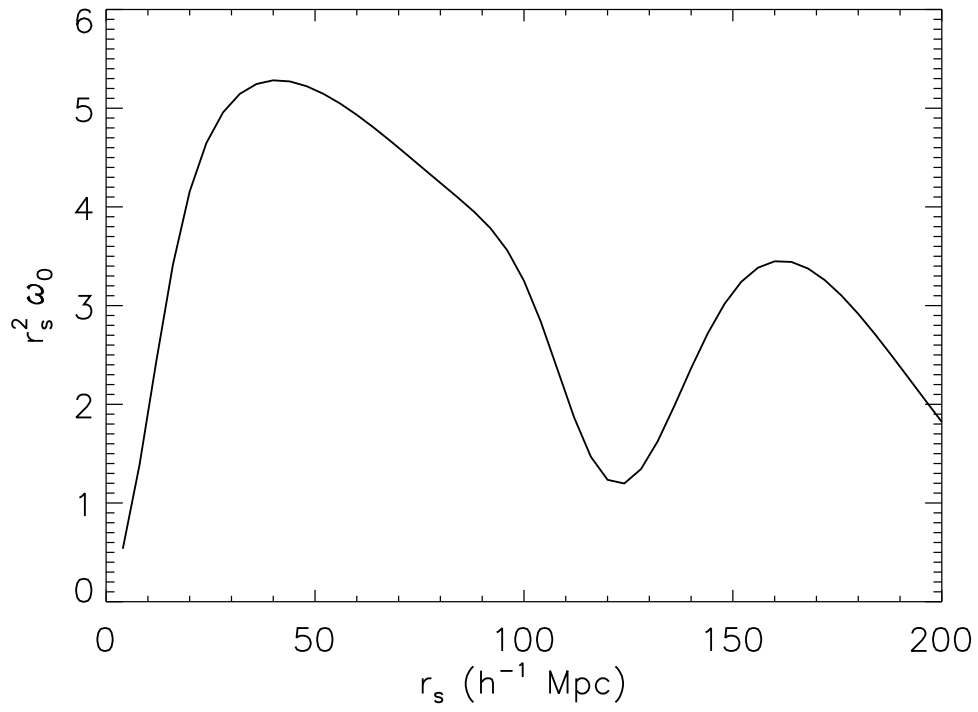


Figure 2.2: Linear theory monopole statistic $\omega_0(r_s)$. The acoustic information can be seen around the acoustic scale, mainly localized into a single dip feature.

The redshift-space correlation function can be estimated as

$$\xi_s(r, \mu) = \frac{DD(r, \mu)}{RR(r, \mu)} - 1, \quad (2.9)$$

where $DD(r, \mu)$ is the number of data tracer pairs separated by r and have LOS angle corresponding to μ . $RR(r, \mu)$ is the analogue for randomly distributed points, normalized to the data counts by a factor of N_D^2/N_R^2 . Here, N_D and N_R are the total number of data and random points respectively. When analyzing observational data, the number of random points needs to be much larger than the number of data points to keep the shot-noise in RR smaller than that in DD , especially at small r . For simulation data, however, it is not necessary to use a very large number of random points to compute RR smoothly at small scales (elicited below).

Equation (2.9) implies that Equation (2.4) can be rewritten as

$$\omega_\ell(r_s) = i^\ell \int d^3r W_\ell(r) L_\ell(\mu) \frac{DD(r, \mu)}{RR(r, \mu)}. \quad (2.10)$$

The -1 integrates to 0 due to the compensated nature of the filter.

The RR piece is purely geometrical and is dependent only on the survey geometry (encoded in $\Phi(r, \mu)$) and the number of random points. Hence we can write RR as

$$RR(r, \mu) = 2\pi n_D N_D r^2 \Phi(r, \mu) dr d\mu \quad (2.11)$$

where n_D is the number density of data points which is easily calculable for surveys with well defined boundaries. The above equation defines $\Phi(r, \mu)$ to be any mismatch between infinite sized surveys/simulations and finite sized ones due to the presence of boundaries. The $n_D N_D$ factor is due to the normalization of the RR counts as mentioned above. For observations, $\Phi(r, \mu)$ can be computed via binning methods and then fit using a smooth function $\hat{\Phi}(r, \mu)$. Note that the binning mentioned here is only required in the computation of the RR counts; there is no need to bin the

data. In the case of simulations in a periodic box, $\hat{\Phi}(r, \mu)$ is constant as the volume is effectively infinite.

With these points in mind, we can now pick arbitrarily small bins when computing the DD counts since RR has been approximated by a smooth function and hence does not suffer from shot-noise induced through pair-counting. As is such, we may employ a binning scheme in which there is either zero or one DD pair per bin. This step reduces the integral in Equation (2.10) to a sum over DD pairs as in

$$\omega_\ell(r_s) = i^\ell \sum_{i \in DD} \frac{W_\ell(r_i) L(\mu_i)}{n_D N_D V \hat{\Phi}(r_i, \mu_i)}. \quad (2.12)$$

Since the estimator can be written as a summation, there is no longer a need to bin data at all.

2.2.3 Covariance Matrix

Since ω_ℓ does not require the binning of data, we can in principle estimate it at as many r_s values as we wish without affecting the signal in the adjacent values: there is no bin which is made smaller. However adjacent points become increasingly correlated as the r_s spacing decreases, compromising the usefulness of very fine sampling.

In the Gaussian limit, the covariance matrix is

$$\begin{aligned} \text{Cov} \quad [\omega_\ell(r_s), \omega_{\ell'}(r'_s)] &= \frac{2(2\ell + 1)(2\ell' + 1)}{V} \\ &\times \int \frac{k^2 dk}{2\pi^2} \widetilde{W}_\ell(kr_s) \widetilde{W}_{\ell'}(kr'_s) \mathcal{I}_{\ell\ell'}(k) \end{aligned} \quad (2.13)$$

with

$$\mathcal{I}_{\ell\ell'} = \frac{1}{2} \int d\mu L_\ell(\mu) L_{\ell'}(\mu) \left[\sum_L P_L(k) L_L(\mu) + \aleph \right]^2 \quad (2.14)$$

where $\sum P_L(k) L_L(\mu)$ is the legendre decomposition of the full 3D power spectrum $P(\vec{k})$ and \aleph is shot-noise. Assuming Poisson shot-noise, $\aleph = \bar{n}^{-1}$, where \bar{n} is the number density of the mass tracer.

2.2.4 Summary of Key Features

We conclude this section with a summary of the key features and advantages of $\omega_\ell(r_s)$ over $\xi(r)$ and $P(k)$ estimators.

1. $\omega_\ell(r_s)$ has a compensated filter that reduces sensitivity to poorly constrained large scale power and hence the integral constraint. $\xi(r)$, on the other hand, experiences these problems. The compensated filter also makes $\omega_\ell(r_s)$ measured in different subvolumes of the survey more independent which is important for attaining robust error estimates from methods such as bootstrap and jackknife.
2. The filter is approximately compact in both configuration and Fourier space. The smoothness in configuration space leads to the steep drop-off at high k in Fourier space. This effectively minimizes the impact of large k or small scale power which is not well constrained in large cosmological surveys. The filter is localized in configuration space which means that, unlike in $P(k)$, the acoustic information is localized in $\omega_\ell(r_s)$. However, it is not as localized as in $\xi(r)$ (see §2.4.2.1).
3. Like $\xi(r)$, $\omega_\ell(r_s)$ can be easily adapted into a pair count statistic, so the relative positions of tracers and each pair's angle from the LOS is accurately recorded. Hence, it estimates the underlying galaxy distribution without the need to deconvolve a window function (as in the case of $P(k)$) and is sensitive to any anisotropies in the clustering of tracers. The anisotropies can be used to determine the underlying cosmology. $P(k)$ estimators do not typically allow this type of analysis.
4. There is no need to bin data when computing $\omega_\ell(r_s)$, unlike when estimating $\xi(r)$ and $P(k)$.

While the setbacks of traditional $P(k)$ and $\xi(r)$ estimators are minor, it is beneficial to have a statistic like $\omega_\ell(r_s)$ which combines many of the advantages of both.

2.3 Simulations and Analysis Methods

A major goal in developing this new statistic is to use it for better measuring and calibrating the acoustic scale. The monopole statistic $\omega_0(r_s)$ is especially useful in this regard as it is a direct map from the traditional 2-point correlation function and power spectrum. Therefore, any results obtained from BAO analysis via these three statistics is readily comparable. As with the quadrupole of the power spectrum $P_2(k)$ (Padmanabhan & White, 2008), anisotropic BAO analysis can be performed using the quadrupole $\omega_2(r_s)$. However, as the main goal of this chapter is to give a broad introduction to the $\omega_\ell(r_s)$ statistic and a simple demonstration of its application, we defer detailed discussion of $\omega_2(r_s)$ and anisotropic BAO to a future paper (the analysis of anisotropic correlation functions is discussed in 5).

In this section, we implement $\omega_0(r_s)$ through the use of pure dark matter N-body simulations. It is possible to model a variety of different galaxy populations and biases through application of appropriate HODs to the halos found in the simulations. This is important in demonstrating the robustness of the $\omega_\ell(r_s)$ statistic over a diverse set of galaxy populations. We compute $\omega_0(r_s)$ for dark matter and the mock galaxy populations created via the HODs, and demonstrate how it can be used to measure the shift in the acoustic peak. This quantity is important in constraining the precise size of the acoustic scale, which may be slightly different from that predicted by linear theory due to nonlinear structure growth. In order to quote the shift with accurate errors, we use a resampling technique described in §2.3.4 which gives us a large number of shifts from which to calculate a mean and a standard error of that mean.

2.3.1 Simulations

Our simulations were performed using a code developed by Metchnik and Pinto which employs a new method (Metchnik & Pinto, 2010) to compute N-body forces under periodic boundary conditions. Rather than resorting to the Fourier methods of PM schemes or using Ewald sums to represent periodicity, this new method represents periodicity directly, expressing the force on a particle as due to the rest of the simulation volume and an infinite sum over its periodic images.

This is made more efficient by partitioning the computational domain into a three-dimensional grid. The acceleration on particles within a grid cell is divided into two parts: a near field and a far field. The near field is that due to the other particles in the cell and to particles in the adjacent 26 cells. In these calculations, the near-field acceleration was computed using the direct, $O(N^2)$ method, with Plummer softening.

The far field acceleration on particles in the cell due to each more distant cell on the grid is represented as a Taylor series expansion based on the multipole moments in the distant cell. The contribution from all periodic images of the distant cell is included by recognizing that the multipole moments in a cell are identical to those in all of its images. Thus, the sum over images depends only on the (fixed) geometry of the grid and need be performed only once. The (relatively) small set of values which results provides a simple and rapidly-evaluated relation between the multipole moments in distant grid cells and the Taylor coefficients of the expansion for the acceleration in a given cell, all under periodic boundary conditions. The acceleration due to all of the periodic images of the cell and its 26 neighbors is included in a similar manner.

The calculations described here used order-16 expansions, providing an overall force accuracy per particle which agrees with Ewald summation to better than six

decimal digits. Overall, the method is significantly faster and requires significantly less memory than other methods for computing accelerations in large, periodic N-body problems, while providing accelerations to machine precision for all particles. Time integration was performed using a standard kick-drift-kick algorithm, using independent time steps for each particle.

We derive our results in redshift-space at $z = 1$ from a set of 44 simulations with 1024^3 dark matter particles in each. The simulations were performed in $1h^{-1}$ Gpc periodic boxes with the WMAP5+SN+BAO best-fit cosmological parameters: $\Omega_m = 0.279$, $\Omega_\Lambda = 0.721$, $h = 0.701$, $\Omega_b = 0.0462$, $n_s = 0.96$ and $\sigma_8 = 0.817$ (Komatsu et al., 2009) which implies a particle mass of $7.2 \times 10^{10} h^{-1} M_\odot$. The initial conditions are generated via the second-order Lagrangian perturbation theory code of Sirko (2005) at $z = 50$ with no extra power for the box scale.

2.3.2 Halo Occupation Distributions

We use a simple friends-of-friends (Davis et al., 1985) method with a linking length equal to 0.16 of the interparticle spacing to identify the collapsed dark matter halos in our simulations. We then populate these halos with galaxies by applying simple HODs based on the form

$$\langle N_g(M) \rangle = [1 + (M/M_{\text{sat}})^\gamma] \exp(-M_{\text{cen}}/M) \quad (2.15)$$

where M is the halo mass, M_{cen} is the minimum mass for a halo to contain a central galaxy, M_{sat} is the minimum mass for a halo to contain at least one satellite, and γ is an exponential parameter that we set to 1 (Guzik & Seljak, 2002; Berlind et al., 2003; Kravtsov et al., 2004; Zheng et al., 2005). We assign a central galaxy to a halo if $M > M_{\text{cen}}$, this is a good approximation to $\langle N_{\text{cen}}(M) \rangle = \exp(-M_{\text{cen}}/M)$. The central galaxy is taken to be at the halo's center of mass and assigned the center of mass velocity. If a halo is assigned a central galaxy, then the number of

satellite galaxies is determined by generation of a random integer based on a Poisson distribution with mean equal to $\langle N_{\text{sat}}(M) \rangle = (M/M_{\text{sat}})^\gamma$. We then randomly pick a corresponding number of halo particles and assign their positions and velocities to the satellites.

In order to compare the peak shifts derived using $\omega_0(r_s)$ and $P(k)$ in a range of models, we apply three different HODs to our simulations. The properties of these HODs are described in Table 2.1 and obtained by adjusting the values of M_{cen} and M_{sat} . We also list the properties of a dark matter (DM) only case that is merely a 0.4% subsample of the particles in each simulation. We compute $\omega_0(r_s)$ in redshift-space via the pair counting method detailed in §2.2.2 within the range $5h^{-1}\text{Mpc} \leq r_s \leq 200h^{-1}\text{Mpc}$ using $5h^{-1}\text{Mpc}$ spacing. We also compute σ_8 , the RMS mass fluctuation within a $8h^{-1}\text{Mpc}$ radius, using a similar pair counting method derived from the configuration space equation for a general radius R (Zehavi et al. (2005))

$$\sigma_R^2 = \int_0^{2R} \frac{1}{R^3} \left[3 - \frac{9}{4} \frac{r}{R} + \frac{3}{16} \left(\frac{r}{R} \right)^3 \right] r^2 \xi(r) dr. \quad (2.16)$$

2.3.3 Fitting $\omega_0(r_s)$ to Measure the Peak Shift

We fit the redshift-space $\omega_0(r_s)$ using the form

$$P_{\text{sim}}(k) = B(k)P_m(k/\alpha) + A(k) \quad (2.17)$$

where

$$B(k) = \frac{(b_1^2 + b_2^2 k + b_3^2 k^2)}{1 + r_{\text{scale}} k} \quad (2.18)$$

and $A(k)$ transforms into $A(r_s) = a_1 r_s^{-9}$ in r_s space. Such a form for $A(k)$ is motivated by the fact that we want to marginalize over the shape of the correlation function at small scales (i.e., the contribution of the 1-halo term). Expanding Equation (2.8), we see that $W(x) = (-4x^5 + 2x^4 - 8x^3 + 2x^2) \frac{1}{r_s^3}$. This implies that the

Table 2.1: HOD properties. HODs are referred to by the designations under the “Model” heading throughout the paper.

Model	Total # of Galaxies ¹	Satellite Fraction (%)	M_{cen} ($h^{-1}M_{\odot}$)	M_{sat} ($h^{-1}M_{\odot}$)	\bar{n} ² ($h^3\text{Mpc}^{-3}$)	$\bar{n}P_{0.2}$	\aleph_{nonlin}
DM	4×10^6	-	-	-	0.004	4.60	0.0
HOD1	2×10^6	5	1.4×10^{12}	9.2×10^{13}	0.002	5.78	450.0
HOD2	1×10^6	5	2.6×10^{12}	1.5×10^{14}	0.001	3.59	700.0
HOD3	3×10^5	5	6.4×10^{12}	3.1×10^{14}	0.0003	1.59	1550.0

¹Number of DM particles in the DM only case.

²The nominal Poisson shot-noise is \bar{n}^{-1} .

highest order term in r_s is r_s^{-9} . At small scales, this is the term that will dominate in the transformation from $\xi(r)$ to $\omega_0(r_s)$ as defined by Equation (2.4).

$P_m(k)$ is the template power spectrum we use for our fitting. To account for the degradation of the acoustic peak through nonlinear evolution and redshift distortions, the template model $P_m(k)$ is obtained from the linear power spectrum $P_{\text{lin}}(k)$ at $z = 1$ by the modification

$$P_m(k) = [P_{\text{lin}}(k) - P_{\text{smooth}}(k)]\exp(-k^2\Sigma_{\text{nl}}^2/2) + P_{\text{smooth}}(k) \quad (2.19)$$

where P_{smooth} is the dewiggled power spectrum described in Eisenstein & Hu (1998) and Σ_{nl} is a nonlinear parameter used to degrade the peak (Eisenstein et al., 2005; Tegmark et al., 2006; Crocce & Scoccimarro, 2006; Eisenstein, Seo & White, 2007; Crocce & Scoccimarro, 2008; Matsubara, 2008a). To allow maximum flexibility in our marginalization, we marginalize over Σ_{nl} and the other nonlinear nuisance parameter in equation (2.18), r_{scale} .

Our scale dilation parameter α represents the shift in the acoustic peak. Under this formalism, $\alpha > 1$ indicates a shift towards smaller scales and $\alpha < 1$ indicates a shift towards larger scales. Physically, α is the ratio between the linear theory acoustic scale (150 Mpc) to the measured acoustic scale. Since all the terms in the fitting function are additive, the basis functions $P_m(k/\alpha)/(1 + r_{\text{scale}}k)$, $kP_m(k/\alpha)/(1 + r_{\text{scale}}k)$, $k^2P_m(k/\alpha)/(1 + r_{\text{scale}}k)$, and r_s^{-9} for a fixed α , Σ_{nl} and r_{scale} can be easily mapped into r_s space (if necessary) using equation (2.6). A least-squares fit using the mapped basis functions is then performed against $\omega_0(r_s)$ from the simulations to obtain values for the linear nuisance parameters b_1 , b_2 , b_3 and a_1 . As we are interested in the acoustic feature, we use a fitting range of $30 \leq r_s \leq 200h^{-1}\text{Mpc}$. For an r_s spacing of $5h^{-1}\text{Mpc}$, this implies 28 degrees of freedom in the fit, where the number of degrees of freedom is defined as the difference between the number of data points being fit and the number of parameters in

Table 2.2: Fit results for each HOD model. Fitting range: $30 \leq r_s \leq 200h^{-1}\text{Mpc}$. σ_α is the error on the mean α of the 44 simulations.

Model	$\alpha - 1$	σ_α	Σ_{nl}	r_{scale}	χ^2	bias ¹	σ_8
	(%)	(%)			(per d.o.f)	(b)	
DM	0.0457	0.2333	6.66	19.99	0.92	1.25	0.63
HOD1	0.1065	0.2243	5.61	19.78	0.94	2.04	1.11
HOD2	0.1634	0.2449	5.85	19.98	0.86	2.28	1.25
HOD3	0.4897	0.3326	6.27	20.04	0.72	2.77	1.55

¹Bias is not equal to 1 for the DM only case because we are working in redshift space.

the fitting form.

We assume that the errors on $\omega_0(r_s)$ can be well approximated by the covariance matrix C assuming Poisson shot-noise (see §2.3.4) with the addition of nonlinear shot-noise (see equation (2.20) and surrounding text). We also assume that the monopole ($\ell = 0$) dominates $P(\vec{k})$ so that all higher order contributions to the power spectrum are effectively zero. This amounts to computing C using $P(\vec{k}) = P_m(k)$ as the input power spectrum, where we take a fixed $\Sigma_{nl} = 7.0h^{-1}\text{Mpc}$ at $z = 1$ in redshift-space following Seo et al. (2008). We normalize this power spectrum to the amplitude of the redshift-space power spectrum through multiplication by the bias squared defined initially as $b^2 = (\sigma_{8,\text{case}}/\sigma_{8,\text{matter}})^2$. The values for $\sigma_{8,\text{case}}$ are given in Table 2.2 and $\sigma_{8,\text{matter}} = 0.506$ in real space at $z = 1$ in linear theory. We want to ensure that the input power spectrum to the covariance matrix calculation is as close as possible to the simulation data so that the covariance matrix is a reliable estimate of the errors. To do this, we marginalize over the average $\omega_0(r_s)$ of the 44 simulations for each case to obtain a value for the leading order term that scales $P_m(k)$: b_1^2 in

the fitting form of equation (2.18). We then iterate this marginalization and scale b^2 by the values of b_1^2 obtained until the output b_1^2 from this iterative fitting is close to 1. We expect that scaling $P_m(k)$ by this final value of b^2 will approximate the simulation data well and hence be valid input to the covariance matrix calculation for the resampling techniques described in §2.3.4.

The shot-noise we enter into the calculation of C includes a nonlinear component (quoted in Table 2.1) in addition to the Poisson shot-noise \bar{n}^{-1} as described in Equation (2.13). This additional shot-noise is a result of nonlinear structure formation on small scales. We estimate this nonlinear shot-noise as

$$\aleph_{\text{nonlin}} = \int_0^{r_{\text{nonlin}}} 4\pi r^2 [\xi(r) - \xi_{\text{lin}}(r)] dr \quad (2.20)$$

where $\xi(r)$ is the correlation function averaged over the 44 simulations for each HOD, $\xi_{\text{lin}}(r)$ is the linear correlation function at $z = 1$ and r_{nonlin} is the scale above which nonlinear effects become unimportant. We take r_{nonlin} to be $10h^{-1}\text{Mpc}$. The resulting \aleph_{nonlin} is a rough estimate of the excess small scale correlation due to nonlinear evolution. Since it makes little difference whether all of this extra shot-noise comes in at zero separation in r or through the extended effects of the one-halo term, which is only important at small r , we assume the excess correlation to be a spike at $r = 0$ for convenience. When transformed into k space, this gives a constant and becomes extra white noise that we add on to every mode equally, in addition to the Poisson shot-noise. For the subsampled DM case, the linear and the measured correlation functions were sufficiently similar at $1\text{-}10h^{-1}\text{Mpc}$ to warrant taking $\aleph_{\text{nonlin}} = 0$ for this case. Alternatively, one can also account for nonlinear shot-noise by computing the covariance matrix using the nonlinear power spectrum, but this is more computationally challenging.

The χ^2 likelihood indicator corresponding to the best-fit linear nuisance param-

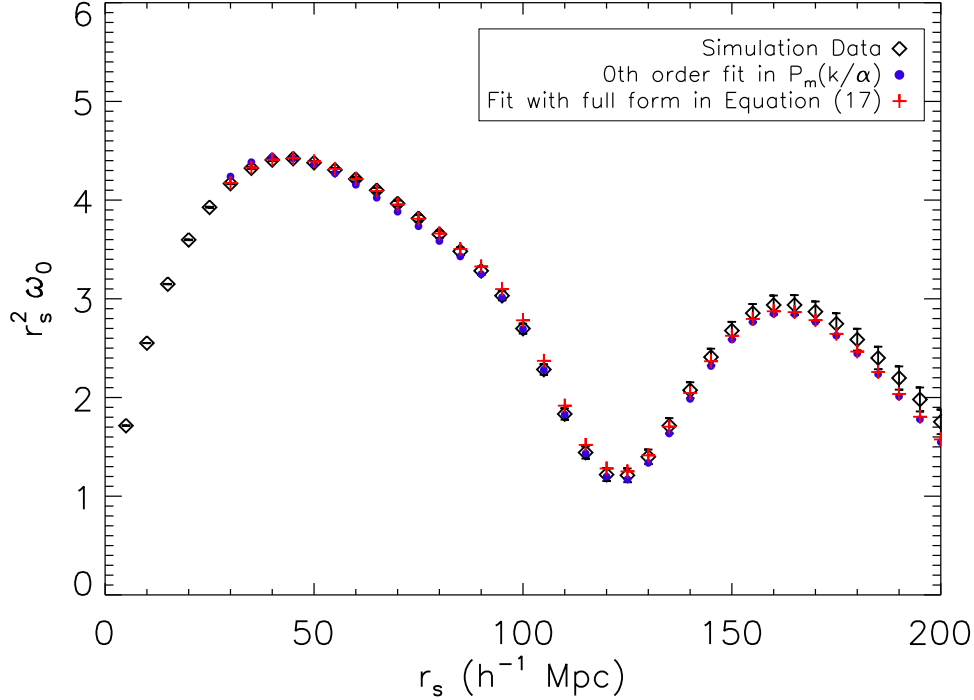


Figure 2.3: $\omega_0(r_s)$ averaged over all 44 simulations for HOD1 (black diamonds). Overplotted are a fit obtained through the form in Equation (2.17) (red crosses) and a 0th order fit in $P_m(k/\alpha)$ (purple dots), both over a range of $30 \leq r_s \leq 200 h^{-1} \text{Mpc}$. One can see that the 0th order fit already appears quite good with $\chi^2 = 2.20$ per dof. However, by introducing additional nuisance parameters, the quality of the fit over the specified range improves further to $\chi^2 = 0.94$ per dof.

eters for fixed α , Σ_{nl} and r_{scale} is then

$$\chi^2 = (\vec{\omega}_0 - \vec{m})^T C^{-1} (\vec{\omega}_0 - \vec{m}) \quad (2.21)$$

where $\vec{\omega}_0$ is $\omega_0(r_s)$ measured from the simulations, \vec{m} is the best-fit model and C^{-1} is the inverse of the covariance matrix. We compute the best-fit values of α , Σ_{nl} and r_{scale} by minimizing χ^2 of the fits for the DM case and for each HOD using a generalized reduced gradient method from IDL. We quote the bias for each case as $\sigma_{8,\text{case}}/\sigma_{8,\text{matter}}$ multiplied by the additional scaling factors of b_1 described above.

We plot $\omega_0(r_s)$ averaged over all 44 simulations for HOD1 in Figure 2.3. Overplotted are the marginalization obtained through the form in Equation (2.17) and

a *0th* order fit obtained by just a rescaling of $P_m(k/\alpha)$, i.e. $b^2 P_m(k/\alpha)$ where b is the only fit parameter. Although the *0th* order fit already appears quite good, one can see that introducing additional nuisance parameters improves the quality of the fit even more over the fitting range. The χ^2 per degree of freedom (dof) improves from 2.20 to 0.94.

Using this fitting technique, we derive values of bias, α and associated errors for each of our three HODs and our DM case via the resampling methods described in the following section.

2.3.4 Resampling Methods

We use two different methods to measure the mean peak shift α and the scatter in the mean σ_α for each case in Table 2.1. The first is a modified jackknife technique in which we randomly select M out of N simulations at a time without replacement, average their $\omega_0(r_s)$ and fit this average. We repeat this 1000 times and extract an average α and a scatter in α . This scatter needs to be rescaled by an additional factor of $f = \sqrt{M}/\sqrt{N-M}$ in order to reflect the scatter associated with the mean of α for N simulations. For our simulations we have $N = 44$ and take $M = 22$. With this choice of M , $f = 1$ and so the scatter in α reflects the error in the mean of α . This method is useful in that it provides us with a large set of α 's from which we can accurately derive a mean α and σ_α .

The fit results for the subsampled DM case as well as for each HOD model are quoted in Table 2.2. The average values of Σ_{nl} and r_{scale} are also included for completeness, however the focus of this chapter is on α . The values of α we obtain are 1σ consistent with those derived using the perturbation theory results of Padmanabhan & White (2009). The somewhat low value of χ^2 per dof for HOD3 suggests that we are overestimating the amount of nonlinear shot-noise. We are also approaching the shot-noise limited regime for HOD3 as evidenced by the fact

Table 2.3: Difference in mean α between $\omega_0(r_s)$ and $P(k)$.

Model	$\langle \Delta\alpha_{\omega P} \rangle$
	(%)
DM	0.0516 ± 0.1205
HOD1	0.0076 ± 0.0672
HOD2	0.0205 ± 0.0600
HOD3	0.1035 ± 0.0665

$\bar{n}P_{0,2} \approx 1.6$. We note here that we used χ^2 only to find the best-fit α for each HOD, not to generate the errors. Hence, the fact that our reduced χ^2 values are slightly deviant from unity does not hinder the error estimation.

The second method we use is jackknife resampling. The results obtained using this method are in good agreement with the first method. This indicates that the error estimates obtained using our first method are robust in comparison to more traditional methods.

By using these resampling techniques, any non-Gaussian effects not accounted for by assuming a Gaussian covariance matrix while fitting (as in §2.3.3) will be reflected in σ_α .

2.4 Comparison to the Power Spectrum

2.4.1 Comparison from Simulations

An important step in implementing this new statistic is to show that it produces consistent results when compared to established methods and can therefore be an effective calibrator of the acoustic scale. We do this by comparing the peak shifts measured from the same set of simulations via the new $\omega_0(r_s)$ statistic and the

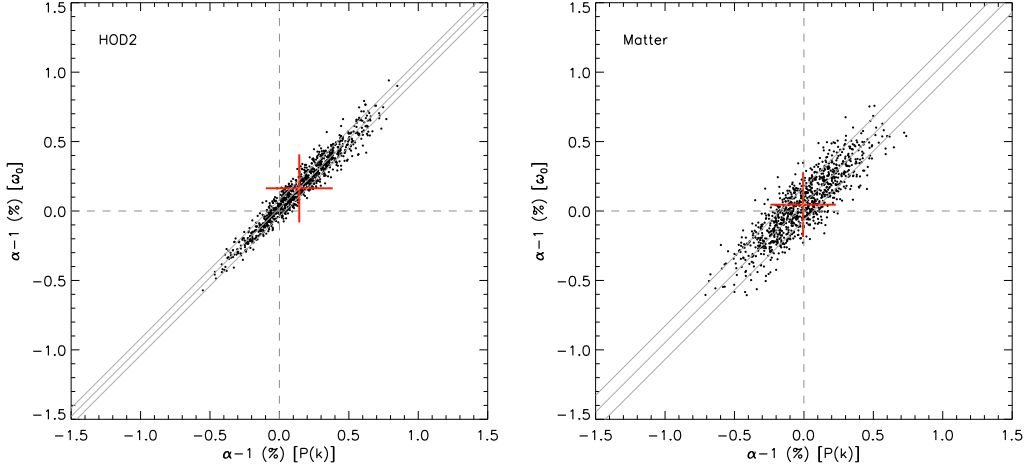


Figure 2.4: α from $\omega_0(r_s)$ versus α from $P(k)$ for HOD2 (top) and DM (bottom). The data points are from a resampling technique in which we randomly pick $M = 22$ simulations out of $N = 44$ total and fit the averaged $\omega_0(r_s)$ from these M simulations. We repeat this 1000 times and hence obtain 1000 values of α . The scatter on α needs to be rescaled by $\sqrt{M}/\sqrt{N-M}$ to reflect the true scatter on the mean. For our choice of M , this scaling factor is equal to 1. Hence the scatter in the plot truly reflects the scatter on the mean of α . The red cross marks the mean α values with their associated errors. The central grey line has unity slope and passes through the mean. The two outer grey lines delineate the 1σ boundaries associated with $\Delta\alpha_{\omega P}$. As the data points lie largely in between the 1σ lines with a slope similar to unity for both HOD2 and the DM case (see Table 2.3), we conclude that the two α sets are consistent with each other. The same correlation is observed for HOD1. HOD3 shows 1.6σ agreement between $\omega_0(r_s)$ and $P(k)$. This slightly larger discrepancy may be due to the fact that shot-noise is becoming significant in this low number density case. Also, shot-noise may affect $P(k)$ and $\omega_0(r_s)$ differently or the nuisance parameters may not be fully handling the scale-dependence of a high-bias HOD such as HOD3. The large scatter in the DM case is likely due to the subsampling of matter in the computation of $\omega_0(r_s)$ but not in $P(k)$. The overall agreement between the $\omega_0(r_s)$ and $P(k)$ results imply that distance measures will be consistent between the two.

traditional $P(k)$ method (see S&M for details).

As we use the same 1000 random sets of M simulations as S&M, there should be a 1:1 correspondence between the α 's derived from $\omega_0(r_s)$ and $P(k)$ for the DM case and for each HOD. It should be noted that S&M use different $P(k)$ fitting forms from the one detailed in §2.3.3. They employ two fitting forms, both of which can also be described by equation (2.17). The first form has $B(k)$ as a 2nd order polynomial and $A(k)$ as a 7th order polynomial. The second form uses Pade approximants for $B(k)$, i.e., $B(k) = b_0(1 + c_1k + c_3k^2 + c_5k^3)/(1 + c_2k + c_4k^2)$ and a 2nd order polynomial for $A(k)$. We have chosen a different form in this work to induce better convergence of the integral from Fourier space to r_s space while transforming the basis functions. We compare the α 's measured from $\omega_0(r_s)$ against those measured from $P(k)$ by Seo et al. (2010) (DM) and Mehta et al. (2011) (HODs) using the first form. It should also be noted here that the $P(k)$ results obtained for the DM case by Seo et al. (2010) utilize the full DM sample whereas we have subsampled to reduce computation time in this work. The methodology used to derive the $P(k)$ results are described in detail in Seo et al. (2010).

Figure 2.4 shows α from $\omega_0(r_s)$ versus α from $P(k)$ for the 1000 fit iterations performed on HOD2 (top) and DM (bottom). The red cross indicates the mean α values with their associated errors. The central grey line is a line with slope unity that passes through the mean. The two outer grey lines indicate the 1σ boundaries associated with $\Delta\alpha_{\omega P} = \alpha_{\omega} - \alpha_P$. The mean difference between α_{ω} and α_P along with the standard deviation is quoted in Table 2.3 under $\langle\Delta\alpha_{\omega P}\rangle$ for the DM case as well as each HOD case. The plots indicate that the correlation between α_{ω} and α_P is 1σ consistent with a line of slope unity that has a y-intercept of 0 for both HOD2 and the DM case. This implies that the two α sets are consistent with each other. The same holds for HOD1 as evidenced through the table, but

HOD3 is slightly more deviant with 1.6σ agreement between $\omega_0(r_s)$ and $P(k)$. The larger discrepancy between the HOD3 results may be due to the fact that shot-noise is becoming significant in this case (as shown in §2.3.4). It could also be that shot-noise affects $P(k)$ and $\omega_0(r_s)$ differently or the nuisance parameters are not fully handling the scale-dependence of a high-bias HOD such as HOD3. The large scatter in the DM case is likely due to the fact that we have subsampled the matter in our computation of $\omega_0(r_s)$ but not in $P(k)$. The α 's from most of the cases are 1σ consistent between $\omega_0(r_s)$ and $P(k)$, indicating that distance measures will be consistent between the two statistics. This also indicates that any systematics introduced by using the different fitting forms for $P(k)$ and $\omega_0(r_s)$ are minor. Hence we conclude that $\omega_0(r_s)$ is a well-tuned statistic for analysis of BAOs.

2.4.2 Theory Constraints on σ_α

As we wish to promote $\omega_0(r_s)$ as an alternative method for analyzing the BAO, it is necessary to show how much acoustic information can be extracted from $\omega_0(r_s)$ relative to $P(k)$ and $\xi(r)$ for surveys of the same size. If our fitting ranges were infinite, then by the definitions in §2.2, all three estimators should yield the same amount of BAO information. However, in reality, fitting ranges are finite.

We investigate the effects of this by shifting the acoustic feature in the linear theory $\omega_0(r_s)$, $P(k)$ and $\xi(r)$ by a given α and then running our fit algorithms to see how well we can recover this input α . For $\omega_0(r_s)$ we fit between $r_s = 30\text{-}210h^{-1}\text{Mpc}$ in r_s spacings of $2.5h^{-1}\text{Mpc}$; for $P(k)$ we fit between $k = 0.0\text{-}1.2h\text{Mpc}^{-1}$ in $\log(k)$ spacings of ~ 0.002 ; and for $\xi(r)$ we fit between $r = 20\text{-}200h^{-1}\text{Mpc}$ in r spacings of $1h^{-1}\text{Mpc}$. We use the same fitting technique as described in §2.3.3 but with different forms for $B(k)$ and $A(k)$ that are then transformed to r and r_s space to fit $\xi(r)$ and $\omega_0(r_s)$ respectively. This means that the fitting forms for $P(k)$, $\xi(r)$ and $\omega_0(r_s)$ all derive from the same $B(k)$ and $A(k)$ functions. By enforcing this

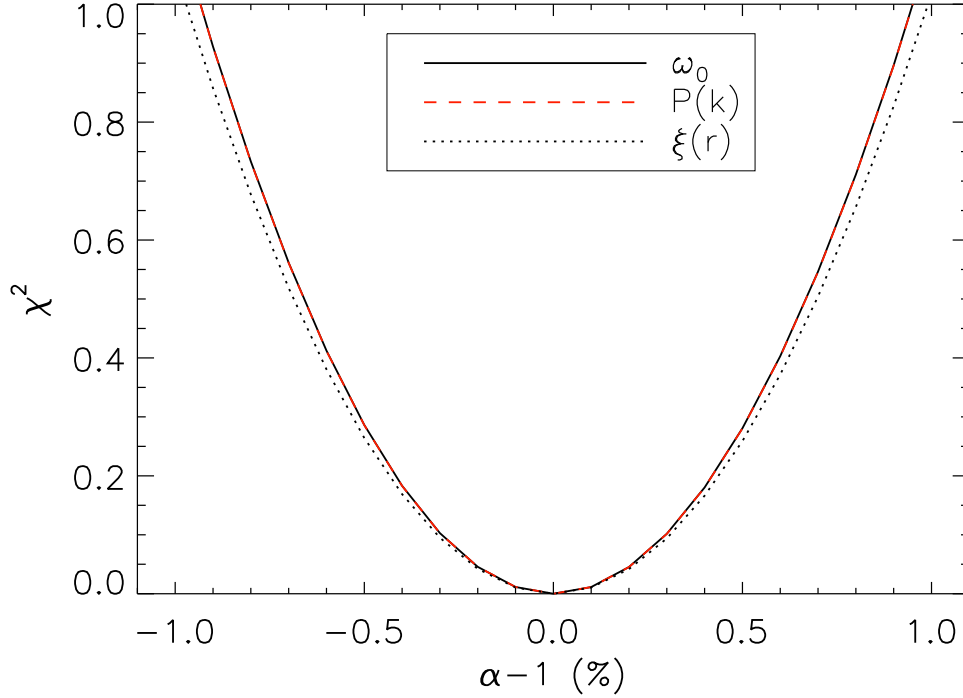


Figure 2.5: χ^2 versus α for fits in $\omega_0(r_s)$, $P(k)$ and $\xi(r)$. We shift the acoustic feature from linear theory by a given α (here $\alpha_{given} = 1.0$) and run our fit algorithms to see how well we can recover this input. For $\omega_0(r_s)$ we fit between $r_s = 30\text{-}210h^{-1}\text{Mpc}$, for $P(k)$ we fit between $k = 0.0\text{-}1.2h\text{Mpc}^{-1}$ and for $\xi(r)$ we fit between $r = 20\text{-}200h^{-1}\text{Mpc}$. The parabolic shape of the curves is due to the fact that $\omega_0(r_s)$, $P(k)$ and $\xi(r)$ are derived from a Gaussian random field in linear theory. The width of the parabola at $\chi^2 = 1$ is then the theoretical σ_α of the fit. The $\omega_0(r_s)$ and $P(k)$ curves overlap nicely, implying that the σ_α ratio between $\omega_0(r_s)$ and $P(k)$ is ~ 1 . This indicates that for the given finite fitting ranges, $\omega_0(r_s)$ and $P(k)$ contain equal amounts of acoustic information (trivially true for infinite fitting ranges by definition of $\omega_0(r_s)$, however, real surveys are finite in size). Hence, the same amount of acoustic information can be obtained through either $\omega_0(r_s)$ or $P(k)$ analysis of equal volume surveys.

consistency between fitting forms, any potential systematics that may arise due to the use of different fitting forms for each statistic can be avoided.

We pick $B(k) = b$, where b is the large-scale bias, and $A(k)$ to be the cold dark matter-only power spectrum multiplied by a set of cubic spline functions specified at $k = 0.01-1.09h\text{Mpc}^{-1}$. The spline points are picked so that seven of them are logarithmically spaced in the range $k = 0.01-0.25$ and seven of them are linearly spaced in the range $k = 0.25-1.09$ giving a total of 14 spline points. The basis functions specified by the small k spline points are necessary to allow flexibility in the marginalization of $\omega_0(r_s)$ at large scales. The derivative is also specified at the first spline point to derive an additional spline function. The spline functions are taken to be natural (i.e., second derivative equal to 0) at the first and last spline points, beyond which linear extrapolations are implemented. This choice of $A(k)$ ensures convergence when transformed to r_s space and makes the fits in $P(k)$, $\xi(r)$ and $\omega_0(r_s)$ readily comparable. We assume a survey volume of $1h^{-1}\text{Gpc}$ with $\aleph = 1000$ (i.e., one million particles). As a cross check, we confirmed that this new fitting form does in fact give similar results to the form used in §2.3.3.

Figure 2.5 plots the χ^2 versus α for $\omega_0(r_s)$, $P(k)$ and $\xi(r)$. Here the input α is equal to 1. If $\omega_0(r_s)$, $P(k)$ and $\xi(r)$ are derived from a Gaussian random field as they are in linear theory, we would expect that χ^2 versus α be parabolic as shown in the figure. The width of the parabola at $\chi^2 = 1$ is then the theoretical σ_α from the fit. The overlap between the $\omega_0(r_s)$ and $P(k)$ curves indicates that the ratio of σ_α for $\omega_0(r_s)$ to $P(k)$ is ~ 1 . This means that for the given fitting ranges $\omega_0(r_s)$ and $P(k)$ contain equal amounts of acoustic information. Since volume is proportional to χ^2 which is proportional to σ^{-2} , an important implication is that we are able to obtain the same amount of acoustic information using either $\omega_0(r_s)$ or $P(k)$ analysis of equal volume surveys. We emphasize here that the results presented in this section

assume idealized linear theory forms for $P(k)$, $\xi(r)$ and $\omega_0(r_s)$. In practice, numerous physical and observational effects distort the measured statistics from these ideals. However, we expect that the features described in §2.2 will reduce the impact of troublesome observational effects in any BAO analysis using $\omega_0(r_s)$.

2.4.2.1 Locating the Acoustic Information

It is useful to track down where the acoustic information lies and how it changes with α in $\omega_0(r_s)$, $\xi(r)$ and $P(k)$. This is reflected in the derivatives $d\omega_0/d\alpha$, $d\xi/d\alpha$ and $dP/d\alpha$ after marginalizing out the broadband shape. To do this, we calculate the residuals from the $P(k)$ fits described in §2.4.2 for $\alpha = 0.996$ and $\alpha = 1.004$. These residuals should be representative of the acoustic signature after the broadband shape has been marginalized out. We then take $dP/d\alpha$ as the difference between these residuals divided by $1.004 - 0.996 = 0.008$. The transformations of $dP/d\alpha$ into r_s and r space then give us $d\omega_0/d\alpha$ and $d\xi/d\alpha$ respectively. We have plotted $dP/d\alpha$ in the top panel of Figure 2.6, $d\xi/d\alpha$ in the middle panel and $d\omega_0/d\alpha$ in the bottom panel. If one plots the ratio of $dP/d\alpha$ to $P(k)/k$, one is left with the approximate shape of the signal-to-noise ratio ² (SNR). This is plotted in the top right-hand corner of the top panel in Figure 2.6. One can see that the SNR is small at $k < 0.05h\text{Mpc}^{-1}$, indicating that the small k ringing in $dP/d\alpha$ is merely noise from the spline basis functions attempting to match the shape of $P(k)$ at these scales, and is not indicative of the shift in acoustic information with α . The shifting of the acoustic information with α is only truly evident at $k > 0.05h\text{Mpc}^{-1}$ where the SNR is larger. It is evident from these plots that the acoustic information is not as localized in $\omega_0(r_s)$ as in $\xi(r)$, but it is still reasonably well localized. The bottom panel of Figure 2.6 indicates that the optimal fitting range that will include

²The noise term $\sigma_P = P(k)/\sqrt{dN}$ where $dN = k^2 dk$ is the number of modes out to k . For constant increments in k , $dN \propto k^2$ and hence $\sigma_P \propto P(k)/k$

all of the acoustic information encoded in $\omega_0(r_s)$ is somewhere within the range $r_s = 30\text{-}300h^{-1}\text{Mpc}$.

The top panel of Figure 2.7 shows how σ_α changes as the minimum r_s of the fitting range is stepped up from $30\text{-}80h^{-1}\text{Mpc}$ with the maximum r_s of the fitting range fixed at $300h^{-1}\text{Mpc}$. The bottom panel of Figure 2.7 shows how σ_α changes as the maximum r_s of the fitting range is stepped down from $300\text{-}120h^{-1}\text{Mpc}$ with the minimum r_s of the fitting range fixed at $30h^{-1}\text{Mpc}$. The regions of the plots where σ_α begins to modulate are blown up for clarity. One can see that when the minimum of the fitting range is larger than $40h^{-1}\text{Mpc}$, σ_α begins to deviate, indicative of missing some of the acoustic information. This also happens when the maximum of the fitting range is smaller than $200h^{-1}\text{Mpc}$. Hence, the minimum fitting range that allows one to extract all of the acoustic information appears to be $r_s = 40\text{-}200h^{-1}\text{Mpc}$. Hence, to ensure we are encapsulating all of the acoustic information, we picked the fitting range to be $r_s = 30\text{-}210h^{-1}\text{Mpc}$ in Figure 2.5.

2.5 Conclusions

We have presented a new statistic $\omega_\ell(r_s)$ for analyzing baryon acoustic oscillations. This new statistic is advantageous over the traditional methods used to estimate $\xi(r)$ and $P(k)$ as it does away with many of their setbacks. Estimators of $\xi(r)$ are sensitive to poorly measured large scale power through effects such as the integral constraint, whereas the compensated nature of the filter $W_\ell(r)$ used to compute $\omega_\ell(r_s)$ circumvents this problem. We expect that this feature of the filter will also make $\omega_\ell(r_s)$ measured in different subvolumes of a survey more independent which makes error estimation methods such as bootstrap and jackknife more robust. Estimators of $P(k)$ give the true density field convolved with a window function making the measured statistic biased. Attempting to deconvolve the window function intro-

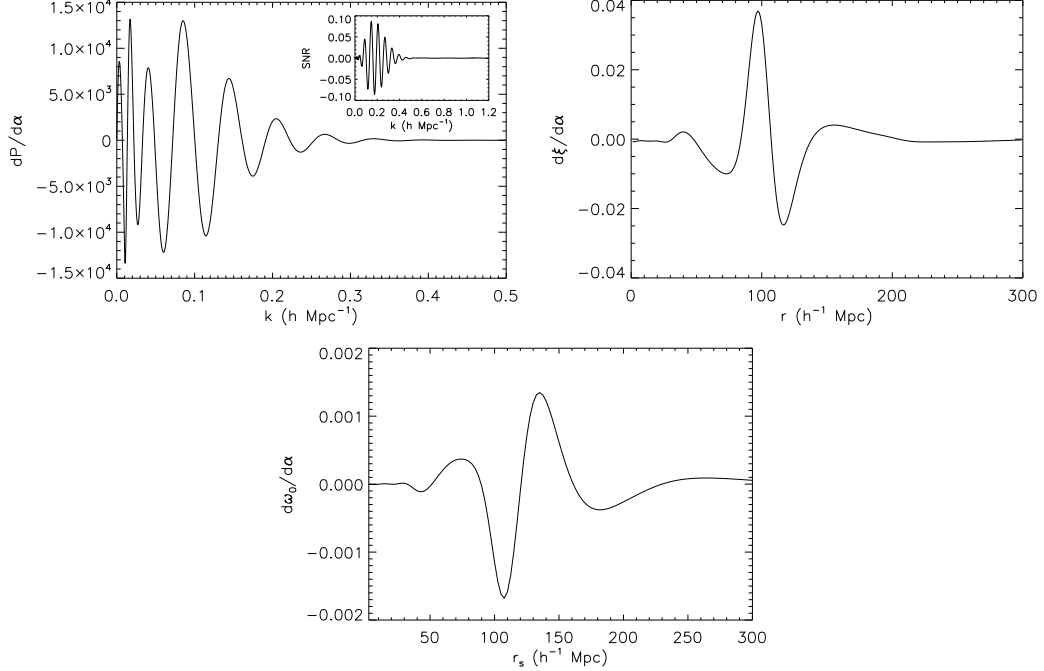


Figure 2.6: (top left) $dP/d\alpha$ calculated from the residuals of the $P(k)$ fits after marginalizing out the broadband shape. The change in $P(k)$ with α captured by $dP/d\alpha$ should correspond to how the acoustic information is shifted as α changes. The ratio of $dP/d\alpha$ to $P(k)/k$ approximates the shape of the signal-to-noise ratio and is shown in the top right-hand corner of the plot. The fact that the ratio is very small at $k < 0.05h\text{Mpc}^{-1}$ indicates that all the ringing in $dP/d\alpha$ at these scales is just noise from the spline basis functions attempting to match the broadband shape of $P(k)$ at these scales. Hence, this small k ringing does not actually reflect the shifting of acoustic information as α changes. The ratio is larger for $k > 0.05h\text{Mpc}^{-1}$ indicating that the oscillations in $dP/d\alpha$ at these k truly reflect the shifting of acoustic information with α . (top right) $d\xi/d\alpha$ obtained by transforming $dP/d\alpha$. This shows where the acoustic information is located in configuration space and how it changes with α . (bottom) $d\omega_0/d\alpha$ obtained by transforming $dP/d\alpha$ to r_s space. This shows where the acoustic information is located in r_s space and how it changes with α . Comparison with the middle panel indicates that the acoustic information is not as localized in $\omega_0(r_s)$ as it is in $\xi(r)$, however, it is still reasonably well localized. All of the acoustic information is located within $r_s \sim 30\text{-}300h^{-1}\text{Mpc}$, indicating that the optimal fitting range for $\omega_0(r_s)$ is somewhere within these limits.

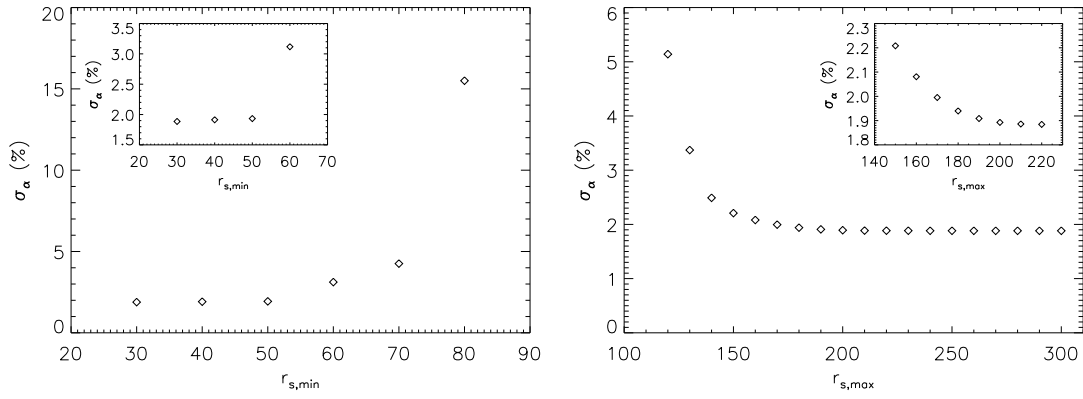


Figure 2.7: (left) Plots how σ_α changes as the minimum r_s of the fitting range is stepped up from $30\text{-}80h^{-1}\text{Mpc}$ with the maximum r_s of the fitting range fixed at $300h^{-1}\text{Mpc}$. The deviation of σ_α at $r_{s,min}$ larger than $40h^{-1}\text{Mpc}$ indicates that some of the acoustic information is being missed by these fitting ranges. (right) Plots how σ_α changes as the maximum r_s of the fitting range is stepped down from $300\text{-}120h^{-1}\text{Mpc}$ with the minimum r_s of the fitting range fixed at $30h^{-1}\text{Mpc}$. The deviation of σ_α at $r_{s,max}$ smaller than $200h^{-1}\text{Mpc}$ indicates that some of the acoustic information is being missed by these fitting ranges. The above analysis implies that in order to extract all of the acoustic information, one needs to fit between $r_s = 40\text{-}200h^{-1}\text{Mpc}$ at minimum.

duces artificial smoothing at small separations in k due to their near delta function shapes in real observational surveys. $\omega_\ell(r_s)$, on the other hand, does not suffer from this as it is a pair count statistic. Pair counting estimators allow us to record the relative locations of tracer pairs as well as their angles from the LOS direction. This provides us with an accurate map of the underlying galaxy distribution. The fact that LOS angle is recorded also means that any anisotropic clustering should be apparent in $\omega_\ell(r_s)$. Hence we expect that it can also be used to probe the underlying cosmology. In addition, there is less need to worry about binning related issues when computing $\omega_\ell(r_s)$ as we never need to bin the data. The smoothness of the filter in configuration space causes the rapid fall-off of the filter in Fourier space. This reduces the impact of large k modes or small scales which are not well constrained in large cosmology surveys. The localized nature of $W_\ell(r)$ is conducive to minimal smearing of the acoustic information so that it is mostly concentrated in a single dip around the acoustic scale. This translates to a cleaner representation of the acoustic information when plotted, as opposed to the oscillatory features of $P(k)$.

We also showed that with the present form for $W_\ell(r)$ and a finite fitting range encompassing the acoustic scale, it is possible to extract the same amount of acoustic information using either $\omega_0(r_s)$ or $P(k)$ from equal volume surveys. It is important to note that these results were obtained through analysis of idealized linear theory forms for $P(k)$, $\xi(r)$ and $\omega_0(r_s)$. In practice, the measured forms of these statistics are distorted by various physical and observational effects. However, we expect that the features described in §2.2 will reduce the impact of troublesome observational effects in any BAO analysis using $\omega_0(r_s)$. We also demonstrated where the acoustic information is located in $\omega_0(r_s)$, $\xi(r)$ and $P(k)$ and how it changes with α . From this analysis, the minimum fitting range required to extract all of the acoustic

information from $\omega_0(r_s)$ appears to be $r_s = 40\text{-}200h^{-1}\text{Mpc}$.

We compared the acoustic peak shifts derived using $\omega_0(r_s)$ to those derived using $P(k)$ for a pure DM case as well as for three halo based galaxy models. The results for the DM and the higher number density cases are all much better than 1σ consistent with each other. The low number density case is slightly deviant with 1.6σ agreement between $\omega_0(r_s)$ and $P(k)$. This may be a result of approaching the shot-noise limited regime or our lack of understanding of shot-noise in general and how it may affect $P(k)$ and $\omega_0(r_s)$ differently. It may also be caused by our fitting form not handling the scale-dependence of high-bias models in full. The general consistency between $\omega_0(r_s)$ and $P(k)$ is encouraging and implies that distance measures will be consistent between the two methods. From this and the features listed above, we conclude that $\omega_0(r_s)$ is a well-tuned new statistic for BAO analysis.

CHAPTER 3

A 2% DISTANCE TO $z = 0.35$ BY RECONSTRUCTION BARYON ACOUSTIC
OSCILLATIONS

We present results from fitting the baryon acoustic oscillation (BAO) signal in the correlation function obtained from the first application of density-field reconstruction to a galaxy redshift survey, namely, the Sloan Digital Sky Survey (SDSS) Data Release 7 (DR7) luminous red galaxy (LRG) catalogue. Reconstruction works to partially remove the effects of non-linear structure growth on the BAO by reconstructing the linear matter density field from the observed galaxy density field using the continuity equation. The algorithm we employ is an extension from that first introduced by Eisenstein et al. (2007), including the effects of survey geometry as well as redshift-space distortions. We also introduce more careful approaches for measuring the acoustic scale from the data using suitable covariance matrix and fitting models for galaxy correlation functions. Our covariance matrix technique guarantees smooth diagonal and off-diagonal terms by fitting a modified Gaussian covariance matrix to that calculated from mock catalogues. Our proposed fitting model is effective at removing broadband effects such as redshift-space distortions, scale dependent bias and any artifacts introduced by assuming the wrong model cosmology. These all aid in obtaining a more accurate measurement of the acoustic scale and its error. We validate our reconstruction and fitting techniques on 160 mock catalogues obtained from the LasDamas simulations. We find that the nonlinear BAO damping scale Σ_{nl} is reduced from $8.1h^{-1}\text{Mpc}$ to $4.4h^{-1}\text{Mpc}$ in the LasDamas mocks after reconstruction. This sharpening of the BAO peak allows us to centroid it better leading to a factor of 1.6 reduction in the scatter between sound horizon measurements obtained from the mocks. We then apply these techniques to the DR7 LRG

sample and find that the error on the acoustic scale decreases from $\sim 3.5\%$ before reconstruction to $\sim 1.9\%$ after reconstruction, a factor of 1.8. We also see an increase in our BAO detection confidence from $\sim 3\sigma$ to $\sim 4\sigma$ after reconstruction with our confidence level in measuring the correct acoustic scale increasing from $\sim 3\sigma$ to $\sim 5\sigma$. Using the mean of the acoustic scale probability distributions produced from our fits, we find $D_v(z)/r_s = 8.89 \pm 0.31$ before reconstruction and 8.88 ± 0.17 after reconstruction where $z = 0.35$ is the median redshift of the LRG sample.

3.1 Introduction

The baryon acoustic oscillations (BAO) lie at sufficiently large scales such that they are not significantly affected by non-linear structure growth, which dominates the complicated formation of stars and galaxies at small scales. However, in the present era of precision cosmology, these small effects are becoming increasingly more important to quantify. An understanding of these effects can be achieved through perturbation theory-based approaches as well as using full cosmological simulations (Seo & Eisenstein, 2003; Jeong & Komatsu, 2006; Huff et al., 2007; Guzik, Bernstein & Smith, 2007; Eisenstein, Seo & White, 2007; Angulo et al., 2008; Crocce & Scoccimarro, 2008; Smith et al., 2008; Seo et al., 2008; Padmanabhan & White, 2009; Seo et al., 2010; Mehta et al., 2011). These studies have found that non-linear structure growth has 2 notable effects on the BAO, namely a smearing effect and a shifting effect. Seo et al. (2008, 2010) & Mehta et al. (2011) have shown that any shifting of the BAO is small, on the $\sim 0.5\%$ level, which is well below the statistical precision of any current BAO distance measures. However, the smearing of the acoustic feature can significantly degrade our ability to accurately centroid the BAO, which results in a poorer measurement of the acoustic scale.

The BAO smearing is well understood (Eisenstein, Seo & White, 2007; Crocce

& Scoccimarro, 2008; Matsubara, 2008a,b; Padmanabhan & White, 2009; Seo et al., 2010) and originates from large-scale gravitational flows at small scales ($\sim 20h^{-1}\text{Mpc}$). It can be modeled as a Gaussian damping of the BAO with an associated smoothing scale of Σ_{nl} (Eisenstein, Seo & White, 2007). Since the origin of this smearing is gravitational and we understand gravity reasonably well, Eisenstein et al. (2007) proposed a method to “run gravity backwards” in order to partially undo these non-linear effects on the matter density field. This procedure is known as reconstruction and effectively reverses the smearing of the BAO feature. Reconstruction has been tested extensively on N-body simulations (Padmanabhan et al., 2009; Noh et al., 2009; Seo et al., 2010; Mehta et al., 2011) and has been shown to sharpen the BAO feature which simultaneously improves distance constraints. We emphasize here that reconstruction is not a deconvolution of non-linear effects from the 2-point statistics used to measure the clustering of galaxies such as the correlation function. The operation is performed on the measured matter density field itself.

The work outlined in this chapter demonstrates the first application of reconstruction to a galaxy redshift survey. The Sloan Digital Sky Survey (SDSS) Luminous Red Galaxy (LRG) Data Release 7 (DR7) sample is currently the largest dataset for performing low redshift ($z = 0.35$) BAO measurements and hence we will use it for our reconstruction here. This paves the way for applying reconstruction to future BAO surveys such as the Baryon Oscillation Spectroscopic Survey (see Chapter 4).

Since the goal of all BAO galaxy surveys is to measure the acoustic scale to high precision, we also intend for this chapter to present a viable procedure for attaining this goal. We include a discussion of the necessary statistical tools, such as a new method for deriving a reliable, smooth covariance matrix, and a robust

fitting framework for measuring the acoustic scale. We use our mock catalogues to demonstrate that making slight adjustments to our fiducial model parameters such as Σ_{nl} (used to model the degradation of the BAO signal due to non-linear structure growth), the fitting range, the number of marginalization terms and the input cosmology, do not alter the measured acoustic scale. A similar exercise is also performed for various reconstruction parameters with likewise consistent results. This indicates the robustness of our techniques.

Using these tools and the DR7 LRG sample, we measure the acoustic scale to 3.5% before reconstruction and 1.9% after reconstruction. Our post-reconstruction result is the highest precision measurement of the acoustic scale at $z = 0.35$ obtained through galaxy surveys to date. Without reconstruction, we would need to increase the survey volume by nearly a factor of 3 to achieve this same factor of 1.8 reduction in the error. We also find that both measures of BAO significance we consider improve by at least 1σ after reconstruction.

The contents of this chapter will be as follows. In §3.2 we introduce the LasDamas and DR7 datasets used in this chapter. §3.3 details the methods we use to measure the acoustic scale including a discussion of reconstruction, covariance matrices and fitting models. §3.4 gives a qualitative discussion and comparison of the effects of reconstruction on the overall shape of the real and redshift-space correlation functions based on results from mock catalogues. §3.5 & §3.6 present the fitting results to the LasDamas mocks in redshift space and real space respectively with a more quantitative discussion of the effects of reconstruction on the measurement of the BAO scale. Finally we apply reconstruction and present our key distance constraints from the DR7 LRG data in §3.7. We conclude in §3.8. §3.3.1 & §3.4 in addition to the reconstruction robustness tests described in §3.5 & §3.7 are paraphrased from Padmanabhan et al. (2012a).

3.2 Datasets

3.2.1 Simulations

We use the Large Suite of Dark Matter Simulations (LasDamas; McBride et al. 2012, in prep) to calibrate our reconstruction parameters, fitting template and covariance matrix. The LasDamas collaboration ¹ has provided publicly available mock galaxy catalogues based on these simulations for the Sloan Digital Sky Survey (SDSS) data release 7 (DR7) luminous red galaxy (LRG) sample.

The LasDamas simulations were run assuming a flat Λ CDM cosmology with $\Omega_b = 0.04$, $\Omega_m = 0.25$, $h = 0.7$, $n_s = 1.0$ and $\sigma_8 = 0.8$. Although various box sizes were implemented, the 40 simulations used to construct the LRG mocks were $2.4h^{-1}$ Gpc on a side with 1280^3 particles in each. The initial particle positions were set using second-order Lagrangian perturbation theory at $z = 49$. To construct mock galaxy catalogues from the simulations, the dark matter halos were populated according to halo occupation parameters tuned to match the observed clustering of the DR7 LRGs. In addition, the mock catalogues include observational effects such as redshift-space distortions and mimic the angular selection function of the LRG sample. The redshift range covered by the mocks is $0.16 < z < 0.44$. We note that this is slightly different to the flux-limited LRG sample described in the following section which will be employed in this study. To address this point, we downsample the radial selection function to match the flux-limited region of the LRG selection at $z > 0.36$. Our region of interest, the SDSS Northern Galactic Cap, covers ~ 7200 deg² on the sky. The resulting geometry allows 4 mocks to be constructed from each simulation and hence we have a total of 160 mocks for our analysis.

¹<http://lss.phy.vanderbilt.edu/lasdamas>

3.2.2 SDSS DR7

Our main goal in this chapter is to demonstrate the methods needed to obtain precision measurements of the BAO scale from galaxy surveys. In this study, we perform this measurement on the SDSS (York et al., 2000) DR7 (Abazajian et al., 2009) LRG sample.

The SDSS has taken photometric observations of $\sim 10,000 \text{ deg}^2$ on the sky and obtained spectroscopic followup of nearly a million of these detected objects. It uses a dedicated 2.5m telescope (Gunn et al., 2006) at Apache Point Observatory which has a specially designed wide field camera (Gunn et al., 1998). Photometric observations were taken in the *ugriz* bands (Fukugita et al., 1996; Smith et al., 2002) by drift scanning the sky under favourable conditions (Hogg et al., 2001). These images were then fed through an automated pipeline that performed the necessary astrometric and photometric calibrations. The pipeline also detected and measured the photometric properties of the observed objects (Pier et al., 2003; Ivezić et al., 2004; Tucker et al., 2006; Padmanabhan et al., 2008). Select subsamples (Strauss et al., 2002; Eisenstein et al., 2001) were then designated for spectroscopic followup using a 640 fiber spectrograph.

The DR7 LRG sample is part of the last data release of SDSS-II, the second phase of SDSS which was completed in 2009. The LRG sample was selected according to the prescription in Eisenstein et al. (2001). This selection was optimized to identify the most luminous (and hence most massive and highly biased) galaxies which can be observed out to high redshifts. Since the volume encompassed by equal angles on the sky increases with redshift, we can probe the large volumes necessary for cosmological studies using these luminous galaxies. The LRGs tend to be old systems with uniform spectral energy distributions that exhibit a strong 4000\AA break. This gives them a distinct colour-flux-redshift relation which allows them to be uniformly

selected over a wide redshift range. Our sample matches exactly that of Kazin et al. (2010) and we refer the interested reader there for details of its construction. We use the flux-limited LRG sample in the SDSS Northern Galactic Cap only. This sample spans a redshift range of $0.16 < z < 0.47$ and has a number density of $\sim 10^{-4}h^3\text{Mpc}^{-3}$.

3.3 Methods

A variety of statistics such as the correlation function, the power spectrum, and more recently $\omega_\ell(r_s)$ (obtained through band-filtering the power spectrum or the correlation function with filtering scale r_s ; Xu et al. 2010) are available for measuring clustering and the BAO scale. The measurement of this scale is affected by non-linear structure growth. Hence, in order to obtain an accurate measurement of the acoustic scale through fitting the observational data, we must first employ an algorithm known as reconstruction to partially undo the effects of this non-linear evolution. We also need to develop a technique that returns reliable error estimates for our chosen clustering statistic (i.e. the covariances between different scales) and a method to marginalize out the broadband (non-BAO) information from the statistic. In this section, we discuss these techniques in detail.

3.3.1 Reconstruction

3.3.1.1 Understanding Reconstruction

A pictorial summary of the reconstruction procedure is given in Figure 3.1. A detailed description of the panels is given in the caption. Reconstruction attempts to partially undo the large-scale gravitational flows that smear the BAO feature (Eisenstein et al., 2007). The peculiar motions of particles is not a dominant effect here. The displacement field induced by the gravitational interaction between particles is completely defined by the particle distribution. This means that the

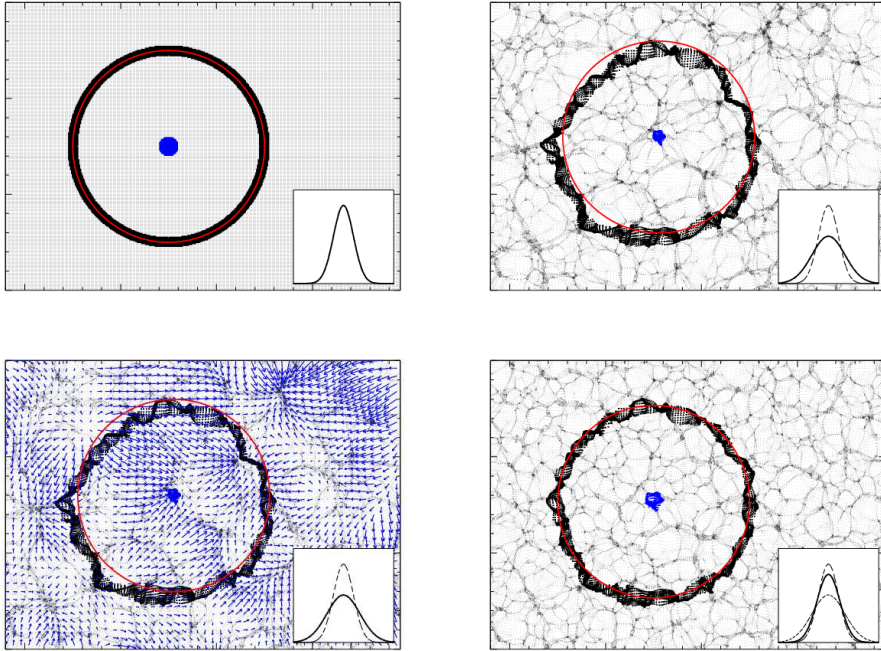


Figure 3.1: A pictorial explanation of density-field reconstruction and how it can improve the precision of acoustic scale measurements. The panels correspond to thin slices through a cosmological simulation. The particles representing the BAO feature are highlighted. The insets show the positional rms of the highlighted particles relative to the blue center (solid line-current, dashed line-initial, dotted line-before reconstruction). (top left) The initial smooth density field in the early universe. (top right) The present-day density field. Here we have evolved the simulation using the Zel'dovich approximation (Zel'dovich, 1970). The red ring marks the radius of the initial BAO ring. The particles in the BAO ring have spread out, causing the BAO feature to smear as evidenced by the larger rms shown in the inset. (bottom left) The density field at the present day with the Lagrangian displacement field overplotted as the blue arrows. The displacement field here has been smoothed using a Gaussian with $10h^{-1}\text{Mpc}$ width. Reconstruction aims to estimate this displacement field from the present-day observed density field. We can then move the particles back along these displacement vectors (bottom right panel) to their linear-theory positions. One can see that the recovered BAO ring is not perfectly circular due to the smoothing of the displacement field, however, it does show a significant improvement. Analogously, the rms radius does not return to its initial state but is much tighter than before reconstruction. The actual reconstruction algorithm applied to the data is slightly more complex than what is illustrated here, but this figure clearly demonstrates the basic principles and effectiveness of reconstruction.

observed galaxy distribution we use to measure the BAO scale is also responsible for the BAO smearing and hence serves as the basis for reconstruction. From the observed density field we can infer the large-scale motions that smear the BAO. Running these motions backwards allows us to undo this smearing.

The illustration in Figure 3.1 is based on slices through an N-body simulation where the particles constituting the BAO are highlighted for clarity. The top left panel shows the initial state of the universe, where the distribution of particles is very smooth. The top right panel shows the distortion of the BAO ring as non-linear structure growth occurs. The bottom left panel shows the predicted displacement field using our reconstruction technique and the bottom right panel shows the particles shifted back along their approximate displacement vectors, thus restoring them to their linear-theory positions and ending reconstruction. These figures emphasize that reconstruction works at the level of the actual density field and utilizes information beyond what lies in the 2-point statistics used to analyze galaxy clustering.

3.3.1.2 A Reconstruction Algorithm

This section gives an account of our reconstruction algorithm which is based on the version first proposed by Eisenstein et al. (2007). The underlying theoretical considerations are detailed in Padmanabhan et al. (2009) & Noh et al. (2009) and the method itself has been validated on simulations in Seo et al. (2010) & Mehta et al. (2011). This description is adapted from Padmanabhan et al. (2012a).

Before we can perform reconstruction, we must first estimate the unreconstructed power spectrum $P(k)$ or correlation function $\xi(r)$. These 2-point statistics are used to measure the clustering of galaxies from redshift surveys. In this work we focus on the correlation function which can be measured using the Landy-Szalay estimator (Landy & Szalay, 1993)

$$\xi(r) = \frac{DD - 2DR + RR}{RR} \quad (3.1)$$

where DD , DR and RR are the number of galaxy-galaxy, galaxy-random and random-random pairs with separation r . The random points serve as a baseline for measuring the correlation function and are generated in a manner in which they are randomly distributed according to the angular and radial selection functions of the galaxy survey. We weight the galaxies and random points using the approximate minimum variance weighting proposed by Feldman et al. (1994)

$$w_i = \frac{1}{1 + \bar{n}(z_i)P(k_0)} \quad (3.2)$$

where $\bar{n}(z_i)$ is the number density at redshift z_i and $P(k_0) = 40000h^{-3}\text{Mpc}^3$ is an approximate value for the power spectrum near the BAO scale.

Using the unreconstructed $\xi(r)$ we can compare it to the matter correlation function at large scales and estimate the linear galaxy bias b . We must also estimate the linear growth rate $f = \frac{d \log D}{d \log a} \sim \Omega_m(z)^{0.55}$ (Caroll, Press & Turner, 1992; Linder, 2005), where $D(a)$ is the linear growth function and a is the scale factor. $\Omega_m(z)$ is the matter density relative to the critical density at redshift z ,

$$\Omega_m(z) = \Omega_m(1+z)^3 \frac{H_0^2}{H^2(z)} \quad (3.3)$$

where $H(z)$ is the Hubble parameter at redshift z and H_0 is the present-day value.

Next, we embed the survey into a volume that is much larger than the volume of the survey. This is necessary because the gravitational potential (and hence the displacement field) is sensitive to these regions, especially at the survey boundaries. In our implementation, we use $200h^{-1}\text{Mpc}$ padding. We then smooth over the density field using a Gaussian with smoothing length l to avoid having to deal with highly non-linear effects at small scales $< 10h^{-1}\text{Mpc}$. We experiment with various values of l and pick a fiducial value of $15h^{-1}\text{Mpc}$ (see §3.4).

We fill in the density field in the larger volume through generating constrained Gaussian realizations of the data (Hoffman & Ribak, 1991; Zaroubi et al., 1995). The

constrained Gaussian realizations are generated using the Hoffman-Ribak algorithm. Suppose we organize the observed density field into a vector δ and we wish to generate a constrained realization density field $\bar{\delta}$ where the 2 are related by the projection \mathbf{P} , i.e. $\delta = \mathbf{P}\bar{\delta}$. Then we have

$$\bar{\delta} = \bar{\delta}_{\mathbf{U}} + \bar{\mathbf{C}}\mathbf{C}^{-1}(\delta - \mathbf{P}\bar{\delta}_{\mathbf{U}}) \quad (3.4)$$

where $\bar{\delta}_{\mathbf{U}}$ is an unconstrained Gaussian realization generated using an assumed power spectrum $P(k)$. \mathbf{C} is the covariance matrix from the data as defined by

$$C_{ij} = \langle \delta(r_i)\delta(r_j) \rangle \quad (3.5)$$

and $\bar{\mathbf{C}}$ is the analogous quantity between the data and the constrained realization. This technique also provides an interpolation over any gaps within the volume of the redshift survey.

We now arrive at the point where we can actually estimate the displacement field Ψ . Nusser & Davis (1994) showed that to first order, the displacement field and the density field in redshift space (our observed space) can be related as

$$\nabla \cdot \Psi + \beta \nabla \cdot (\Psi_s \hat{\mathbf{s}}) = -\frac{\delta_{gal}}{b} \quad (3.6)$$

where $\Psi_s = \Psi \cdot \hat{\mathbf{s}}$ is the line-of-sight displacement (note that this is essentially the continuity equation). δ_{gal} is the galaxy density field and is roughly related to the matter density field as $\delta_{matter} \sim \delta_{gal}/b$, where b is the linear galaxy bias. The second term results from large-scale redshift-space distortions. Since we cannot directly observe line-of-sight positions but rather must infer them through redshifts, the clustering of galaxies along the radial direction will appear distorted. This is because galaxies have intrinsic motions that impart additional redshifts on top of cosmological redshift. At large scales, these motions are due to the coherent infall of galaxies towards overdense regions, known as the Kaiser effect (Kaiser, 1987).

The magnitude of these distortions is related to the linear growth rate f . Hence, in addition to partially undoing non-linear structure growth, reconstruction can also correct for the Kaiser redshift-space distortion.

If we assume that the displacement field is irrotational, we can write $\Psi = \nabla\phi$ for some scalar field ϕ . Equation 3.6 then becomes similar to Poisson’s equation, with an additional redshift-space distortion term. The derivatives can be converted to finite differences and we can solve for ϕ using the resulting linear equations. From ϕ we can calculate Ψ and shift the galaxies by $-\Psi$ to recover their linear-theory positions. The galaxies must be shifted by an additional $-f\Psi_s$ to undo the Kaiser effect. A set of random points must also be shifted by $-\Psi$ to ensure that we are not removing power from the density field. We denote this shifted random set as S . Note that the random points used can be a subset of the original randoms (if that original set was large enough), or a completely separate set. The reconstructed correlation function can then be calculated as

$$\xi(r) = \frac{DD - 2DS + SS}{RR}. \quad (3.7)$$

We compute correlation functions in both real and redshift space with and without reconstruction from SDSS DR7 LRG mock catalogues created using the Las-Damas simulations (see §3.2.1; McBride et al. 2012, in prep). We also compute the correlation functions of the SDSS DR7 LRG data (see §3.2.2) before and after reconstruction. All correlation functions were computed in $3h^{-1}\text{Mpc}$ bins from $2.5\text{-}197.5h^{-1}\text{Mpc}$.

3.3.2 Covariance Matrices

In past studies involving observational data, the most common method for deriving the covariance matrix was to construct it from mock catalogues generated from either simulations (Hamilton, Rimes & Scoccimarro, 2006; Takahashi et al., 2009) or

perturbation theory approaches (Scoccimarro & Sheth, 2002). Perturbative methods are less accurate than we would like and as we will show, the covariance matrices calculated from mocks can still be noisy, even if the number of mocks used is large. One can also assume the smooth Gaussian covariance matrix from linear theory, however this neglects the non-linear contribution to the noise. Hence, it is necessary to devise a scheme for approximating the mock covariances with a smooth function or find alternate methods to regularize the matrix. In this chapter, we present a robust approximation scheme, which we will show produces a faithful representation of the expected covariances.

We perform the analyses in this chapter using the correlation function statistic and hence, we require an estimate of the correlation function covariances. As mentioned previously, the most obvious choice is to use the covariance matrix calculated directly from the mock catalogues. The value of the i th row and j th column of such a covariance matrix is

$$C_{ij} = \frac{1}{N-1} \sum_{n=1}^N [\xi_n(r_i) - \bar{\xi}(r_i)][\xi_n(r_j) - \bar{\xi}(r_j)], \quad (3.8)$$

where N is the total number of mocks, $\xi_n(r)$ is the correlation function calculated from the n th mock and $\bar{\xi}(r)$ is the average of the mock correlation functions. However, we find that the covariances calculated from 160 mocks are still noisy (see Figure 3.2). To obtain a smooth approximation to the mock covariances, we introduce a new technique which involves fitting a modified form of the Gaussian covariance matrix to the data using a maximum likelihood approach.

The simplest analytic form we can write down for the covariance matrix assumes a Gaussian random field in which all Fourier modes grow independently. Such a Gaussian covariance matrix is guaranteed to be smooth along the diagonal and off-diagonal elements and is a suitable starting point for deriving an approximation to

the covariances calculated from the mocks. It has the form

$$C_{ij} = \frac{2}{V} \int \frac{k^2 dk}{2\pi^2} j_0(kr_i) j_0(kr_j) [P_c(k) + \aleph]^2 \quad (3.9)$$

where V is the volume of each mock, \aleph is the shot-noise and

$$j_0(kr) = \frac{\sin(kr)}{kr} \quad (3.10)$$

is the 0th order spherical Bessel function. It does not intrinsically include the effects of survey geometry or redshift-space distortions, however, these can be incorporated into the volume and $P_c(k)$ terms as shown below. \aleph has 2 basic components, linear shot-noise and non-linear shot-noise. In the standard Gaussian covariance matrix, the linear shot-noise is assumed to be Poisson, which implies $\aleph_{lin} = \bar{n}^{-1}$. Realistically however, surveys span a range of redshifts, so \bar{n} is dependent on z . In addition, we must also consider the non-linear shot-noise which arises due to non-linear structure growth at small scales. This is typically not included in the calculation of the standard Gaussian covariance matrix. We will address these issues in more detail shortly.

Due to the binning of data in our correlation function calculations, we must also adjust our Gaussian covariance matrix calculation to reflect this. We estimate the correlation function by taking the ratio between the number of galaxy pairs and the number of pairs of randomly generated particles in various radial and angular bins. Assuming that we spherically average over the correlation function itself and not the pair-counts, the value of the binned correlation function at the bin center r_i is

$$\xi(\bar{r}_i) = \frac{\int_{\Omega} \int_{r_{i1}}^{r_{i2}} d^3r \xi(r)}{\int_{\Omega} \int_{r_{i1}}^{r_{i2}} d^3r} \quad (3.11)$$

$$= \frac{3}{r_{i2}^3 - r_{i1}^3} \int_{\Omega} \int_{r_{i1}}^{r_{i2}} r^2 dr \frac{d\Omega}{4\pi} \int \frac{k^2 dk}{2\pi^2} P(k) j_0(kr) \quad (3.12)$$

where the bin limits are (r_{i1}, r_{i2}) and $\xi(r)$ is the true unbinned correlation function. In reality, this is an approximation as the correlation function we measure

also depends on the weighting determined by the random paircounts which encode information about the survey geometry and distribution of galaxies. Analogously, we may write the expression for the binned covariance matrix as

$$\begin{aligned}
C_{ij} &= \frac{2}{V} \frac{3}{r_{i2}^3 - r_{i1}^3} \frac{3}{r_{j2}^3 - r_{j1}^3} \\
&\cdot \int_{\Omega} \int_{r_{i1}}^{r_{i2}} r^2 dr \frac{d\Omega}{4\pi} \int_{\Omega'} \int_{r_{j1}}^{r_{j2}} r'^2 dr' \frac{d\Omega'}{4\pi} \\
&\cdot \int \frac{k^2 dk}{2\pi^2} j_0(kr_i) j_0(kr_j) [P_c(k) + \aleph]^2.
\end{aligned} \tag{3.13}$$

This can be shown to give

$$C_{ij} = \frac{2}{V} \int \frac{k^2 dk}{2\pi^2} \Delta j_1(kr_i) \Delta j_1(kr_j) [P_c(k) + \aleph]^2 \tag{3.14}$$

where

$$\Delta j_1(kr) = \frac{3}{r_2^3 - r_1^3} \frac{[r_2^2 j_1(kr_2) - r_1^2 j_1(kr_1)]}{k}, \tag{3.15}$$

$$j_1(kr) = \frac{\sin(kr)}{(kr)^2} - \frac{\cos(kr)}{kr} \tag{3.16}$$

is the 1st order spherical Bessel function. Here, we have intentionally written Equation (3.14) to resemble Equation (3.9).

The input power spectrum $P_c(k)$ determines the sample variance of the signal. In redshift space before reconstruction, we take $P_c(k)$ to have the form,

$$P_c(k) = b_0^2 \int_{-1}^1 (1 + \beta\mu^2)^2 F(\mu, k) P_t(k) d\mu \tag{3.17}$$

where $(1 + \beta\mu^2)^2$ is the standard model for the Kaiser effect (Kaiser, 1987) with $\beta = f/b_0$, $f \sim \Omega_m^{0.6}$ and b_0 equal to the large-scale bias. $F(\mu, k)$ is a streaming model term used to account for the Finger of God (FoG) effect. We take this term to be exponential in configuration space and hence

$$F(\mu, k) = \frac{1}{(1 + k^2\mu^2\sigma_s^2)^2} \tag{3.18}$$

in Fourier space, where σ_s is the dispersion within a cluster and is typically around $3\text{--}4h^{-1}\text{Mpc}$. A Gaussian form for $F(\mu, k)$ can also be used; however, we find little difference between the results. Kaiser squashing and FoG are known as redshift-space distortions which affect our measurement of cosmological redshift. These effects arise from the redshifting of galaxies due to their intrinsic (non-expansion related) motions along the line-of-sight direction which are not observed in the transverse direction.

We determine b_0^2 by matching the configuration space transform of $P_c(k)$ to the average of the mock correlation functions at $r = 50h^{-1}\text{Mpc}$. This ensures that the amplitude of $P_c(k)$ matches the average clustering amplitude in the mocks.

Our template power spectrum, $P_t(k)$, takes on the form

$$P_t(k) = [P_{\text{lin}}(k) - P_{\text{smooth}}(k)]e^{-k^2\Sigma_{nl}^2/2} + P_{\text{smooth}}(k), \quad (3.19)$$

where $P_{\text{lin}}(k)$ is the linear power spectrum at $z = 0$. $P_{\text{smooth}}(k)$ is the dewiggled power spectrum described in Eisenstein & Hu (1998) and Σ_{nl} is a smoothing parameter that is used to model the degradation in the acoustic peak due to non-linear evolution (Croce & Scoccimarro, 2006; Eisenstein, Seo & White, 2007; Croce & Scoccimarro, 2008; Matsubara, 2008a; Seo et al., 2008). Before reconstruction, the overall shape of the acoustic peak in the template matches the data best when $\Sigma_{nl} \sim 8h^{-1}\text{Mpc}$; hence we fix $\Sigma_{nl} = 8h^{-1}\text{Mpc}$. We will show that varying this value has little effect on the resulting covariance matrix later in this section.

In order to address the z dependence of \bar{n} , we use the fact that Equation (3.9) is really just the transform of the variance in Fourier space, $[P_c(k) + \aleph]^2/V$, to the expected covariance in configuration space. One can then imagine building up the

inverse of this variance, $I^2(k)$, as an integral over volume,

$$\begin{aligned}
I^2(k) &= \int \frac{dV}{[P_c(k) + \aleph]^2} \\
&= \frac{c\Omega}{H_0} \int_{z_l}^{z_u} \left[P_c(k) + \frac{1}{\bar{n}(z)} \right]^{-2} \\
&\quad \cdot \frac{r^2(z)}{\sqrt{\Omega_m(1+z)^3 + \Omega_\Lambda}} dz, \tag{3.20}
\end{aligned}$$

where we use

$$dV = \frac{c}{H_0} \frac{r^2(z)}{\sqrt{\Omega_m(1+z)^3 + \Omega_\Lambda}} dz d\Omega \tag{3.21}$$

for a flat universe and assume $\bar{n}(z)$ has no angular dependence. z_u and z_l are the upper and lower redshift limits of the survey respectively. Now we can redefine the binned Gaussian covariance matrix, Equation (3.14), as

$$C_{ij} = 2 \int \frac{k^2 dk}{2\pi^2} \Delta j_1(kr_i) \Delta j_1(kr_j) \mathfrak{P}^2(k) \tag{3.22}$$

where $\mathfrak{P}^2(k) = [I^2(k)]^{-1}$. We calculate a model for $\bar{n}(z)$ that suits the DR7 data from the LasDamas random catalogue and scale this to other cosmologies when necessary using the appropriate volume ratios.

Since our binned Gaussian covariance matrix does not include non-linear shot-noise, it underpredicts the mock covariance matrix. However, one can imagine applying some modifications to the Gaussian covariance matrix so that its shape better emulates that of the mock covariance matrix. We assume a modification to the Gaussian covariance matrix of

$$C_{ij}^m = 2 \int \frac{k^2 dk}{2\pi^2} \Delta j_1(kr_i) \Delta j_1(kr_j) \mathfrak{P}^2(k; c_0, c_1, c_2) + c_3 \tag{3.23}$$

where $\mathfrak{P}^2(k; c_0, c_1, c_2)$ corresponds to an $I^2(k)$, Equation (3.20), in which we make

the substitution

$$P_c(k) + \frac{1}{\bar{n}(z)} \rightarrow c_0 P_c(k) + \frac{c_1}{\bar{n}(z)} \int_{-1}^1 (1 + \beta\mu^2)^2 F(\mu, k) d\mu + \frac{c_2}{\bar{n}(z)} \quad (3.24)$$

$$= \left[c_0 b_0^2 P_t(k) + \frac{c_1}{\bar{n}(z)} \right] \cdot \int_{-1}^1 (1 + \beta\mu^2)^2 F(\mu, k) d\mu + \frac{c_2}{\bar{n}(z)}. \quad (3.25)$$

The c_0 term accounts for any remaining large-scale bias discrepancies between $P_c(k)$ and the mock data. The c_1 term is used to represent any effects streaming or Kaiser squashing may have on shot-noise. This is associated with non-linear shot-noise. The c_2 term corresponds to the standard Poisson shot-noise from linear theory. The c_0 , c_1 and c_2 are parameters we use to scale the amplitudes of the various components that go into the Gaussian covariance matrix in order to modify its shape and c_3 can be associated with the integral constraint which manifests itself as an additive offset in the correlation function.

The likelihood of any such $C^m(c_0, c_1, c_2, c_3)$ given a set of mock catalogues is

$$\mathcal{L} = \prod_{i=0}^N \mathcal{L}_i \quad (3.26)$$

$$= \prod_{i=0}^N (2\pi)^{-q/2} (\det C^m)^{-1/2} e^{-\chi_i^2/2} \quad (3.27)$$

where N is the total number of mocks and q is the number of points to fit. $\chi_i^2 = \vec{x}_i (C^m)^{-1} \vec{x}_i^T$ where $\vec{x}_i = \xi_i(r) - \bar{\xi}(r)$ is a vector of dimension q . $\xi_i(r)$ is the correlation function calculated from the i th mock and $\bar{\xi}(r)$ is the average of the mock correlation functions. Equation (3.27) can be re-written as

$$L = -2 \log \mathcal{L} = Nq \log(2\pi) + N \log(\det C) + \sum_{i=0}^N \chi_i^2. \quad (3.28)$$

We would like to find C^m corresponding to the maximum of the likelihood function. This is equivalent to finding the C^m that corresponds to the minimum of L .

Using a downhill simplex minimization scheme and fixing $\sigma_s = 4h^{-1}\text{Mpc}$, we arrive at $c_0 = 0.89$, $c_1 = 0.46$, $c_2 = 1.34$ and $c_3 = 2.32 \times 10^{-7}$ for redshift space before reconstruction. Here, we have fixed the value of σ_s to reduce computation time, however, it is possible to include it as a parameter in the maximum likelihood fit. Allowing σ_s to vary gives $\sigma_s = 3.9h^{-1}\text{Mpc}$ with most modification parameters changing by less than 1%. Only c_1 changes by $\sim 3\%$ due to its partial degeneracy with σ_s (when σ_s is increased, a larger damping effect is placed on the power spectrum term which can be compensated for by making c_1 larger). The fact that the likelihood of the fixed σ_s case is 0.99 of the unfixed case also suggests that fixing σ_s is reasonable.

We also investigate the outcome of fixing $c_0 = 1$, i.e. assuming that the sample variance given by our model power spectrum suits the data perfectly. This does not change the log likelihood significantly and we find that the acoustic scales and errors measured from the mocks as well as the DR7 data are consistent with the case where c_0 is allowed to vary. In addition, we find that changing the value of Σ_{nl} that goes into $P_t(k)$ makes very little difference to the resulting covariance matrix. Using $\Sigma_{nl} = 9h^{-1}\text{Mpc}$ instead of $\Sigma_{nl} = 8h^{-1}\text{Mpc}$ only changes all the modification parameters and the maximum likelihood by $< 1\%$.

The black dots in the top panel of Figure 3.2 show the diagonal (i.e. the $j = i$ elements) of the mock covariance matrix in redshift space before reconstruction and the black crosses show the corresponding diagonal of the modified Gaussian covariance matrix. Likewise, the 6th off-diagonal (i.e. the $j = i + 6$ elements) is overplotted in red. The noise in the mock covariance matrix is obvious. It is evident from the plot that the modified Gaussian covariance matrix is a good

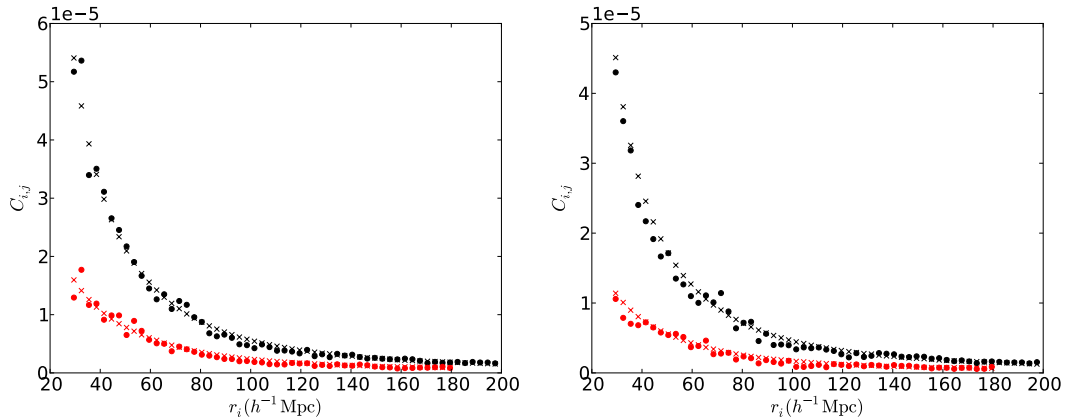


Figure 3.2: The diagonal (black) and 6th off-diagonal (red) of the mock (circles) and modified Gaussian (crosses) covariance matrices in redshift space before reconstruction (top) and after reconstruction (bottom). The mock covariance matrix shows clear signs of noise. The modified Gaussian covariance matrices take on the form given in Equations (3.23 & 3.24) with $\sigma_s = 4h^{-1}\text{Mpc}$. Before reconstruction, $c_0 = 0.89$, $c_1 = 0.46$, $c_2 = 1.34$, $c_3 = 2.32 \times 10^{-7}$ and after reconstruction $c_0 = 0.89$, $c_1 = 0.30$, $c_2 = 1.45$, $c_3 = 1.87 \times 10^{-7}$. One can see that the modified Gaussian covariance matrices are good smoothed approximations to the mock covariance values.

smooth approximation to the mock covariance values. Hence, we use the modified Gaussian covariance matrix derived from this maximum likelihood technique with fixed $\sigma_s = 4h^{-1}\text{Mpc}$ as our estimate of the expected errors on the mock correlation functions. The fitting technique described in §3.3.3 utilizes this covariance matrix.

In redshift space after reconstruction, we take the input power spectrum $P_c(k)$ to be

$$P_c(k) = b_0^2 \int_{-1}^1 F(\mu, k) P_t(k) d\mu \quad (3.29)$$

which is just Equation (3.17) without the Kaiser term since our reconstruction algorithm is designed to undo Kaiser squashing. We assume $\Sigma_{nl} = 4h^{-1}\text{Mpc}$ and retain $\sigma_s = 4h^{-1}\text{Mpc}$ since we did not apply any FoG compression. Fitting for the parameters of the modified Gaussian covariance matrix using the maximum

likelihood prescription, we find $c_0 = 0.89$, $c_1 = 0.30$, $c_2 = 1.45$, $c_3 = 1.87 \times 10^{-7}$. The diagonals and 6th off-diagonals of the post-reconstruction mock and modified Gaussian covariance matrices are plotted in the bottom panel of Figure 3.2. One can see that, as in the pre-reconstruction case, our modified Gaussian approximation fits the mock covariances well.

In the post-reconstruction case, we also test that by using a different cosmology from LasDamas to derive $P_t(k)$, it is still possible to obtain a modified Gaussian covariance matrix that suits the mock data using our maximum likelihood method. In Figure 3.3, we show $\mathfrak{P}(k; c_0, c_1, c_2)$ for the WMAP7+BAO+ H_0 cosmology (Komatsu et al., 2011) divided by the corresponding LasDamas values (solid line). For reference, the WMAP7 cosmological parameters of relevance are $H_0 = 70.2 \pm 1.4$, $100\Omega_b h^2 = 2.255 \pm 0.054$, $\Omega_c h^2 = 0.1126 \pm 0.0036$, $n_s = 0.968 \pm 0.012$ and $\sigma_8 = 0.816 \pm 0.024$. The dotted (dashed) lines are for cosmologies derived by adding (subtracting) the 1σ errors from the WMAP7 values quoted above. One can see that the 3 lines are all ~ 1 to within $\sim 5\%$ near the acoustic scale indicating that the modification parameters are capable of adjusting the power spectrum and the noise terms in the Gaussian covariance matrix to match the LasDamas covariances. In §3.5.2, we show that using these different covariance matrices yield consistent acoustic scale measurements and errors to those obtained using the correct LasDamas cosmology.

3.3.3 Fitting the Acoustic Feature

To measure the acoustic scale, we fit a model of the correlation function or power spectrum in some fiducial cosmology to the data and measure the shift in the acoustic peak position relative to this fiducial cosmology. We parameterize this shift by α defined as

$$\alpha = \frac{[D_V(z)/r_s]}{[D_V(z)/r_s]_{fiducial}} \quad (3.30)$$

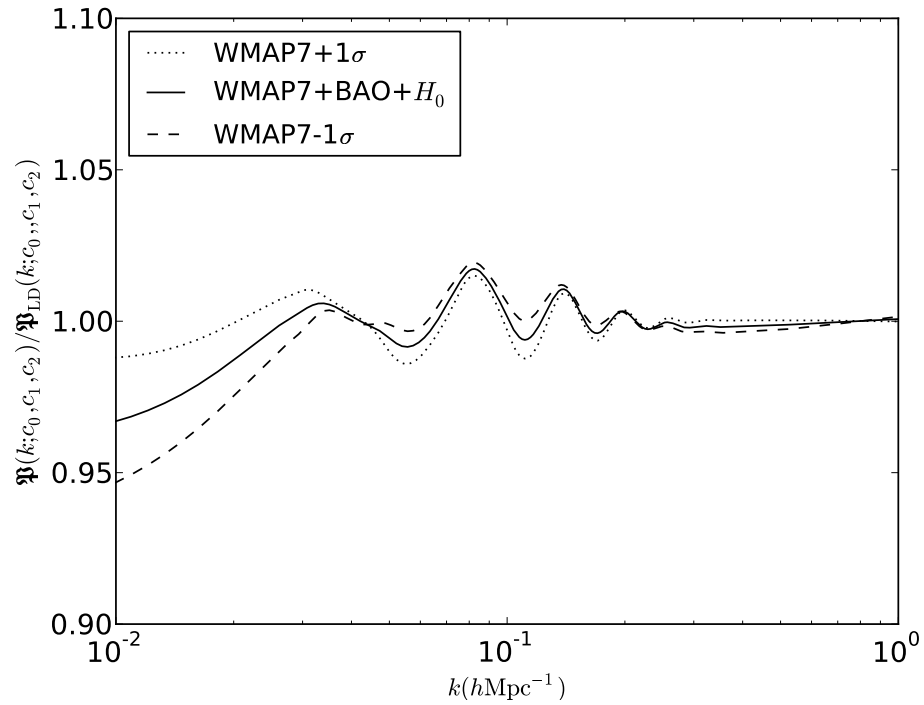


Figure 3.3: The ratio of $\mathfrak{P}(k; c_0, c_1, c_2)$ terms (see Equation (3.23) and surrounding text) found in the definition of the modified Gaussian covariance matrix (MGCM). These MGCMs were all fit to the covariances calculated from the LasDamas mocks in redshift space after reconstruction. The numerator corresponds to MGCMs constructed using 3 non-LasDamas cosmologies. The denominator corresponds to the MGCM in the LasDamas cosmology. The 3 non-LasDamas cosmologies are WMAP7+BAO+ H_0 (solid line) and the 1σ limits of this cosmology ($+1\sigma$ is shown as the dotted line and -1σ is shown as the dashed line). It is seen that the 3 lines are all ~ 1 to within $\sim 5\%$. This indicates that if we input a power spectrum with cosmology different to LasDamas, our modification parameters can balance this input and the noise terms to recover a covariance matrix that matches the expected LasDamas covariances fairly well.

where $D_V(z) \propto \sqrt[3]{D_A^2(z)/H(z)}$ is the spherically averaged distance to redshift z and r_s is the sound horizon (Eisenstein et al., 2005).

Typically in Fourier space, this requires a fitting model of the form

$$P(k) = B(k)P_m(k/\alpha) + A(k). \quad (3.31)$$

Here, $P_m(k)$ is the template power spectrum based in linear theory. $A(k)$ and $B(k)$ are functions involving nuisance parameters that can be used to marginalize out the broadband shape of the power spectrum (i.e. scale-dependent bias and redshift-space distortions). The broadband shape does not contain BAO information but may bias the measurement of the BAO scale if not accounted for properly. These terms can also help mitigate the effects of using the wrong model cosmology. Analogously, in configuration space we have

$$\xi(r) = B(r)\xi_m(\alpha r) + A(r). \quad (3.32)$$

In order to obtain an accurate measure of the acoustic scale, we require this fitting model to be robust. This simply means that if we slightly change the parameters that go into the model, the measured value of α should always be consistent. For a fitting form where this is true, even if we use model parameters that are not optimal, we will still measure the correct acoustic scale. This is necessary since we use this fitting form to derive the acoustic scale in the SDSS DR7 data and in practice we are not certain of the exact model parameters to use.

In Fourier space, Padé approximates and basis functions based on cubic splines work well for both $A(k)$ and $B(k)$, while high order polynomials may also be used for $A(k)$. This has been demonstrated for simulated data (e.g. Seo et al. (2008); Padmanabhan & White (2009); Seo et al. (2010); Mehta et al. (2011)) as well as SDSS-II observational data (e.g. Tegmark et al. (2006); Percival et al. (2007, 2010)). However, high order polynomials and cubic spline forms do not transform particularly

nicely to configuration space due to poor numerical convergence of the integration.

In configuration space, there have been attempts to model the scale-dependent bias associated with the $B(r)$ term such as in (Blake et al., 2011a). As for $A(r)$, an array of forms have been used. In theoretical works (Crocco & Scoccimarro, 2008; Sanchez et al., 2008) and the DR6 motivated observational work (Sanchez et al., 2009), $A(r)$ was motivated by perturbation theory and contained derivatives and integrations of the linear theory correlation function. Other works based in simulations (e.g. Cabré & Gaztañaga (2011)) and SDSS observations (e.g. Eisenstein et al. (2005); Kazin et al. (2010)) did not use an $A(r)$ term at all. However, as we will show in this work, having a non-zero $A(r)$ term aids greatly in removing unwanted broadband information and ameliorating errors in the assumed model cosmology. This is especially true if one is to take $B(r) = B$ and delegate the marginalization of scale-dependent bias to the $A(r)$ term, as is done in most correlation function analyses. We note here though, that the form for $A(r)$ does not need to be complicated as we show next.

We fit the mock redshift-space correlation functions $\xi_s(r)$ over the range $30 < r < 200h^{-1}\text{Mpc}$ using the fiducial form (justification to follow)

$$\xi^{fit}(r) = B^2\xi_m(\alpha r) + A(r) \quad (3.33)$$

where

$$A(r) = \frac{a_1}{r^2} + \frac{a_2}{r} + a_3. \quad (3.34)$$

The parameters of the fit are B^2 , α , a_1 , a_2 and a_3 . The latter are linear nuisance parameters.

As mentioned above, the scale dilation parameter α represents how much the acoustic peak in the data is shifted relative to that in the model. Therefore, it is our measurement of the acoustic scale and the parameter we are most interested in

extracting robustly from our fits. An $\alpha > 1$ indicates a shift towards smaller scales and an $\alpha < 1$ indicates a shift towards larger scales.

The template correlation function, $\xi_m(r)$, takes on the form

$$\xi_m(r) = \int \frac{k^2 dk}{2\pi^2} P_m(k) j_0(kr) e^{-k^2 a^2}, \quad (3.35)$$

where $P_m(k) = b^2 P_t(k)$ and $P_t(k)$ is defined as in Equation (3.19). We perform the transformation from Fourier space to configuration space using an additional Gaussian term to provide high- k damping for the oscillatory transform kernel $j_0(kr)$. This is conducive to better numerical convergence in the integration. We pick $a = 1h^{-1}\text{Mpc}$, a scale small enough such that the effects of the damping will not be significant within our fitting range.

The b^2 term is a constant normalization factor that we obtain by taking the ratio of the mock correlation function being fit and the configuration space transform of $P_t(k)$ at $r = 50h^{-1}\text{Mpc}$. This ensures that the fitting normalization B^2 is of order unity. The normalization must be positive, so we perform our fits with the non-linear parameter $\log(B^2)$. Note that B^2 can vary substantially as long as the $A(r)$ function can compensate. This creates large variation in the amplitude of the acoustic peak which is not physically motivated. We find that the scatter in B^2 can be large with values being as high as ~ 2.1 and as low as ~ 0.3 , especially in the mocks where the acoustic signal does not appear to be as strong. This is summarized in Figure 3.4 where we have plotted B^2 versus best-fit α obtained through fitting the 160 mock correlation functions in redshift space. For a careful description of the information plotted, please see the figure caption. To disfavour extreme values of B^2 , we place a weak Gaussian prior on $\log(B^2)$ with a mean of 0 and standard deviation of 0.4. For simplicity, we also apply this prior to redshift space with reconstruction and real space with and without reconstruction.

We pick the form for $A(r)$ in Equation (3.34) due to its simplicity. In addition

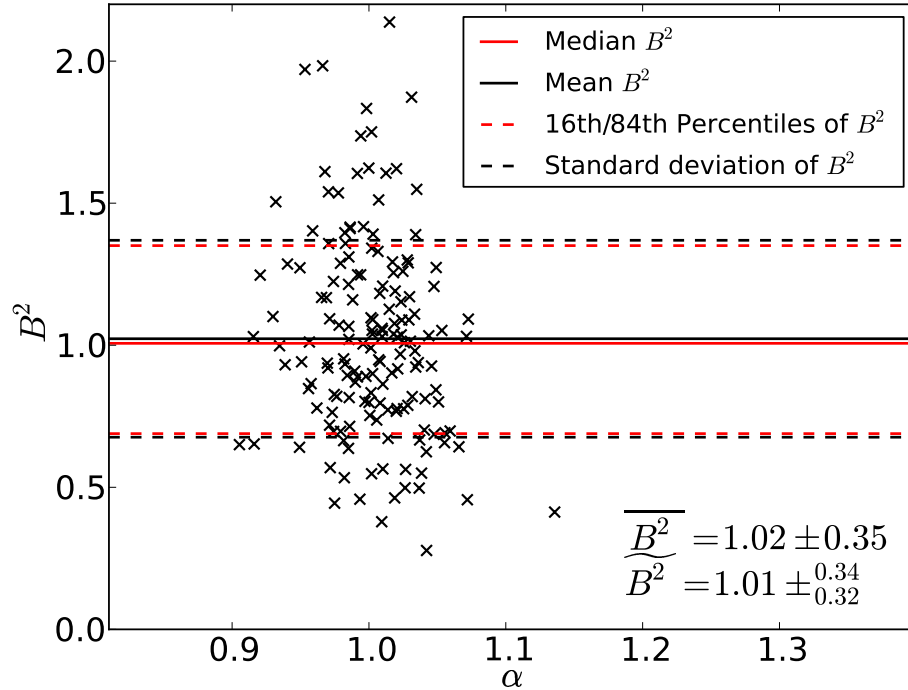


Figure 3.4: The values of B^2 versus α fit from the mocks in redshift space before reconstruction. To ensure that B^2 is non-negative, these values were obtained through fitting the 160 mock redshift-space correlation functions using the non-linear parameter $\log(B^2)$ instead of B^2 . The solid red line indicates the median B^2 value and the solid black line indicates the mean. The dashed red lines indicate the 16th and 84th percentiles of B^2 (quoted with the median $\widetilde{B^2}$). The dashed black lines correspond to the 1σ deviations from the mean (quoted with the mean $\overline{B^2}$). One can see that B^2 can reach values as high as ~ 2.1 and as low as ~ 0.3 . This substantial variation is possible because the $A(r)$ term can compensate, and is therefore not physically motivated. Hence to disfavour these extreme values, we place a weak Gaussian prior on $\log(B^2)$ that has mean equal to 0 and standard deviation equal to 0.4.

Table 3.1: Fit results to average mock correlation functions

	α	Σ_{nl} ($h^{-1}\text{Mpc}$)
Redshift space w/o reconstruction	1.003	8.1
Real space w/o reconstruction	1.002	6.6
Redshift space w/ reconstruction	1.003	4.4
Real space w/ reconstruction	0.999	3.0

to the fiducial $A(r)$ form in Equation (3.34), we will also be analyzing various other forms of $A(r)$ throughout this chapter. We will refer to $A(r) = 0$ as *poly0*, $A(r) = a_1/r^2$ as *poly1*, $A(r) = a_1/r^2 + a_2/r$ as *poly2* and $A(r) = a_1/r^2 + a_2/r + a_3 + a_4r$ as *poly4*. Note that the fiducial form corresponds to *poly3*.

We find that going up to the constant term in $A(r)$ as in the fiducial form gives a good fit to the average of the mock correlation functions. This is shown in Figure 3.5 where in the left panel we have plotted the fits to the average mock, redshift-space correlation function (black crosses) using Equation (3.33) and various forms for $A(r)$. The *poly0*, *poly2*, fiducial form and *poly4* cases are shown as the dotted green, dash-dotted blue, solid black and the dashed red lines respectively. The corresponding residuals are shown in the right panel.

We have also allowed Σ_{nl} to vary in these fits and find that for the fiducial form, $\Sigma_{nl} = 8.1h^{-1}\text{Mpc}$. This is close to the value of $8h^{-1}\text{Mpc}$ we assumed in the estimation of the covariance matrix. The results from fits to the mean mock correlation functions using the fiducial form are summarized in Table 3.1.

The χ^2 per degree-of-freedom (dof) goes down from 2.7 for *poly0* to 1.4 for the fiducial form. The decrease from the fiducial form to *poly4* is much smaller (only

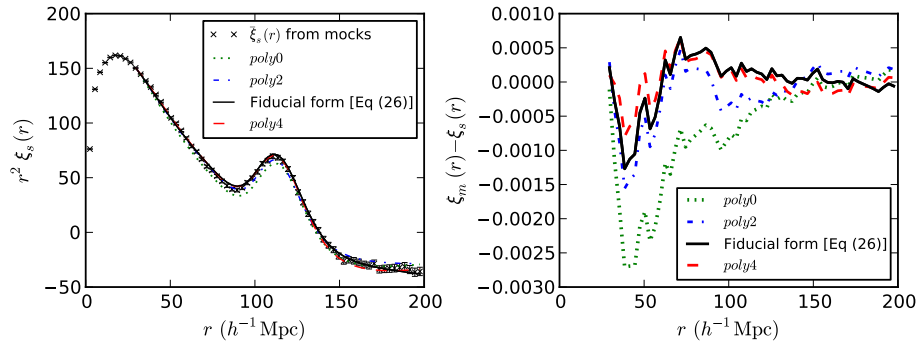


Figure 3.5: (left) Fits to the average redshift-space correlation function of the mocks (black crosses) using Equation (3.33) with $A(r)$ being $poly0$ (dotted green line), $poly2$ (dash-dotted blue line), fiducial form (Equation (3.34)) (solid black line) and $poly4$ (dashed red line). (right) The corresponding residuals of the fits (note that the fitting range is $30 < r < 2000h^{-1}\text{Mpc}$). One can see that the fit using the fiducial form matches the data better than the fits with $poly0$ and $poly2$. However, the improvement between the fiducial form and $poly4$ is negligible as reflected by the similar shapes of the solid and dashed curves. These results motivate our choice of $A(r)$ given in Equation (3.34). We have also allowed Σ_{nl} to vary in these fits. Using the fiducial form, we find $\Sigma_{nl} = 8.1h^{-1}\text{Mpc}$, which is close to the value we assumed in deriving the covariance matrix.

~ 0.2) as evidenced by the similarity in shape between the solid curve and the dashed curve. Although the value of χ^2 per dof is still large for the fiducial form, we note that the error bars expected when fitting each individual mock will be much larger and thus result in reasonable values of χ^2 as will be shown in §3.5.1. In principle we could further lower χ^2 by taking $A(r)$ out to higher orders of r , however we then run the risk of having the nuisance parameters fit the noise in the data.

Recall that our ultimate goal is to measure the acoustic scale, α , from the data. This can be done by finding the value of α that gives rise to the best-fit model to the data. Our models are non-linear in α and the normalization factor $\log(B^2)$, so we can nest a linear least-squares fitter inside a non-linear fitting routine, which in our case is a downhill simplex. The former calculates a_1 , a_2 and a_3 for each value

of α and B^2 the latter steps to. Then, to find the best-fit α , we use the non-linear fitter to minimize the χ^2 goodness-of-fit indicator

$$\chi^2(\alpha, B^2) = [\vec{d} - \vec{m}(\alpha, B^2)]^T C^{-1} [\vec{d} - \vec{m}(\alpha, B^2)] \quad (3.36)$$

where \vec{d} is the correlation function measured from the mocks and $\vec{m}(\alpha, B^2)$ is the best-fit model at each α and B^2 . C^{-1} is the inverse of the covariance matrix. Recall that we use the modified Gaussian covariance matrix (MGCM) described in Equation (3.23) of §3.3.2 here.

Based on our fiducial form defined in Equations (3.33 & 3.34), we define a fiducial model for redshift space over a fitting range of $30 < r < 200h^{-1}\text{Mpc}$. $\xi_m(r)$ is derived from the LasDamas cosmology using $\Sigma_{nl} = 8h^{-1}\text{Mpc}$. We denote the fiducial model with subscript $[f]$ throughout this chapter unless otherwise stated. We perform the above prescribed fitting algorithm on all 160 of our mock catalogues using the fiducial model to obtain a best-fit value of α for each.

For redshift space with reconstruction, we use the same fiducial fitting form defined by Equations (3.33 & 3.34). In this case we find $\Sigma_{nl} = 4.4h^{-1}\text{Mpc}$ when fitting the average of the mocks. The results from these fits are also summarized in Table 3.1. The factor of 1.8 reduction in Σ_{nl} versus the pre-reconstruction case corresponds to a sharpening up of the acoustic peak after reconstruction as shown in Figure 3.7 of the next section, attesting the effectiveness of reconstruction.

We define the fiducial model in redshift space after reconstruction to be identical to the pre-reconstruction model except with $\Sigma_{nl} = 4h^{-1}\text{Mpc}$. This is the same value as that used to derive the MGCM for post-reconstruction redshift space. This is not a bad approximation as we have just shown the fit to the average of the mock correlation functions has $\Sigma_{nl} = 4.4h^{-1}\text{Mpc}$.

3.4 Reconstructing Simulations

In this section we outline the major results from reconstructing the LasDamas mocks. A more detailed discussion of the fitting results and robustness checks of the fitting model are given in the next 2 sections. Here we will only concern ourselves with qualitative results from the reconstruction technique and the insights we glean from these.

Figure 3.6 shows the average 2D correlation function of the 160 mocks in real and redshift space, both before and after reconstruction. Real space is in the left column and redshift space is in the right column. The pre-reconstruction result is shown in the top row and the post-reconstruction result is shown in the bottom row. The line-of-sight direction (r_{\parallel} or s_{\parallel}) is on the x -axis and the transverse direction (r_{\perp} or s_{\perp}) is on the y -axis.

Real space is free of the redshift-space distortions caused by the additional redshifting of galaxies due to their peculiar motions. As discussed previously, these affect our measurements of galaxy positions along the radial direction. Hence, we do not expect the real-space 2D correlation function to show any anisotropy. The top left panel of Figure 3.6 demonstrates this nicely where we see a circular (isotropic) BAO ring. In the presence of redshift-space distortions (top right panel), we see that the clustering indeed appears highly anisotropic with maximal distortions along the line-of-sight direction. The squashing seen at large scales is due to the Kaiser effect discussed previously and the elongation at small scales is due to the Finger-of-God (FoG) effect. The FoG arises from the virial motions of galaxies within their host halos.

We see that after reconstruction, the redshift space 2D correlation function becomes much more isotropic at the BAO scale. This is reflected in the recovery of a circular BAO ring in the bottom right panel and indicates that the Kaiser cor-

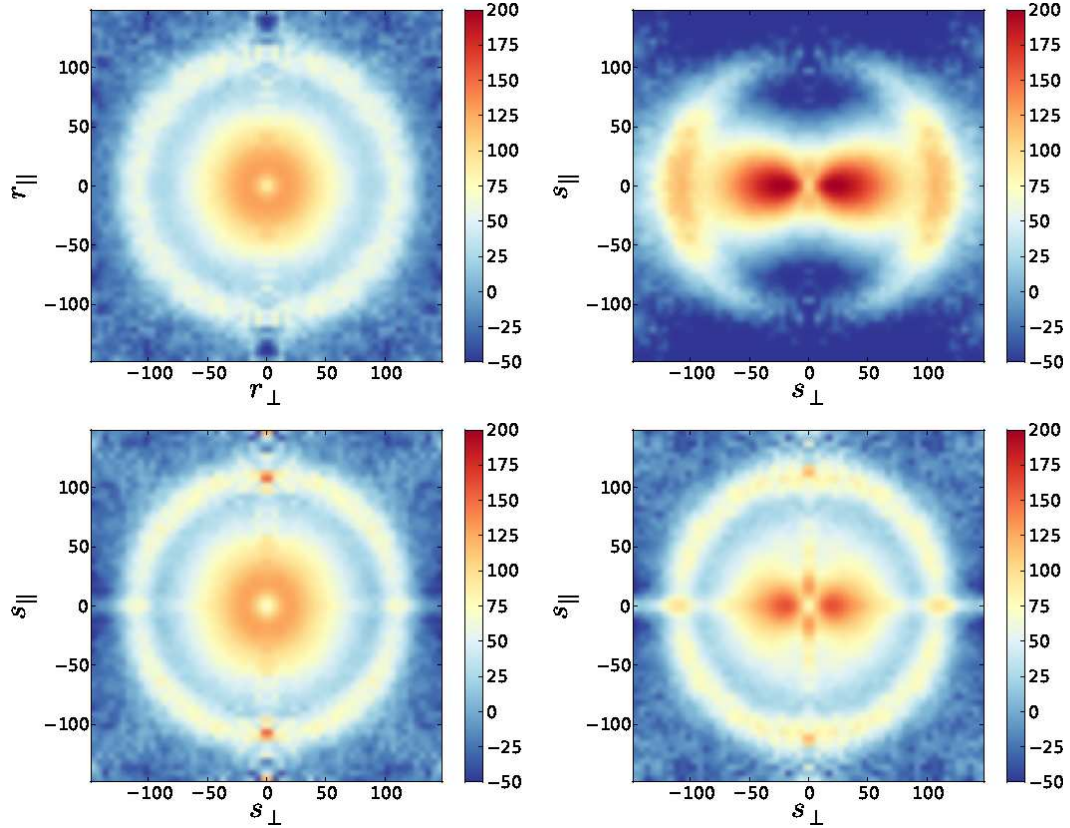


Figure 3.6: The average 2D correlation functions of the mocks before and after reconstruction in real and redshift space. (top left) 2D correlation function in real space before reconstruction. (bottom left) 2D correlation function in real space after reconstruction. (top right) 2D correlation function in redshift space before reconstruction. (bottom right) 2D correlation function in redshift space after reconstruction. The line-of-sight direction is on the x -axis and the transverse direction is on the y -axis. One can see that in real space, the clustering is isotropic due to the lack of redshift-space distortions and the BAO feature appears as a ring at the BAO scale. However, in redshift space, the clustering is highly anisotropic due to the non-cosmological motions of galaxies with the distortion greatest along the line-of-sight direction (Kaiser and Finger-of-God distortions). After reconstruction the anisotropy is reduced in redshift space at large scales reflecting the success of our Kaiser correction. Most importantly, we see that in both real and redshift space, the BAO ring is more prominent than in the pre-reconstruction case. This implies that reconstruction was effective at removing the degradation of the acoustic feature due to large-scale flows arising from non-linear structure growth.

rection we apply during reconstruction is effective at large scales. At small scales the clustering still appears anisotropic as we do not apply any corrections for the FoG effect. In fact, the FoG appears to be enhanced after reconstruction suggesting that reconstruction tends to blow up collapsed objects such as dark matter halos. In addition, since our reconstruction technique is only to first-order, the highly non-linear small scales will not experience as significant a correction. We note here that this small-scale anisotropy has no effect on the acoustic scale.

Most importantly, we see that the BAO signal stands out much more clearly after reconstruction. This indicates that our reconstruction technique was effective at partially undoing the smearing of the BAO by non-linear structure growth. A similar increase in contrast is seen in real space after reconstruction as well (bottom left panel of Figure 3.6). Here we have performed the reconstruction using $b = 2.2$, $f \sim \Omega_m^{0.55}$ and a smoothing length of $= 15h^{-1}\text{Mpc}$ which will henceforth be denoted the fiducial reconstruction parameters. We have also assumed an input power spectrum for generating constrained Gaussian realizations corresponding to the LasDamas cosmology.

Spherically averaging over the mock redshift-space 2D correlation functions gives the monopole correlation functions. The average of these is shown in Figure 3.7 with the post-reconstruction real-space average overplotted as the dashed blue line. One can see that the BAO peak has sharpened up after reconstruction, corresponding to the increased contrast seen in the 2D correlation function. This again implies that we were successful at partially removing the effects of non-linear structure growth on the BAO. The amplitude of the correlation function overall is also reduced due to the removal of Kaiser squashing. The reconstructed real and redshift-space correlation functions do not match perfectly at small scales which again suggests that the reconstruction technique is breaking down on these scales. However, the

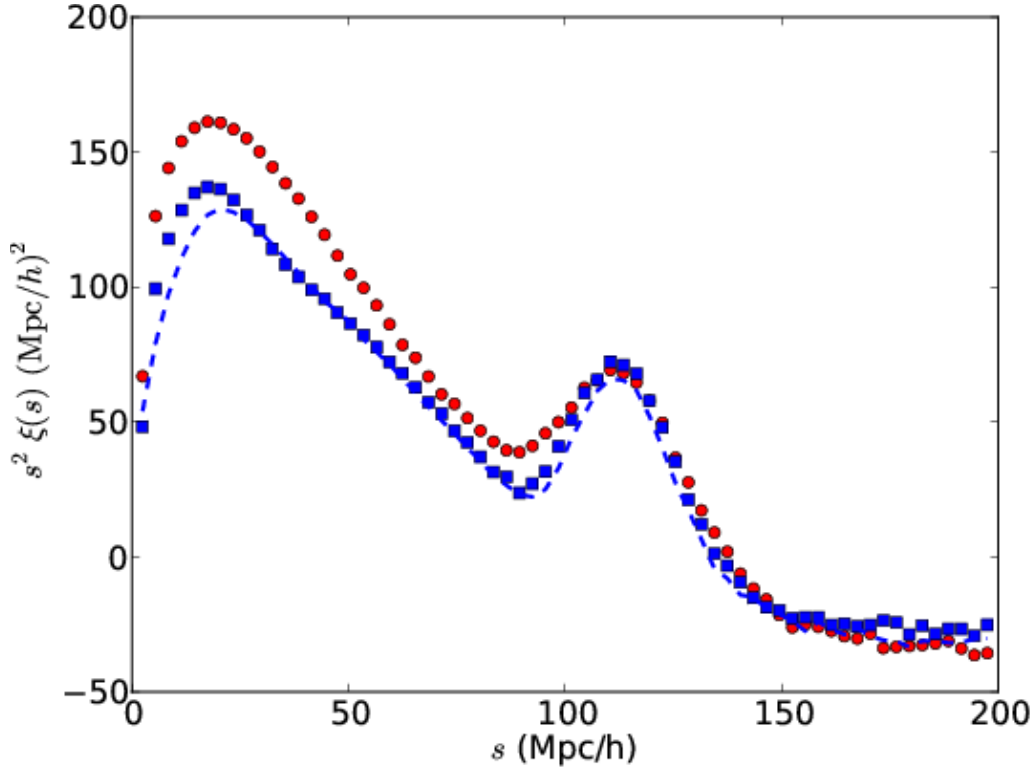


Figure 3.7: The average spherically averaged redshift space correlation function of the mocks before and after reconstruction. The post-reconstruction real space correlation function is overplotted as the dashed blue line. One can see that the redshift space and real space results do not match exactly at small scales, indicating that our reconstruction scheme is breaking down at these scales. Most importantly, we see that the BAO peak has sharpened up significantly after reconstruction: Σ_{nl} decreases from $8.1h^{-1}\text{Mpc}$ to $4.4h^{-1}\text{Mpc}$. This implies that our reconstruction technique is successful at partially undoing the effects of non-linear structure growth on the BAO.

similarity of the two at scales larger than $30h^{-1}\text{Mpc}$ indicates that reconstruction is very effective in removing large-scale redshift-space distortions.

The change in shape of the correlation function before and after reconstruction has a simple physical interpretation. Reconstruction takes pairs and redistributes them over different scales which implies that the area under $\xi(r)$ must be conserved. The transferring of pairs from small $< 20h^{-1}\text{Mpc}$ scales to larger scales $\sim 50h^{-1}\text{Mpc}$ is due to the reversing of galaxy infall towards overdense regions (the Kaiser effect). The correlation function is higher at scales slightly smaller than the BAO scale before reconstruction due to pairs flowing out from the BAO ring (recall that these flows are what cause the smearing of the BAO). After reconstruction, these pairs are moved back into the BAO ring, sharpening up the BAO peak. This sharpening can be quantified using the BAO damping scale Σ_{nl} used to model the degradation of the acoustic peak due to non-linear structure growth in our fitting model. As discussed in the previous section, fitting the average redshift-space correlation function of the mocks gives $\Sigma_{nl} = 8.1h^{-1}\text{Mpc}$ before reconstruction and $\Sigma_{nl} = 4.4h^{-1}\text{Mpc}$ after reconstruction. Hence, the damping is nearly a factor of 2 smaller after reconstruction which is consistent with theoretical estimates (Padmanabhan et al., 2009).

The most important reconstruction parameter is the smoothing length l . When we perform reconstruction, we must infer the displacement field from the matter density field which is roughly related to the measured galaxy density field by the galaxy bias. However, galaxies are finite points and therefore do not smoothly trace the underlying matter distribution. Hence we smooth over the galaxy density field, effectively smearing the galaxy “spike” across its surroundings to better approximate the matter density field. If l is too small, we smooth over fewer galaxies which increases the noise in our reconstruction. However, if l is too large, the estimated displacements are reduced leading to less effective reconstruction (in fact, if the

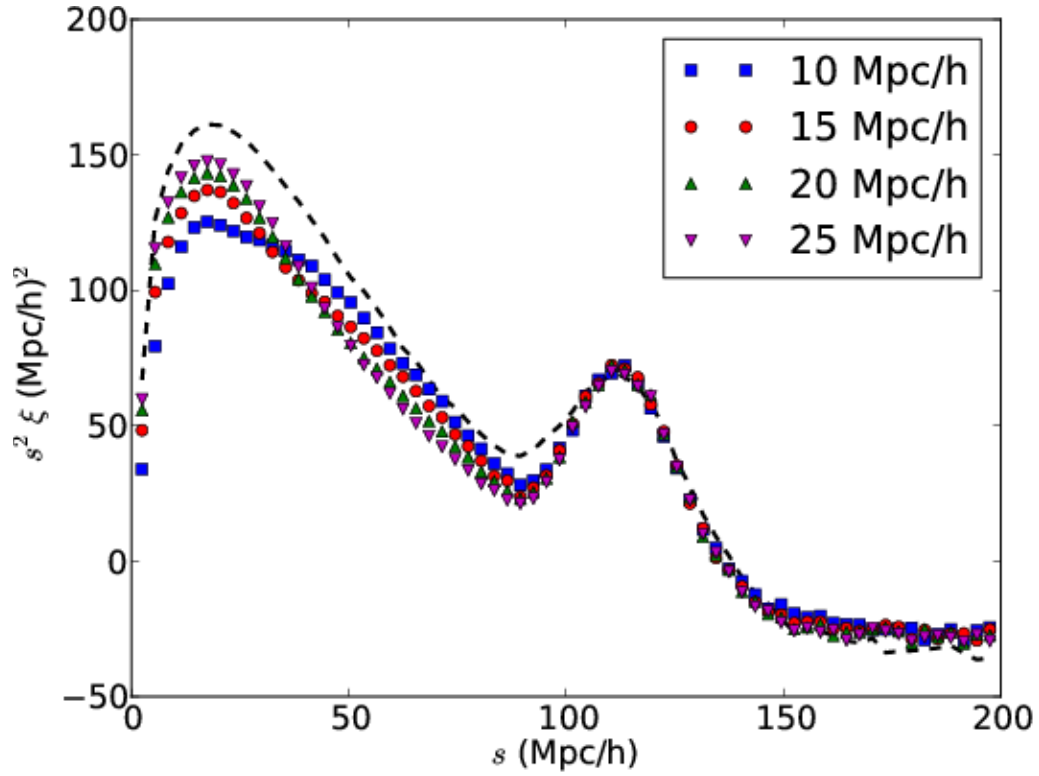


Figure 3.8: The average redshift-space correlation function of the mocks after reconstruction for various reconstruction smoothing scales l . We see that using a fairly large smoothing scale already has a noticeable affect on the BAO peak. Choosing $l = 10h^{-1}\text{Mpc}$, however, introduces significant distortions of the correlation function at small scales, indicating a breakdown in your algorithm. Since it is optimal to select the smallest reasonable smoothing scale, we take $l = 15h^{-1}\text{Mpc}$ as our fiducial value.

smoothing length is infinite, the estimated displacements are 0). Hence it is optimal to choose the smallest smoothing scale possible. For the LRG number density, $n \leq 10^{-4}h^3\text{Mpc}^{-3}$, the power spectrum amplitude becomes comparable to the shot-noise at $k \sim 0.15h\text{Mpc}^{-1}$, which suggests a smoothing length $\gtrsim 10h^{-1}\text{Mpc}$.

Figure 3.8 shows the average correlation function of the mocks in redshift space after reconstruction for various smoothing lengths. The unreconstructed correlation function is overplotted as the dashed line. One can see that the correlation function becomes noticeably distorted for $l = 10h^{-1}\text{Mpc}$. Also of note is that even with a fairly large smoothing scale of $25h^{-1}\text{Mpc}$, the sharpening up of the acoustic peak is significant. This reflects the fact that large-scale flows are what smear the acoustic peak: as long as we do not smooth on scales significantly larger than these flows, we will recover a more prominent acoustic peak. Since we would like to choose the smallest smoothing length that is reasonable, we pick $l = 15h^{-1}\text{Mpc}$ as our fiducial reconstruction value.

3.5 LasDamas Redshift Space Fitting Results

3.5.1 Without Reconstruction

We now concern ourselves with presenting the results and validating the reconstruction and fitting techniques described in §3.3.3 for measuring the acoustic scale. We begin with the LasDamas mocks in redshift space without reconstruction. Through fitting the mocks using the fiducial model, we find that a few of the mocks do not give compelling measurements of α due to their relatively weak acoustic features. We attempt to identify which mocks have poorly constrained values of α by performing our fits at different test values of α_i using our fiducial model and measuring the resulting χ^2 . This allows us to calculate

$$p(\alpha_i) = \frac{e^{-\chi^2(\alpha_i)/2}}{\sum_j e^{-\chi^2(\alpha_j)/2} \Delta\alpha}, \quad (3.37)$$

the probability of measuring the acoustic scale to be $\alpha = \alpha_i$ from a particular mock. Here, the denominator is a normalization factor equivalent to integrating over all test values of α where $\Delta\alpha$ is the difference between the test values. We calculate a mean and a standard deviation for our $p(\alpha)$ distributions as

$$\langle\alpha\rangle = \sum_i \alpha_i p(\alpha_i) \Delta\alpha \quad (3.38)$$

$$\sigma_\alpha = \sqrt{\sum_i [\alpha_i - \langle\alpha\rangle]^2 p(\alpha_i) \Delta\alpha}. \quad (3.39)$$

A small standard deviation indicates that the best-fit α measured from the mock is well constrained. Conversely, a large standard deviation indicates that it is difficult to measure an accurate value of α from the mock.

In Figure 3.9, we have plotted the fit results using the fiducial model for 2 of our mock redshift-space correlation functions, $\xi_s(r)$, that appear to have well constrained values of α (upper 2 panels) and 2 that do not (lower 2 panels). These are representative of the other well and poorly constrained mocks in our set. For a detailed description of the information plotted, please see the figure caption.

The left column in each set shows the actual fit to the mock correlation function using the fiducial model. The best-fit values of α and their corresponding minimum χ^2/dof are given on the plots. In comparing the well constrained mocks to the poorly constrained mocks, we can see that in order to obtain a fairly certain measurement of best-fit α , the mock must have a prominent acoustic peak. If one ignores the best-fit models which can be used to guide the eye, the acoustic features in both of the poorly constrained mocks are much weaker than in the well constrained mocks.

The middle column in each set shows the $\Delta\chi^2 = \chi^2(\alpha) - \chi_{min}^2$ curve for each mock. The $\chi^2(\alpha)$ here is the same as that which appears in Equation (3.37) and

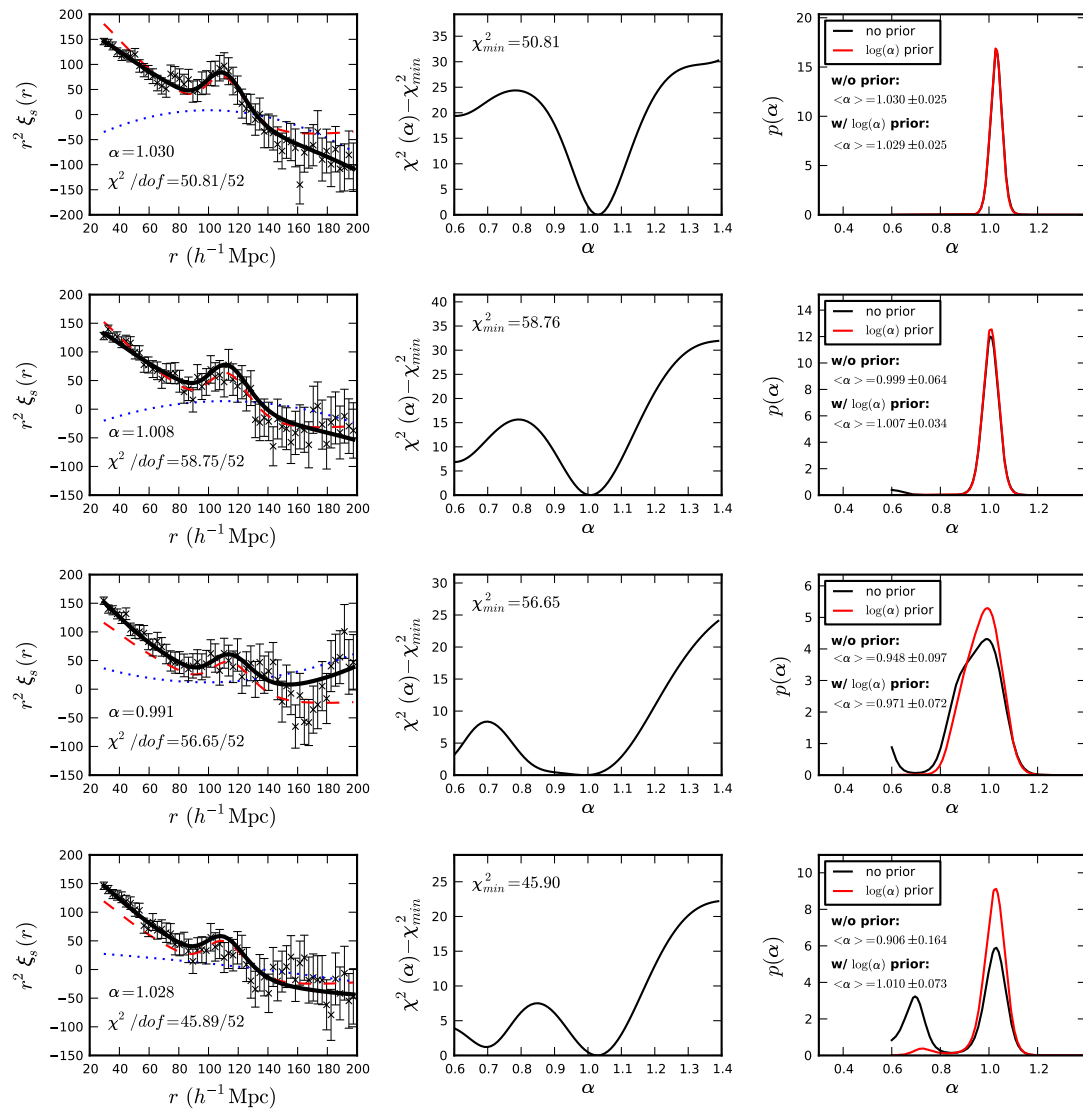


Figure 3.9

(Figure 3.9 caption on next page)

(Figure 3.9 continued)

Figure 3.9: Sample fit results from the fiducial model for our redshift-space mocks, $\xi_s(r)$. (rows 1+2) Results from mocks that have well constrained measures of α . (rows 3+4) Results from mocks that have poorly constrained measures of α . (left column) Actual fits using the fiducial model. The model (black line) is overplotted on the mock data (black crosses with error bars). The dotted blue line corresponds to the $A(r)$ term in the model and the dashed red line corresponds to the $B^2\xi_m(\alpha r)$ term. Comparing rows 1 & 2 with rows 3 & 4 suggests that there must be a fairly prominent acoustic peak in order to obtain a well constrained measurement of α . (middle column) The $\Delta\chi^2 = \chi^2(\alpha) - \chi^2_{min}$ curve. The large differences in χ^2 between the minimum and the plateaus of the well constrained cases indicate that we have robust detections of the χ^2 minimum and hence the best-fit α which corresponds to this minimum. In the poorly constrained mocks, the difference is much smaller and there may be double minima at small $\Delta\chi^2$ from each other, indicating a poor detection of the best-fit α . (right column) The $p(\alpha)$ distribution versus α (black line) calculated from $\chi^2(\alpha)$, Equation (3.37). The red line is the same curve but with a 15% Gaussian prior on $\log(\alpha)$. We say best-fit α is well constrained in a mock, when the standard deviation of the $p(\alpha)$ distribution is small, and not well constrained when the standard deviation is large, even after the prior is applied. In some mocks, we see significant χ^2 differences between the minimum and the plateau, however, the σ_α measured may still be large. This is due to a downturn in the $\chi^2(\alpha)$ curve at $\alpha \sim 0.7$ (see the second row). Such a downturn is not physically motivated because it is caused by the model attempting to hide the acoustic peak in the larger errors at large r . Hence, we introduce the prior on $\log(\alpha)$ to suppress this effect.

χ_{min}^2 is the minimum of $\chi^2(\alpha)$, i.e. χ^2 at the best-fit value of α . One can see that for the well constrained mocks, the curve is nearly parabolic around the minimum (expected if α is Gaussian distributed) and then plateaus at extreme values of α . The height in $\Delta\chi^2$ of these plateaus can be used as a proxy for the significance of the χ^2 minimum. In the poorly constrained mocks, the plateau occurs at much smaller $\Delta\chi^2$ values. In addition, there may be double minima at small differences in χ^2 . These indicate that we are not detecting the χ^2 minimum (and hence best-fit α) robustly.

In the right panels, we use these $\chi^2(\alpha)$ curves to calculate their corresponding $p(\alpha)$ distributions using Equation (3.37). These are plotted as the black lines. The red lines include an additional 15% Gaussian prior on $\log(\alpha)$, i.e. $\chi^2(\alpha) \rightarrow \chi^2(\alpha) + \left(\frac{\log(\alpha)}{0.15}\right)^2$. We apply this weak prior because in some of the cases where the best-fit α should be well constrained, i.e. in the second row where the $\Delta\chi^2$ curve is nicely parabolic around a minimum that is at a significant $\Delta\chi^2 \sim 15$ away from the plateau, we still measure a large σ_α from the $p(\alpha)$ distribution. This is due to a slight downturn in the χ^2 versus α curve (and hence an upturn in the $p(\alpha)$ distribution) at $\alpha \sim 0.7$. At these small α , the acoustic peak in the model is getting pushed out to large r . Here, the error bars are larger so the fitter is having an easier time hiding the acoustic peak in the errors. Since this downturn in χ^2 is not physically motivated, we apply this prior to downweight the χ^2 values at extreme α . One can see the effectiveness of the prior by noticing that the upturn in $p(\alpha)$ disappears after the prior is applied to the mock in the second row.

As mentioned previously, the acoustic scale is well constrained in the mocks that have very small standard deviations in α . In these cases, the inferred standard deviation can become even smaller after the prior is applied, not due to any dramatic change in the general shape of the curve but rather because the tails become sup-

pressed by the prior. The mocks where α is not well constrained, however, have very broad distributions with large standard deviations even after a prior is applied. This suggests that we may segregate the well constrained mocks from the poorly constrained mocks by setting a cutoff in the standard deviation after applying the prior on $\log(\alpha)$. We also note here that, after applying the prior, the mean α of the $p(\alpha)$ distribution should be fairly close to the best-fit α from the fiducial model for the well constrained mocks. This is indeed what we observe. Any discrepancy is likely due to the fact that the $p(\alpha)$ distribution is not exactly Gaussian.

A plot of the standard deviations versus the best-fit α values from the fiducial model are shown in Figure 3.10. The median of the standard deviations is indicated by the solid grey line and the 98th, 84th, 16th and 2nd percentile levels are indicated by the dashed grey lines. We see that the poorly constrained mocks mostly lie at standard deviations larger than 7% (indicated by the black horizontal line in the plot). Hence, we make a cutoff in standard deviation at 7% and take all mocks that lie above this cutoff to have poorly constrained measurements of α (circled in black). Both of the poorly constrained mocks shown in Figure 3.9 fall into this category. For our redshift-space mocks before reconstruction, we find that 8 (5%) have fairly poor measurements of α . The mean and median values of the best-fit α from the fiducial model are given in the plot after removing the poorly constrained mocks. We use this procedure to remove these poorly constrained mocks from our α -fitting sample before proceeding. Note that they are still included in our covariance matrix derivation.

Using the fiducial model, we find $\bar{\alpha} = 0.999 \pm 0.033$ and $\tilde{\alpha} = 1.003 \pm_{0.034}^{0.030}$ after removing the poorly constrained mocks as just described. Here and throughout this chapter we quote the mean of any quantity x and its standard deviation (rms scatter) from the mocks as \bar{x} and we quote the median with the 84th/16th percentiles from

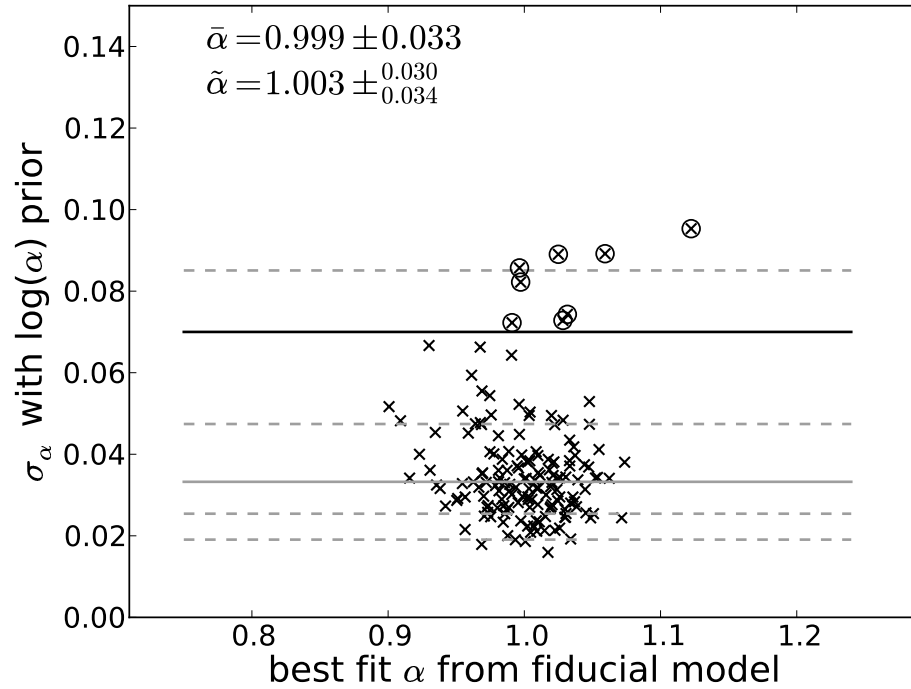


Figure 3.10: The standard deviations of $p(\alpha)$ for the redshift-space mocks plotted against their best-fit α values measured using the fiducial model. A large standard deviation indicates that α is poorly constrained in its corresponding mock. The solid grey line indicates the median of the standard deviations while the dashed grey lines indicate the 98th, 84th, 16th and 2nd percentiles. We see that most of these poorly constrained mocks fall above a standard deviation of 7%. Hence we impose a 7% cutoff (black horizontal line) in standard deviation and remove all the mocks with standard deviations above this cutoff from our fitting sample. The mocks with uncertain α measurements based on this metric are circled. There are 8 of such mocks, which is 5% of our sample. The mean and median values of best-fit α measured using the fiducial model after removing the poorly constrained mocks are listed on the plot.

the mocks as \tilde{x} . Note that to obtain the standard error on the mean, one should divide the rms by \sqrt{N} , where N is the number of mocks. If we take the rms as an estimate of the error on the acoustic scale in a single mock, we see that before reconstruction, we expect a $\sim 3 - 3.5\%$ measurement.

It is important to recall here that α measures the shift in the acoustic peak location relative to the fiducial cosmology used to construct the fitting model. Since we know the true LasDamas cosmology and we construct our model using this cosmology, we should recover a mean $\alpha = 1$, i.e. no peak shift, if our fitting method is unbiased. This is indeed what we see. The very small discrepancy is likely due to non-linear structure growth which we expect will shift α by $\sim 0.5\%$ or less (Padmanabhan & White, 2009; Mehta et al., 2011).

Table 3.2: Redshift space fitting results for various models. Here we test the effects of varying fit parameters on our measured acoustic scale from the mocks. The first column indicates how the fiducial model was changed. The second and third columns show the mean and median α values of the mocks. The fourth and fifth columns show the mean and median differences in α between the fiducial model and the model listed in column 1 on a mock-by-mock basis. The last column shows the mean χ^2 value from the mocks.

Model	$\bar{\alpha}^1$	$\tilde{\alpha}$	$\overline{\Delta\alpha}^2$	$\widetilde{\Delta\alpha}$	$\overline{\chi^2}/dof$
Redshift Space without Reconstruction					
Fiducial [f]	0.999 ± 0.033	$1.003 \pm_{0.034}^{0.030}$	–	–	52.96/52
Fit with 15% larger Ω_m using fiducial $A(r)$. ³	0.998 ± 0.034	$1.001 \pm_{0.035}^{0.029}$	-0.002 ± 0.002	$-0.001 \pm_{0.002}^{0.001}$	53.29/52
Fit with $n_s = 0.96$ using fiducial $A(r)$.	1.001 ± 0.033	$1.004 \pm_{0.034}^{0.030}$	0.002 ± 0.001	$0.001 \pm_{0.001}^{0.001}$	52.92/52
Fit with $N_{rel} = 4$ using fiducial $A(r)$.	1.006 ± 0.033	$1.008 \pm_{0.033}^{0.032}$	0.007 ± 0.005	$0.006 \pm_{0.001}^{0.001}$	52.85/52
Fit with $\Sigma_{nl} \rightarrow 0$.	0.996 ± 0.036	$0.997 \pm_{0.032}^{0.032}$	-0.003 ± 0.020	$-0.004 \pm_{0.013}^{0.013}$	54.29/52
Fit with $\Sigma_{nl} \rightarrow \Sigma_{nl} + 2$.	1.001 ± 0.034	$1.005 \pm_{0.034}^{0.028}$	0.002 ± 0.005	$0.002 \pm_{0.005}^{0.004}$	53.28/52
Fit with <i>poly0</i> .	0.995 ± 0.035	$0.996 \pm_{0.030}^{0.034}$	-0.004 ± 0.012	$-0.003 \pm_{0.008}^{0.007}$	56.03/55
Fit with <i>poly2</i> .	0.997 ± 0.033	$1.002 \pm_{0.035}^{0.030}$	-0.002 ± 0.004	$-0.001 \pm_{0.003}^{0.002}$	54.44/53
Fit with <i>poly4</i> .	0.999 ± 0.033	$1.002 \pm_{0.033}^{0.031}$	0.000 ± 0.001	$0.000 \pm_{0.000}^{0.000}$	51.81/51
Fit with $50 < r < 200h^{-1}\text{Mpc}$ fitting range.	1.000 ± 0.033	$1.004 \pm_{0.033}^{0.030}$	0.001 ± 0.005	$0.001 \pm_{0.003}^{0.003}$	45.73/45
Fit with $20 < r < 200h^{-1}\text{Mpc}$ fitting range.	1.002 ± 0.033	$1.004 \pm_{0.033}^{0.033}$	0.003 ± 0.008	$0.003 \pm_{0.006}^{0.006}$	59.45/57

Continued on next page

Table 3.2 – continued from previous page

Model	$\bar{\alpha}$	$\tilde{\alpha}$	$\overline{\Delta\alpha}$	$\widetilde{\Delta\alpha}$	$\overline{\chi^2}/dof$
Fit with $70 < r < 150h^{-1}\text{Mpc}$ fitting range.	0.999 ± 0.033	$1.001 \pm_{0.031}^{0.033}$	0.000 ± 0.010	$-0.000 \pm_{0.008}^{0.009}$	21.83/22
Fit using mock covariance matrix.	1.002 ± 0.027	$1.003 \pm_{0.026}^{0.025}$	0.003 ± 0.022	$0.003 \pm_{0.017}^{0.018}$	52.80/52
Redshift Space with Reconstruction					
Fiducial [f]	1.001 ± 0.021	$1.001 \pm_{0.022}^{0.020}$	–	–	53.69/52
Fit with 15% larger Ω_m using fiducial $A(r)$.	1.001 ± 0.021	$1.001 \pm_{0.022}^{0.020}$	-0.000 ± 0.001	$-0.000 \pm_{0.001}^{0.001}$	51.86/52
Fit with $n_s = 0.96$ using fiducial $A(r)$.	1.002 ± 0.021	$1.002 \pm_{0.022}^{0.020}$	0.001 ± 0.000	$0.001 \pm_{0.000}^{0.000}$	51.84/52
Fit with $N_{rel} = 4$ using fiducial $A(r)$.	1.006 ± 0.021	$1.006 \pm_{0.022}^{0.020}$	0.005 ± 0.001	$0.005 \pm_{0.001}^{0.001}$	51.95/52
Fit with $\Sigma_{nl} \rightarrow 0$.	1.001 ± 0.022	$1.001 \pm_{0.020}^{0.022}$	-0.000 ± 0.004	$-0.001 \pm_{0.003}^{0.004}$	53.83/52
Fit with $\Sigma_{nl} \rightarrow \Sigma_{nl} + 2$.	1.002 ± 0.021	$1.001 \pm_{0.020}^{0.022}$	0.001 ± 0.004	$0.001 \pm_{0.004}^{0.002}$	53.99/52
Fit with <i>poly0</i> .	1.000 ± 0.021	$1.000 \pm_{0.020}^{0.019}$	-0.002 ± 0.004	$-0.001 \pm_{0.004}^{0.004}$	57.34/55
Fit with <i>poly2</i> .	1.000 ± 0.021	$1.001 \pm_{0.022}^{0.021}$	-0.001 ± 0.002	$-0.001 \pm_{0.001}^{0.001}$	55.41/53
Fit with <i>poly4</i> .	1.001 ± 0.021	$1.001 \pm_{0.022}^{0.021}$	-0.000 ± 0.000	$-0.000 \pm_{0.000}^{0.000}$	52.68/51
Fit with $50 < r < 200h^{-1}\text{Mpc}$ fitting range.	1.001 ± 0.021	$1.000 \pm_{0.021}^{0.023}$	0.000 ± 0.002	$0.000 \pm_{0.002}^{0.001}$	46.58/45
Fit with $20 < r < 200h^{-1}\text{Mpc}$ fitting range.	1.005 ± 0.021	$1.004 \pm_{0.020}^{0.022}$	0.004 ± 0.003	$0.004 \pm_{0.003}^{0.003}$	60.06/57
Fit with $70 < r < 150h^{-1}\text{Mpc}$ fitting range.	1.001 ± 0.026	$1.003 \pm_{0.019}^{0.022}$	-0.000 ± 0.012	$0.000 \pm_{0.005}^{0.004}$	22.69/22

Continued on next page

Table 3.2 – continued from previous page

Model	$\bar{\alpha}$	$\tilde{\alpha}$	$\overline{\Delta\alpha}$	$\widetilde{\Delta\alpha}$	$\overline{\chi^2}/dof$
Fit using mock covariance matrix.	1.004 ± 0.017	$1.003 \pm_{0.014}^{0.017}$	0.003 ± 0.015	$0.001 \pm_{0.010}^{0.015}$	54.22/52

¹ Note that the error quoted with the mean is the rms scatter from the mocks and not the standard error in the mean. To obtain the standard error, divide the rms by \sqrt{N} , where N is the number of mocks.

² $\Delta\alpha = \alpha_{[i]} - \alpha_{[f]}$, where i is the model listed in column 1.

³ We scale the measured sound horizons to the LasDamas cosmology where necessary.

To verify the robustness of our covariance modeling and the fiducial model, we compare the α values we measure from the fiducial model to those we measure when the fiducial model parameters are slightly changed or if we fit using a different covariance matrix. A summary of the results of these fits can be found in Table 3.2, where we have removed the mocks with poorly constrained measurements of α .

Our first test is to see whether we can recover the true acoustic scale using our fiducial model but with $P_m(k)$ derived from slightly different cosmologies to that used by LasDamas. Figure 3.11 shows the α values derived from these incorrect cosmologies versus the α values obtained through fits using the fiducial model (i.e. with the correct cosmology). The α values obtained from the incorrect cosmologies have been scaled to the correct cosmology where necessary by multiplying the ratio of the sound horizons, $r_{s,\text{lin}}(\text{correct})/r_{s,\text{lin}}(\text{incorrect})$, where the $r_{s,\text{lin}}$ are calculated using Equation (6) in Eisenstein & Hu (1998). For a more detailed discussion of the sound horizon calculation, please refer to Paper III. The figure caption gives an explicit description of the items plotted. Note that we define $\Delta\alpha \equiv \alpha_{y\text{-axis}} - \alpha_{x\text{-axis}}$, where we always have $\alpha_{x\text{-axis}}$ equal to the values of α measured using the fiducial model.

The top left panel shows the α values from a fit using $A(r) = 0$ (i.e. *poly0*) and a cosmology with a 15% larger value of Ω_m (and hence Ω_b). This difference should give rise to an acoustic scale that is about 5% smaller. The top right panel shows the results from the same fit with the fiducial $A(r)$ form instead of *poly0*. We expect the mean and median $\Delta\alpha$ values to be ~ 0 if we can recover the true acoustic scale using an incorrect cosmology template (i.e. if the α values plotted on the 2 axes are perfectly correlated). We see that this result is recovered with $\sim 0.2\%$ scatter when we fit using the fiducial $A(r)$ form. This is $\sim 1\%$ smaller than the scatter found when fitting with *poly0*, another indication of the advantages of fitting with

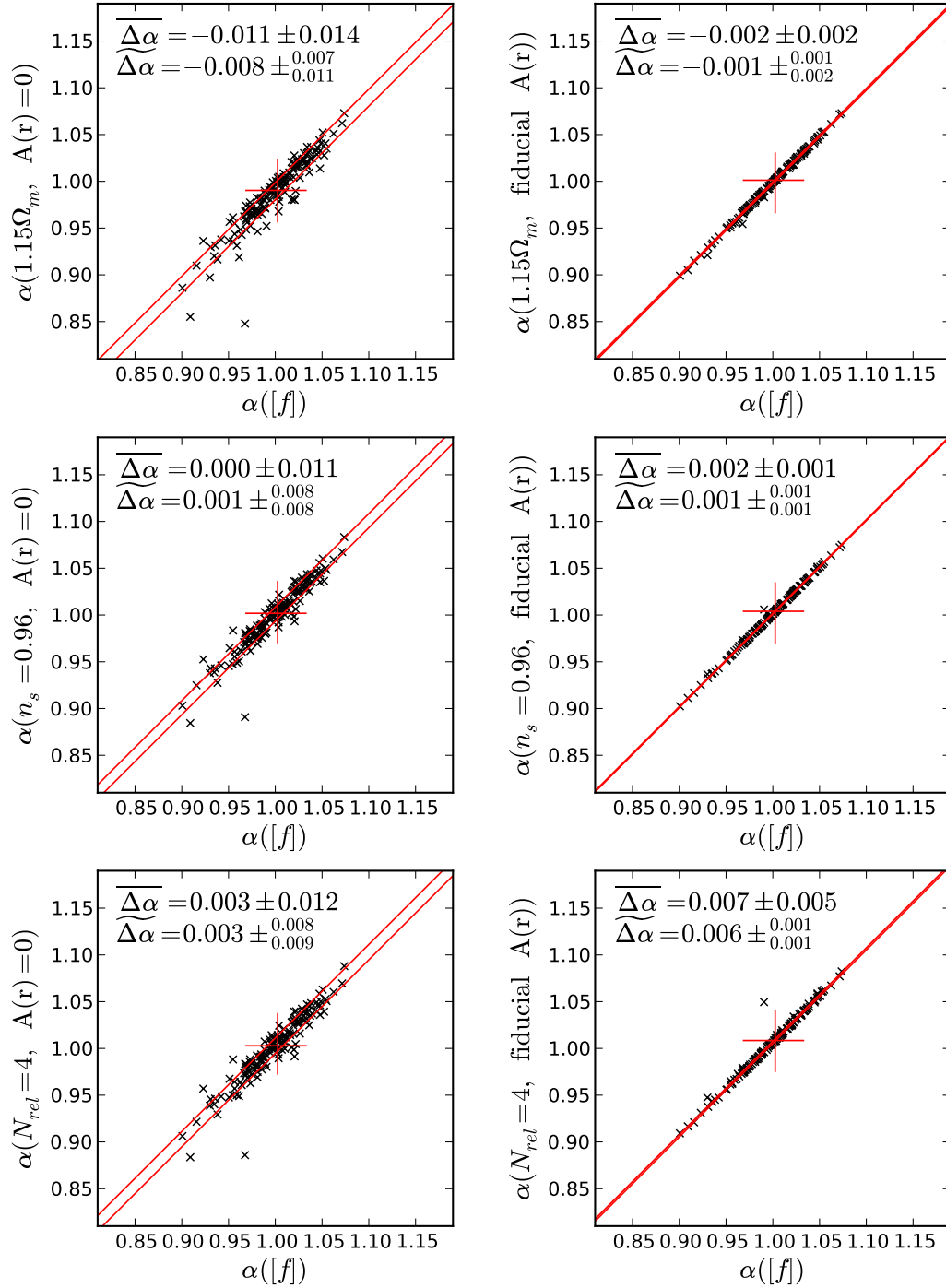


Figure 3.11

(Figure 3.11 caption on next page)

(Figure 3.11 continued)

Figure 3.11: Validation of our fitting method using LasDamas mocks: varying template cosmology. Here we have plotted the redshift-space α values measured using the fiducial model (i.e. using the true LasDamas cosmology) on the x -axis versus the α values measured using templates derived from slightly different cosmologies on the y -axis. For the incorrect cosmology templates, we have performed the fits using *poly0* (left) and the fiducial $A(r)$ form (right). The α values from the incorrect cosmologies have been scaled to the correct cosmology where necessary. The red cross indicates the median α values with their 16th and 84th percentiles. The red lines indicate the 16th and 84th percentiles of $\Delta\alpha = \alpha_{y\text{-axis}} - \alpha_{x\text{-axis}}$. These values are given in the plots. Overall, we see that the fiducial $A(r)$ form is better at recovering the correct acoustic scale than *poly0* and that our fiducial model is robust in recovering the correct acoustic scale even when the template power spectrum is derived from a slightly different cosmology. (top) Results when we fit with a template cosmology where Ω_m is 15% higher than LasDamas. (middle) Results when we fit with a template cosmology where $n_s = 0.96$. (bottom) Results when we fit with a template where there are 4 relativistic neutrino species. We see that the $\Delta\alpha$ offset is larger in this case, especially when fitting with the fiducial $A(r)$ form. This $\sim 0.6\%$ offset is likely a result of the template BAO shape deviating slightly from that in the mock data.

a non-zero $A(r)$.

The middle left panel of Figure 3.11 shows the α values from fits using *poly0* and a cosmology with $n_s = 0.96$ plotted against the results from the fiducial model ($n_s = 1.0$). The difference in n_s should not affect the position of the acoustic scale, but only the shape of the model. The analogous results using the fiducial $A(r)$ form instead of *poly0* are shown in the middle right. The correct acoustic scale is recovered with $\Delta\alpha$ very close to 0 and $\sim 0.1\%$ scatter when the fiducial $A(r)$ form is used. The corresponding *poly0* fit does a poorer job with a scatter in $\Delta\alpha \sim 0$ of about 1%. Overall, the fiducial model seems to be able to recover the true acoustic scale even if its power spectrum template has a slightly different cosmology. This and the previous example show how important it is to fit with a non-zero $A(r)$ term if we are not certain of the true model cosmology to be used (i.e. in the case of actual observations).

The y -axis of the bottom panels in Figure 3.11 correspond to α values measured using *poly0* (left) and fiducial $A(r)$ (right) with a template cosmology consisting of 4 relativistic neutrino species ($N_{rel} = 4$) instead of the standard 3. We use the same Ω_m , $\Omega_b h^2$, and epoch of matter-radiation equality as the $N_{rel} = 3$ case, so that the rough shape of the power spectrum is preserved. This requires $H_0 = 74.3$ km/s/Mpc. As in the previous cases, the scatter in $\Delta\alpha$ is smaller if we employ the fiducial $A(r)$ rather than *poly0*. However, we find a mean offset of 0.6% when using an $N_{rel} = 4$ template, after scaling by the appropriate sound horizon. We believe this is because the shape of the template around the BAO feature is slightly different from the $N_{rel} = 3$ case, e.g., because the baryon fraction in this model is different. While the 0.6% offset is much smaller than the statistical errors of the DR7 data set, larger surveys might need to iterate their fits to converge to a sufficiently accurate template when investigating variations in the number of relativistic species.

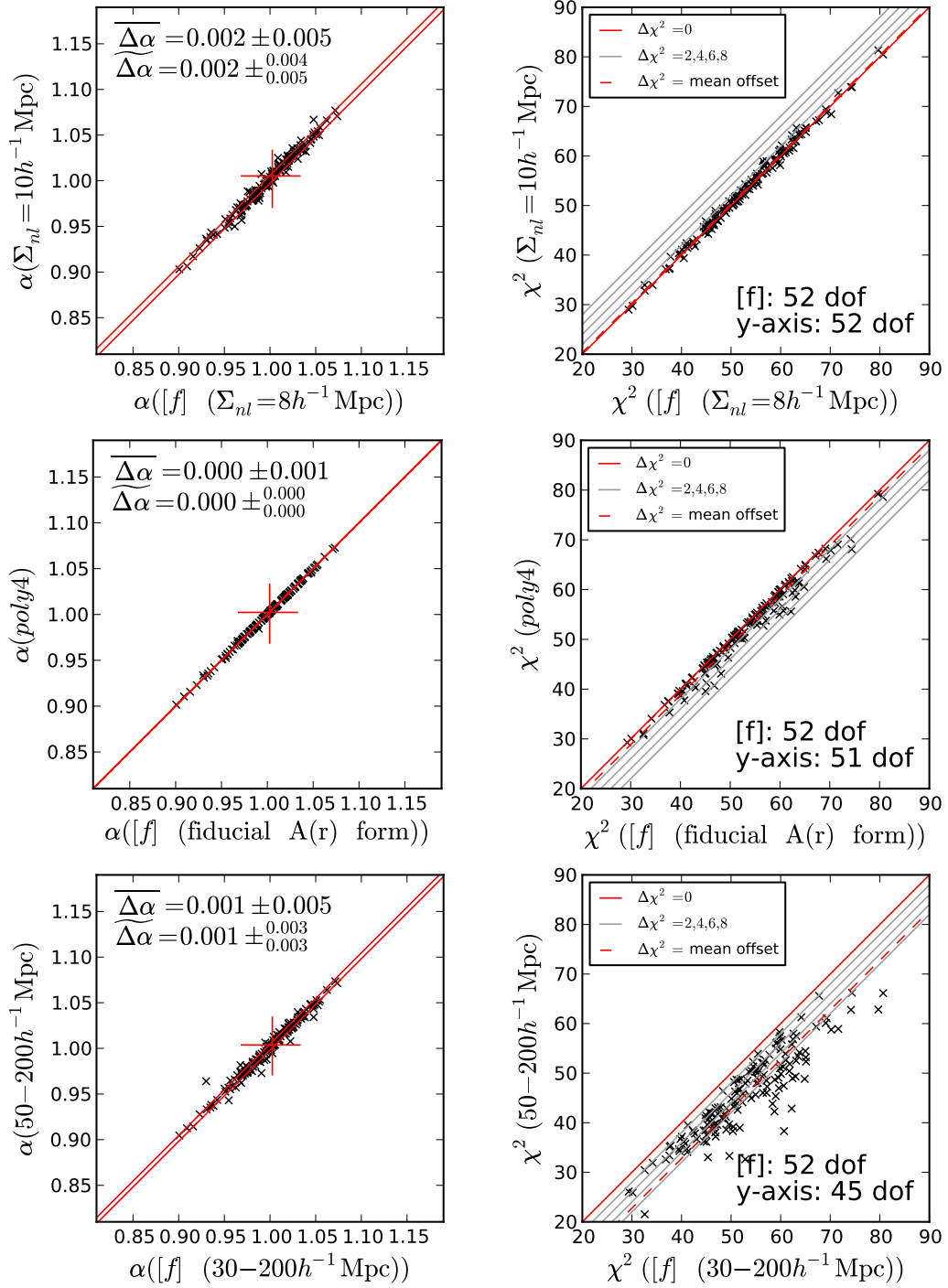


Figure 3.12

(Figure 3.12 continued on next page)

(Figure 3.12 continued)

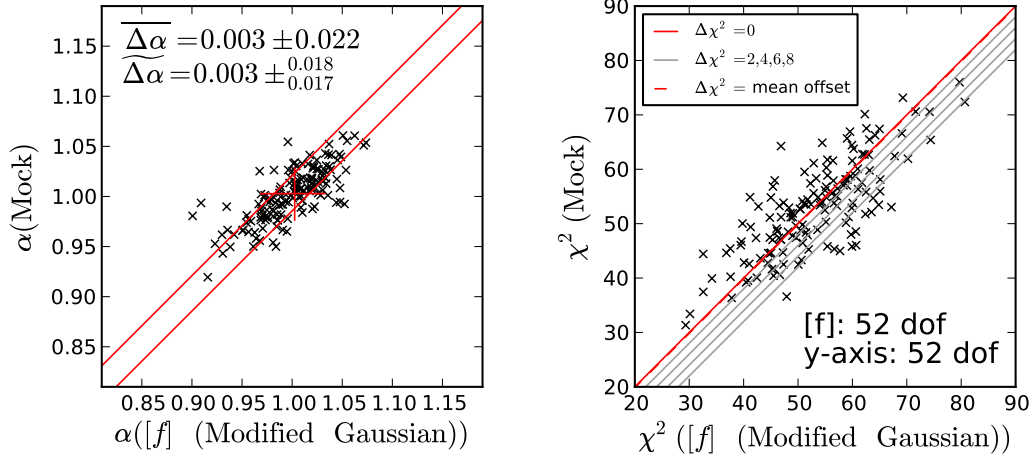


Figure 3.12: Validation of our fitting method using LasDamas mocks: varying fitting/model parameters. This figure is akin to Figure 3.11 in that the left panels show similar plots of redshift-space α values measured using the fiducial model (x -axis) versus those measured using models in which the fiducial parameters are slightly tweaked (y -axis). However, instead of varying the template cosmology, here we vary other fiducial model parameters such as Σ_{nl} (top), the order of $A(r)$ (2nd row) and the fitting range (3rd row). The tight correlations shown in all of these plots indicate the robustness of our covariance matrix estimators and the robustness of our fiducial model to small changes in model parameters. The right panels show corresponding plots of the measured best-fit χ^2 values. In all cases we see that the χ^2 values shift by reasonable amounts given the addition or subtraction of degrees-of-freedom as we change the fiducial parameters. (top) Results when we fit using $\Sigma_{nl} = 10h^{-1}\text{Mpc}$. (2nd row) Results when we fit using *poly4*. (3rd row) Results when we use a fitting range of $50 < r < 200h^{-1}\text{Mpc}$. (bottom) For completeness, we show the comparison between fits using the mock covariance matrix (Equation (3.8)) and fits using the MGCM. A correlation between the 2 sets of α can be seen, but the noisiness of the mock covariance matrix is responsible for the larger scatter. Similarly, the corresponding χ^2 plot shows a fair bit of scatter. However, the average χ^2 values obtained using these 2 different covariance matrices match nicely.

Next we test how changing the value of Σ_{nl} in $P_m(k)$ of the fiducial model affects the measured acoustic peak position. In the top left panel of Figure 3.12, we plot the α values measured using fits with $\Sigma_{nl} = 10h^{-1}\text{Mpc}$ versus those derived from the fiducial model ($\Sigma_{nl} = 8h^{-1}\text{Mpc}$) in redshift space. One can see a tight correlation between the 2 sets of α with consistent mean and median values. The mean and median $\Delta\alpha$ values are consistent with 0 and only have $\sim 0.5\%$ scatter. The top right panel shows the corresponding χ^2 values from the fits. The number of degrees of freedom is calculated by subtracting the number of fitting parameters (5 in our fiducial form: B^2 , a_1 , a_2 , a_3 and α) from the number of data points being fit (57 for our fiducial fitting range of $30 < r < 200h^{-1}\text{Mpc}$). The tight correlation in α and the very small change in χ^2/dof between the 2 models suggest that the value of α is not sensitive to small changes in Σ_{nl} . However, if we use a less sensible value of Σ_{nl} like $\Sigma_{nl} = 0h^{-1}\text{Mpc}$ which corresponds to no acoustic peak smearing (very unlikely, especially before reconstruction), $\Delta\alpha$ is still consistent with 0 but the scatter increases to 1 – 2%. This suggests that the fiducial form defined by Equations (3.33 & 3.34) returns consistent values of α as long as a reasonable value of Σ_{nl} is used.

The left panel of the 2nd row in Figure 3.12 shows the α values measured from fits using an $A(r)$ that is an order higher than the fiducial form (i.e. *poly4*) versus the α values measured using the fiducial model. Again, a tight correlation exists between the 2 sets of α with the mean and median values agreeing nicely. The mean and median values of $\Delta\alpha$ are consistent with 0 and have negligible scatter. The right panel in the 2nd row shows the analogous plot for the χ^2 values. One can see that the average χ^2 decreases by ~ 1 as one expects when increasing the number of nuisance parameters by 1. This suggests that continuing to increase the order of $A(r)$ beyond that in the fiducial model offers little improvement to the fits.

However, as long as one does not increase the order to a point where noise in the data is being fit, one should measure consistent values of α . When $A(r)$ is taken to be an order less than fiducial (i.e. *poly2*), the scatter goes up slightly to $\sim 0.3\%$ and when *poly0* is used, the scatter increases to $\sim 1\%$. Hence, decreasing the order of $A(r)$ is feasible, but decreasing the order by too much will give a less consistent measurement of α .

Finally we test how adjusting the fitting range affects our measurements of α . Changing the minimum of the fitting range from $30h^{-1}\text{Mpc}$ (fiducial) to $50h^{-1}\text{Mpc}$ seems to have little affect on α . The 3rd row of Figure 3.12 shows the α and χ^2 values obtained using these 2 fitting ranges. One can see that the mean and median α values agree nicely and that the 2 sets of α values are obviously correlated. $\Delta\alpha$ is again consistent with 0 and has very small scatter ($\sim 0.4\%$). The χ^2 values decreased by about 7 on average, which is expected since the number of data points fit decreased by 7. We perform similar experiments by shifting the fitting range to $20 < r < 200h^{-1}\text{Mpc}$ and $70 < r < 150h^{-1}\text{Mpc}$. In both cases, $\Delta\alpha = 0$ lies within slightly larger scatter ($\sim 0.7 - 1\%$). In the prior case, this is likely due to non-linear effects at small scales coming into play. These effects are not well modeled by our fitting template. In the latter case, the larger scatter is likely caused by some of the acoustic information being cut out by using such a small fitting range.

For completeness, we also show the α values obtained through using the mock covariance matrix (Equation (3.8)) versus those obtained using the MGCM and the fiducial model. Since the mock covariance matrix is noisy, we expect there to be significant scatter in the α versus α and χ^2 versus χ^2 plots. These are shown in the bottom panels of Figure 3.12. A correlation between the two α sets is still visible, but it is not as tight as those in the upper panels. $\Delta\alpha$ is still consistent with 0 but the scatter is now $\sim 2\%$. Note that the average χ^2 values of the 2 cases match well.

This indicates that the MGCM is a reasonable approximation to the covariances we expect in our mock data.

3.5.2 With Reconstruction

Next we study the LasDamas mocks in redshift space after reconstruction. We find that after reconstruction, our ability to constrain the acoustic scale in each individual mock as measured by the standard deviation of α is greatly improved. We plot σ_α before reconstruction against those after reconstruction in Figure 3.14. The black diagonal line is the 1-1 line. One can see that only a few of the mocks have larger standard deviations after reconstruction but they are not much larger. Most of the points lie significantly below the line with the median change in σ_α equal to 1.1% as indicated on the plot. Hence, in general, reconstruction can significantly improve our ability to constrain α .

One can also see that after reconstruction, there are no longer any poorly constrained mocks that lie above the 7% cutoff (black horizontal line) imposed in the unreconstructed case. The solid grey line indicates the mean σ_α after reconstruction and the dashed grey lines correspond to the 98th, 84th, 16th and 2nd percentiles, similar to Figure 3.10 for redshift space without reconstruction.

As we saw in §3.5.1, the mocks where α is well constrained have strong acoustic features. Figure 3.14 showed that in reconstructed redshift space our measurements of best-fit α should be much more reliable. This implies that the acoustic peak in the poorly constrained mocks from before should be more prominent after reconstruction as we would expect. In Figure 3.13, we show the same 2 poorly constrained mocks as in Figure 3.9. The fit results from both of these mocks clearly demonstrate how effective reconstruction is. The acoustic peaks can be clearly seen now and the χ^2 minima corresponding to the best-fit α values are significantly different from the plateau values. The $p(\alpha)$ curves have also become more Gaussian in shape

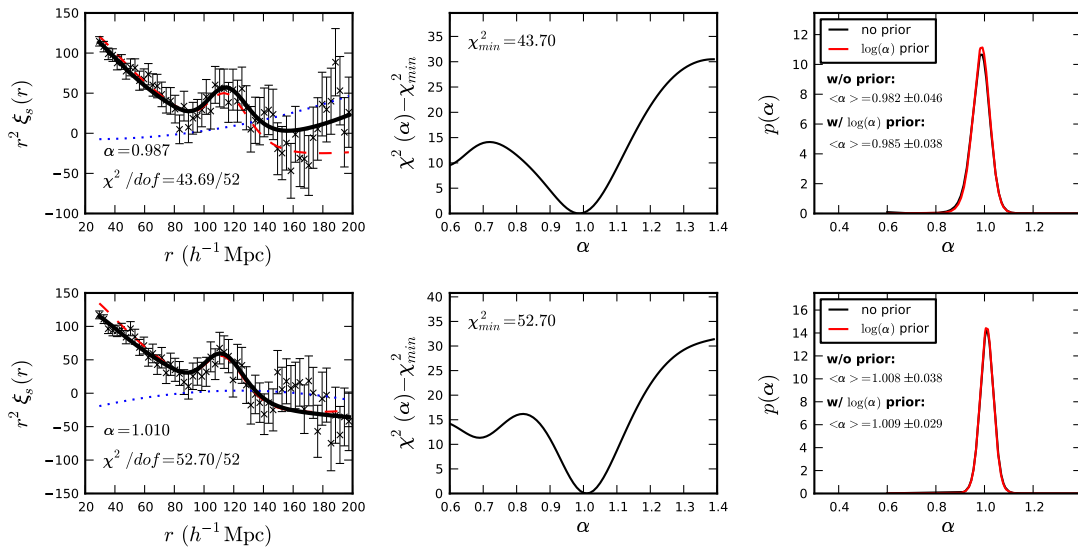


Figure 3.13: The same poorly constrained mocks as in Figure 3.9 after reconstruction. One can see that reconstruction has improved our ability to obtain a solid measurement of α in both cases. The acoustic peaks are now clearly visible, there are significant differences in χ^2 between the minima of the $\Delta\chi^2$ curves and the plateaus, and the $p(\alpha)$ distributions are now regular Gaussians with standard deviations ~ 1.9 and ~ 2.5 times smaller than before reconstruction. This type of improvement is characteristic of the other previously poorly constrained mocks in our sample and again emphasizes the utility of reconstruction.

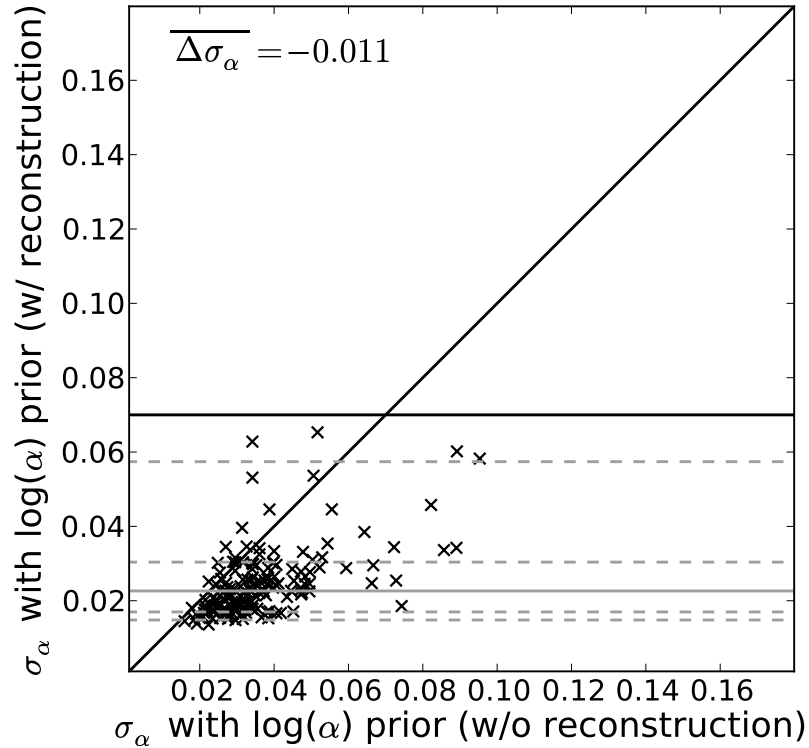


Figure 3.14: The standard deviations of $p(\alpha)$ for each mock before reconstruction versus those after reconstruction. The diagonal black line is a 1-1 line to guide the eye. Only a few of the mocks have slightly larger standard deviations after reconstruction, most of the mocks lie very much below the diagonal line. The median change in standard deviation is 1.1% which implies that our ability to constrain α increases significantly after reconstruction. Note that also, after reconstruction, there are no longer any poorly constrained mocks with standard deviations larger than 7% (black horizontal line), the cutoff imposed in Figure 3.10. The grey solid and dashed lines are as in Figure 3.10.

with standard deviations much smaller than before (by factors of ~ 1.9 and ~ 2.5 respectively). These are characteristic of the improvements seen for the other mocks which were poorly constrained before reconstruction.

In Figure 3.15, we have plotted the distribution of $(\alpha_{bf} - \bar{\alpha})/\sigma_\alpha$ which is a proxy for the signal-to-noise of our α measurement. Here, α_{bf} is the best-fit value of α for each mock and $\bar{\alpha}$ is the mean of the best-fit values. The distribution before reconstruction is shown in black and the distribution after reconstruction is shown in red. One can see that both distributions are roughly Gaussian. A standard K-S test gives a D_n value of ~ 0.05 before reconstruction and ~ 0.08 after reconstruction (recall that a value close to 0 indicates a better match to the normal distribution). These correspond to 83% and 28% probabilities that our pre- and post-reconstruction values are drawn from a Gaussian distribution. Hence α is sufficiently Gaussian which implies that the standard deviation of $p(\alpha)$ is representative of the error on α for each mock.

The fiducial model measures a mean $\bar{\alpha}_{[f]} = 1.001 \pm 0.021$ and a median $\tilde{\alpha}_{[f]} = 1.001 \pm_{0.022}^{0.020}$ from the post-reconstruction mocks (recall that before reconstruction these were $\bar{\alpha} = 0.999 \pm 0.033$ and $\tilde{\alpha} = 1.003 \pm_{0.034}^{0.030}$). Hence, the rms (standard deviation) of the measured α values drops by about a factor of 1.6 after reconstruction. Such an improvement is a direct consequence of reconstruction sharpening the BAO peak, allowing a more precise centroiding of its location. We know that $V \propto \sigma^{-2}$, where V is the survey volume required to achieve a variance σ^2 . Therefore, we would have to increase the survey volume by ~ 2.5 times to achieve this same factor of 1.6 decrease in the error.

Next, we again tweak the fiducial model parameters slightly and test the robustness of our fitting form and our covariance matrix. The results of the fits are summarized in Table 3.2 and in Figure 3.17. This figure is essentially analogous to

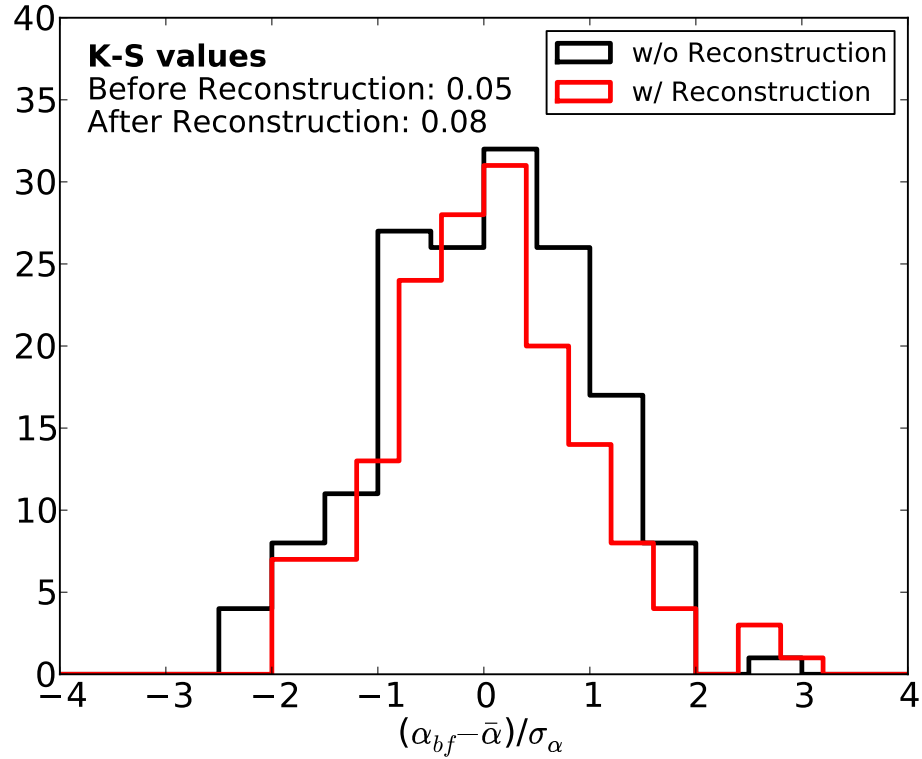


Figure 3.15: The distributions of $(\alpha_{bf} - \bar{\alpha}) / \sigma_{\alpha}$ before (black) and after (red) reconstruction, where α_{bf} is the best-fit value of α for each mock and $\bar{\alpha}$ is the mean of the best-fit values. This is a good measure of the signal-to-noise ratio of our best-fit α values. Both distributions are nearly Gaussian as indicated by the small K-S D_n values shown in the plot. Before reconstruction, our K-S value implies that there is an 83% probability that our values are drawn from a normal distribution. After reconstruction there is a 28% probability, which is still non-trivial. This implies that α is sufficiently Gaussian and hence the σ_{α} values measured from $p(\alpha)$ are representative estimates of the error on α for each mock.

Figure 3.11 and Figure 3.12, however, we have replaced the scatter plots with histograms of $\Delta\alpha = \alpha_{[i]} - \alpha_{[f]}$. Here, $\alpha_{[i]}$ are the slightly tweaked models as indicated by the titles. Note that in general, the scatters in the mean and median α and $\Delta\alpha$ values from the various fits are smaller after reconstruction, another indication of its effectiveness.

The various panels of Figure 3.17 show $\Delta\alpha$ values for different tweaks to the fiducial model. The median values are marked by the red lines (see caption for more details). Further cases are summarized in Table 1. The only case that shows a relatively large scatter in $\Delta\alpha$ is when we fit using the mock covariance matrix instead of the MGCM; this can be attributed to the higher noise in the mock covariance matrix. Also, as in the pre-reconstruction case, we see that for $N_{rel} = 4$, $\Delta\alpha \sim 0.5\%$ which is slightly larger than the other cases. However, in general, $\Delta\alpha \sim 0$ with very small scatter.

It should also be noted here that the cases which had noticeably larger scatter in $\Delta\alpha$ before reconstruction ($\Sigma_{nl} = 0h^{-1}\text{Mpc}$, *poly0* and fitting ranges of $20 < r < 200h^{-1}\text{Mpc}$ and $70 < r < 150h^{-1}\text{Mpc}$), no longer do post-reconstruction. This is because reconstruction undoes non-linear structure growth and brings the correlation function closer to its linear theory form (i.e. $\xi_s(r) \rightarrow \xi_m(r)$ and $\Sigma_{nl} \rightarrow 0h^{-1}\text{Mpc}$). The consistency in the measured values of α indicate that after reconstruction, our fiducial model is even more robust against changes in model parameters.

The left panel of Figure 3.16 shows the α values measured using the WMAP7 cosmology and its MGCM described in §3.3.2 versus the α values measured using the MGCM for the LasDamas cosmology. One can see that, after rescaling by the ratio of the sound horizons, a perfect correlation exists between the 2 sets of α values. This is also true for the WMAP7 $\pm 1\sigma$ cosmologies shown in Figure 3.3. The right panel of Figure 3.16 shows the corresponding values of σ_α measured from

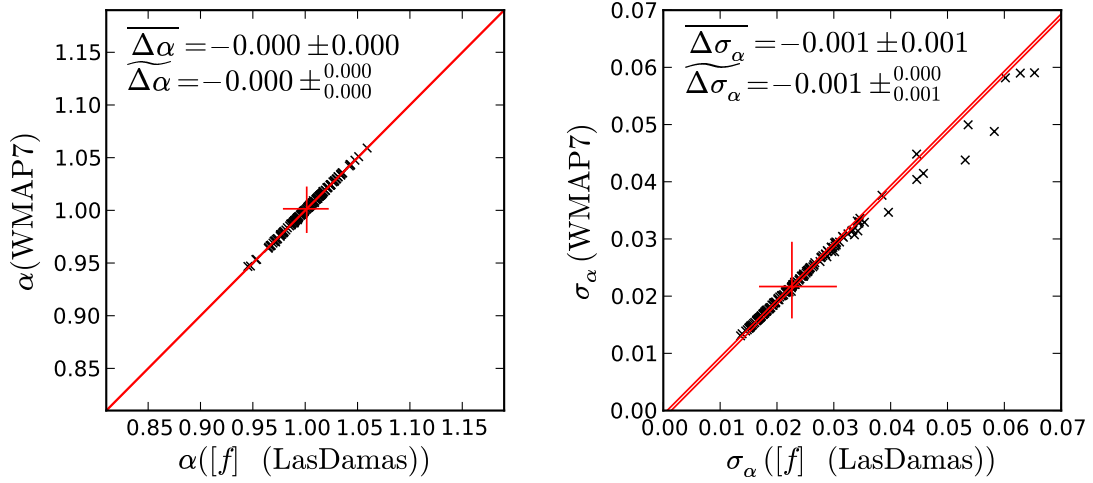


Figure 3.16: Testing the effects of using the wrong cosmology to derive the covariance matrix and construct the model template. (left) α values measured from the LasDamas mocks in redshift space after reconstruction using a fitting template and MGCM (see Figure 3.3) based on the WMAP7 cosmology versus those measured using the fiducial model (LasDamas fitting template and its corresponding MGCM). The α values from the WMAP7 cosmology have been rescaled to the LasDamas cosmology. (right) The analogous plot for σ_α measured from $p(\alpha)$. One can see that perfect correlations exist between the axes of both plots. This indicates that our acoustic scale measurements are not affected by deriving the MGCM using the wrong cosmology. Our maximum likelihood method is capable of modifying the matrix from the incorrect cosmology to match that expected from the correct cosmology.

$p(\alpha)$. Again, a strong correlation exists and similar trends are observed for the 2 other WMAP7-like cosmologies. Hence, the measurement of the acoustic scale is not affected by the cosmology used for the covariance matrix or the fitting model. This demonstrates the robustness of our fiducial model in dealing with a fitting template constructed using the wrong cosmology as well as our maximum likelihood approach for deriving a suitable covariance matrix for the data.

Now that we have validated our fitting model, we must also test the robustness of our reconstruction technique. The following investigates what happens when

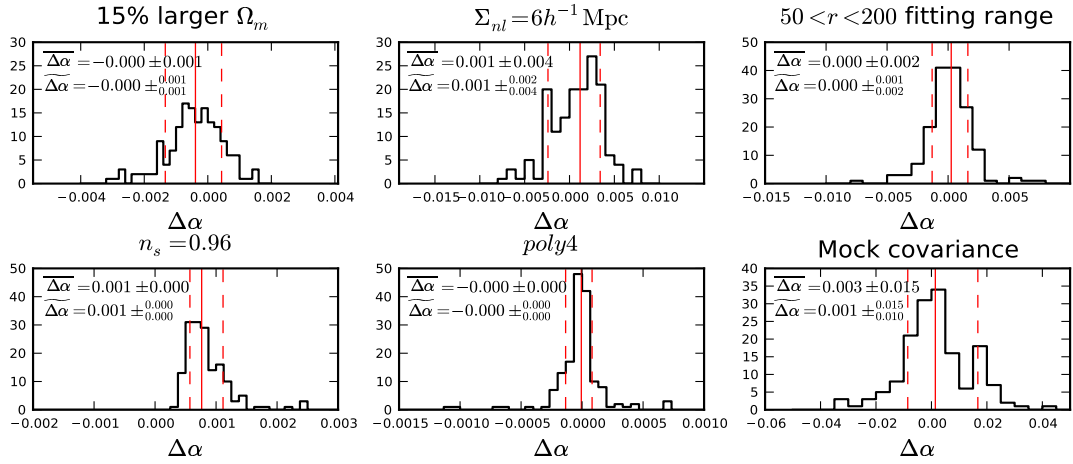


Figure 3.17: Validation of our fitting method in redshift space after reconstruction using LasDamas mocks. The contents of this figure are comparable to Figures 3.11 & 3.12, however, the scatter plots have been replaced by histograms of $\Delta\alpha = \alpha_{[i]} - \alpha_{[f]}$ here. The $\alpha_{[i]}$ are measured from models that are derived by slightly changing the fiducial model parameters. These are indicated above each plot. The solid red lines mark the median $\Delta\alpha$. The dashed red lines indicate the 16th and 84th percentiles. One can see that $\Delta\alpha$ is very close to 0 with small scatter in most of these cases. The slightly larger scatter in the case where we fit using the mock covariance matrix is likely due to the noisiness of that matrix. This indicates that the value of α is insensitive to small changes in template cosmology, Σ_{nl} , order of $A(r)$, fitting range and covariance matrix estimator used. Hence, our basic fitting form and our covariance matrix estimators are robust. The results shown in this figure are all consistent with those found in unreconstructed redshift space.

Table 3.3: The effect of varying reconstruction smoothing length l on the measured values of α from the mocks in redshift space.

Smoothing	mean α	rms of α
$15h^{-1}\text{Mpc}$ (fiducial)	1.001	0.021
$20h^{-1}\text{Mpc}$	1.004	0.023
$25h^{-1}\text{Mpc}$	1.006	0.026

we change the fiducial reconstruction parameters. As mentioned previously, the smoothing scale we choose for reconstruction is very important. Table 3.3 shows the average values of α obtained through our fits and the rms scatter between the mocks for different smoothing lengths. One can see that $l = 15h^{-1}\text{Mpc}$ (our fiducial value) is most effective at reducing the scatter.

Next we vary the other fiducial reconstruction parameters and re-perform the fits to see if we recover consistent values of the acoustic scale α and errors σ_α (see §3.3.3). We vary the bias b , the linear growth rate f and the power spectrum used for generating the constrained realizations. In all cases, the average $\Delta\alpha$ and $\Delta\sigma_\alpha$ are essentially 0 which implies that overall we recover consistent measurements regardless of the reconstruction parameters used. How well these values are consistent with 0 is illustrated in Table 3.4 which summarizes the average scatter in $\Delta\alpha$ and $\Delta\sigma_\alpha$ between fits to the fiducial reconstruction output and the cases where we change the fiducial parameters. Correlation coefficients ρ are given for both α and σ_α as well.

We expect that the input bias should have the largest effect on reconstruction. This is because an overestimate of the bias implies an underestimate of the matter density field (recall we use $\delta_{matter} = \delta_{gal}/b$). If we underestimate the matter density field, then we will also underpredict the displacement field. The opposite holds if we underestimate the bias. One can see that this is indeed reflected in Table 3.4 where

Table 3.4: The effects of varying reconstruction parameters on the measured acoustic scale α from the mocks in redshift space. ρ is the correlation coefficient between the case listed in column 1 and the fiducial case.

Case	rms of $\Delta\alpha^1$	ρ	rms of $\Delta\sigma_\alpha$	ρ
b=1.8 (-20%)	0.009	0.92	0.003	0.94
b=2.6 (+20%)	0.006	0.97	0.002	0.97
f=0.5 (-20%)	0.002	1.00	0.001	1.00
f=0.8 (+20%)	0.002	1.00	0.001	1.00
Pk, no-wiggle	0.000	1.00	0.000	1.00
Pk, shot-noise	0.003	0.99	0.001	0.99

¹ Here Δ denotes the difference between the quantity measured using the fiducial reconstruction parameters and that measured using different parameter values.

the scatters in $\Delta\alpha$ and $\Delta\sigma_\alpha$ are the greatest for the changing bias cases, implying that the measured values slosh around the most in this case. However, the $\Delta\alpha$ rms is only $\sim 0.5 - 1.0\%$ which is much smaller than the typical σ_α error we expect to measure from each mock. Hence, it is not detectable in an individual mock at our current level of statistical precision. The fact that the correlation coefficients are nearly 1 underscores the point that overall we are measuring consistent values of α and σ_α despite changing the bias in our reconstruction.

The input value of f affects the magnitude of the Kaiser correction. If we pick a value that is too large or too small, we will either introduce additional or leave behind residual anisotropy in the 2D correlation function. However, we see that this parameter has little affect on the measured values of α and σ_α as indicated in Table 3.4. Finally we test the effects of changing the input power spectrum for generating the constrained Gaussian realizations. We use a power spectrum without an acoustic

signal (Pk, no-wiggle) and another one with no clustering signal at all (Pk, shot-noise). Table 3.4 indicates that reconstruction is insensitive to these choices as well, although we note that these results are sensitive to survey geometry. If the DR7 survey geometry had been different, the choice of power spectrum could prove to be more important. Hence we see that overall, the acoustic scale measured is robust to different choices of reconstruction parameters.

We conclude this section by demonstrating and comparing the detectabilities of the BAO in the reconstructed (solid red line) and unreconstructed (solid black line) mocks as shown in Figure 3.18. We have plotted the normalized cumulative distribution of $\Delta\chi^2 = \chi_{\text{BAO}}^2 - \chi_{\text{no BAO}}^2$ for fiducial $A(r)$ (left) and $poly0$ (right). Here, the χ^2 values for each mock are calculated by marginalizing over the nuisance parameters only while fixing α at the best-fit value from the fiducial model or $poly0$ fits. χ_{BAO}^2 is the χ^2 obtained in this fashion using a template $\xi_m(r)$ containing BAO. $\chi_{\text{no BAO}}^2$ is the analogous value obtained using a template that has no BAO feature. While it is true that in the no BAO fits, the value of α we impose may not give the minimum χ^2 , the lack of a BAO feature in the model eliminates its ability to constrain α in these fits. Hence, comparing the BAO and no BAO χ^2 values at the fiducial or $poly0$ best-fit α is a reasonable way to circumvent this problem. We obtain the BAO-less model by setting $\Sigma_{nl} = 1000h^{-1}\text{Mpc}$ to completely damp out any acoustic signal. This cumulative distribution indicates the fraction of mocks that lie more negative of a given $\Delta\chi^2$ value. Note that we have plotted all 160 mocks here (i.e. we did not throw out any poorly constrained mocks).

If the data favours a model containing BAO, χ_{BAO}^2 should be smaller than $\chi_{\text{no BAO}}^2$ (i.e. $\Delta\chi^2$ should be negative). The intersections of the dashed horizontal black lines and the distributions correspond to values of $\Delta\chi^2$ that halve the data and hence indicate the median $\Delta\chi^2$ values. One can see that these medians are negative for all

cases which indicates that on average the data favours models containing BAO. The median $\Delta\chi^2$ before reconstruction is ~ -10 and after reconstruction, it is ~ -16 for the fits performed using fiducial $A(r)$. The two vertical dashed black lines indicate where $\Delta\chi^2 = 0$ and $\Delta\chi^2 = -9$. The latter corresponds to where a model containing BAO is favoured at 3σ above a model without BAO. Before reconstruction, about 56% of the mocks lie above (more negative of) this 3σ line. After reconstruction, this number increases to 88%. This again indicates that our reconstruction algorithm is helping to restore acoustic information back into the acoustic peak. Hence, the robustness of the BAO detection is further improved by reconstruction.

Although there are some mocks that do not favour a model with BAO at very high confidence and even a few mocks that do not favour a model with BAO at all ($\Delta\chi^2 > 0$), this does not indicate that we are not detecting the BAO. It is merely a statement that if we take observations of many different regions of the universe, there is a finite chance that the BAO signal will not be robustly detected in some of these regions. This is in contrast to the conclusions drawn in Cabré & Gaztañaga (2011).

The median value of $\Delta\chi^2$ is slightly more negative when the fit is performed using the fiducial model versus when it is performed using *poly0* both before and after reconstruction. However, we see that even the simple *poly0* fits favour a model containing BAO over one without BAO. Before reconstruction, about 53% of the mocks lie above the 3σ line and after reconstruction, about 82% lie above this line. These numbers are very similar to those obtained in the fiducial model case.

We have also performed this experiment for a few other fitting ranges (50-200 h^{-1} Mpc and 70-150 h^{-1} Mpc). The former yielded similar results, however, the latter had slightly less dramatic $\Delta\chi^2$ values. This is not unexpected because in these cases, the $A(r)$ terms are less constrained and can therefore absorb some of

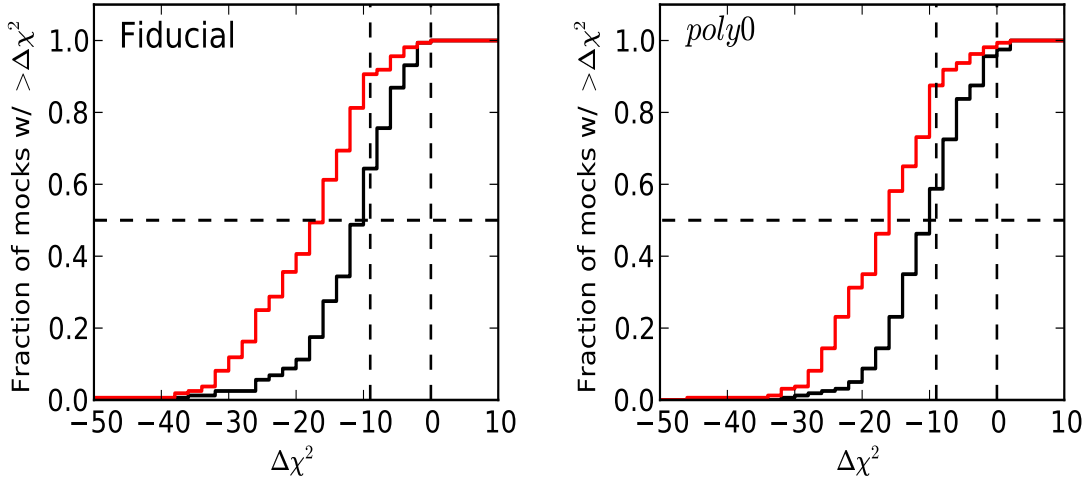


Figure 3.18: The detectability of the BAO feature in redshift space before and after reconstruction. (left) The normalized cumulative distribution function of $\Delta\chi^2 = \chi_{\text{BAO}}^2 - \chi_{\text{no BAO}}^2$ from fits using the fiducial $A(r)$ term. The solid black line shows the distribution before reconstruction and the solid red line shows the distribution after reconstruction. The horizontal dashed black line at fraction=50% indicates the value of $\Delta\chi^2$ that splits the mocks in half (i.e. the median $\Delta\chi^2$ value). We can see that the average $\Delta\chi^2$ is negative in both of these cases. The vertical dashed black lines indicate where $\Delta\chi^2 = 0$ and -9 (3σ). (right) The distribution of $\Delta\chi^2$ values from fits using *poly0*. Again the average $\Delta\chi^2$ is negative both before and after reconstruction. In all cases, the majority of mocks lie beyond the 3σ line, especially in the reconstructed case. This indicates that a detection of the BAO in our mock data is favoured over a non-detection.

the BAO signal.

3.6 LasDamas Real Space Results

3.6.1 Covariance Matrices

Although our observations will always lie in redshift space, it is still useful to demonstrate our results for real space as past works involving reconstruction and perturbation theory have been based in real space (Padmanabhan, White & Cohn, 2009; Noh et al., 2009). In addition, we will demonstrate that after reconstruction, our mocks show comparable scatter between real and redshift space, again indicating

the utility of reconstruction.

As in redshift space, the covariance matrix derived from the mock correlation functions through Equation (3.8) is noisy. Hence, we again use a modified Gaussian covariance matrix as a smooth approximation to the mock covariance matrix. However, in real space, we do not have any redshift-space observational effects such as Kaiser squashing or FoG. Therefore, we take the input power spectrum to the covariance matrix calculation to be

$$P_c(k) = b_0^2 P_t(k) \quad (3.40)$$

where the value of b_0^2 is determined as it was in redshift space.

We then introduce similar modification parameters to the redshift-space case, namely, we assume the covariance matrix can be modeled by the form

$$C_{ij}^m = 2 \int \frac{k^2 dk}{2\pi^2} \Delta j_1(kr_i) \Delta j_1(kr_j) \mathfrak{P}^2(k; c_0, c_2) + c_3. \quad (3.41)$$

Here, $\mathfrak{P}^2(k; c_0, c_2)$ corresponds to an $I^2(k)$, Equation (3.20), in which we make the substitution

$$P_c(k) + \frac{1}{\bar{n}(z)} \rightarrow c_0 P_c(k) + \frac{c_2}{\bar{n}(z)}. \quad (3.42)$$

Note that this is the same as Equation (3.24) except with $c_1 = 0$ and a different form for $P_c(k)$. Using the same maximum likelihood prescription as that described in §3.3.2, we can derive values for the modification parameters c_0 , c_2 and c_3 .

We use $\Sigma_{nl} = 7h^{-1}\text{Mpc}$ for calculating $P_c(k)$ in real space before reconstruction. As in the redshift-space case, the value of Σ_{nl} used has negligible affect on the derived matrix. With this $P_c(k)$ we find $c_1 = 0.98$, $c_2 = 1.50$ and $c_3 = 5.57 \times 10^{-8}$.

After reconstruction, we take $\Sigma_{nl} = 3h^{-1}\text{Mpc}$ in real space. The modified Gaussian covariance matrix we obtain has the modification parameters $c_0 = 0.89$, $c_2 = 1.57$ and $c_3 = 8.85 \times 10^{-8}$.

3.6.2 Fitting Forms

We use the same fiducial fitting form in both real space with and without reconstruction as in redshift space for measuring the shift in the acoustic scale, α . This is described by Equations (3.33 & 3.34). In real space before reconstruction, we define the fiducial model to make use of this fiducial form with $\xi_m(r)$ derived from the LasDamas cosmology and $\Sigma_{nl} = 7h^{-1}\text{Mpc}$ over a fitting range of $30 < r < 200h^{-1}\text{Mpc}$. If we fit the average mock real-space correlation function allowing Σ_{nl} to vary, we obtain $\alpha = 1.002$ and $\Sigma_{nl} = 6.6h^{-1}\text{Mpc}$, so our assumption for Σ_{nl} is not bad. In practice, like in redshift space, the measured α values for each individual mock are insensitive to our choice of Σ_{nl} as is shown in Table 3.5. The error bars on our mock data are approximated by the modified Gaussian covariance matrix (MGCM) derived in the previous section.

Table 3.5: Real space fitting results for various models. The columns are as in Table 3.2.

Model	$\bar{\alpha}$	$\tilde{\alpha}$	$\overline{\Delta\alpha}$	$\widetilde{\Delta\alpha}$	$\overline{\chi^2}/dof$
Real Space without Reconstruction					
Fiducial [f]	1.001 ± 0.030	$1.000 \pm_{0.027}^{0.031}$	–	–	53.34/52
Fit with 15% larger Ω_m using fiducial $A(r)$.	1.000 ± 0.030	$0.999 \pm_{0.028}^{0.031}$	-0.001 ± 0.001	$-0.001 \pm_{0.001}^{0.001}$	53.58/52
Fit with $n_s = 0.96$ using fiducial $A(r)$.	1.002 ± 0.030	$1.001 \pm_{0.027}^{0.030}$	0.001 ± 0.001	$0.001 \pm_{0.000}^{0.001}$	53.39/52
Fit with $N_{rel} = 4$ using fiducial $A(r)$.	1.007 ± 0.030	$1.005 \pm_{0.027}^{0.030}$	0.006 ± 0.001	$0.005 \pm_{0.001}^{0.001}$	53.36/52
Fit with $\Sigma_{nl} \rightarrow 0$.	0.998 ± 0.032	$0.997 \pm_{0.029}^{0.032}$	-0.003 ± 0.013	$-0.003 \pm_{0.012}^{0.009}$	53.79/52
Fit with $\Sigma_{nl} \rightarrow \Sigma_{nl} + 2$.	1.003 ± 0.030	$1.003 \pm_{0.031}^{0.031}$	0.002 ± 0.005	$0.002 \pm_{0.005}^{0.004}$	53.83/52
Fit with <i>poly0</i> .	0.999 ± 0.031	$1.001 \pm_{0.031}^{0.030}$	-0.002 ± 0.008	$-0.001 \pm_{0.007}^{0.006}$	56.19/55
Fit with <i>poly2</i> .	1.000 ± 0.030	$0.999 \pm_{0.028}^{0.031}$	-0.001 ± 0.003	$-0.001 \pm_{0.002}^{0.002}$	54.65/53
Fit with <i>poly4</i> .	1.001 ± 0.029	$1.000 \pm_{0.027}^{0.031}$	0.000 ± 0.000	$0.000 \pm_{0.000}^{0.000}$	52.03/51
Fit with $50 < r < 200h^{-1}$ Mpc fitting range.	1.002 ± 0.029	$1.001 \pm_{0.025}^{0.031}$	0.001 ± 0.003	$0.001 \pm_{0.003}^{0.003}$	46.18/45
Fit with $20 < r < 200h^{-1}$ Mpc fitting range.	1.002 ± 0.028	$1.000 \pm_{0.026}^{0.029}$	0.001 ± 0.006	$0.002 \pm_{0.006}^{0.005}$	59.33/57
Fit with $70 < r < 150h^{-1}$ Mpc fitting range.	1.002 ± 0.031	$0.999 \pm_{0.020}^{0.031}$	0.001 ± 0.011	$0.001 \pm_{0.008}^{0.008}$	21.99/22
Fit using mock covariance matrix.	1.002 ± 0.023	$1.003 \pm_{0.025}^{0.021}$	0.001 ± 0.016	$0.002 \pm_{0.016}^{0.013}$	53.15/52

Continued on next page

Table 3.5 – continued from previous page

Model	$\bar{\alpha}$	$\tilde{\alpha}$	$\overline{\Delta\alpha}$	$\widetilde{\Delta\alpha}$	$\overline{\chi^2}/dof$
Real Space with Reconstruction					
Fiducial [f]	0.998 ± 0.020	$0.999 \pm_{0.019}^{0.019}$	–	–	53.44/52
Fit with 15% larger Ω_m using fiducial $A(r)$.	0.998 ± 0.020	$0.999 \pm_{0.020}^{0.019}$	-0.001 ± 0.002	$-0.000 \pm_{0.001}^{0.001}$	53.78/52
Fit with $n_s = 0.96$ using fiducial $A(r)$.	0.999 ± 0.020	$1.000 \pm_{0.019}^{0.020}$	0.001 ± 0.001	$0.001 \pm_{0.001}^{0.001}$	53.48/52
Fit with $N_{rel} = 4$ using fiducial $A(r)$.	1.003 ± 0.020	$1.003 \pm_{0.019}^{0.020}$	0.004 ± 0.001	$0.004 \pm_{0.000}^{0.001}$	53.68/52
Fit with $\Sigma_{nl} \rightarrow 0$.	0.998 ± 0.020	$0.999 \pm_{0.020}^{0.021}$	-0.000 ± 0.002	$-0.000 \pm_{0.002}^{0.002}$	53.47/52
Fit with $\Sigma_{nl} \rightarrow \Sigma_{nl} + 2$.	0.999 ± 0.020	$0.999 \pm_{0.019}^{0.020}$	0.000 ± 0.003	$0.001 \pm_{0.003}^{0.002}$	53.66/52
Fit with <i>poly0</i> .	0.997 ± 0.021	$0.999 \pm_{0.020}^{0.019}$	-0.001 ± 0.005	$-0.001 \pm_{0.004}^{0.003}$	56.44/55
Fit with <i>poly2</i> .	0.998 ± 0.020	$0.999 \pm_{0.021}^{0.019}$	-0.001 ± 0.002	$-0.001 \pm_{0.001}^{0.001}$	54.82/53
Fit with <i>poly4</i> .	0.998 ± 0.020	$0.999 \pm_{0.019}^{0.019}$	0.000 ± 0.000	$-0.000 \pm_{0.000}^{0.000}$	52.00/51
Fit with $50 < r < 200h^{-1}$ Mpc fitting range.	0.999 ± 0.020	$1.001 \pm_{0.020}^{0.019}$	0.001 ± 0.002	$0.001 \pm_{0.002}^{0.001}$	46.80/45
Fit with $20 < r < 200h^{-1}$ Mpc fitting range.	0.996 ± 0.020	$0.999 \pm_{0.021}^{0.018}$	-0.002 ± 0.004	$-0.001 \pm_{0.004}^{0.002}$	58.24/57
Fit with $70 < r < 150h^{-1}$ Mpc fitting range.	0.999 ± 0.021	$1.000 \pm_{0.022}^{0.019}$	0.001 ± 0.007	$0.001 \pm_{0.005}^{0.004}$	21.89/22
Fit using mock covariance matrix.	0.999 ± 0.017	$1.001 \pm_{0.019}^{0.014}$	0.001 ± 0.012	$-0.000 \pm_{0.010}^{0.010}$	52.85/52

Fitting the average of the reconstructed real-space mock correlation functions while allowing Σ_{nl} to vary gives $\alpha = 0.999$ and $\Sigma_{nl} = 3.0h^{-1}\text{Mpc}$. As in redshift space, the value of α prior to reconstruction is already very close to 1 and hence, we do not expect reconstruction to shift the acoustic peak much closer to its predicted linear theory position. However, Σ_{nl} decreased by a factor of ~ 2.2 from its pre-reconstruction value, implying that reconstruction was effective at removing the smearing of the acoustic peak caused by non-linear structure growth.

In our fiducial model for real space after reconstruction, we take $\Sigma_{nl} = 3h^{-1}\text{Mpc}$, as we did in the calculation of the modified Gaussian covariance matrix. All other parameters of the fiducial model are analogous to the unreconstructed case described above. The same fitting algorithm as described in §3.3.3 is used.

3.6.3 Without Reconstruction Fitting Results

We use the same technique as that described in §3.5.1 to identify and remove the mock correlation functions that do not provide a well constrained measurement of α from our fitting sample. The corresponding real-space plot to Figure 3.10 is shown in Figure 3.19. We use the same 7% cutoff in standard deviation (σ_α) as in redshift space. This is marked by the black horizontal line. There are 5 mocks ($\sim 3\%$) that lie above this cut off (circled in black) which we take to have poorly constrained values of α and discard from our sample. The mean and median values of α after removing these poorly constrained mocks are indicated on the plot.

We test the robustness of our covariance matrix modeling and the fiducial model as we did in redshift space. Namely, we compare the values of α we measure using the fiducial model to those measured using a model in which the fiducial parameters are slightly changed, or by a fit in which we use the mock covariances rather than the MGCM. The resultant α , $\Delta\alpha$ and χ^2 values are given in Table 3.5. Note that in general, the values of $\Delta\alpha$ and their scatters are slightly smaller in real space

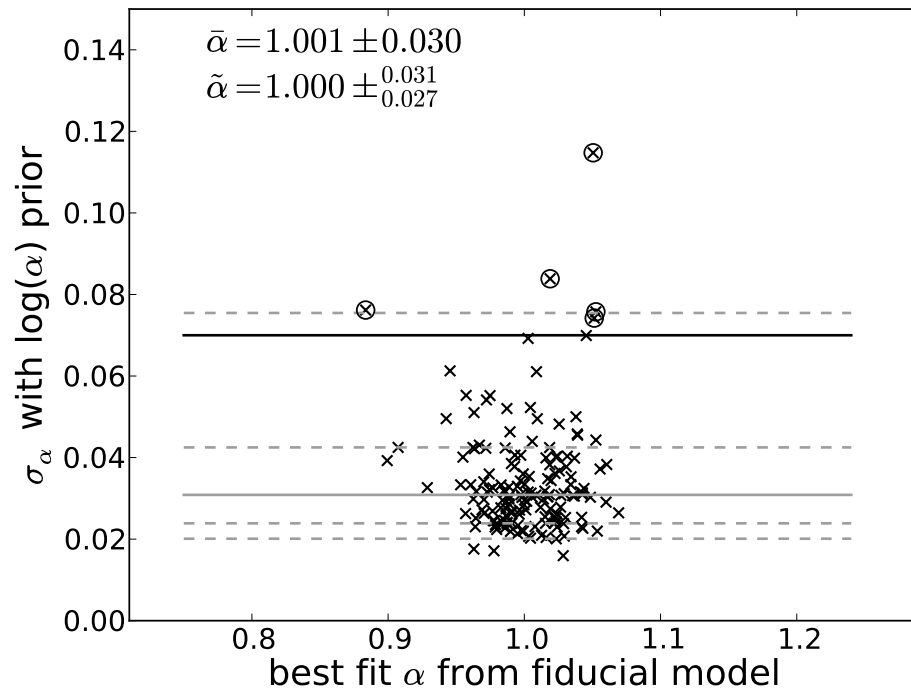


Figure 3.19: The standard deviations measured from $p(\alpha)$ versus the best-fit values of α from the fiducial model for each mock in real space. We impose a cutoff at a standard deviation of 7% (marked by the black horizontal line) as in redshift space. There are 5 mocks that lie above this line (circled in black). We take these mocks to have poorly measured values of α and discard them from our sample. The mean and median value of α after discarding these poorly constrained mocks are given on the plot.

than in redshift space. This is not unexpected since observational effects in redshift space such as FoG and Kaiser squashing tend to broaden the acoustic peak further, making it more difficult to obtain a precise measurement.

The results listed in Table 3.5 indicate that the trends in real space are the same as those found in redshift space. In particular, the values of α measured by slightly changing the input cosmology, Σ_{nl} , the order of $A(r)$ and the fitting range are consistent with the values measured using the fiducial model, usually with $\Delta\alpha < 0.2\%$. As in redshift space, the worst case is when we change the template to use $N_{rel} = 4$; this has a deviation of 0.6%. Again, this is likely the result of the $N_{rel} = 4$ correlation function template having a BAO peak that does not quite match the mocks well enough. If we go to less sensible Σ_{nl} such as $\Sigma_{nl} = 0h^{-1}\text{Mpc}$, or decide to not use an $A(r)$ term, or fit using a less optimal fitting range, the scatter in $\Delta\alpha$ increases as it did in redshift space. Noise in the mock covariance matrix is again the likely culprit causing the larger scatter in $\Delta\alpha$ between the MGCM fits and the mock covariance fits. These results all imply that our covariance modeling and our fiducial model are generally robust in real space as well.

3.6.4 With Reconstruction Fitting Results

As in redshift space, we find that after reconstruction, we are able to obtain much tighter constraints on the α values measured from each individual mock in real space. Figure 3.20 demonstrates this by plotting the standard deviation of $p(\alpha)$ for each mock before reconstruction against the value obtained after reconstruction. Note that this is the analogue to Figure 3.14 for redshift space. One can once again see that most of the points lie significantly below the 1-1 line which indicates that reconstruction effectively sharpened up the acoustic peak allowing for more robust detections. The median decrease in standard deviation is 0.8% and there are no longer any mocks that lie above our σ_α cutoff of 7%.

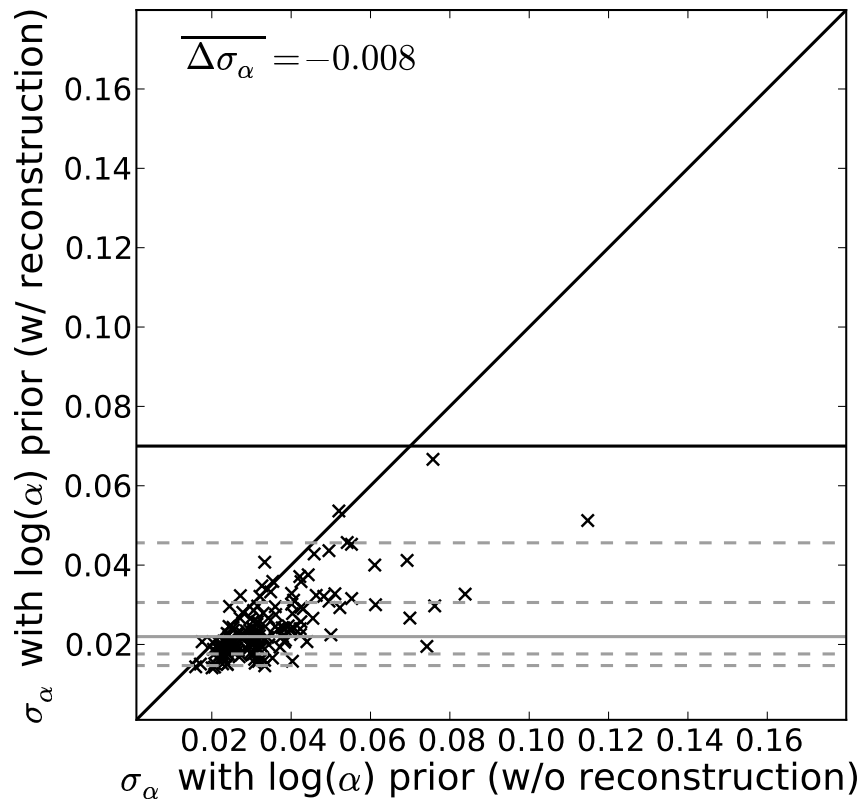


Figure 3.20: The analogous plot in reconstructed real space to Figure 3.14 for reconstructed redshift space. Once again, most of the points lie significantly below the 1-1 line. The median decrease in standard deviation is $\sim 0.8\%$ as shown in the plot. Note that there are no longer any poorly constrained mocks with standard deviations above our 7% cutoff. This once again illustrates how useful and effective reconstruction is.

Next, we once again test how slightly adjusting the fiducial model parameters affects our measurements of α . The results from these fits are given in Table 3.5. One can see that after reconstruction, the scatters in α are very similar between real space and redshift space.

We see that changing the fitting template cosmology, adjusting the value of Σ_{nl} , changing the order of $A(r)$ and altering the fitting range mostly have little effect on the value of α measured. The only case with $\Delta\alpha$ worse than 0.2% is the $N_{rel} = 4$ case, which measures 0.4%. In general, we still find that our fiducial model and our prescription for deriving a suitable covariance matrix such as the MGCM are robust. These results are all consistent with previous results.

Lastly, we investigate the detectability of the BAO in both unreconstructed and reconstructed real space. We find that the median $\Delta\chi^2 = \chi_{\text{BAO}}^2 - \chi_{\text{no BAO}}^2$ values are again negative and similar in magnitude to the redshift-space cases. This suggests that the data is better fit by a model containing BAO rather than a model without BAO. We also note that the post-reconstruction real-space $\Delta\chi^2$ values are more negative than before reconstruction. Hence, we conclude that we have a firm detection of the acoustic signal in our mocks, with the detection being even more robust after reconstruction.

3.7 Measuring the BAO in SDSS DR7

3.7.1 Covariance Matrices

In this section, we apply the techniques described in §3.3 for redshift space to the DR7 LRG full sample. We use the form for the modified Gaussian covariance matrix given in Equation (3.23) for redshift space with and without reconstruction. We adopt the modification parameters (c_0 , c_1 , c_2 and c_3) derived for the LasDamas mocks in both of these cases, assuming that the overall shape of the covariance

matrix should be modified in the same way for both DR7 and LasDamas. However, we now switch to the WMAP7 cosmology in constructing $P_c(k)$.

The b_0^2 coefficient in Equation (3.17) is chosen such that $P_c(k)$ matches the DR7 correlation function at $r = 50h^{-1}\text{Mpc}$. This again ensures that the amplitude of $P_c(k)$ matches the clustering amplitude of DR7, an essential condition when reusing the modification parameters to adjust the shape of the Gaussian covariance matrix.

In computing the pre-reconstruction covariance matrix, we retain $\Sigma_{nl} = 8h^{-1}\text{Mpc}$ and for post-reconstruction, we retain $\Sigma_{nl} = 4h^{-1}\text{Mpc}$. We also note that since the DR7 data goes out to $z = 0.47$, we extend our $\bar{n}(z)$ model derived from the LasDamas random catalogue out to $z = 0.47$ as well, after scaling it to the WMAP7 cosmology.

3.7.2 Fit Results

We compute the DR7 correlation functions in the WMAP7 cosmology. For details of the computation and reconstruction, please see Paper I. We present only the fitting results here.

Figure 3.21 shows the results of our fits to the DR7 data using the fiducial model and fitting algorithm outlined in §3.3. These results are also summarized in Table 3.6 along with the fit results from varying fiducial model parameters such as Σ_{nl} and fitting range.

The 2 panels at the top illustrate the pre-reconstruction results and the 2 panels at the bottom illustrate the post-reconstruction results. We fix Σ_{nl} in our model templates to the same values as in the covariance matrices. The left column shows the data with the fiducial model fit overplotted (black line). The dashed red line corresponds to a fit using *poly0* instead of fiducial $A(r)$. The best-fit α and χ^2 values are quoted on the plot. The right column shows the $p(\alpha)$ distributions for the fits using the fiducial model (black line) and the fits using *poly0* (red line).

Table 3.6: DR7 fit results for various models

Model	α	χ^2
Redshift Space without Reconstruction		
Fiducial [f]	1.017 ± 0.035^1	47.71/52
$\Sigma_{nl} = 0$	1.025 ± 0.029	49.89/52
$\Sigma_{nl} \rightarrow \Sigma_{nl} + 2$	1.011 ± 0.039	47.86/52
<i>poly0</i>	1.002 ± 0.038	55.35/55
<i>poly2</i>	1.016 ± 0.034	47.72/53
<i>poly4</i>	1.016 ± 0.039	42.74/51
50 – 200 h^{-1} Mpc fitting range	1.011 ± 0.040	40.44/45
Redshift Space with Reconstruction		
Fiducial [f]	1.012 ± 0.019	36.82/52
$\Sigma_{nl} = 0$	1.012 ± 0.017	35.99/52
$\Sigma_{nl} \rightarrow \Sigma_{nl} + 2$	1.012 ± 0.021	38.12/52
<i>poly0</i>	1.007 ± 0.020	47.18/55
<i>poly2</i>	1.012 ± 0.019	37.14/53
<i>poly4</i>	1.012 ± 0.019	36.34/51
50 – 200 h^{-1} Mpc fitting range	1.012 ± 0.019	33.21/45

¹ Here, the quoted α is the best-fit value rather than the mean of the probability distribution $p(\alpha)$. These 2 values may be slightly different but are well within error of each other.

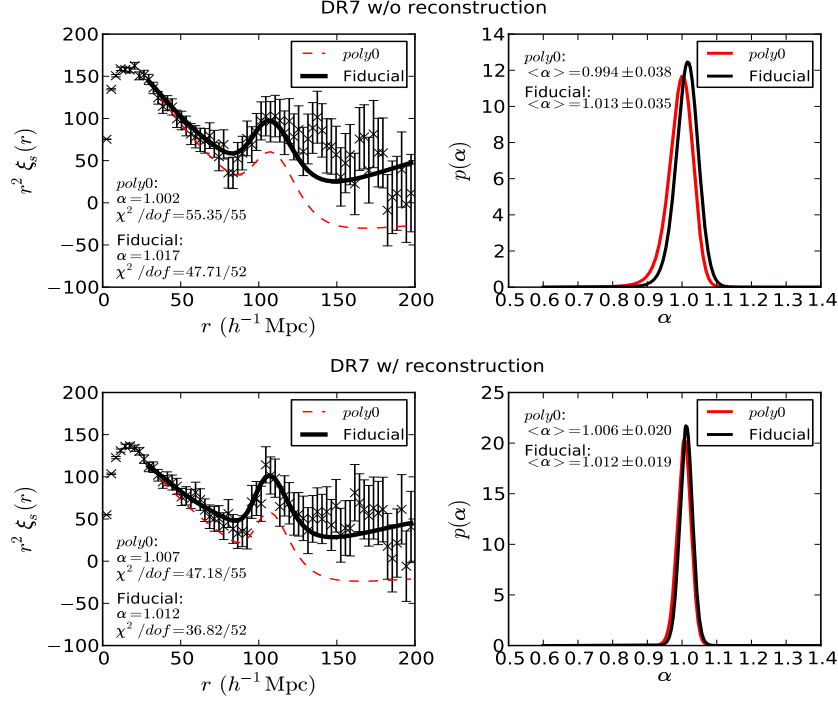


Figure 3.21: DR7 fit results. (top) Before reconstruction. (bottom) After reconstruction. The left column shows the fits to the DR7 data using the fiducial model (solid black line) and $poly0$ (dashed red line). The right column shows the $p(\alpha)$ distributions for fits using the fiducial model (black line) and $poly0$ (red line). Here we have again applied the 15% prior in $\log(\alpha)$ as described in §3.5.1. As with the LasDamas mocks, we use $\Sigma_{nl} = 8h^{-1}\text{Mpc}$ in the fiducial model before reconstruction and $\Sigma_{nl} = 4h^{-1}\text{Mpc}$ after reconstruction. The similarities in χ^2 , α and σ_α between the fiducial and $poly0$ cases indicate that the covariance matrix does not demand an $A(r)$ term in the model. However, our mock correlation function analyses suggest that having an $A(r)$ term is useful for marginalizing out errors due to assuming the wrong cosmology and broadband effects that are not included in our fitting model. The effectiveness of $A(r)$ in marginalizing over the conspicuous excess large-scale power seen in these DR7 correlation functions (left panels) also exemplifies its utility.

The means of the distributions are quoted on the plot along with their standard deviations σ_α . Taking the best-fit α value from the fiducial model fit and the σ_α from the $p(\alpha)$ distribution, we measure the DR7 acoustic scale to correspond to $\alpha = 1.017 \pm 0.035$ before reconstruction and $\alpha = 1.012 \pm 0.019$ after reconstruction. Using the mean of the $p(\alpha)$ probability distribution instead gives $\alpha = 1.013 \pm 0.035$ before reconstruction and $\alpha = 1.012 \pm 0.019$ after reconstruction. One can see that the two values are the same after reconstruction, however, they are slightly different before reconstruction due to the slight asymmetry of the $p(\alpha)$ distribution. The pre-reconstruction error is comparable to the 3.3% found by Percival et al. (2010) for a similar sample.

This factor of 1.8 decrease in the error after applying reconstruction is similar to what we saw for the mock catalogues. Since the survey volume required to achieve a certain variance is inversely proportional to the variance, we would have to increase the survey volume by about a factor of 3 to achieve this same reduction in the error. This clearly shows how effective reconstruction is at improving our measurement of the acoustic scale. We can convert these α values into $D_v(z)/r_s$ measurements at a median redshift of $z = 0.35$ using Equation 3.30. In the WMAP7 cosmology we have $r_{s,f} = 152.76\text{Mpc}$ and $D_{v,f}(z) = 1340.2\text{Mpc}$. The best-fit α values then give $D_v(z)/r_s = 8.92 \pm 0.31$ before reconstruction and $D_v(z)/r_s = 8.88 \pm 0.17$ after reconstruction. The means of the $p(\alpha)$ distributions give $D_v(z)/r_s = 8.89 \pm 0.31$ before reconstruction and $D_v(z)/r_s = 8.88 \pm 0.17$ after reconstruction.

The probability distribution $p(\alpha)$ contains all of the relevant BAO distance information. Since α is easily converted into D_V/r_s , $p(\alpha)$ can also be transformed into $p(D_V/r_s)$ trivially. This distribution is no longer linked to a fiducial cosmology as α is and serves as the key BAO distance constraint that enters into the prediction of cosmological parameters. We will use this distance measurement to infer

cosmological parameters in Chapter 4.

From Table 3.6, we see that the α values obtained by varying Σ_{nl} , order of $A(r)$ and fitting range are all consistent with each other within the errors. In particular, after reconstruction, we see that all cases have very similar errors and all give an α value within 0.1% of the others except the *poly0* case. This is as expected from our analysis of the mock catalogues.

Once again we demonstrate the robustness of our reconstruction technique to bias, linear growth rate, smoothing scale and choice of input power spectrum for generating constrained Gaussian realizations. The measured values of $\alpha \pm \sigma_\alpha$ are given in Table 3.7. One can see that we consistently recover the same α and σ_α which implies that our acoustic scale measurements are robust against small changes in reconstruction parameters.

We also test the impact of changing the assumed fiducial cosmology. These results are listed in the last 2 rows of Table 3.7. Here we have used a flat cosmology with $\Omega_m = 0.2$ and another with $\Omega_m = 0.35$. We adjust h such that $\Omega_m h^2$ is the same as in the WMAP7 case and then we adjust Ω_b such that $\Omega_b h^2$ is consistent with WMAP7. This leaves the time of matter-radiation equality the same, but changes the distance-redshift relation. The measured values of α are significantly different from the WMAP7 case as expected since we have changed the fiducial cosmology. The quantity we should actually compare is the observable $D_V(z)/r_s$ (see Equation (3.30)) which is given in the second column of Table 3.7 at $z = 0.35$, the median redshift of the DR7 LRG sample. One can see that this value is not sensitive to the choice of cosmology. To obtain the last column in the table, we have assumed $r_s = 152.76\text{Mpc}$ which is the sound horizon in the WMAP7 cosmology.

The DR7 correlation function exceeds the linear theory prediction at large r , suggesting extra large-scale power. This can be seen in Figure 3.21 by comparing

Table 3.7: The effects of varying reconstruction parameters on α in the DR7 LRG data. Note that the actual observable is not α but rather $D_V(z)/r_s$ listed in column 2 for $z = 0.35$, the median redshift of our galaxy sample.

Case	α	D_V/r_s	D_V (Gpc)
Unrecon	1.013 ± 0.035	8.89 ± 0.31	1.358 ± 0.047
Recon	1.012 ± 0.019	8.88 ± 0.17	1.356 ± 0.025
Smoothing, 20 Mpc/h	1.009 ± 0.021	8.85 ± 0.18	1.352 ± 0.028
b=1.8 (-20%)	1.014 ± 0.020	8.89 ± 0.18	1.358 ± 0.027
b=2.6 (+20%)	1.014 ± 0.019	8.89 ± 0.16	1.359 ± 0.025
f=0.5 (-20%)	1.011 ± 0.019	8.87 ± 0.16	1.355 ± 0.025
f=0.8 (+20%)	1.015 ± 0.019	8.90 ± 0.16	1.360 ± 0.025
Pk, no-wiggle	1.012 ± 0.019	8.88 ± 0.17	1.356 ± 0.025
Pk, shot-noise	1.015 ± 0.019	8.90 ± 0.17	1.360 ± 0.026
$\Omega_M = 0.20$	1.159 ± 0.024	8.93 ± 0.18	1.377 ± 0.028
$\Omega_M = 0.35$	0.924 ± 0.018	8.93 ± 0.17	1.378 ± 0.026

the data to the fit using the $A(r) = 0$ model (dashed red line). While this offset appears large to the eye, we stress that the data points are correlated such that these coherent offsets are only weakly constrained. This is demonstrated by the fact that the fiducial $A(r)$ fit, which adds three marginalization parameters and largely compensates the offset, does not decrease χ^2 by a very significant amount. Hence, while such extra power could be a sign of unaddressed systematic errors in the data set or some exotic cosmology, the statistical significance of the extra power is weak. In addition, the measured α and σ_α values are consistent, which suggests that the data does not strongly demand a non-zero $A(r)$ in the model. However, we see that the fiducial $A(r)$ fit matches the data much better. Also, our analysis of the mock correlation functions indicates that we should err on the side of caution and marginalize over a non-zero $A(r)$ term to remove any broadband effects not accounted for in the model that could bias our measurement of the acoustic scale.

To further address the excess large-scale power, we study whether the magnitude of the fiducial $A(r)$ term in the best-fit model to the DR7 data is unusual in the context of the LasDamas mocks. Figure 3.22 shows the values of the $A(r)$ term at the edges of the fitting range (i.e. at $r \sim 30h^{-1}\text{Mpc}$ and $r \sim 200h^{-1}\text{Mpc}$) for the LasDamas mocks before reconstruction (black crosses). The large blue cross indicates the mean and standard deviation of the LasDamas values and the large red cross indicates the median and the 16th/84th percentiles. The DR7 point is overplotted as the green circle and clearly falls within 2σ of the LasDamas average. A similar plot can be made for the post-reconstruction fits.

3.7.3 Comparison with LasDamas Cosmology

We also compute the DR7 correlation functions with and without reconstruction using the LasDamas cosmology. We apply the same fitting algorithm, but change the cosmology of the covariance matrix and template model to that of LasDamas.

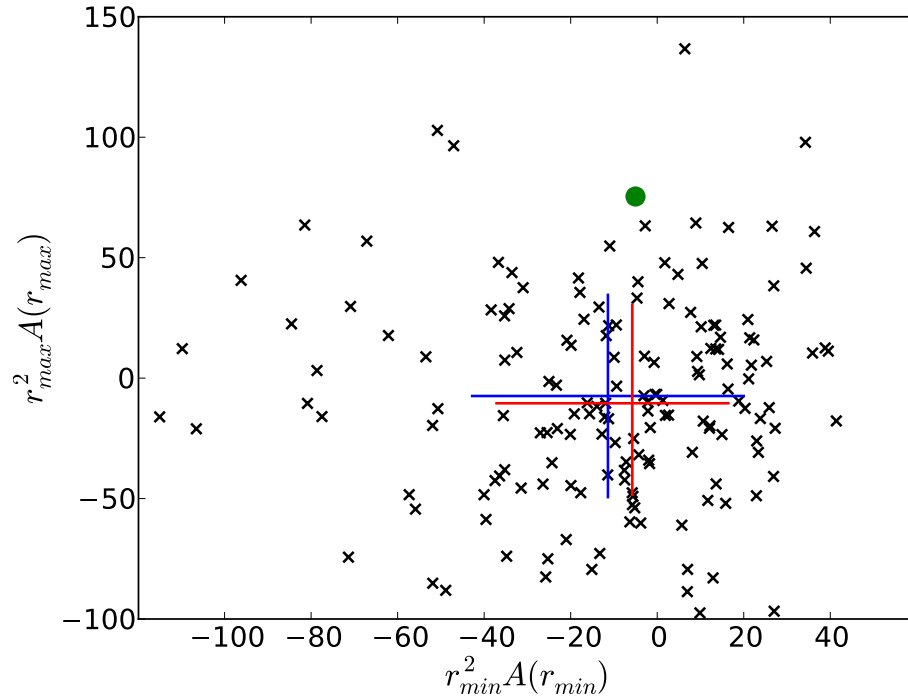


Figure 3.22: The values of the fiducial $A(r)$ term at the edges of the fitting range for the 160 LasDamas mocks (black crosses) in redshift space before reconstruction. The large blue cross indicates the mean and standard deviation. The large red cross indicates the median and 16th/84th percentile levels. The DR7 point is overplotted as the green circle. One can see that this point falls within 2σ of the LasDamas average which implies that the shape of the DR7 $A(r)$ term is not unexpected. Hence, even though $A(r)$ is providing a significant amount of marginalization to account for the excess power at large scales in the DR7 correlation function, it is not an inordinately large amount in the context of LasDamas.

We again adopt the LasDamas modification parameters to the Gaussian covariance matrix and the same Σ_{nl} values.

We find $\alpha = 1.053 \pm 0.034$ in redshift space before reconstruction and $\alpha = 1.044 \pm 0.019$ after reconstruction. Converting these α values to D_v/r_s at a median redshift of $z = 0.35$, we find $D_v/r_s = 8.95 \pm 0.30$ before reconstruction and $D_v/r_s = 8.87 \pm 0.17$ after reconstruction. These values are consistent with those obtained from the DR7 data in the WMAP7 cosmology when we factor in errors. The values of σ_α are also consistent.

3.7.4 Significance of the BAO Detection

The BAO detection significance is an obvious question that must be addressed. However, its characterization is non-trivial. There are essentially 2 different tests which need to be evaluated. The first considers the possibility that we have not detected the BAO signal in our data, either because it does not actually exist or we just have not observed it. The second assumes the BAO peak does exist and asks how robustly we have measured its location.

We attempt to address these 2 questions in Figure 3.23. In the top panels we have plotted $\Delta\chi^2 = \chi_{\text{BAO}}^2 - \chi_{\text{no BAO}}^2$ at various values of α for different $A(r)$. As in Figure 3.18, the χ_{BAO}^2 values are obtained through fits using a model containing BAO and the $\chi_{\text{no BAO}}^2$ are obtained through fits using a model without BAO. The left panel shows the results before reconstruction and the right panel shows the results after reconstruction. These plots answer the first question of whether we have detected the BAO assuming that we are fairly confident in our cosmology. With this assumption, we know that α must be close to 1 and hence we can restrict our attention to this region. One can see that the $\Delta\chi^2$ values are all negative around $\alpha = 1$ and reach a minimum of $\Delta\chi^2 \sim -11$ before reconstruction and ~ -18 after reconstruction for the fiducial $A(r)$ fits (solid black line). This indicates that a model

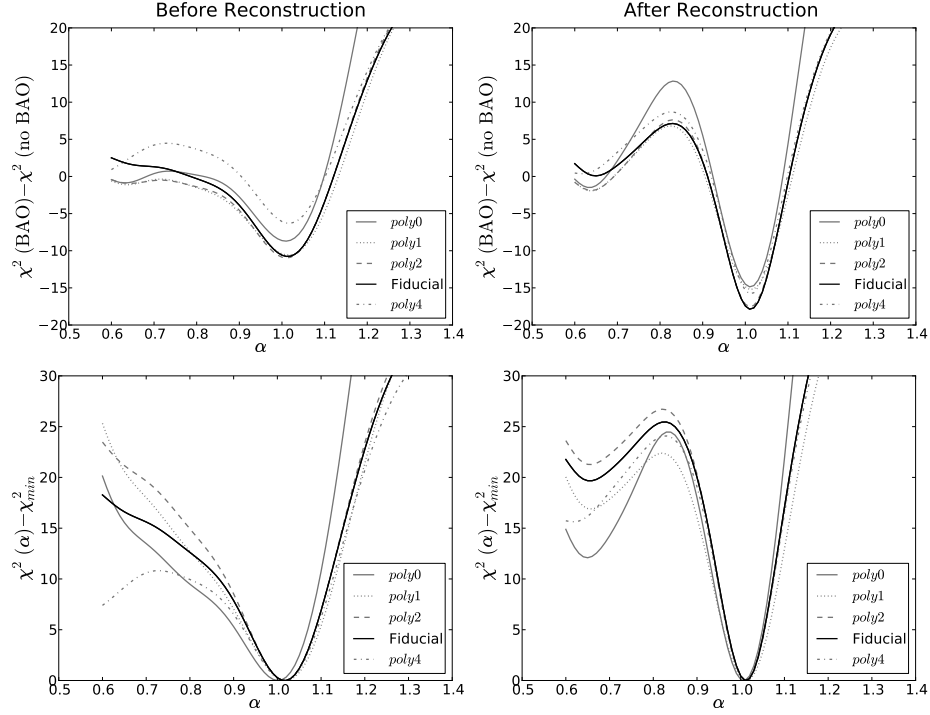


Figure 3.23: Significance of the BAO in the DR7 data. (top) $\Delta\chi^2 = \chi_{\text{BAO}}^2 - \chi_{\text{no BAO}}^2$ versus α for different $A(r)$ before reconstruction (left) and after reconstruction (right). The different forms of $A(r)$ are represented by different line styles as indicated in the legend. For our fiducial form (solid black line), $\Delta\chi^2$ reaches a minimum of ~ -11 before reconstruction and ~ -18 after reconstruction. Hence, a model containing BAO is a better fit to the data than a model without BAO at more than 3σ significance ($\Delta\chi^2 = -9$) before reconstruction and at more than 4σ significance ($\Delta\chi^2 = -16$) after reconstruction. (bottom) $\Delta\chi^2 = \chi^2(\alpha) - \chi_{\text{min}}^2$ versus α for different $A(r)$ before reconstruction (left) and after reconstruction (right). For our fiducial form, the curve is parabolic around the minimum that corresponds to the best-fit value of α . Before reconstruction, the χ^2 difference between the minimum and where the curve starts plateauing at small α is $\sim 10 - 15$. This difference becomes even more pronounced after reconstruction, measuring a $\Delta\chi^2 \sim 25$. Hence, the measured acoustic scale is favoured at slightly more than 3σ ($\Delta\chi^2 = 9$) before reconstruction and at 5σ ($\Delta\chi^2 = 25$) post-reconstruction. Both the top and bottom panels show an increase in significance of the BAO detection after reconstruction. Also, one can see that in general (and especially before reconstruction), the fits with higher order $A(r)$ terms (i.e. *poly2* and fiducial) have more prominent $\Delta\chi^2$ minima in both the top and bottom panels. This indicates that we obtain more robust BAO detections when fitting with non-trivial $A(r)$ terms. However, fits with *poly4* appear to perform worse than the lower order fits before reconstruction. This indicates that we are likely beginning to afford the model too much flexibility.

containing BAO is favoured over a model without BAO at more than 3σ ($\Delta\chi^2 = -9$) confidence before reconstruction and more than 4σ ($\Delta\chi^2 = -16$) confidence after reconstruction. Note that these $\Delta\chi^2$ values are comparable to the median values we measured for the LasDamas mocks (-10 and -16 respectively). While it is true that these χ^2 values are not directly comparable due to the volume difference between DR7 in a LasDamas cosmology and a WMAP7 cosmology, this discrepancy is small. Hence, DR7 should be a fairly typical sample consistent with cosmic variance.

The bottom panels show $\Delta\chi^2 = \chi^2(\alpha) - \chi_{min}^2$ versus α for various $A(r)$. Here, χ_{min}^2 is the value of χ^2 that corresponds to the best-fit value of α . These plots are similar to the middle columns of Figures 3.9 and 3.13. They answer the second question of whether the BAO scale we measure is significantly favoured over other values. Again, the left column corresponds to the results before reconstruction and the right column corresponds to the results after reconstruction. For the fiducial $A(r)$ fit before reconstruction, the curve is parabolic around the best-fit α indicating the Gaussian nature of α . The corresponding χ_{min}^2 lies at $\Delta\chi^2 \sim 10-15$ below where the curve starts plateauing. Recall that the plateau is due to the fitter having an easier time hiding the acoustic peak in the errors at large r and is not actually physical. Post-reconstruction, the parabola becomes tighter around the best-fit α and the χ^2 difference between the minimum and the plateau grows to 25. This indicates that while the measured acoustic scale is favoured at slightly more than 3σ ($\Delta\chi^2 = 9$) before reconstruction, after reconstruction, it becomes favoured at 5σ ($\Delta\chi^2 = 25$). Hence, reconstruction increases the BAO detection significance in both of the tests considered here.

Another point to note is that in general, the $\Delta\chi^2$ minima in both of the above mentioned cases is more prominent when one fits with a higher degree $A(r)$ (i.e. *poly2* or fiducial). This is especially true before reconstruction when the acoustic

scale is more difficult to measure due to non-linear effects. Hence, we see that a more robust BAO detection is achieved when fitting with a non-zero $A(r)$. However, we also see that before reconstruction, *poly4* (dash-dotted line) performs worse than the lower order fits. This is because when we give the model too much freedom, it acquires more flexibility to hide the acoustic peak in the errors at large r while using the $A(r)$ nuisance terms to compensate for the shape of the acoustic peak in the data.

3.8 Conclusions

We demonstrated the first application of reconstruction to a galaxy redshift survey, namely the SDSS DR7 LRG sample. We found that reconstruction was able to reduce the error on the measured acoustic scale from 3.5% to 1.9%, a factor of 1.8. This is equivalent to the effects of tripling the survey volume. Our 1.9% measurement is the most precise BAO distance measure to $z = 0.35$ to date.

Our reconstruction technique is adapted from that originally proposed in Eisenstein et al. (2007) where we have included techniques to account for the effects of survey boundaries and redshift-space distortions. Reconstruction is meant to partially undo the large-scale flows that result from non-linear structure formation which can degrade the acoustic information leading to less precise measurements of the acoustic scale. It also includes a prescription for removing large-scale redshift-space distortions (the Kaiser effect), thereby isotropizing the 2D clustering of galaxies at large scales.

We test our reconstruction technique on 160 LasDamas DR7 mock catalogues and find that it is indeed effective at sharpening the acoustic peak in the correlation function. The non-linear damping scale Σ_{nl} used to model the degradation of the BAO decreases from $8.1h^{-1}\text{Mpc}$ before reconstruction to $4.4h^{-1}\text{Mpc}$ after recon-

struction. This is nearly a factor of 2 improvement and is consistent with previous estimates (Padmanabhan & White, 2009). In addition, reconstruction reduces the rms scatter in α , the measured acoustic scale, from the mocks. Before reconstruction this scatter was 3.3%, however after reconstruction, it dropped to 2.1%.

Using the mocks we find that the optimal smoothing scale for reconstruction is $\sim 15h^{-1}\text{Mpc}$. Choosing a small smoothing scale of $10h^{-1}\text{Mpc}$ resulted in noticeable distortions in the correlation function at small scales. We also vary the bias, linear growth rate and power spectrum input to the reconstruction algorithm and find that the recovered acoustic scale is always consistent. Hence our reconstruction appears to be robust against small changes in these parameters.

Through our analysis of the mocks, we find that the covariance matrix derived directly from the mocks is very noisy. We present a new method for obtaining a smooth approximation to the mock covariance matrix using the analytic Gaussian covariance matrix. This process introduces appropriate modifications to the Gaussian covariance matrix using a maximum likelihood fit to the mock covariances. We show that the modified Gaussian covariance matrix obtained this way is a good fit to the mock covariances and produces consistent measurements of the acoustic scale.

Some of the mocks have weak acoustic signals and hence the acoustic scale can be poorly determined in these. In order to identify these poorly constrained mocks, we find that looking at the probability distribution of α can be a good gauge. For mocks that have distributions with a larger standard deviation, the constraint on α is poorer and vice versa. We impose a cutoff at a standard deviation of 7% in our mocks and find that in redshift space, 8 mocks lie above this cutoff and in real space, 5 do. After reconstruction, no poorly constrained mocks remain in redshift or real space.

We find that in redshift space, we obtain consistent measurements of α when

the fiducial model parameters (template cosmology, Σ_{nl} , degree of $A(r)$ and fitting range) are slightly tweaked. This implies that the values of α we measure are robust against small changes in model parameters. Hence, our fiducial model should return reliable measurements of the acoustic scale. However, we note that in order to afford the model enough flexibility, $A(r)$ should be non-zero as in the fiducial form, Equation (3.34). This is because the $A(r)$ term is required to marginalize out all the broadband contributions not accounted for by the template such as scale-dependent bias and redshift-space distortions (or residual redshift-space distortions in the post-reconstruction case). This term also accounts for any errors in our choice of model cosmology. We find that if we use a template cosmology that does not match the simulations to perform the fit, a low order $A(r)$ does not recover the correct acoustic scale as well. One must also be careful not to use an $A(r)$ term that is very high order as the model will begin fitting the noise in the data.

We demonstrated the detectability of the acoustic signature in redshift space both before and after reconstruction. In both cases we fit each of the mocks using a model containing BAO and a model without BAO and find that $\Delta\chi^2 = \chi_{\text{BAO}}^2 - \chi_{\text{no BAO}}^2$ is negative on average. This indicates that the mock data prefers a model containing BAO over a model without BAO. Hence, we conclude that we have a robust detection of the acoustic signal in our mocks. We note that $\Delta\chi^2$ is even more negative after reconstruction, again revealing the importance of the procedure. In addition, when we fit using *poly0*, we still obtain negative average values of $\Delta\chi^2$ implying that even with this simple model we can robustly detect the BAO in our mocks. Similar results are obtained in real space before and after reconstruction.

We then apply our covariance matrix and fitting techniques to the correlation function calculated from the DR7 data in the WMAP7 cosmology. We again vary the various parameters of the fit and recover consistent values of α . From the probability

distribution of α we measure a mean $\alpha = 1.013 \pm 0.035$ before reconstruction which gives $D_v(z = 0.35)/r_s = 8.89 \pm 0.31$. After reconstruction we measure $\alpha = 1.012 \pm 0.019$ which gives $D_v(z = 0.35)/r_s = 8.88 \pm 0.17$. We see that the error on α has decreased by a factor of 1.8. Such a decrease is equivalent to what we would expect if we increase the survey volume by a factor of 3. This again demonstrates the power of reconstruction in removing the uncertainties introduced by non-linear structure growth.

Assuming $r_s = 152.76\text{Mpc}$ as in the WMAP7 cosmology, we have $D_V(z = 0.35) = 1356 \pm 25 \text{ Mpc}$. The probability distribution of this distance measurement $p(D_V/r_s)$ can be obtained through a trivial conversion of $p(\alpha)$ obtained from the χ^2 versus α relation. This is the key input needed for predicting cosmological parameters as will be discussed in Chapter 4.

Finally we assess the significance of our DR7 BAO measurement using 2 different tests. The first measures how confident we are that our data contains a BAO signature and the second measures how confident we are that our measurement of the BAO scale is correct. We find that before reconstruction, our data favours a model containing BAO at more than 3σ over a model without BAO and the acoustic scale we measure is preferred at more than 3σ . After reconstruction, these confidence levels become even more pronounced. The data favours a model containing BAO at more than 4σ and the measured acoustic scale is preferred at 5σ . Hence, we conclude that our DR7 BAO measurement is robust.

CHAPTER 4

THE CLUSTERING OF GALAXIES IN THE SDSS-III BARYON OSCILLATION
SPECTROSCOPIC SURVEY: BARYON ACOUSTIC OSCILLATIONS IN THE DATA
RELEASE 9 SPECTROSCOPIC GALAXY SAMPLE

We present baryon acoustic oscillation measurements from the Baryon Oscillation Spectroscopic Survey (BOSS), a major program of the third generation Sloan Digital Sky Survey (SDSS-III). We use the Data Release 9 (DR9) constant mass (CMASS) sample which covers a 3275 deg^2 area on the sky and contains 264,283 massive galaxies. This sample spans a redshift range of $0.43 < z < 0.7$ with an effective redshift of $z = 0.57$ and is the largest galaxy sample at an $\bar{n} \sim 3 \times 10^{-4} h^{-3} \text{ Mpc}^3$ number density surveyed to date. Using the angle-averaged correlation function and power spectrum to measure the clustering of these galaxies, we extract the acoustic scale and use it to measure $D_V(z = 0.57)/r_s = 13.67 \pm 0.22$ where D_V is the spherically averaged distance. We make use of the density field reconstruction algorithm presented in (Padmanabhan et al., 2012a) and the fitting techniques presented in (Xu et al., 2012) to arrive at this measurement. Assuming a sound horizon $r_s = 153.19 \text{ Mpc}$, we have $D_V(z = 0.57) = 2094 \pm 34 \text{ Mpc}$ which is a 1.7% distance measure. This is the most precise distance constraint ever achieved from a galaxy redshift survey. In addition, we detect the BAO feature at $\sim 5\sigma$, which combined with the SDSS-II Luminous Red Galaxy sample gives a 6.7σ detection. Placing our distance measure in the distance-redshift relation defined by previous BAO measurements and current supernova measurements gives excellent agreement. Taking these various datasets to constrain cosmological parameters, we find ongoing consistency with a flat Λ CDM universe.

4.1 Introduction

Numerous past works have demonstrated the utility of baryon acoustic oscillations (BAO) in providing stringent constraints on cosmological parameters (Percival et al., 2001; Miller, Nichol & Batuski, 2001; Eisenstein et al., 2005; Cole et al., 2005; Hütsi, 2006; Blake et al., 2007; Padmanabhan, White & Eisenstein, 2007; Percival et al., 2007; Okumura et al., 2008; Gaztanaga, Cabre & Hui, 2009; Kazin et al., 2010; Percival et al., 2010; Reid et al., 2010; Blake et al., 2011a; Beutler et al., 2011; Seo et al., 2012; Mehta et al., 2012). Of particular note (and in order of increasing redshift) are the results from the 6dF Galaxy Redshift Survey (6dF; Jones et al. 2009) at $z = 0.1$, combined Sloan Digital Sky Survey (SDSS; York et al. 2000) and 2dF Galaxy Redshift Survey (2dF; Colless et al. 2003) at $z = 0.275$, SDSS-II Data Release 7 (Abazajian et al., 2009) at $z = 0.35$, and WiggleZ (Drinkwater et al., 2010) at $z = 0.6$. Beutler et al. (2011) was able to obtain a 4.5% distance measure to $z = 0.1$ from 6dF. Percival et al. (2010) obtained a 2.7% distance measure to $z = 0.275$ from SDSS+2dF. Padmanabhan et al. (2012a); Xu et al. (2012) & Mehta et al. (2012) measured the distance to $z = 0.35$ with 1.9% precision (after reconstruction) from SDSS-II. Blake et al. (2011a) obtained a 4% distance measure to $z = 0.6$ from WiggleZ. This last measurement was further broken down into various overlapping bins at $z = 0.44$, 0.60 and 0.73 with 7.2%, 4.5% and 5.0% distance measures respectively (Blake et al., 2011b). Hence we see that the BAO method has been highly prolific recently in constraining the distance-redshift relation.

In this work we will add another point to this distance-redshift relation at $z = 0.57$ using the Sloan Digital Sky Survey III (SDSS-III; Eisenstein et al. 2011) Baryon Oscillation Spectroscopic Survey (BOSS; Schlegel, White & Eisenstein 2009) Data Release 9 (DR9) constant mass (CMASS; White et al. 2011) sample. We ap-

ply the reconstruction technique first proposed by Eisenstein et al. (2007) and later extended by Padmanabhan et al. (2009); Noh et al. (2009) & Padmanabhan et al. (2012a) to partially reverse the large-scale flows arising from non-linear structure growth that smear the BAO feature (Eisenstein, Seo & White, 2007; Crocce & Scoccimarro, 2008; Matsubara, 2008a,b). This technique was demonstrated on the SDSS-II Luminous Red Galaxy sample by Padmanabhan et al. (2012a); Xu et al. (2012) & Mehta et al. (2012) where they were able to reduce the error on the measured acoustic scale from 3.5% to 1.9% simply by applying reconstruction (see Chapter 3). The sharpened acoustic feature that results from reconstruction allows a better centroiding of the BAO position and subsequently a more precise measurement of the acoustic scale.

We calibrate the reconstruction technique on 600 mock catalogues generated via a second order Lagrangian perturbation theory-based approach (Manera et al., 2012). While we do see that in general the errors on the measured acoustic scale decrease after reconstruction in the mocks, it turns out that in the CMASS sample, we do not see any improvement. This can be attributed to luck; we find that in a finite number of mocks we see no improvement or even a degradation of the measurement.

The fitting technique used to measure the acoustic scale in the correlation function is based on the method described in Xu et al. (2012). Details of the power spectrum analysis methods can be found in Percival et al. (2010) and will not be discussed in this chapter. Using these techniques, we obtain a spherically averaged distance $D_V(z = 0.57) = 2094 \pm 34\text{Mpc}$ assuming a sound horizon of 153.19Mpc. This is the sound horizon in the fiducial cosmology assumed throughout this chapter which has $\Omega_m = 0.274$, $h = 0.7$, $\Omega_b h^2 = 0.0224$, $n_s = 0.95$ and $\sigma_8 = 0.8$, similar to the best-fit WMAP7 cosmology (Komatsu et al., 2011). Our 1.7% error on D_V represents the most precise BAO distance measurement to date. Note that CMASS is

observationally split between the Northern Galactic Cap and the Southern Galactic Cap. All results quoted for CMASS in this paper will be for the combined North plus South sample unless otherwise noted.

This chapter will be organized as follows: in §4.2 we introduce the the DR9 CMASS sample and its calibration. In §4.3 we outline the reconstruction and fitting techniques used to analyze the correlation function. In §4.4 we test the robustness of these methods on the mocks and discuss the results of our CMASS correlation function analyses. We also describe how we obtain the final CMASS correlation function plus power spectrum consensus distance measurement here. §4.5 contains the cosmological implications of our CMASS distance measure. We conclude in §4.6.

4.2 The Data

The SDSS-III (Eisenstein et al., 2011) BOSS project extends the survey area of the original SDSS dataset (Abazajian et al., 2009) described in §3.2.2. SDSS (York et al., 2000) used a dedicated 2.5m telescope (Gunn et al., 2006) at Apache Point Observatory to map over a quarter of the sky. BOSS has imaged an additional 3100 deg² in the Southern sky which has increased the total SDSS imaging footprint to 14,055 deg² (7600 deg² at galactic latitudes greater than 20 deg in the North Galactic Cap and 3000 deg² at galactic latitudes greater than 20 deg in the South Galactic Cap). These images were taken using the original SDSS drift-scanning mosaic CCD camera (Gunn et al., 1998) in 5 photometric bandpasses (Fukugita et al., 1996; Smith et al., 2002; Doi et al., 2010) to a limiting magnitude of $r \sim 22.5$. All images were processed using the same pipeline as SDSS to perform astrometric calibration (Pier et al., 2003), photometric reduction (Lupton et al., 2001) and photometric calibration (Padmanabhan et al., 2008). Galactic extinction corrections were performed using the maps of Schlegel, Finkbeiner & Davis (1998). The SDSS-

III BOSS and original SDSS imaging was collectively reprocessed as part of SDSS Data Release 8 (DR8; Aihara et al. 2011). Additional details of the survey design can be found in Eisenstein et al. (2011) and Dawson et al. (2012).

The current SDSS Data Release 9 (DR9) used for analysis in this chapter constitutes the first year of BOSS spectroscopic followup of targets selected based on DR8 photometry. It covers 3275 deg^2 which is roughly a third of the total area that will eventually be observed by BOSS. Upon completion, BOSS is scheduled to obtain spectra and redshifts for about 1.35 million galaxies over a $10,000 \text{ deg}^2$ area on the sky. In addition, BOSS will also observe about 160,000 quasars and 100,000 ancillary targets. The selection of galaxies for BAO analysis is based on the two targeting algorithms for SDSS-II Luminous Red Galaxies (LRGs; Eisenstein et al. 2001) with an extension to pick up fainter and bluer galaxies to achieve a $3 \times 10^{-4} h^3 \text{ Mpc}^{-3}$ number density. Most of these galaxies are old and have prominent 4000\AA breaks, making them easy to select using multiband photometry. BOSS target selection is divided into 2 samples. The first (LOWZ) consists of galaxies in the redshift range $0.2 < z < 0.43$ and the second (CMASS) consists of galaxies in the redshift range $0.43 < z < 0.7$. These are analogous to Cut-I and Cut-II used to select LRGs in SDSS-II (Eisenstein et al., 2001) and are based on when the 4000\AA break falls in the g and r bands respectively. In this chapter, we will focus on the CMASS sample for our BAO analysis.

The CMASS (constant mass) sample was conceived as a roughly constant stellar mass sample based on the passive galaxy template of Maraston et al. (2009). The sample has a uniform mass distribution at all redshifts as verified by the stellar mass distribution analysis of Maraston et al. (2012) and the velocity dispersion analysis of Thomas et al. (2012). The majority of CMASS objects are central galaxies that reside in $10^{13} h^{-1} M_{\odot}$ halos, but a significant number are satellite galaxies that reside

in halos that are roughly 10 times more massive (White et al., 2011; Nuza et al., 2012). As mentioned above, unlike the SDSS-II LRG sample which consisted only of massive early-type galaxies, about 26% of CMASS galaxies are massive spirals (Masters et al., 2011). The CMASS sample is highly biased with $b \sim 2$ and very luminous, making them ideal tracers of the underlying dark matter distribution over large cosmological volumes. They have a sufficiently high number density so that shot-noise ($\sim 1/\bar{n}$) does not dominate our measurements of the power spectrum or correlation function of galaxies. Hence they afford us great leverage in probing large-scale structure. A more detailed discussion of the target selection is given in Anderson et al. (2012) & Padmanabhan et al. (2012b).

To perform spectroscopic observations, the targets are divided into “tiles” with 3° diameters using an algorithm developed by Blanton et al. (2003). Up to 1000 holes are drilled in aluminum plates at locations corresponding to the positions of the targets on the tiles. Optical fibers that feed a pair of double spectrographs are manually plugged into the holes. The BOSS spectrographs are upgraded from the original SDSS spectrographs. BOSS covers the wavelength range $3600\text{\AA} < \lambda < 10000\text{\AA}$ at a resolution of 1500 to 2600 compared to the original SDSS coverage of $3850\text{\AA} < \lambda < 9220\text{\AA}$. The 640-fiber cartridges with $3''$ apertures have been replaced by 1000-fiber cartridges with $2''$ apertures. In addition, the throughputs have been increased by upgrading the CCDs, gratings and optical elements. The exposures are performed in series, each 900 seconds in duration, until a minimum signal-to-noise ratio is achieved for the faintest sources. This results in $> 97\%$ redshift completeness over the full area of the survey.

The exposures are coadded for each source and the resulting spectra fit to eigen-templates of stars, quasars and galaxies. This effectively classifies the targeted object and measures its redshift. To account for residual extinction effects or broadband

continua not included in the templates, a polynomial term is included in the fits. The χ^2 indicator is used to select the best-fit template to the data. Corrections and cuts to account for fiber collisions and redshift measurement failures are made. These are described in detail in Guo, Zehavi & Zheng (2011) & Ross et al. (2012). Additional weights are applied to correct for other systematics such as the effect of stellar density on galaxy density, galactic extinction, seeing, airmass and sky background. The weighting scheme minimizes the spurious fluctuations introduced by these effects in the galaxy density field and is analyzed in depth in Ross et al. (2012).

4.3 Analysis Methods

4.3.1 Measuring the Correlation Function

The BAO feature can be detected in clustering statistics such as the correlation function $\xi(r)$ and the power spectrum $P(k)$. We will focus on the correlation function in this chapter, where the BAO appears as a small peak at the acoustic scale. The 2-point correlation function can be estimated using the Landy-Szalay estimator (Landy & Szalay, 1993) as

$$\xi(r) = \frac{DD - 2DR + RR}{RR} \quad (4.1)$$

where DD , DR and RR are the number of galaxy-galaxy, galaxy-random and random-random pairs with separation r . The random particles serve as an estimate of the average galaxy density and are generated according to the angular and redshift selection functions of the CMASS sample. We generate random sets that contain 70 times the number of CMASS objects to minimize their shot-noise contribution to the clustering measurement. In addition, the randoms account for any difference in selection functions between the Northern and Southern galactic caps, allowing their pair counts to be directly combined to form the correlation functions used in this analysis. A more detailed description of the random catalogue

generation is given in Ross et al. (2012).

We compute our correlation functions from $4h^{-1}\text{Mpc}$ to $200h^{-1}\text{Mpc}$ in bins of $4h^{-1}\text{Mpc}$ widths.

4.3.2 Reconstruction

The reconstruction technique was originally proposed by Eisenstein et al. (2007) in order to partially undo the smearing of the BAO information caused by the large-scale flows that arise from non-linear structure growth. This effectively sharpens the BAO peak in the correlation function which allows us to centroid it more accurately. Since the non-linear growth and displacement of overdensities is governed by the gravitational potential generated by these overdensities themselves, we can use the measured density field to infer the first-order displacement field. We can then shift the galaxies back along their displacement vectors, placing them near their linear theory positions. As mentioned in §4.1, this technique was adapted and first applied to a galaxy redshift survey by Padmanabhan et al. (2012a); Xu et al. (2012) & Mehta et al. (2012) in order to obtain constraints on cosmological parameters from the BAO signal measured from the SDSS-II DR7 LRG sample. Full details of the reconstruction method are described in Padmanabhan et al. (2012a) and Chapter 3. We give a brief summary here.

Before we begin reconstruction, we must first estimate the galaxy bias b and the linear growth rate $f = d \log D / d \log a$, where $D(a)$ is the linear growth function and a is the scale factor. The former can be estimated by calculating the unreconstructed correlation function or power spectrum and comparing its amplitude to linear theory since $\delta_{matter} \sim \delta_{gal}/b$ at large scales. Here, δ is the fractional overdensity relative to the critical density of the universe ρ_c , i.e. $\delta = (\rho - \rho_c)/\rho_c$. The latter can be approximated as $\Omega_m(z)^{0.55}$. We pick our fiducial reconstruction parameters to be $b = 1.85$ and $f = 0.75$.

Reconstruction operates on the matter density field, which we can infer by measuring the galaxy density field and scaling it down by b . We then embed the density field in a volume that is much larger than the boundaries of the survey. The regions of this volume not covered by the survey are filled in by generating constrained Gaussian realizations (see Padmanabhan et al. (2012a) and Chapter 3 for details). The final density field is smoothed using a Gaussian of width $l = 15h^{-1}\text{Mpc}$ to blur the “spiky” density field that results by a trivial scaling of the galaxy density field. The choice of this smoothing scale is discussed in Padmanabhan et al. (2012a) and Chapter 3.

The displacement field \vec{q} can be estimated from the density field by inverting the continuity equation

$$\nabla \cdot \vec{q} = -\frac{\delta_{gal}}{b}. \quad (4.2)$$

We can also include a modification to this equation to undo large-scale redshift-space distortions as shown in Padmanabhan et al. (2012a) and Chapter 3. Redshift-space distortions arise due to the intrinsic motions of galaxies that impart additional redshifts not related to the cosmological redshift that arises from the expansion of the universe. Since the line-of-sight separations of galaxies is inferred from redshift, the clustering along the line-of-sight appears distorted as a result of these additional redshifts. At large scales, the dominant redshift-space distortion arises from the coherent infall of galaxies towards overdense regions known as the Kaiser effect (Kaiser, 1987).

Finally we can shift the galaxies by $-\vec{q}$ to place them back near their linear theory positions. To undo the Kaiser effect, we must shift the galaxies by an additional $-fq_s\hat{s}$, where q_s is the displacement along the line-of-sight direction \hat{s} . We will denote this shifted dataset as D . We must generate an additional set of randomly distributed points and shift these by $-\vec{q}$ as well, to ensure that we are not removing

power from the density field. This set we will denote as S . The reconstructed correlation function can then be calculated as

$$\xi(r) = \frac{DD - 2DS + SS}{RR}. \quad (4.3)$$

where DD , DS and SS are the number of shifted galaxy-galaxy, galaxy-random and random-random pairs with separation r . RR is the number of unshifted random-random pairs with separation r .

Since the separation between the Northern and Southern Galactic Caps is large, we run reconstruction on these separately and combine them at the level of pair-counts during the estimation of the correlation function (see previous section).

4.3.3 Fitting the Correlation Function

We measure the acoustic scale from the correlation function by fitting a template with an assumed fiducial cosmology to the data and measuring the relative shift in the BAO location. As a reminder, the fiducial cosmology we assume is $\Omega_m = 0.274$, $h = 0.7$, $\Omega_b h^2 = 0.0224$, $n_s = 0.95$ and $\sigma_8 = 0.8$. Our fitting procedure is based on the technique described in Xu et al. (2012) and Chapter 3. We give a brief summary of the techniques here.

Our correlation function model is given by

$$\xi^{\text{fit}}(r) = B^2 \xi_m(\alpha r) + A(r) \quad (4.4)$$

where

$$\xi_m(r) = \int \frac{k^2 dk}{2\pi^2} P_m(k) j_0(kr) e^{-k^2 a^2}, \quad (4.5)$$

and

$$A(r) = \frac{a_1}{r^2} + \frac{a_2}{r} + a_3. \quad (4.6)$$

In Equation 4.5, the Gaussian term has been introduced to damp the oscillatory transform kernel $j_0(kr)$ at high- k to induce better numerical convergence. The

exact damping scale used in this term is not important as long as it is significantly below our scales of interest. We set $a = 1h^{-1}\text{Mpc}$ here. The $A(r)$ term is composed of nuisance parameters $a_{1,2,3}$ that help marginalize over the unmodeled broadband signal in the correlation function. Such broadband effects include redshift-space distortions, scale-dependent bias and any errors made in our assumption of the model cosmology. These effects may bias our measurement of the acoustic scale if not removed. B is a multiplicative constant, allowing for an unknown large-scale bias. We use a template $P_m(k)$ of the form

$$P_m(k) = [P_{\text{lin}}(k) - P_{\text{nobao}}(k)]e^{-k^2\Sigma_{\text{nl}}^2/2} + P_{\text{nobao}}(k), \quad (4.7)$$

as given in Eisenstein, Seo & White (2007). Here, $P_{\text{lin}}(k)$ is the linear theory power spectrum and $P_{\text{nobao}}(k)$ is the power spectrum with the BAO feature erased. The Σ_{nl} term is used to damp the acoustic oscillations in the linear theory power spectrum, serving to model the effects of non-linear structure growth. We fix $\Sigma_{\text{nl}} = 8h^{-1}\text{Mpc}$ in our fits to the pre-reconstruction correlation functions and $\Sigma_{\text{nl}} = 4h^{-1}\text{Mpc}$ in our fits to the post-reconstruction correlation functions. We normalize the template to the observed or mock correlation function being fit at $r = 50h^{-1}\text{Mpc}$, thereby ensuring that $B^2 \sim 1$. These parameters were tuned on our mock catalogues, and we explicitly verify that our results are insensitive to these particular choices in §4.4.2.

The scale dilation parameter α is defined as

$$\alpha = \frac{[D_V(z)/r_s]}{[D_V(z)/r_s]_{\text{fid}}} \quad (4.8)$$

where $D_V(z)$ is the spherically averaged distance to the effective redshift of our galaxy sample $z = 0.57$ and r_s is the sound horizon. Note that $D_V(z)$ is defined as

$$D_V(z) = [cz(1+z)^2 D_A^2 H^{-1}]^{1/3} \quad (4.9)$$

The *fid* subscript indicates that the values correspond to the fiducial cosmology used to construct the fitting model. Hence it can be seen that α measures the relative

position of the acoustic peak in the data versus the model, thereby characterizing any observed shift. If $\alpha > 1$, the acoustic peak is shifted towards smaller scales, and vice versa for $\alpha < 1$.

We obtain the best-fit value of α by computing the χ^2 goodness-of-fit indicator at intervals of $\Delta\alpha = 0.001$ in the range $0.8 < \alpha < 1.2$, then identify the value of α that gives the minimum χ^2 and take this as our best-fit value. The χ^2 as a function of α is given by

$$\chi^2(\alpha) = [\vec{d} - \vec{m}(\alpha)]^T C^{-1} [\vec{d} - \vec{m}(\alpha)], \quad (4.10)$$

where \vec{d} is the measured correlation function and $\vec{m}(\alpha)$ is the best-fit model at each α . C is the sample covariance matrix described in the next section, and we use a fitting range of $28 < r < 200h^{-1}\text{Mpc}$. We therefore fit over 44 points using 5 parameters, leaving us with 39 degrees-of-freedom (dof). Assuming a multi-variate Gaussian distribution for the fitted data, the probability distribution of α is

$$p(\alpha) \propto e^{-\chi^2(\alpha)/2}. \quad (4.11)$$

The normalization constant is determined by ensuring that the distribution integrates to 1. In calculating $p(\alpha)$, we also impose a 15% Gaussian prior on $\log(\alpha)$ to suppress values of $\alpha \ll 1$ that correspond to the BAO being shifted to the edge of our fitting range at large scales. The sample variance is larger at these scales, and the fitting algorithm is afforded some flexibility to hide the acoustic peak within the larger errors.

The standard deviation of this probability distribution serves as an error estimate on our distance measurement. The standard deviation σ_α for the data and each individual mock catalogue can be calculated as

$$\sigma_\alpha = \sqrt{\int (\alpha - \bar{\alpha})^2 p(\alpha) d\alpha} \quad (4.12)$$

where

$$\bar{\alpha} = \int \alpha p(\alpha) d\alpha \quad (4.13)$$

is the mean of the distribution.

In reference to the mocks, $\langle \alpha \rangle$ will denote the ensemble mean of the α values measured from each individual mock, and $\tilde{\alpha}$ will denote the median. The term “Quantiles” will denote the scatter in the mocks as indicated by the 16th/84th percentiles, which are approximately the 1σ level if the distribution is Gaussian. The scatter predicted by these quantiles suffers less than the rms from the effects of extreme outliers.

4.3.4 Mocks and Covariance Matrices

The covariance matrix we use for our fits (Equation (4.10)) is calculated directly from the 600 mock catalogues we generate for the CMASS sample. The mocks are generated in a manner similar to the PThalos method introduced by Scoccimarro & Sheth (2002). Using second order Lagrangian perturbation theory (2LPT), we create 600 matter density fields at $z = 0.55$, the median (unweighted) redshift of the CMASS sample. Since we sample the mocks in the same way we sample the data, the effective weighted redshift of the mocks is $z = 0.57$, the same as for the data. Halos are identified in the mocks using a friends-of-friends (fof) algorithm and populated using a halo occupation distribution (HOD) that matches the CMASS clustering at $30 - 80h^{-1}\text{Mpc}$. Details of the fof linking length used to define halos can be found in Manera et al. (2012). The HOD form used is described in detail in Zheng, Coil & Zehavi (2007).

The mocks are generated in $2400h^{-1}\text{Mpc}$ boxes and then reshaped into the DR9 geometry. Redshift-space distortions are included, and sky completeness and number density are matched to CMASS. 2LPT does not allow a full treatment of small scales, where structure growth is highly non-linear. However, we find that our mocks

match the CMASS clustering into the quasi-linear regime at a level similar to mocks generated from full N-body simulations which do account for the non-linear evolution. This comparison was made to simplified mocks made from the LasDamas simulations (McBride et al., 2012, in prep) which were not shaped to match DR9.

The Northern and Southern Galactic Cap mocks were created separately and combined at the paircount level while calculating the correlation function, similar to the data. The sample covariance matrix can be calculated as

$$C_{ij} = \frac{1}{N-1} \sum_{n=1}^N [\xi_n(r_i) - \bar{\xi}(r_i)][\xi_n(r_j) - \bar{\xi}(r_j)], \quad (4.14)$$

where N is the total number of mocks, $\xi_n(r)$ is the correlation function calculated from the n th mock and $\bar{\xi}(r)$ is the average of the mock correlation functions. We compare this sample covariance matrix to 2 other schemes for estimating covariances. The first fits a smooth Gaussian covariance model to a small number of mock catalogues (Xu et al., 2012) and the second computes an analytic estimate from the power spectrum (de Putter et al., 2012). Both of these produce smooth covariance matrices which are free from the noise found in the sample covariance matrix. We find that the acoustic scale and errors measured using the fitting technique described in §4.3.3 is consistent for all 3 of these covariance matrices. In addition, performing singular value decompositions of these 3 matrices reveal that they share similar structure. These tests are described in detail in Manera et al. (2012). We perform the fits in this work using the sample covariance matrix.

4.4 Results

4.4.1 Correlation Function Results

Using the procedure described in §4.3.3, we measure the shift in the acoustic scale from the CMASS DR9 data to be $\alpha = 1.016 \pm 0.017$ before reconstruction and

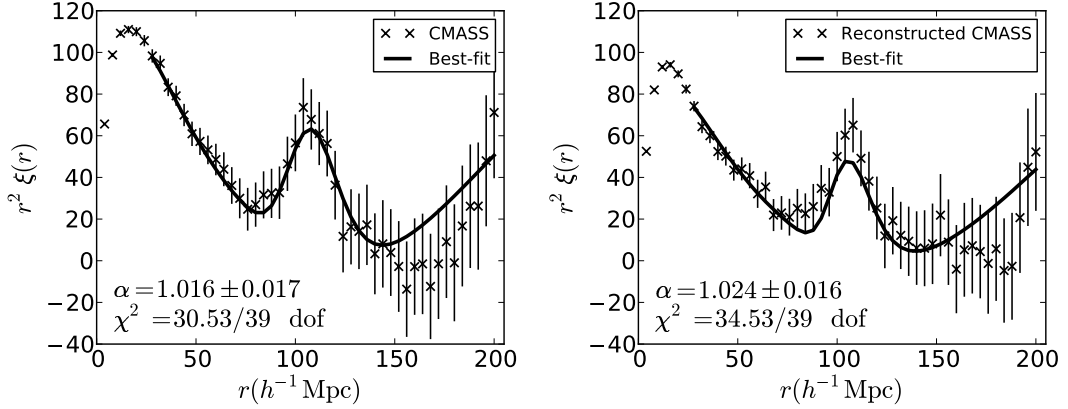


Figure 4.1: The CMASS correlation function before (left) and after (right) reconstruction (crosses) with the best-fit models overplotted (solid lines). Error bars show the square root of the diagonal covariance matrix elements, and data on similar scales are also correlated. The BAO feature is clearly evident, and well matched to the best-fit model. The best-fit dilation scale is given in each plot, with the χ^2 statistic giving goodness of fit. One can see that reconstruction has not significantly improved our measurement of the acoustic scale from the CMASS sample.

$\alpha = 1.024 \pm 0.016$ after reconstruction. The quoted errors are the σ_α values measured from the probability distributions, $p(\alpha)$. Plots of the data and corresponding best-fit models are shown in Figure 4.1 for before (left) and after (right) reconstruction. We see that for CMASS DR9, reconstruction has not significantly improved our measurement of the acoustic scale. However, in the context of the mock catalogues, this result is not surprising.

Figure 4.2 shows the σ_α values measured from the mocks before reconstruction versus those measured after reconstruction from the correlation function fits. The CMASS DR9 point is overplotted as the black star and falls within the locus of mock points. However, we see that before reconstruction, our recovered σ_α for CMASS DR9 is much smaller than the mean expected from the mocks. For typical cases, reconstruction improves errors on α , but if one has a “lucky” realization that yields a low error to begin with, then reconstruction does not produce much

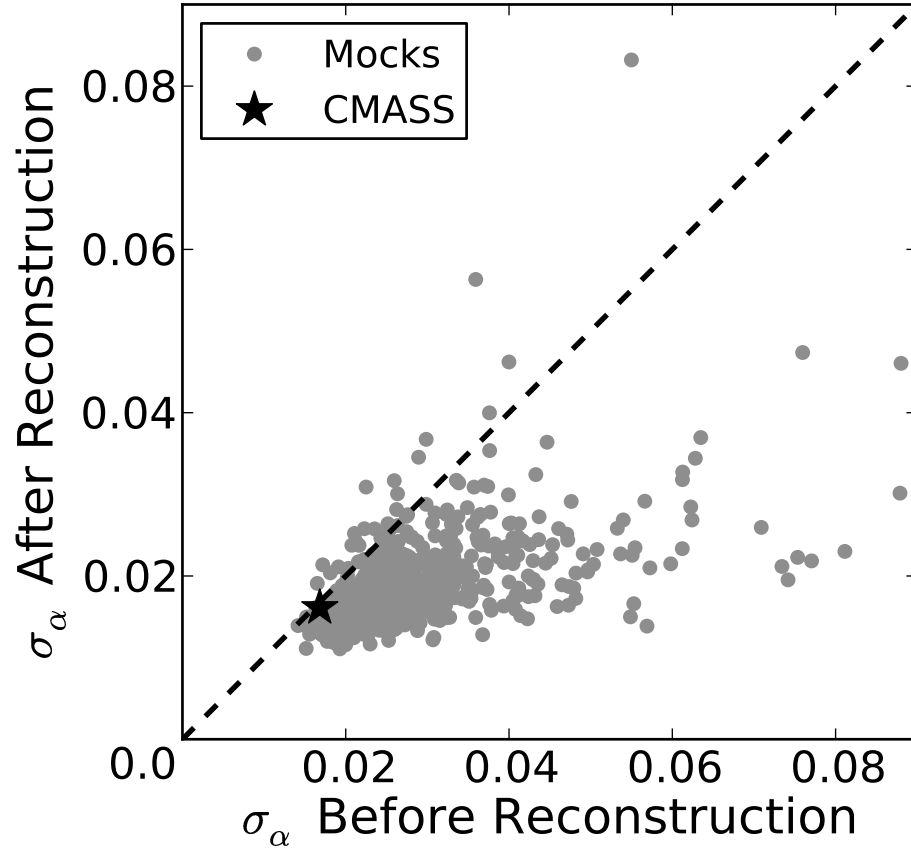


Figure 4.2: Comparisons of σ_α errors in mock catalogues before and after reconstruction as measured from $\xi(r)$. Reconstruction tends to improve our ability to measure α ; on a mock-by-mock basis, the average amount of improvement in σ_α is a factor of 1.54. However, the amount of improvement varies, and 26 (out of 600) of the mocks actually see σ_α increase from pre-reconstruction to post-reconstruction. The CMASS DR9 point is overlotted as the black star and falls within the locus of the mock points. 44 (out of 600) of the mocks have a ratio of σ_α after reconstruction compared to before reconstruction that is greater than the CMASS DR9 value. Hence, the fact that the error on α measured from CMASS DR9 does not decrease significantly after reconstruction is not unexpected in the context of the mocks. One can also see that most of the extreme outliers in σ_α before reconstruction have significantly smaller errors after reconstruction.

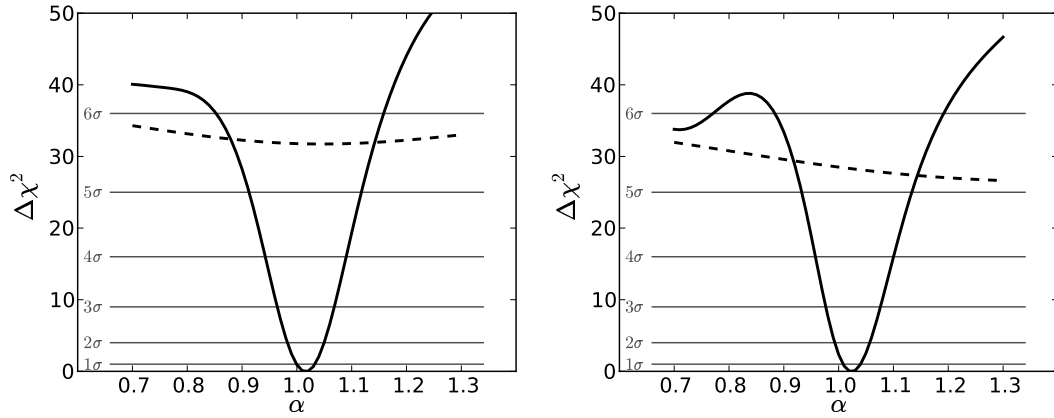


Figure 4.3: Significance of the CMASS DR9 BAO feature before (left) and after (right) reconstruction as measured from $\xi(r)$. The dashed lines correspond to fits to the data using a model without BAO. The quantity $\Delta\chi^2 = \chi^2 - \chi_{min}^2$, where χ_{min}^2 corresponds to the minimum χ^2 where the best-fit value of α lies. By comparing the minimum of the solid curve with the dashed curve, we can quantify how confident we are that the BAO can be measured from the CMASS DR9 sample. Similarly, comparing the minimum and the plateau of the solid curve tells us how confident we are that we have measured the correct local minima for the acoustic scale. One can see that both before and after reconstruction, we detect the BAO at greater than 5σ confidence and the global minimum is itself at 6σ below the χ^2 plateau, implying that the best-fit α is preferred at this level.

improvement. The mock catalogue comparison in Figure 4.2 shows that the BOSS DR9 data volume can be thought of as such a “lucky” realization, with a strong and well defined acoustic peak. It is therefore unsurprising that reconstruction does not reduce the error on α .

The BAO detection in the CMASS DR9 data is highly significant as illustrated in Figure 4.3. Here we have plotted $\Delta\chi^2 = \chi^2 - \chi_{min}^2$, where χ_{min}^2 is the minimum χ^2 that corresponds to the best-fit value of α . The dashed line overplotted corresponds to fits to the data using a model without a BAO signature. This figure captures two tests of BAO significance: the first requires a comparison between the solid and dashed curves, and indicates how confident we are that the BAO feature exists in

the CMASS DR9 data. The second uses the plateau height of the $\Delta\chi^2$ curve to indicate how confident we are that we have measured the correct acoustic scale.

The panel on the left corresponds to our pre-reconstruction results and the panel on the right corresponds to our post-reconstruction results. Before reconstruction, the minimum of the solid curve lies beyond a $\Delta\chi^2$ of 25 from the dashed curve, indicating that the BAO is detected in CMASS DR9 at greater than 5σ confidence. Local maxima are seen at greater than $\Delta\chi^2$ of 36 above the minimum, indicating that the data prefer our best-fit value of α at more than 6σ . We see similar confidence levels post-reconstruction.

Before reconstruction our mocks yield $\langle\alpha\rangle = 1.004$ with an average error on any single realization (i.e. the rms or standard deviation) of 0.027 and a standard error on the mean of 0.001. The median is $\tilde{\alpha} = 1.004$ with quantiles of ${}^{+0.026}_{-0.026}$. After reconstruction, we obtain $\langle\alpha\rangle = 1.004$ with average error on any single realization of 0.018 and standard error on the mean of 0.001. The median is $\tilde{\alpha} = 1.004$ with quantiles of ${}^{+0.017}_{-0.018}$. One can see that given the error on the mean, we detect a statistically significant shift in our measured mean from the true acoustic scale ($\alpha = 1$) expected in the mocks. This small systematic offset before reconstruction is mostly due to non-linear structure growth and galaxy bias which can shift the location of the BAO by $\sim 0.5\%$ (Crocco & Scoccimarro, 2008; Padmanabhan & White, 2009; Seo et al., 2010; Mehta et al., 2011). Reconstruction has been shown to remove this shift in periodic box simulations and the SDSS-II mock catalogues (Seo et al., 2010; Mehta et al., 2011; Padmanabhan et al., 2012a), so the fact that we still see a slight bias after reconstruction suggests that something intrinsic to the CMASS sample may be the culprit. For example, the DR9 survey geometry (which is donut-shaped) may be too disjointed to fully remove these shifts. In addition, systematics may exist in the galaxy catalogue itself and can also arise if the fitting

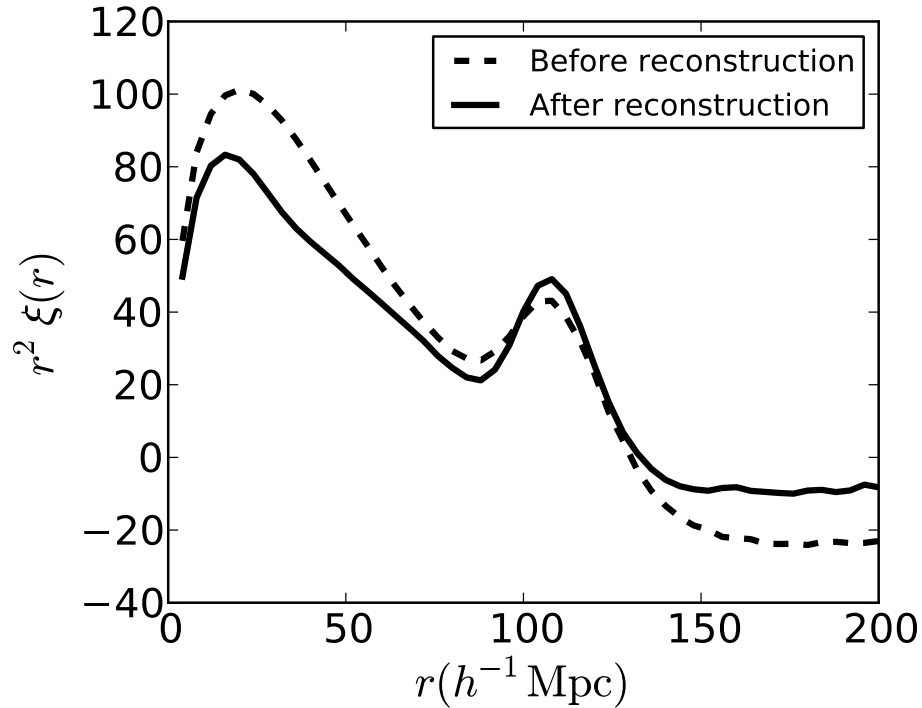


Figure 4.4: Average of the mock correlation functions before and after reconstruction showing that the average acoustic peak sharpens up significantly after reconstruction. This indicates that, in general, our reconstruction technique effectively removes some of the smearing caused by non-linear structure growth, affording us the ability to more precisely centroid the acoustic peak.

model does not match the data well enough. We ameliorate these effects as best as possible by including the broadband $A(r)$ marginalization term. In any case, the current statistical precision does not allow us to detect this offset at any significance in each mock or the CMASS data as indicated by the level of scatter in the mocks.

Most important, the average error on α recovered from the mocks has decreased after reconstruction. This is illustrated in Figure 4.2, where an overall improvement in σ_α is evident after reconstruction. The greatest improvements occur when the pre-reconstruction errors are the worst. The average decrease in σ_α is a factor of 1.54, which is equivalent to the effects of increasing the survey volume by a factor

of 2.3. Therefore on average, reconstruction appears to significantly improve our ability to measure α . This point is further illustrated in Figure 4.4, where we have plotted the average mock correlation function before and after reconstruction. One can see the sharpening up of the acoustic peak, indicating the effectiveness of the reconstruction algorithm in partially removing the smearing of the BAO caused by non-linear structure growth. This improvement is what allows a more precise centroiding of the peak location. In fitting the average mock correlation function before and after reconstruction, we find Σ_{nl} , the damping of the BAO due to non-linear evolution, decreases from $7.6h^{-1}\text{Mpc}$ to $3.2h^{-1}\text{Mpc}$. Beyond reducing the distance errors, reconstruction also makes our distance estimates more robust to parameter choices in our fitting algorithms and reduces the scatter between the distance estimates from the the correlation function and the power spectrum. We quantify these improvements further in following sections.

We next compare the observed scatter in the best-fit α in the mocks to the σ_α estimated in each fit from the $\chi^2(\alpha)$ curve. In Figure 4.5, we plot a histogram of $(\alpha - \langle\alpha\rangle)/\sigma_\alpha$ from the mocks and compare the result to the unit normal distribution. We find excellent agreement; a Kolmogorov-Smirnov (K-S) test finds a high likelihood that the observed distribution is drawn from a unit normal. Hence the Gaussian probability distribution obtained from the χ^2 statistic is an appropriate characterization of the error on α .

4.4.2 Robustness of Techniques

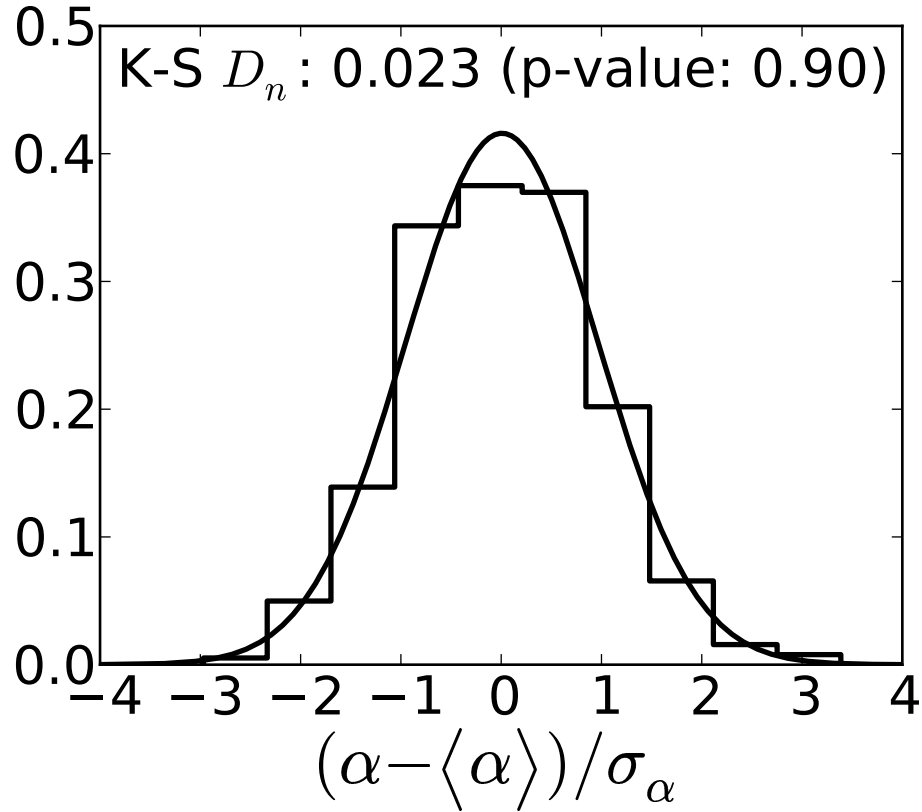


Figure 4.5: Histogram of $(\alpha - \langle \alpha \rangle) / \sigma_\alpha$ measured from $\xi(r)$ of the post-reconstruction mocks, where $\langle \alpha \rangle$ is the mean. This quantity is a proxy for the signal-to-noise ratio of our BAO measurement. We see that this distribution is close to Gaussian as indicated by the near-zero K-S D_n . The corresponding p-value indicates that we are 90% certain our values are drawn from a Gaussian distribution, indicating that the values of σ_α we measure from the χ^2 distribution are reasonable descriptors of the error on α measured by fitting $\xi(r)$.

Table 4.1: Fitting results for various models, found by varying the fiducial fitting model and reconstruction parameters on the ensemble distance scale measurement from the mocks (i.e. the mean $\langle\alpha\rangle$ and the median $\tilde{\alpha}$) as well as the difference in the observed distance scale with respect to the fiducial model on a mock-by-mock basis ($\Delta\alpha$). The results for the fiducial model, and for different broadband $A(r)$ fitting functions (*poly0*, *poly2*, *poly4*), fitting ranges, and non-linear damping Σ_{nl} of the acoustic scale, are shown for the correlation function before and after reconstruction. We also present the results of fitting with a different covariance matrix (ML) derived based on the technique in Xu et al. (2012). For our reconstruction tests, we present the effects of changing the fiducial galaxy bias by -20% and $+20\%$ ($b = 1.5$ and $b = 2.2$), the fiducial growth rate by -20% and $+20\%$ ($f = 0.6$ and $f = 0.9$), and the smoothing length to $20h^{-1}\text{Mpc}$, a more conservative choice than our fiducial smoothing of $15h^{-1}\text{Mpc}$.

Model	$\langle\alpha\rangle$	rms	$\tilde{\alpha}$	Quantiles	$\langle\Delta\alpha\rangle^{1,2}$	rms	$\widetilde{\Delta\alpha}$	Quantiles	$\langle\chi^2\rangle/dof$	
Before Reconstruction										
Fiducial [f]	1.004	0.027	1.004	$^{+0.026}_{-0.026}$	–	–	–	–	39.60/39	
Fit with <i>poly0</i> .	0.999	0.026	1.000	$^{+0.024}_{-0.024}$	-0.005	0.009	-0.004	$^{+0.007}_{-0.008}$	42.93/42	
Fit with <i>poly2</i> .	1.001	0.027	1.002	$^{+0.025}_{-0.025}$	-0.002	0.004	-0.002	$^{+0.003}_{-0.003}$	41.24/40	
Fit with <i>poly4</i> .	1.004	0.027	1.004	$^{+0.025}_{-0.025}$	0.000	0.001	-0.000	$^{+0.001}_{-0.001}$	38.27/38	
Fit between $20 < r < 200h^{-1}\text{Mpc}$.	1.001	0.028	1.003	$^{+0.025}_{-0.028}$	-0.002	0.006	-0.002	$^{+0.004}_{-0.004}$	41.78/41	
Fit between $50 < r < 200h^{-1}\text{Mpc}$.	1.005	0.027	1.005	$^{+0.025}_{-0.026}$	0.001	0.003	0.001	$^{+0.003}_{-0.002}$	34.20/34	
Fit with $\Sigma_{nl} \rightarrow 0$.	1.000	0.030	0.999	$^{+0.028}_{-0.026}$	-0.004	0.015	-0.005	$^{+0.012}_{-0.011}$	41.60/39	
Fit with $\Sigma_{nl} \rightarrow \Sigma_{nl} - 2$.	1.002	0.028	1.003	$^{+0.026}_{-0.025}$	-0.001	0.005	-0.002	$^{+0.004}_{-0.004}$	39.72/39	
Fit with $\Sigma_{nl} \rightarrow \Sigma_{nl} + 2$.	1.005	0.028	1.005	$^{+0.026}_{-0.027}$	0.001	0.005	0.001	$^{+0.004}_{-0.004}$	40.11/39	

Continued on next page

Table 4.1 – continued from previous page

Model	$\langle\alpha\rangle$	rms	$\tilde{\alpha}$	Quantiles	$\langle\Delta\alpha\rangle$	rms	$\widetilde{\Delta\alpha}$	Quantiles	$\langle\chi^2\rangle/dof$
Fit using ML covariance matrix.	1.003	0.029	1.005	$^{+0.023}_{-0.028}$	-0.001	0.008	-0.000	$^{+0.006}_{-0.007}$	40.07/39
After Reconstruction									
Fiducial [f]	1.004	0.018	1.004	$^{+0.017}_{-0.018}$	–	–	–	–	40.95/39
Fit with $poly0$.	1.002	0.018	1.002	$^{+0.017}_{-0.018}$	-0.002	0.004	-0.002	$^{+0.003}_{-0.004}$	45.15/42
Fit with $poly2$.	1.004	0.018	1.003	$^{+0.017}_{-0.017}$	-0.001	0.001	-0.001	$^{+0.001}_{-0.001}$	42.53/40
Fit with $poly4$.	1.004	0.018	1.004	$^{+0.017}_{-0.017}$	-0.000	0.000	-0.000	$^{+0.000}_{-0.000}$	39.94/38
Fit between $20 < r < 200h^{-1}\text{Mpc}$.	1.010	0.017	1.010	$^{+0.017}_{-0.017}$	0.006	0.003	0.005	$^{+0.003}_{-0.003}$	47.38/41
Fit between $50 < r < 200h^{-1}\text{Mpc}$.	1.004	0.018	1.003	$^{+0.017}_{-0.018}$	-0.001	0.002	-0.001	$^{+0.002}_{-0.002}$	34.55/34
Fit with $\Sigma_{nl} \rightarrow 0$.	1.003	0.019	1.003	$^{+0.017}_{-0.018}$	-0.001	0.003	-0.001	$^{+0.003}_{-0.003}$	40.87/39
Fit with $\Sigma_{nl} \rightarrow \Sigma_{nl} - 2$.	1.003	0.018	1.004	$^{+0.017}_{-0.018}$	-0.001	0.002	-0.001	$^{+0.002}_{-0.002}$	40.84/39
Fit with $\Sigma_{nl} \rightarrow \Sigma_{nl} + 2$.	1.006	0.018	1.006	$^{+0.016}_{-0.018}$	0.001	0.003	0.001	$^{+0.002}_{-0.002}$	41.62/39
Fit using ML covariance matrix.	1.004	0.019	1.003	$^{+0.019}_{-0.018}$	-0.000	0.004	-0.000	$^{+0.005}_{-0.004}$	41.02/39
Fit to recon. with $b \rightarrow 1.5$.	1.004	0.019	1.004	$^{+0.016}_{-0.022}$	0.000	0.006	0.000	$^{+0.006}_{-0.006}$	42.56/39
Fit to recon. with $b \rightarrow 2.2$.	1.003	0.019	1.005	$^{+0.015}_{-0.023}$	-0.000	0.006	-0.001	$^{+0.006}_{-0.005}$	41.01/39

Continued on next page

Table 4.1 – continued from previous page

Model	$\langle\alpha\rangle$	rms	$\tilde{\alpha}$	Quantiles	$\langle\Delta\alpha\rangle$	rms	$\widetilde{\Delta\alpha}$	Quantiles	$\langle\chi^2\rangle/dof$
Fit to recon. with $f \rightarrow 0.6$.	1.003	0.018	1.004	$^{+0.017}_{-0.021}$	-0.000	0.002	-0.000	$^{+0.001}_{-0.002}$	40.50/39
Fit to recon. with $f \rightarrow 0.9$.	1.004	0.018	1.005	$^{+0.015}_{-0.022}$	0.001	0.002	0.001	$^{+0.001}_{-0.002}$	41.09/39
Fit to recon. with $l \rightarrow 20h^{-1}\text{Mpc}$.	1.006	0.019	1.008	$^{+0.016}_{-0.023}$	0.003	0.007	0.002	$^{+0.005}_{-0.005}$	45.04/39

¹ $\Delta\alpha = \alpha_{[i]} - \alpha_{[f]}$, where i is the model indicated in the first column.

² Note that the error on the mean $\Delta\alpha$ is \sqrt{N} smaller than the rms from the mocks quoted in the table, where N is the number of mocks. These much smaller numbers would indicate that there is a significant detection of the change in the mean as we change fitting model or reconstruction parameters; however, such a small change would not be significantly detected in each mock given the dispersion.

We test the robustness of our correlation function fitting model by slightly varying the fiducial model parameters and then re-performing the fits to see if we recover consistent values of the acoustic scale α . These tests are performed on the mocks as well as the CMASS DR9 data. Recall that the fiducial model takes on the form given in Equations (4.4) and (4.6), where we have taken $\Sigma_{nl} = 8h^{-1}\text{Mpc}$ before reconstruction and $\Sigma_{nl} = 4h^{-1}\text{Mpc}$ after reconstruction. In addition, we specify a fiducial fitting range of $28 < r < 200h^{-1}\text{Mpc}$ and use the sample covariance matrix. The fiducial model parameters we alter in performing these tests are the order of $A(r)$, the value of Σ_{nl} , the fitting range, and the covariance matrix used. In modifying the form of $A(r)$, *poly0* corresponds to $A(r) = 0$, *poly2* corresponds to a 2-parameter $A(r) = a_1/r^2 + a_2/r$, and *poly4* corresponds to a 4-parameter $A(r) = a_1/r^2 + a_2/r + a_3 + a_4r$.

The fiducial and tweaked model fit results for 600 mocks are shown in Table 4.1. We remove mock results with poorly measured values of α since a BAO feature was not clearly identified ($\sigma_\alpha > 7\%$). The similarity between the α and σ_α values listed in the table for the “tweaked” models and the fiducial model implies that our fiducial model returns unbiased measurements of the acoustic scale. The only cases that have somewhat larger discrepancies are the pre-reconstruction *poly0* and $\Sigma_{nl} = 0h^{-1}\text{Mpc}$ cases which is not surprising. The prior implies that before reconstruction, there is non-negligible broadband smooth signal that may bias our measurement of the acoustic scale and hence a non-zero form for $A(r)$ is required to marginalize over this contribution. The latter implies that using a BAO model that does not account for the effects of non-linear evolution, which are clearly evident before reconstruction, will also bias the measurement of α . After reconstruction, the scatter in these cases is greatly reduced as reconstruction partially undoes large-scale redshift space distortions and non-linear structure growth.

Table 4.2: Fitting results for various models. Here we explore the effects of varying the fiducial fitting model and reconstruction parameters on our measurements of the distance scale from CMASS DR9. The results for the fiducial model, for different broadband $A(r)$ fitting functions ($poly0$, $poly2$, $poly4$), fitting ranges, and non-linear damping Σ_{nl} of the acoustic scale are shown for the correlation function before and after reconstruction. We also present the results of fitting with a different covariance matrix (ML) derived based on the technique in Xu et al. (2012). For our reconstruction tests, we present the effects of changing the fiducial galaxy bias by -20% and $+20\%$ ($b = 1.5$ and $b = 2.2$), the fiducial growth rate by -20% and $+20\%$ ($f = 0.6$ and $f = 0.9$), and the smoothing length to $20h^{-1}\text{Mpc}$, which is a more conservative choice than our fiducial smoothing of $15h^{-1}\text{Mpc}$.

Model	α	χ^2
Before Reconstruction		
Fiducial [f]	1.016 ± 0.017	30.53/39
Fit with $poly0$.	1.018 ± 0.020	40.84/42
Fit with $poly2$.	1.017 ± 0.016	30.74/40
Fit with $poly4$.	1.016 ± 0.017	30.33/38
Fit between $20 < r < 200h^{-1}\text{Mpc}$.	1.020 ± 0.017	32.47/41
Fit between $50 < r < 200h^{-1}\text{Mpc}$.	1.018 ± 0.018	22.99/34
Fit with $\Sigma_{nl} \rightarrow 0$.	1.005 ± 0.013	30.84/39
Fit with $\Sigma_{nl} \rightarrow \Sigma_{nl} - 2$.	1.012 ± 0.015	29.93/39
Fit with $\Sigma_{nl} \rightarrow \Sigma_{nl} + 2$.	1.019 ± 0.019	32.02/39

Continued on next page

Table 4.2 – continued from previous page

Model	α	χ^2
Fit using ML covariance matrix.	1.022 ± 0.018	30.64/39
After Reconstruction		
Fiducial [f]	1.024 ± 0.016	34.53/39
Fit with <i>poly0</i> .	1.026 ± 0.017	41.82/42
Fit with <i>poly2</i> .	1.025 ± 0.015	36.12/40
Fit with <i>poly4</i> .	1.024 ± 0.017	33.29/38
Fit between $20 < r < 200h^{-1}\text{Mpc}$.	1.031 ± 0.018	47.31/41
Fit between $50 < r < 200h^{-1}\text{Mpc}$.	1.022 ± 0.016	25.94/34
Fit with $\Sigma_{nl} \rightarrow 0$.	1.019 ± 0.015	34.18/39
Fit with $\Sigma_{nl} \rightarrow \Sigma_{nl} - 2$.	1.020 ± 0.015	34.27/39
Fit with $\Sigma_{nl} \rightarrow \Sigma_{nl} + 2$.	1.029 ± 0.017	35.10/39
Fit using ML covariance matrix.	1.022 ± 0.017	34.30/39
Fit to recon. with $b \rightarrow 1.5$.	1.033 ± 0.020	42.97/39
Fit to recon. with $b \rightarrow 2.2$.	1.021 ± 0.015	46.89/39
Fit to recon. with $f \rightarrow 0.6$.	1.024 ± 0.015	33.19/39

Continued on next page

Table 4.2 – continued from previous page

Model	α	χ^2
Fit to recon. with $f \rightarrow 0.9$.	1.025 ± 0.017	36.53/39
Fit to recon. with $l \rightarrow 20h^{-1}\text{Mpc}$.	1.026 ± 0.015	43.79/39

Similar results for the CMASS DR9 data are shown in Table 4.2. In general, our choice of model parameters does not affect the outcome of the fits. A few cases measure slightly larger or smaller values of α , but all fall well within the 1σ errorbars.

We also investigate our measurements of BAO significance with respect to the form of $A(r)$. The results are shown in Figure 4.6 after reconstruction. The right panel shows the difference in χ^2 between a fit to the data using a model containing BAO and a fit to the data using a model without BAO. These curves demonstrate how well we have detected the BAO in the CMASS DR9 data. The solid black curves correspond to subtracting the solid line from the dashed line in Figure 4.3. The other lines correspond to various other forms of $A(r)$, some with more and some with less nuisance terms. Here, the more negative $\Delta\chi^2$ is, the more a model containing BAO is preferred. Allowing more or less flexibility in the broadband marginalization as parameterized by $A(r)$ does not change the fact that a model containing BAO is favoured and we have a robust detection of the BAO in the CMASS DR9 data. The actual confidence level changes slightly between the different $A(r)$ forms; however, the variation is small and consistently falls between $5 - 6\sigma$.

The right panel shows the $\Delta\chi^2$ values from the minimum (or best-fit value) and demonstrates how well we have measured the acoustic scale. The solid black curve is identical to the solid line in Figure 4.3. The other curves correspond to various other forms of $A(r)$. In all cases, the minima lie at the same value of α with the plateaus lying at significant $\Delta\chi^2$ above the minima. Although $\Delta\chi^2$ shows significant variation between the $A(r)$ forms, we see at least a 6σ ($\Delta\chi^2 \sim 36$) preference for the best-fit value of α . It appears that a lower order or less flexible form for $A(r)$ may return α at a higher confidence, which indicates that higher order $A(r)$ may give the model too much flexibility to start fitting noise.

Next we test the robustness of our reconstruction by varying our fiducial recon-

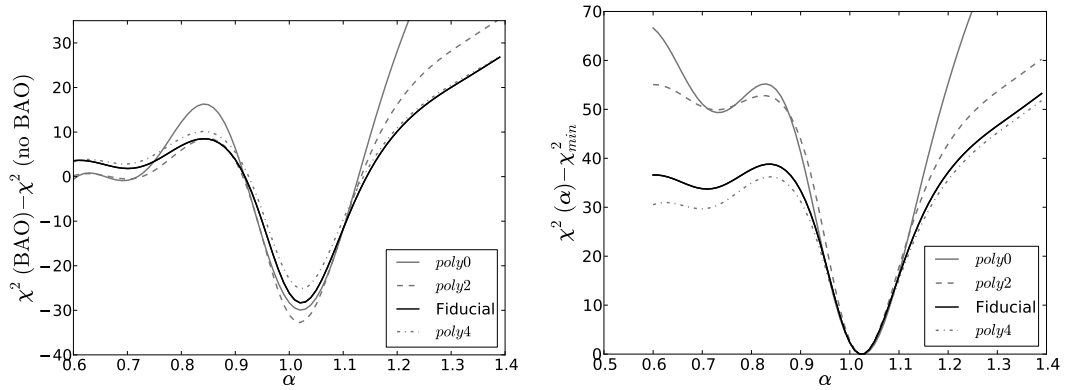


Figure 4.6: $\Delta\chi^2$ for CMASS DR9 using various forms of $A(r)$. These plots are analogous to Fig. 4.3, except we have split the two tests of BAO significance into separate panels. The left panel shows how robustly we have detected the BAO in the CMASS DR9 sample and the right panel shows how confident we are that we have measured the correct acoustic scale. In the left panel, we have plotted the difference in χ^2 between 2 fits to the data, one using a model containing BAO and one using a model without BAO. We see that this $\Delta\chi^2$ is consistently around -30 for all forms of $A(r)$ indicating that the amount of flexibility in the broadband marginalization (i.e. the number of nuisance parameters in $A(r)$) does not have a significant impact on how well we detect the BAO in the CMASS DR9 sample. In the right panel, we have plotted the $\Delta\chi^2$ of the minimum as a function of α . The various forms of $A(r)$ all identify the same best-fit value of α and this best-fit is at a $\Delta\chi^2$ well below the plateau in the curve. However, it appears that lower orders of $A(r)$ allow more confident measures of α , possibly due to the increased flexibility in higher order forms to fit noise. Regardless, we have at least a 6σ measurement of best-fit α in all cases which is robust.

struction parameters. Recall that the fiducial parameters are galaxy bias $b = 1.85$, linear growth rate $f = 0.75$ and smoothing length $l = 15h^{-1}\text{Mpc}$. We run our reconstruction algorithm using $b \pm 20\%$, $f \pm 20\%$ and $l = 20h^{-1}\text{Mpc}$ on both the mocks and the CMASS data. Then we re-perform our fits to see if we recover consistent values of α and σ_α . The results of these fits are listed in the bottom section of Table 4.1 for the mocks and Table 4.2 for the CMASS data. One can see that in all cases the values of α we measure are fairly consistent with those measured in the fiducial case for both the mocks and the CMASS data. The only case that has a slightly larger discrepancy is $b + 20\%$ for the CMASS data. This is because the shape of the correlation function near the BAO in this case appears suppressed relative to the other cases. Hence we cannot pick completely arbitrary reconstruction parameters. However, as long as we choose reasonable values, the acoustic scale and errors we measure are insensitive to the reconstruction parameters used.

4.4.3 Consensus Results

Up to this point we have only discussed the BAO measurement from the CMASS correlation function. A parallel analysis using the power spectrum was also performed. The $P(k)$ methods and results are discussed in detail in Percival et al. (2010) & Anderson et al. (2012). In this section, we discuss how we combine the $\xi(r)$ and $P(k)$ results into a consensus distance measure to $z = 0.57$ from the CMASS sample.

Although the correlation function and the power spectrum are Fourier transforms of each other and should contain the same information, we find that the α values we measure for the mocks and the CMASS data are discrepant at the $\sim 1\sigma$ level. Before reconstruction from the CMASS correlation function we measure $\alpha = 1.016 \pm 0.017$, whereas from the power spectrum we measure $\alpha = 1.022 \pm 0.017$. After reconstruction, we measure $\alpha = 1.024 \pm 0.016$ from the correlation function and $\alpha = 1.042 \pm 0.016$ from the power spectrum. Our analysis of the mock catalogues

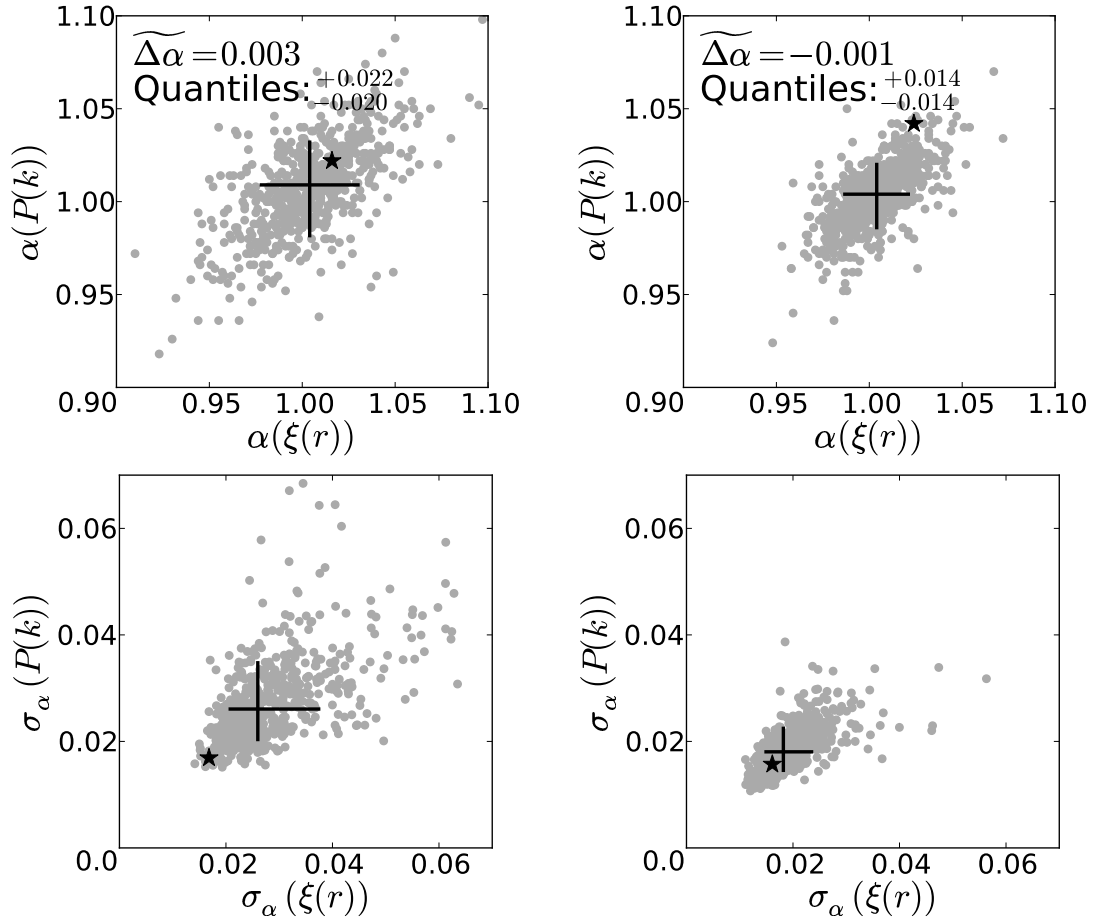


Figure 4.7: Comparison of acoustic scale measurements from $\xi(r)$ and $P(k)$. The left column shows the pre-reconstruction results and the right column shows the post-reconstruction results. The top panels show the values of α measured using $\xi(r)$ versus those measured using $P(k)$; the bottom panels show analogous plots for σ_α . The mock points are shown in grey and the CMASS point is overplotted as the black star. The black cross marks the median values of α or σ_α along with their quantiles. One can see that there is notable scatter between the values of α and σ_α measured from the two different statistics. For example, α from ξ and P vary by 0.014 after reconstruction.

suggests that this level of discrepancy is not unexpected. Figure 4.7 shows the values of α and σ_α measured from the mocks using $\xi(r)$ versus those measured using $P(k)$. The CMASS value is overplotted as the black star. One can see that the $\xi(r)$ and $P(k)$ α measures are correlated, but the scatter is quite large: $\sim 2.1\%$ before reconstruction and $\sim 1.4\%$ after reconstruction. In both cases the CMASS point falls within the locus of mock points and although in the post-reconstruction case, the star appears to lie at the edge of the mock locus, $\alpha_P - \alpha_\xi \sim 0.018$ is only $1.3\times$ the scatter.

The lower panels of Figure 4.7 show that the σ_α error estimates we obtain from χ^2 are comparable between $\xi(r)$ and $P(k)$. Hence, none of these statistics performs notably better than the other. This implies that both $P(k)$ and $\xi(r)$ return reasonable estimates of the acoustic scale. The discrepancy between $\xi(r)$ and $P(k)$ is then likely due to binning and the fact that we only consider these statistics over a finite domain. The noise from small scales and shot-noise enter differently into $\xi(r)$ and $P(k)$ in this case.

As is such, we choose to average the results from $\xi(r)$ and $P(k)$ to obtain our consensus distance measurement. Note that we only use the post-reconstruction result for our cosmological analysis. To estimate the errorbar on this value, we use the rms scatter (0.017) of $(\alpha_P + \alpha_\xi)/2$ from the post-reconstruction mocks. Figure 4.8 shows the distribution of these values from the mocks which appears very close to Gaussian. This is supported by the small D_n value which corresponds to a 96% certainty that these average α values are drawn from a Gaussian distribution. Since we expect our CMASS α measurement to be Gaussian, it is reasonable to use the rms scatter from the mocks as an estimate of the acoustic scale error in CMASS. Note that this 1.7% scatter is comparable to the 1.6% error measured on α from the post-reconstruction CMASS correlation function. It is also comparable to the 1.8%

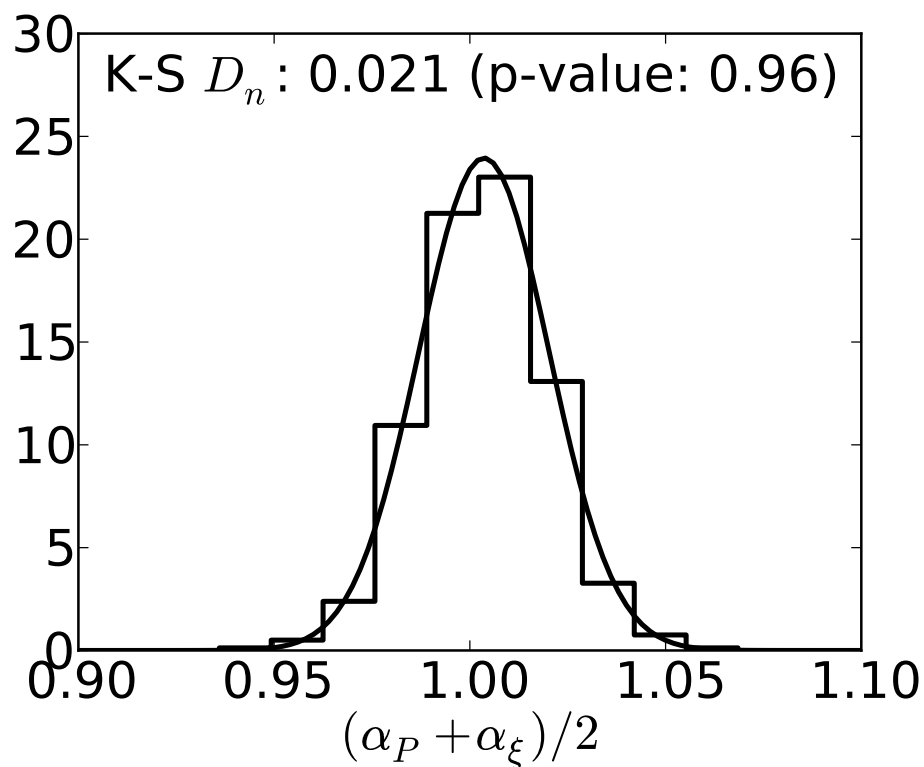


Figure 4.8: Histogram of averaged α values from $\xi(r)$ and $P(k)$ as measured from the post-reconstruction mocks. This distribution is very close to Gaussian. The near-zero K-S D_n value and the corresponding p-value indicate we are 96% certain that our α values are drawn from a Gaussian. This result justifies our using a Gaussian probability distribution for our CMASS distance measure based on the standard deviation of this distribution.

scatter measured from the correlation functions of the post-reconstruction CMASS mocks. Hence we adopt a consensus α measurement of 1.033 ± 0.017 . Given that $D_{V, fid}(z = 0.57) = 2027\text{Mpc}$ and $r_{s, fid} = 153.19\text{Mpc}$, our α measurement implies $D_V(z = 0.57)/r_s = 13.67 \pm 0.22$. This post-reconstruction distance measure is the CMASS contribution to the distance-redshift relation and will be used in conjunction with other datasets to constrain cosmological models in the next section.

4.5 Cosmological Implications

4.5.1 Comparison with Past Results

As mentioned in §4.1, there are now percent-level BAO distance measures (D_V) to many redshifts between $z = 0.1$ and $z = 0.6$. There has also been recent work in measuring relative luminosity distances (D_L) to the percent level at $z < 1$ using supernovae observations made by the 3-year Supernova Legacy Survey (SNLS3; Conley et al. 2011). In addition, Riess et al. (2011) has lately made a direct measurement of the Hubble constant H_0 using Hubble Space Telescope (HST) data with a $\sim 3\%$ errorbar. Combining these datasets now gives an extraordinarily well measured distance-redshift relation at $z \lesssim 1$. Observations of the Cosmic Microwave Background (CMB) at $z \sim 1000$ provides a high-redshift anchor for this relation. These measurements are provided by missions such as the Wilkinson Microwave Anisotropy Probe (WMAP; Bennett et al. 2003) which recently released its 7th year results (WMAP7; Jarosik et al. 2011).

It is particularly interesting to compare our current CMASS results with the SDSS-II DR7 LRG results presented in Chapter 3 (Padmanabhan et al., 2012a; Xu et al., 2012; Mehta et al., 2012). Although these two datasets have some minor overlap at $0.43 < z < 0.47$, we find that the overlapping volume is less than 9% of the CMASS effective (number density weighted) volume and less than 5% of

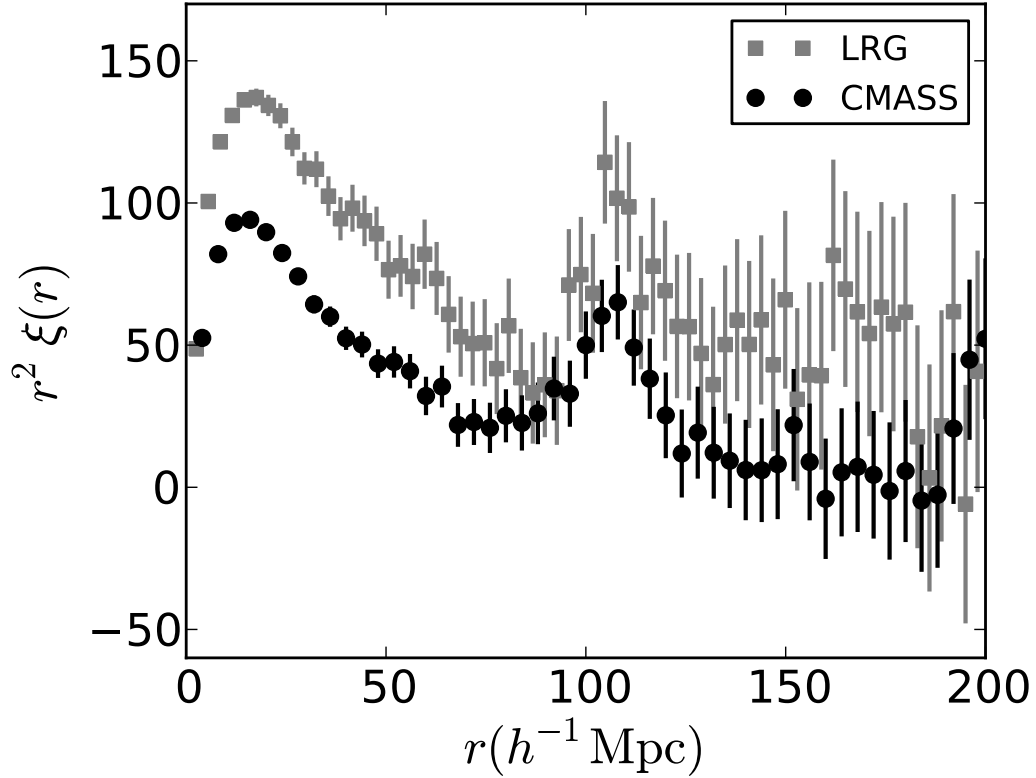


Figure 4.9: The post-reconstruction correlation function measured from CMASS data (black circles) versus that from SDSS-II LRG data (grey squares) as shown in Padmanabhan et al. (2012a). The vertical offset is due to the difference in galaxy bias between the samples. On average the SDSS-II LRGs are more luminous and reside in more massive halos. Since these 2 analyses used slightly different cosmologies, we have scaled the SDSS-II LRG points to match the fiducial cosmology of this paper. One can clearly see that the acoustic peak is located at the same position in both datasets. As an aside, we note that the difference in the size of the errors is due to 3 main effects. The first is that the CMASS sample is larger and the second is that the CMASS sample has a higher number density and hence less shot-noise. Lastly the CMASS sample uses $4h^{-1}\text{Mpc}$ bins, whereas the SDSS-II analysis uses $3h^{-1}\text{Mpc}$ bins, and the linear scaling of the vertical axis causes equal fractional errors to appear larger in the higher bias (LRG) sample.

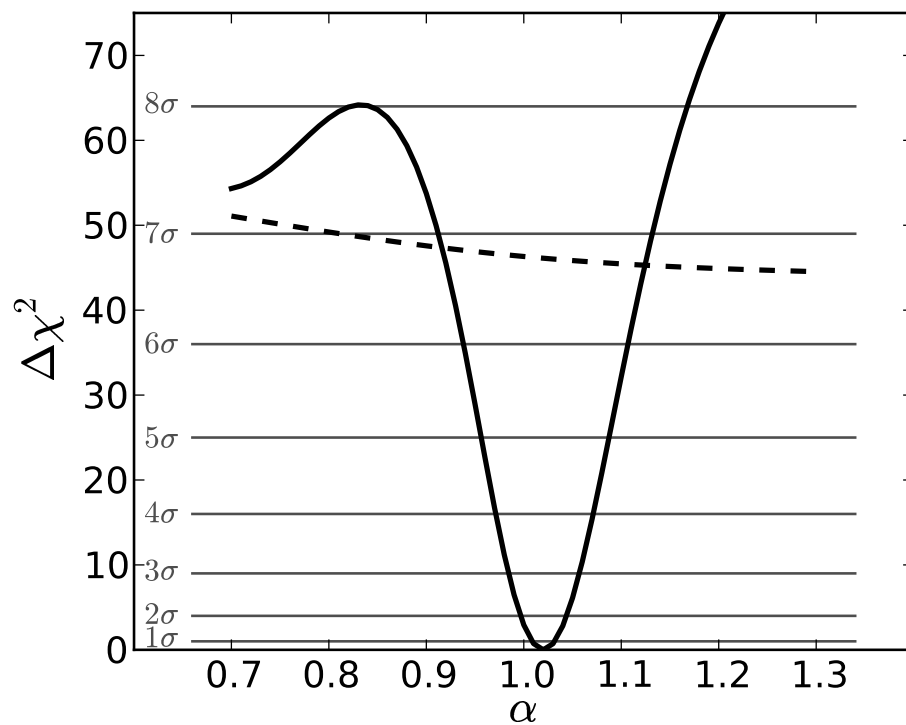


Figure 4.10: The total significance of the BAO feature, combining the CMASS and SDSS-II LRG results, both after reconstruction. This figure is analogous to Figure 4.3 and indicates that in the combined CMASS and LRG data sets, we have detected the acoustic peak at greater than 6.5σ , with a $\sim 8\sigma$ preference for the best-fit α .

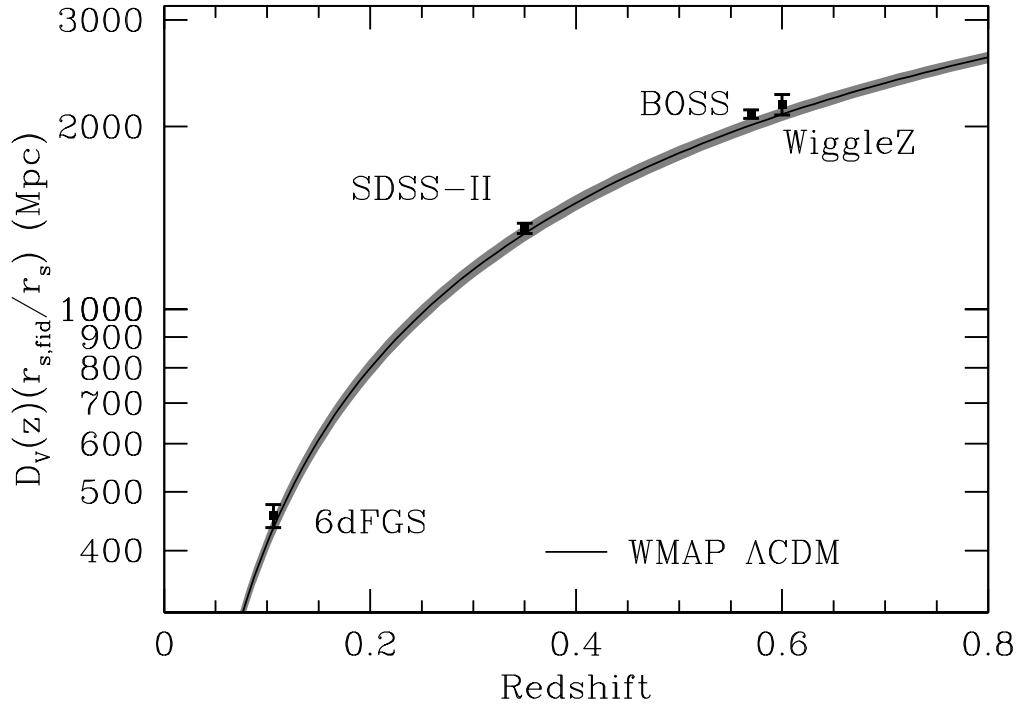


Figure 4.11: The distance-redshift relation as measured using the BAO method from various spectroscopic galaxy surveys. Note that the actual observable from BAO analyses is $D_V(z)/r_s$, so here we have multiplied all of these constraints by the sound horizon in our fiducial cosmology. At low redshift we have the 6dF measurement (Beutler et al., 2011) and at intermediate redshift we have the SDSS-II LRG measurement from Chapters 3 & 3 (Padmanabhan et al., 2012a; Xu et al., 2012; Mehta et al., 2012). The two higher redshift points correspond to the WiggleZ measurement (Blake et al., 2011a) and our new CMASS measurement. The overplotted line corresponds to the flat Λ CDM cosmology measured by WMAP7 (Komatsu et al., 2011). One can see that the BAO distance-redshift relation agrees remarkably well with the WMAP7 prediction.

the LRG effective volume. Hence for the analyses here, we will assume that these two datasets are independent. Figure 4.9 shows the post-reconstruction CMASS ($z = 0.57$) and LRG ($z = 0.35$) correlation functions in the same fiducial cosmology. The offset between the two is a result of differing galaxy bias and redshift. One can see that the alignment of the acoustic peaks is excellent, given the distance-redshift relation in the fiducial cosmology. Figure 4.10 shows the combined significance of the BAO detection in the CMASS plus LRG samples. This figure is identical to Figure 4.3 which shows the BAO detection significance for the CMASS sample only. A full description of what is plotted can be found there. One can see that in the combined dataset we detect the BAO at $\sim 6.5\sigma$ with the best-fit α preferred at $\sim 8\sigma$.

Figure 4.11 shows the distance-redshift relation in $D_V(z)$ versus z measured from various BAO analyses using spectroscopic data. We have included the recent 6dF result at low redshift (Beutler et al., 2011) and SDSS-II LRG result at intermediate redshift (Chapters 3 & 3; Padmanabhan et al. 2012a; Xu et al. 2012; Mehta et al. 2012). At the higher redshift end we have the WiggleZ point (Blake et al., 2011a) and our new CMASS point. Recall that BAO actually constrains $D_V(z)/r_s$. Here we have multiplied these constraints by the sound horizon in our fiducial cosmology to arrive at the plotted points. The overplotted curve corresponds to the flat Λ CDM cosmology measured by WMAP7 (Komatsu et al., 2011) and is *not* a fit to the data. The grey regions correspond to taking the 1σ ranges of $\Omega_m h^2$ and $\Omega_b h^2$ from WMAP7. One can see that there is clear agreement between the BAO measurements and a standard flat Λ CDM cosmology. However, the BAO distance-redshift relation tends to lie near the upper end of the 1σ errorbar from WMAP7. We also note the excellent agreement between our CMASS result and the WiggleZ result at nearly the same redshift, although the errorbar on our datapoint is a factor of 2.3 smaller.

Next we compare our CMASS distance measurement to supernova distance measures. Note that supernovae are used to measure the relative luminosity distance D_L as a function of redshift. Without a measure of the Hubble parameter which links the rungs of this relative distance ladder, the supernova distances cannot be directly compared to the BAO distance measures. However, using a Markov Chain Monte Carlo (see next section) approach it is possible to infer the ratios of $D_V(z)$ at different redshifts using supernova data. We use SNLS3 (Conley et al., 2011) plus CMB data from WMAP to measure these ratios for a cosmological model including spatial curvature and varying dark energy (i.e. $w(a) = w_0 + w_a(1 - a)$) (Chevallier & Polarski, 2001; Linder, 2003), where $w(a)$ is the equation of state of dark energy as a function of scale factor a). This is the most general cosmological model we can test.

The supernova data predict a D_V ratio between $z = 0.35$ and $z = 0.57$ of 0.6579 ± 0.0063 , which implies that $D_V(z = 0.35)/r_s = 8.99 \pm 0.14 \pm 0.09$ using our measured CMASS value of $D_V(z = 0.57)/r_s = 13.67 \pm 0.22$. The first error reflects the error on our CMASS distance measure and the second reflects the error in the distance ratio predicted by the supernova. The inferred $D_V(z = 0.35)/r_s$ value matches the SDSS-II LRG measurement of 8.88 ± 0.17 very well. Performing the same exercise for 6dF at $z = 0.1$ we find $D_V(0.1)/D_V(0.57) = 0.2018 \pm 0.0038$ from the supernova data. Combined with our CMASS measurement, this gives $D_V(z = 0.1)/r_s = 2.759 \pm 0.044 \pm 0.052$, in excellent agreement with the 6dF measurement of $D_V(z = 0.1)/r_s = 2.81 \pm 0.13$ (note that here we have scaled the 6dF result from $z = 0.106$ to $z = 0.1$).

Overall we see very good agreement between our CMASS distance measure and distance measures from other BAO analyses and supernova analyses. Since the BAO method returns absolute distance measures given a value of r_s , it provides leverage on

the Hubble parameter which is needed to calibrate the relative supernova distance scale. Hence the combination of these two datasets is particularly powerful for constraining cosmological parameters as will be shown in the next section.

4.5.2 Cosmological Parameters

The observed distance-redshift relation can be used to measure the values of cosmological parameters in a myriad of different cosmological models. Of particular interest are constraints on the behaviour of dark energy, which can be probed through measuring its equation of state w . In this section, we explore a number of cosmological models using various combinations of BAO and supernova distance measurements as well as direct measurements of H_0 . The BAO datasets we use are the current CMASS measurement, the SDSS-II LRG measurement at $z = 0.35$ (Padmanabhan et al., 2012a; Xu et al., 2012; Mehta et al., 2012) and the 6dF measurement at $z = 0.1$ (Beutler et al., 2011). We do not include the Percival et al. (2010) BAO measurement at $z = 0.275$ and the WiggleZ measurement at $z = 0.6$ (Blake et al., 2011a) due to their significant overlap with the LRG and CMASS samples respectively. However, as discussed previously these were in good agreement with the LRG and CMASS distance measures. For the supernova data we use the SNLS3 compilation (Conley et al., 2011) and for the direct measurement of H_0 we use the Riess et al. (2011) measurement. In addition, we use the 7-year WMAP CMB measurements (Jarosik et al., 2011) to anchor the distance-redshift relation at high redshift ($z \sim 1000$).

Our effort is aimed at exploring 6 major cosmological models. The most basic (and most restrictive) is the standard flat, constant dark energy Λ CDM model. We then open up additional directions in the parameter space by allowing the universe to have spatial curvature and/or allowing dark energy to deviate from a cosmological constant and vary in time. These are known as

1. ω CDM - allowing curvature
2. w CDM - allowing non-cosmological constant dark energy
3. ωw CDM - allowing curvature and non-cosmological constant dark energy
4. $w_0 w_a$ CDM - allowing non-cosmological constant and time-varying dark energy
5. $\omega w_0 w_a$ CDM - allowing curvature, and non-cosmological constant and time-varying dark energy.

The last of these is also known as the Dark Energy Task Force (DETF) cosmology and is currently the most general cosmological model. In the cases where we allow varying dark energy, we are effectively employing the parameterization $w(a) = w_0 + (1-a)w_a$ for the equation of state $w(a)$ as a function of scale factor a . The departure of dark energy from a standard cosmological constant model is encoded in any deviation of w_0 from -1 and the time dependence of dark energy is encoded in w_a . In a standard Λ CDM model, $w_0 = -1$ and $w_a = 0$.

We input the distance constraints from our datasets of interest to CosmoMC (Lewis & Bridle, 2002), a Markov Chain Monte Carlo code that maps the posterior probability distributions of the parameters that define a certain cosmological model. This is identical to the method employed by Mehta et al. (2012) to measure cosmological constraints from the SDSS-II LRG BAO distance measurement. Many of the numbers quoted in this section are taken directly from that analysis.

Table 4.3: Cosmological constraints from CMASS, LRG and other datasets. Column one shows the cosmological model and column 2 shows the datasets used. All remaining columns show parameter constraints from the posterior distribution. The quoted value is the mean of this distribution and the quoted error is the standard deviation (these are parenthesized and only show the changes to the last significant digits). Empty cells imply that the parameter was kept fixed at a fiducial value in the cosmological model, i.e. for flat models $\Omega_K = 0$, for spatially constant dark energy models $w_0 = -1$ and for time-constant dark energy models $w_a = 0$.

Model	Data Sets ¹	Ω_m	H_0 (km/s/Mpc)	Ω_K	w_0	w_a
Λ CDM	CMB	0.268(29)	71.0(26)	–	–	–
Λ CDM	CMB+CMASS	0.298(17)	68.4(13)	–	–	–
Λ CDM	CMB+LRG	0.280(14)	69.8(12)	–	–	–
Λ CDM	CMB+LRG+CMASS	0.293(12)	68.8(10)	–	–	–
Λ CDM	CMB+LRG+CMASS+6dF	0.293(12)	68.7(10)	–	–	–
Λ CDM	CMB+LRG+CMASS+SN	0.287(11)	69.2(10)	–	–	–
Λ CDM	CMB+LRG+CMASS+SN+6dF	0.288(11)	69.1(10)	–	–	–
oCDM	CMB	0.423(175)	60.0(123)	-0.039(44)	–	–
oCDM	CMB+CMASS	0.299(16)	67.0(15)	-0.008(5)	–	–
oCDM	CMB+LRG	0.278(15)	69.3(16)	-0.004(5)	–	–
oCDM	CMB+LRG+CMASS	0.288(12)	68.1(11)	-0.006(5)	–	–

Continued on next page

Table 4.3 – continued from previous page

Model	Data Sets ¹	Ω_m	H_0 (km/s/Mpc)	Ω_K	w_0	w_a
oCDM	CMB+LRG+CMass+6dF	0.288(12)	68.1(11)	-0.006(5)	–	–
oCDM	CMB+LRG+CMass+SN	0.284(12)	68.3(12)	-0.006(5)	–	–
oCDM	CMB+LRG+CMass+SN+6dF	0.284(12)	68.2(11)	-0.007(5)	–	–
w CDM	CMB	0.263(105)	75.4(138)	–	-1.12(41)	–
w CDM	CMB+CMass	0.323(43)	65.4(60)	–	-0.87(24)	–
w CDM	CMB+LRG	0.285(25)	69.0(39)	–	-0.97(17)	–
w CDM	CMB+LRG+CMass	0.294(27)	68.6(44)	–	-0.99(21)	–
w CDM	CMB+LRG+CMass+6dF	0.298(20)	67.8(31)	–	-0.95(15)	–
w CDM	CMB+LRG+CMass+SN	0.280(13)	70.8(18)	–	-1.09(8)	–
w CDM	CMB+LRG+CMass+SN+6dF	0.282(13)	70.4(17)	–	-1.08(8)	–
ow CDM	CMB+LRG+CMass	0.250(42)	74.1(70)	-0.008(5)	-1.31(34)	–
ow CDM	CMB+LRG+CMass+6dF	0.271(31)	70.5(43)	-0.007(6)	-1.14(23)	–
ow CDM	CMB+CMass+SN	0.280(17)	69.2(21)	-0.009(5)	-1.10(8)	–
ow CDM	CMB+LRG+CMass+SN	0.275(14)	69.8(18)	-0.007(5)	-1.09(8)	–

Continued on next page

Table 4.3 – continued from previous page

Model	Data Sets ¹	Ω_m	H_0 (km/s/Mpc)	Ω_K	w_0	w_a
ow CDM	CMB+LRG+CMass+SN+6dF	0.276(13)	69.6(17)	-0.008(5)	-1.09(8)	–
w_0w_a CDM	CMB+LRG+CMass	0.282(52)	70.7(68)	–	-1.11(51)	0.18(122)*
w_0w_a CDM	CMB+LRG+CMass+6dF	0.292(41)	68.9(48)	–	-1.02(42)	0.44(113)*
w_0w_a CDM	CMB+CMass+SN	0.281(17)	70.3(23)	–	-1.07(16)	-0.85(96)*
w_0w_a CDM	CMB+LRG+CMass+SN	0.280(14)	70.6(19)	–	-1.08(15)	0.10(87)
w_0w_a CDM	CMB+LRG+CMass+SN+6dF	0.281(14)	70.2(17)	–	-1.08(15)	0.08(81)
ow_0w_a CDM	CMB+LRG+CMass	0.263(54)	72.7(79)	-0.009(6)	-1.13(54)	-0.70(139)*
ow_0w_a CDM	CMB+LRG+CMass+6dF	0.284(40)	69.2(50)	-0.009(7)	-0.93(41)	-0.93(130)*
ow_0w_a CDM	CMB+CMass+SN	0.280(17)	69.5(21)	-0.012(6)	-0.91(17)	-1.31(102)*
ow_0w_a CDM	CMB+LRG+CMass+SN	0.277(14)	69.8(18)	-0.012(5)	-0.89(16)	-1.44(93)*
ow_0w_a CDM	CMB+LRG+CMass+SN+6dF	0.278(14)	69.5(17)	-0.012(5)	-0.88(15)	-1.40(94)*
ow_0w_a CDM	CMB+LRG+CMass+SN+H0	0.270(12)	71.1(15)	-0.010(5)	-0.93(16)	-1.46(95)*
ow_0w_a CDM	CMB+LRG+CMass+SN+H0+6dF	0.270(12)	70.8(14)	-0.010(5)	-0.93(16)	-1.39(96)*

¹ CMB+LRG values are taken directly from Mehta et al. (2012).

* Datasets allow chains to explore parameter space outside the $-3.0 \leq w_a \leq 2.0$ prior.

Our cosmological constraints for the various models listed above are summarized in Table 4.3. There is a slight degeneracy between Ω_m and H_0 in the standard Λ CDM cosmology if we only use the CMB data to constrain this model. This degeneracy is completely broken by adding either BAO or supernova (SN) data at low redshift. We see that the LRG and CMASS samples give similar errors on H_0 (± 1.2 km/s/Mpc and ± 1.3 km/s/Mpc respectively). The combined constraint (± 1.0 km/s/Mpc) gives a 1.4% measurement of H_0 . For comparison, the direct measurement of H_0 by Riess et al. (2011) has a 3.3% error.

The CMB-only constraint on the simple Λ CDM model is much better than the CMB-only constraints on the other models. This is because allowing spatial curvature or varying dark energy introduces degeneracies between these parameters and H_0 . In terms of the distance-redshift relation, at low redshifts allowing curvature offsets this relation and allowing variations in dark energy changes its shape. These differences can only be probed using low-redshift distance measures from BAO or SN. Hence, if we open up spatial curvature (o CDM) or allow varying dark energy (w CDM) in our cosmological model, we can use BAO or SN to break the degeneracy between these parameters and H_0 .

There is one key difference between using BAO data versus SN data. The SN distance ladder is calibrated on measurements of H_0 at low redshift and extends to higher redshifts, while the BAO distance ladder is actually inverted. It uses the sound horizon calibrated at $z \sim 1000$ from CMB observations and extends downwards to low redshift. As a result SN are more sensitive to dark energy and w since the transition between matter domination and dark energy domination occurs at low redshift $z \sim 2$. BAO on the other hand is more sensitive to curvature which is more important at high redshift. Hence combining CMASS and LRG BAO distance measures is more effective at breaking the degeneracy between Ω_K and H_0 in an

Λ CDM universe, reflected in the $\sim 25\%$ drop in error on H_0 when the CMASS and LRG results are combined.

We see from Table 4.3 that SN are very poor at constraining curvature in an Λ CDM universe as expected. This is reflected in the fact that the CMB+BAO+SN dataset does not improve the constraints on the various cosmological parameters over the CMB+BAO case. However, in the w CDM case, although BAO does not provide tight constraints on w , its degeneracy direction is different from SN. The CMB+BAO+SN constraints listed in the table actually show a slight improvement over the CMB+SN case. This is reflected in Figure 4.12, where the solid red (CMB+BAO+SN) 1σ contour is tighter than the dashed blue (CMB+SN) 1σ contour in the w_0 versus H_0 plane.

The different sensitivities of BAO and SN make them particularly good for constraining curvature and the equation of state in an ow CDM universe as illustrated in Figure 4.13. The BAO and SN degeneracies in the w_0 versus Ω_K plane are virtually perpendicular to each other. Hence, we can simultaneously constrain Ω_K and w_0 to high precision in this cosmological model. The CMB+BAO and CMB+SN contours are also moderately misaligned in the w_0 versus w_a plane for a w_0w_a CDM cosmology. Hence the combined constraints on w_0 and w_a from CMB+BAO+SN is an improvement over any single dataset.

The most generalized DETF cosmology cannot be constrained by BAO or SN separately due to the limited sensitivities of current data. Hence we combine the CMB, BAO and SN datasets to calculate the ‘‘Figure of Merit’’ (FoM), a recommended baseline comparison between dark energy experiments, that corresponds to the inverse of the area of the 95% contour in the w_0 versus w_a plane (Albrecht et al., 2006). Using CMB+LRG+SN+CMASS gives an FoM of 14.4, a noticeable improvement over the FoM of 11.5 from CMB+LRG+SN (Mehta et al., 2012). The

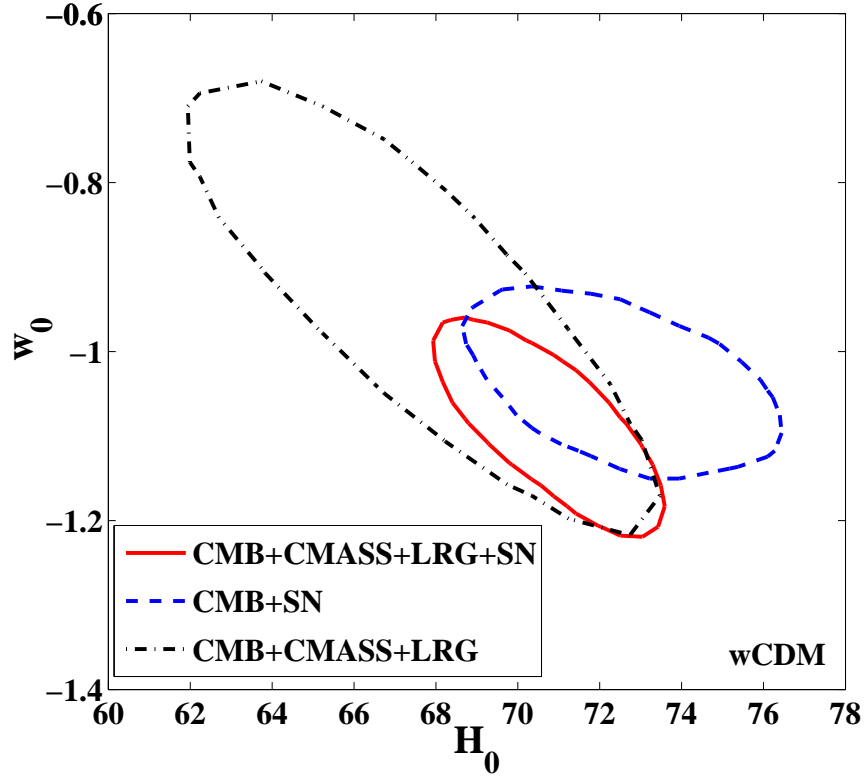


Figure 4.12: The 1σ contours in the w_0 versus H_0 plane for a w CDM universe. One can see that BAO alone is very poor at constraining the equation of state w_0 . This is because BAO is an inverse distance ladder calibrated on the acoustic scale measured from the CMB at $z \sim 1000$ and extended downwards to lower redshifts. Dark energy does not become dominant until $z \lesssim 2$ and hence is not well constrained by BAO distance measures. However the BAO degeneracy direction is not parallel to that of SN and hence the combined CMB+BAO+SN constraint (solid red contour) is better than the CMB+SN constraint (dashed blue contour) alone.

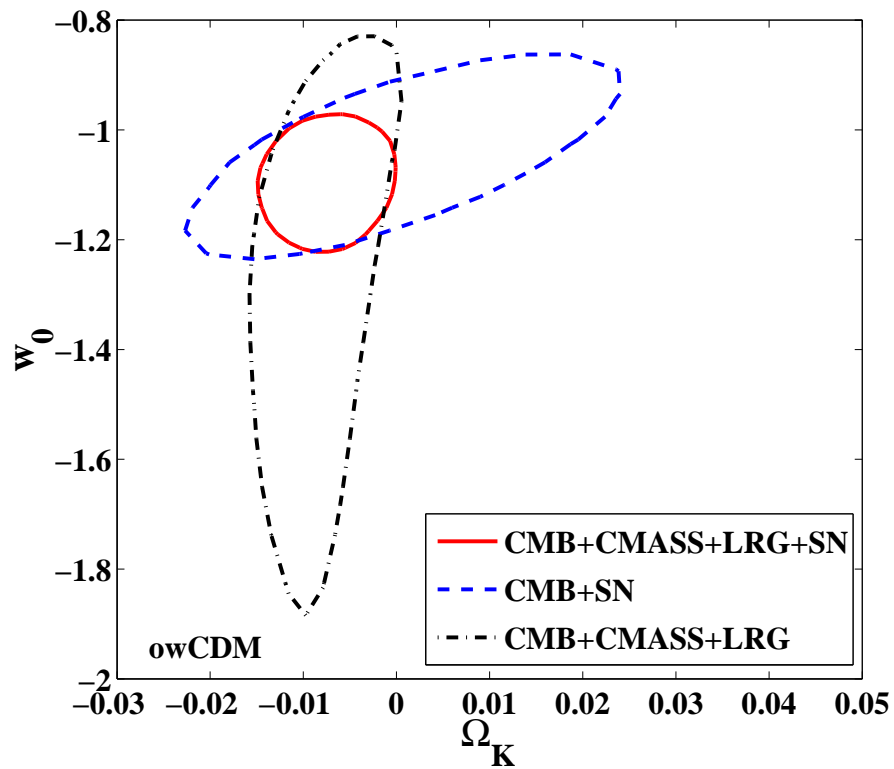


Figure 4.13: The 1σ contours in the w_0 versus Ω_K plane for an ow CDM universe. One can see that the degeneracy directions of the BAO and SN contours are almost orthogonal to each other. BAO is more constraining in Ω_K and SN is more constraining in w_0 . Combining the two gives particularly good constraints on Ω_K and w_0 simultaneously in an ow CDM universe.

contribution of our high precision CMASS BAO measurement in improving cosmological constraints is clear.

Lastly we plot our CMB+BAO+SN inferred values of H_0 for each of our 6 cosmological models and the Riess et al. (2011) direct measurement from HST ($H_0 = 73.8 \pm 2.4 \text{ km/s/Mpc}$) in Figure 4.14. One can see that the value of H_0 we measure is robust against changes in cosmological model. However, there appears to be a slight tension between our values and the Riess et al. (2011) value, albeit, at a statistically insignificant level ($\sim 1 - 2\sigma$). This is consistent with the BAO results of Beutler et al. (2011) & Mehta et al. (2012) using 6dF data and SDSS-II LRGs respectively. These H_0 values can be brought into better agreement with the introduction of additional relativistic species. This was first pointed out by Eisenstein & White (2004) who found that extra energy density in relativistic particles will cause CMB and BAO measurements to underestimate the values of $\Omega_m h^2$ and H_0 . Combining the CMB, BAO, SN and direct H_0 measurement, we find a best-fit energy density equivalent to 4.26 ± 0.56 neutrino species (recall that the standard model has 3.04). Improved measurements of the CMB power spectrum in the near future are expected to resolve this issue.

4.6 Conclusions

We have analyzed the BAO signal in the clustering of galaxies from the SDSS-III DR9 CMASS sample and obtained a 1.7% distance measure to $z = 0.57$. This is the most precise distance measure achieved using the BAO method to date.

The CMASS sample contains 264,283 massive galaxies covering 3275 deg^2 over a redshift range of $0.43 < z < 0.7$. This amounts to a number density of $\bar{n} \lesssim 3 \times 10^{-4} h^3 \text{ Mpc}^{-3}$. The CMASS sample is the largest sample of the universe ever surveyed at this high number density, making it ideal for BAO analysis.

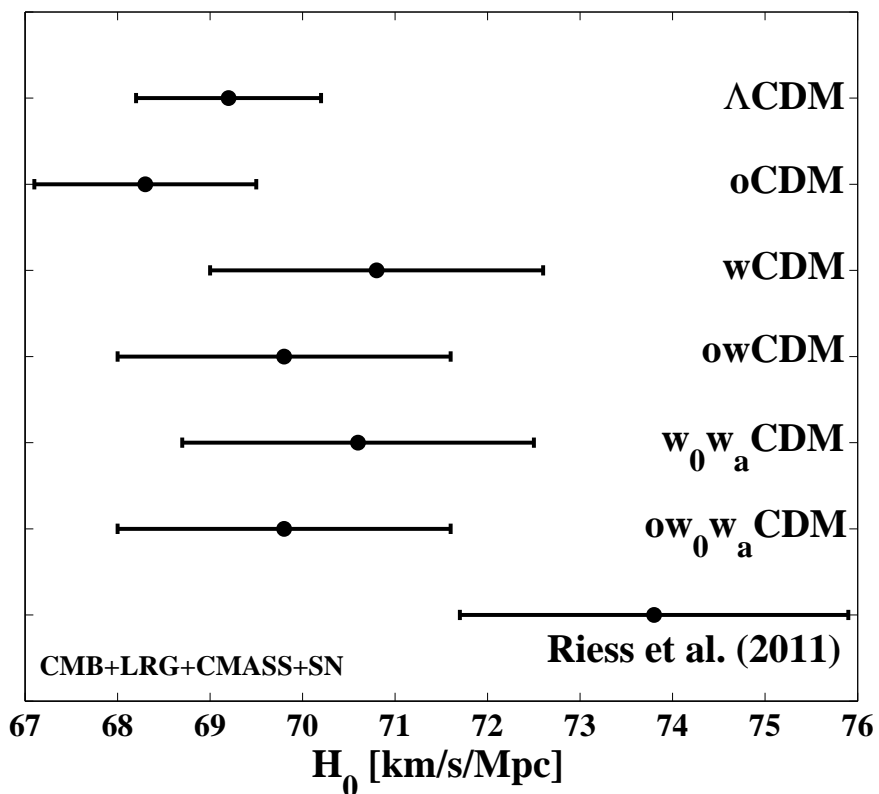


Figure 4.14: H_0 values inferred from our CMB+BAO+SN datasets versus the direct H_0 measurement from HST (Riess et al., 2011). The agreement between the H_0 values we measure is good between different cosmological models, however, there appears to be some slight tension with the direct measurement at the $1-2\sigma$ level. Introducing additional relativistic species can alleviate this tension, suggesting at a low significance that there may be an extra neutrino species.

We analyze the BAO signal in the correlation function calculated using the CMASS galaxies. We apply reconstruction (Eisenstein et al., 2007; Padmanabhan et al., 2012a) to partially undo the smearing of the BAO caused by large-scale flows that arise from non-linear structure growth and to remove large-scale redshift-space distortions. The former allows us to obtain a more precise centroiding of the acoustic peak and hence a better measurement of the acoustic scale. We measure the relative shift (α) in the acoustic peak between a fiducial cosmology and the data using the fitting technique presented in Xu et al. (2012). This can be trivially transformed into a measure of the spherically averaged distance $D_V(z)$ to redshift z given a value of the acoustic scale (which we can obtain from CMB measurements). We verify the robustness of our fitting and reconstruction techniques on 600 PTHalo mocks generated using second order Lagrangian perturbation theory (Manera et al., 2012). The covariance matrix used in our fitting is also calculated directly from these mocks.

We find that reconstruction does not significantly improve the precision of our CMASS BAO distance measurement. However, this is not unexpected in the context of the mocks. We find that 44 out of 600 mocks have post-to-pre-reconstruction error ratios that are larger than the CMASS value. Using the techniques mentioned above we measure the BAO scale to be $\alpha = 1.024 \pm 0.016$ from the post-reconstruction CMASS correlation function. We also find the significance of our CMASS BAO detection to be $\sim 5\sigma$ with the best-fit α value preferred at $\sim 6\sigma$.

A parallel analysis was also performed on the power spectrum which gave $\alpha = 1.042 \pm 0.016$ after reconstruction. We find that this $\sim 1\sigma$ tension between the $\xi(r)$ and $P(k)$ measurements is not unusual given the mocks. The different ways in which noise from small scales and shot-noise enter into $\xi(r)$ and $P(k)$, calculated via binning over a finite domain, is the likely culprit here. We therefore decide

to average our $\xi(r)$ and $P(k)$ distance measures to obtain a consensus value. We estimate the errorbar on this value as the rms of $(\alpha_P + \alpha_\xi)/2$ from the mocks. This distribution is very close to Gaussian and we expect the CMASS α measurement to be Gaussian as well. Hence the rms should be a reasonable estimate of the error. This resulted in a consensus $\alpha = 1.033 \pm 0.017$ which translates into a distance measure of $D_V(z = 0.57)/r_s = 13.67 \pm 0.22$.

We showed that the combined BAO detection significance of the CMASS sample and the LRG sample of Chapter 3 (Padmanabhan et al., 2012a; Xu et al., 2012; Mehta et al., 2012) is $> 6.5\sigma$. Plotting the CMASS and LRG BAO results along with other spectroscopic BAO distance measures from 6dF (Beutler et al., 2011) and WiggleZ (Blake et al., 2011a) reveals their mutual consistency. We also showed the consistency between the relative distance scale predicted by SNLS3 (Conley et al., 2011) and our BAO results. Combining all of these datasets and the CMB measurements from WMAP7 (Jarosik et al., 2011) predicts cosmological parameters consistent with a flat Λ CDM universe.

CHAPTER 5

MAPPING THE COSMIC EXPANSION HISTORY USING THE ANISOTROPIC
BARYON ACOUSTIC OSCILLATIONS SIGNAL IN SDSS DR7

We present the first measurement of isotropic dilation (α) and anisotropic warping (ϵ) of the sound horizon from the reconstructed density field derived from a galaxy redshift survey. This is done using the baryon acoustic oscillations (BAO) signal in the luminous red galaxy (LRG) sample from the 7th data release (DR7) of the Sloan Digital Sky Survey (SDSS), which has a median redshift of $z = 0.35$. We present the theoretical framework behind the anisotropic BAO signal and give a detailed account of the fitting model we use to extract this signal from the data. We apply density field reconstruction to partially remove the effects of non-linear evolution and redshift-space distortions in order to sharpen up the acoustic signal. The robustness of our reconstruction and fitting techniques are tested on 160 LasDamas DR7 mock catalogues. We find that our ability to measure the anisotropic warping, ϵ , from DR7 is only marginal. We measure $\alpha = 1.012 \pm 0.024$ and $\epsilon = -0.014 \pm 0.036$ after reconstruction. These translate into $D_A = 1050 \pm 38$ Mpc and $H = 84.4 \pm 7.1$ km/s/Mpc at $z = 0.35$ assuming a sound horizon of $r_s = 152.76$ Mpc. Our ϵ measurement is consistent with predictions from current datasets. The methods laid out in this work pave the path for future anisotropic BAO analyses using larger datasets such as SDSS DR9.

5.1 Introduction

In this chapter, we will use an extension of the baryon acoustic oscillations method, namely its anisotropic signature, to probe the cosmic expansion history. To use the BAO method, we must first measure the acoustic scale from the clustering of

galaxies. This is typically done in a statistical sense using the 2-point correlation function of galaxy separations or its Fourier transform, the power spectrum. Past BAO studies have primarily been focused on the spherically-averaged monopoles of these statistics (Cole et al., 2005; Eisenstein et al., 2005; Hütsi, 2006; Tegmark et al., 2006; Padmanabhan, White & Eisenstein, 2007; Kazin et al., 2010; Percival et al., 2010; Beutler et al., 2011; Blake et al., 2011a), which only allows us to measure the spherically-averaged distance $D_V(z) \propto D_A(z)^2/H(z)$, where z is the median redshift of the galaxy sample. This effectively assumes that the clustering of galaxies is isotropic. Most importantly, the Hubble parameter $H(z)$ is degenerate with $D_A(z)$ in this measure and hence we cannot directly probe the cosmic expansion history encoded by $H(z)$.

The clustering of galaxies, however, is not truly isotropic. Anisotropies arise from large-scale redshift-space distortions caused by the line-of-sight velocity of galaxies (Kaiser, 1987) and from assuming the wrong cosmology when calculating the 2-point statistics. This second point can be used to break the degeneracy between $H(z)$ and $D_A(z)$. One can imagine that if we assume the wrong cosmology, then the BAO will appear at slightly different locations along the line-of-sight and transverse directions because the line-of-sight distances are measured from redshifts and $H(z)$, whereas the transverse distances are measured using the angular separation and $D_A(z)$.

The use of such anisotropies to measure the cosmic expansion history was first proposed by Alcock & Paczynski (1979). In the case of the BAO, the anisotropy can be measured using the clustering signal along different directions (Okumura et al., 2008; Blake et al., 2011b; Chuang & Wang, 2011; Kazin, Sánchez & Blanton, 2012) or by looking at higher order multipoles of the 2-point statistics (Padmanabhan & White, 2008; Taruya, Saito & Nishimichi, 2011). If the clustering were isotropic, then all higher order multipoles should be zero, however, anisotropies introduce

power into the even multipoles. The second method listed above exploits this fact to measure the amount of anisotropy relative to some assumed fiducial cosmology. This can then be used to infer the values of $H(z)$ and $D_A(z)$ based on the fiducial values (see §5.2). Hence, we can directly measure the cosmic expansion history parameterized by $H(z)$.

In this chapter, we will focus on the multipole method and apply the technique described in Padmanabhan & White (2008) to the 7th data release (DR7) of the Sloan Digital Sky Survey (SDSS). We present the first application of this method to a galaxy redshift survey and thoroughly demonstrate its feasibility. We calibrate our covariance matrix and fitting model on 160 LasDamas mocks and perform detailed tests of the model to ensure its robustness. We also apply reconstruction, a technique for partially removing the effects of non-linear structure growth on the BAO (Eisenstein et al., 2007). This technique has been tested extensively on the monopole through simulations (Seo et al., 2008; Noh et al., 2009; Seo et al., 2010; Mehta et al., 2011) and has recently been applied to SDSS DR7 data (Padmanabhan et al., 2012a; Xu et al., 2012; Mehta et al., 2012). The current work takes a first look at how reconstruction affects the quadrupole and uses the measured anisotropy to infer $H(z)$ and $D_A(z)$ from the DR7 data.

After reconstruction we obtain a 3.6% measurement of $D_A(z)$ and an 8.4% measurement of $H(z)$ at $z = 0.35$. The large error on $H(z)$ reflects our marginal measurement of the anisotropic BAO signal parameterized by ϵ from the LRG dataset. However, with datasets containing more galaxies such as SDSS DR9, we should be able to directly apply the same methods outlined in this chapter to obtain much tighter constraints on ϵ and subsequently $D_A(z)$ and $H(z)$.

In §5.2 we present the theoretical background for the multipole method. In §5.3 we present our analysis techniques with emphasis on the intricacies of the fitting

model. §5.4 and §5.5 present our fitting results and detailed tests of our fitting model and reconstruction technique on the mocks and data respectively. We present the cosmological implications of our $D_A(z)$ and $H(z)$ measurements in §5.6 and conclude in §5.7. Note that the mock catalogues and DR7 dataset we use in this chapter are the same as those described in §3.2.

5.2 Theory

5.2.1 Background, Basics and Definitions

There are two main effects that give rise to anisotropic galaxy clustering. The first are redshift-space distortions, which arise due to the line-of-sight velocities of galaxies such as their peculiar motions within clusters (the Finger-of-God effect) or their coherent infall towards overdense regions (the Kaiser effect, Kaiser (1987)). These impart additional redshifts that affect our measurement of cosmological redshift and hence the line-of-sight separation between galaxies. In measures of galaxy clustering, these effects are broadband effects that vary smoothly with scale and affect the overall shape of the clustering statistic.

Anisotropic clustering can also arise if we assume the wrong cosmology when calculating the separations between galaxies, a necessary step in all measures of galaxy clustering. Since the distribution of matter is mostly isotropic at large scales, artificial anisotropies are introduced by calculating distances assuming the wrong cosmology as each cosmology predicts a unique distance scale. Specifically, we calculate line-of-sight distances using redshifts and the Hubble parameter $H(z)$ while transverse distances are calculated using the angular size of an object and the angular diameter distance $D_A(z)$. Both $H(z)$ and $D_A(z)$ are predicted given a set of cosmological parameters; however, if these do not match the true cosmology of the universe, we will measure different clustering signals along the line-of-sight and

transverse directions. This implies that the BAO signal in the line-of-sight direction will be slightly offset from its location in the transverse direction. This is a manifestation of the Alcock-Paczynski technique (Alcock & Paczynski, 1979), which uses the measured anisotropy in an object thought to be isotropic to constrain the true cosmology of the universe.

In the past, limited survey volume has made it difficult to analyze the differential clustering along the line-of-sight and transverse directions. As a result, most BAO analyses have been based on the spherically-averaged (i.e. monopole) clustering statistics (e.g. Percival et al. (2010) and Padmanabhan et al. (2012a)), which only allow us to measure $D_V(z)$, the spherically-averaged distance to redshift z . This quantity is defined as

$$D_V(z) = \left[(1+z)^2 D_A^2(z) \frac{cz}{H(z)} \right]^{1/3} \quad (5.1)$$

which corresponds to 2 powers of $D_A(z)$ from our transverse distance measure along the 2 transverse directions on the sky and 1 power of $H(z)$ from our line-of-sight distance measure. However, with anisotropic measurements, we will be able to break this degeneracy between $D_A(z)$ and $H(z)$, and measure these two quantities separately.

To measure the anisotropy, we must derive a clustering model that includes a parameterization of the anisotropic signal. We can then fit this model to the data and measure this parameter. Essentially one is presented with 2 choices. The first is to perform fits to the transverse and radial correlation functions (e.g. Okumura et al. (2008)) and the second is to simultaneously fit the monopole and higher order multipoles of the clustering statistics (Padmanabhan & White, 2008). If clustering were perfectly isotropic then the higher multipoles would all be zero, however, any anisotropic signal bleeds power into the even order multipoles.

In this work, we will present the formalism for the multipole method based on the

work of Padmanabhan & White (2008). We note that the BAO can additionally be shifted in an isotropic manner if the assumed cosmology is not the true cosmology. Isotropic shifts also occur due to non-linear structure growth. We define the isotropic shift in BAO position as

$$\alpha = \frac{D_V(z)/r_s}{D_{V,f}(z)/r_{s,f}} \quad (5.2)$$

$$= \left[\frac{D_A^2(z)}{D_{A,f}^2(z)} \frac{H_f(z)}{H(z)} \right]^{1/3} \frac{r_{s,f}}{r_s} \quad (5.3)$$

where D_V is defined as above and r_s is the sound horizon (BAO scale). The f subscripts correspond to the fiducial cosmology used in the fitting template and in calculating the clustering statistic. This parameterization has been used extensively in past BAO studies focusing on the monopole.

We parameterize the anisotropic BAO signal as ϵ

$$1 + \epsilon = \left[\frac{H_f(z)}{H(z)} \frac{D_{A,f}(z)}{D_A(z)} \right]^{1/3}. \quad (5.4)$$

These parameterizations of α and ϵ are derived from isotropic coordinate dilations and anisotropic coordinate warpings between the true and fiducial cosmology spaces (see Equations (5.12) & (5.13)). Combining Equations (5.3) & (5.4), we arrive at

$$\frac{D_A(z)}{r_s} = \frac{\alpha}{1 + \epsilon} \frac{D_{A,f}(z)}{r_{s,f}} \quad (5.5)$$

$$H(z)r_s = \frac{1}{\alpha(1 + \epsilon)^2} H_f(z)r_{s,f}. \quad (5.6)$$

By measuring both the isotropic and anisotropic BAO shifts, we can separately constrain the angular diameter distance $D_A(z)$ and the Hubble parameter $H(z)$ at the median redshift of our galaxy sample z . If we denote the errorbars on α and ϵ as σ_α and σ_ϵ , and the covariance between them as $\sigma_{\alpha\epsilon}$, then the errorbars on $D_A(z)$ and $H(z)$ can be calculated as

$$\begin{pmatrix} \sigma_{D_A}^2 & \sigma_{D_A H} \\ \sigma_{D_A H} & \sigma_H^2 \end{pmatrix} = \begin{pmatrix} \frac{\partial D_A}{\partial \alpha} & \frac{\partial H}{\partial \alpha} \\ \frac{\partial D_A}{\partial \epsilon} & \frac{\partial H}{\partial \epsilon} \end{pmatrix} \begin{pmatrix} \sigma_\alpha^2 & \sigma_{\alpha\epsilon} \\ \sigma_{\alpha\epsilon} & \sigma_\epsilon^2 \end{pmatrix} \begin{pmatrix} \frac{\partial D_A}{\partial \alpha} & \frac{\partial H}{\partial \alpha} \\ \frac{\partial D_A}{\partial \epsilon} & \frac{\partial H}{\partial \epsilon} \end{pmatrix}^T. \quad (5.7)$$

This yields,

$$\frac{\sigma_{D_A}^2}{D_A^2} = \alpha^{-2}\sigma_\alpha^2 + (1 + \epsilon)^{-2}\sigma_\epsilon^2 - 2\alpha^{-1}(1 + \epsilon)^{-1}\sigma_{\alpha\epsilon} \quad (5.8)$$

$$\frac{\sigma_H^2}{H^2} = \alpha^{-2}\sigma_\alpha^2 + 4(1 + \epsilon)^{-2}\sigma_\epsilon^2 + 4\alpha^{-1}(1 + \epsilon)^{-1}\sigma_{\alpha\epsilon}. \quad (5.9)$$

We will also need a method for distinguishing between anisotropies introduced by redshift-space distortions into the broadband shape of our clustering statistic and those introduced through assuming the wrong cosmology (i.e. the Alcock-Paczynski signal). There exist simple redshift-space distortion models that can be used if we are only interested in analyzing the anisotropy in the BAO signal and not the details of the redshift-space distortions themselves. Any residual inadequate matching between these models and the actual broadband shape of the data can be mostly compensated by including a few additional marginalization terms (Seo et al., 2008; Xu et al., 2012) such as Equation (5.50) described in §5.3.3.

5.2.2 Formalism for the Correlation Function

The clustering of galaxies can be measured using the correlation function $\xi(r)$, the power spectrum $P(k)$ or $\omega_\ell(r_s)$, a band-filtered statistic optimized to pick out the acoustic information in $\xi(r)$ or $P(k)$ (Xu et al., 2010). Since our analysis will focus on the correlation function, we will present the formalism for configuration space here and state the analogue for the power spectrum in Fourier space, which can also be found in Padmanabhan & White (2008).

We begin with a few basic coordinate definitions,

$$r^2 = r_{\parallel}^2 + r_{\perp}^2 \quad (5.10)$$

$$\mu^2 = \cos^2 \theta = \frac{r_{\parallel}^2}{r^2} \quad (5.11)$$

where r is the separation between 2 galaxies and θ is the angle between a galaxy pair and the line-of-sight direction. In the following, unprimed coordinates will denote

the fiducial cosmology space and primed coordinates will denote the true cosmology space.

The dilation (α) and warping (ϵ) parameters are then defined by

$$r'_{\parallel} = \alpha(1 + \epsilon)^2 r_{\parallel} \quad (5.12)$$

$$r'_{\perp} = \alpha(1 + \epsilon)^{-1} r_{\perp}. \quad (5.13)$$

Substituting Equations (5.12) & (5.13) into the definitions of r' and μ' as in Equations (5.10) & (5.11), we see that

$$\begin{aligned} r' &= \alpha \sqrt{(1 + \epsilon)^4 r_{\parallel}^2 + (1 + \epsilon)^{-2} r_{\perp}^2} \\ &= \alpha r [1 + 2\epsilon L_2(\mu)] \end{aligned} \quad (5.14)$$

where in the last line we have substituted the second order Legendre polynomial $L_2(\mu) = (3\mu^2 - 1)/2$. Also,

$$\begin{aligned} \mu'^2 &= \frac{\alpha^2(1 + \epsilon)^4 r_{\parallel}^2}{\alpha^2(1 + \epsilon)^4 r_{\parallel}^2 + \alpha^2(1 + \epsilon)^{-2} r_{\perp}^2} \\ &= \mu^2 + 6\epsilon(\mu^2 - \mu^4) \end{aligned} \quad (5.15)$$

where in the last line we have only kept terms up to first order in ϵ .

The true 2D correlation function $\xi(\vec{r}')$ can be Legendre decomposed into multipole moments as

$$\xi(\vec{r}') = \sum_{\ell'=0}^{\infty} \xi_{\ell'}(r') L_{\ell'}(\mu') \quad (5.16)$$

where the $L_{\ell'}(\mu')$ are Legendre polynomials of order ℓ' . Again, if clustering were perfectly isotropic the $\ell > 0$ moments would all be zero. Anisotropy introduces power into the even order multipoles. We can substitute Equation (5.14) into $\xi_{\ell'}(r')$ and Equation (5.15) into $L_{\ell'}(\mu')$ and write

$$\begin{aligned} \xi(\vec{r}') &= \sum_{\ell'=0}^{\infty} \left[\xi_{\ell'}(\alpha r) + 2\epsilon L_2(\mu) \frac{d\xi_{\ell'}(\alpha r)}{d \log(r)} \right] \\ &\quad \cdot \left[L_{\ell'}(\mu) + 3\epsilon \mu(1 - \mu^2) \frac{dL_{\ell'}(\mu)}{d\mu} \right], \end{aligned} \quad (5.17)$$

where we have made a Taylor expansion in both large brackets.

Finally, in the fiducial cosmology space, we measure the multipole moments

$$\begin{aligned}
\xi_\ell(r) &= \frac{2\ell+1}{2} \int_{-1}^1 \xi(\vec{r}') L_\ell(\mu) d\mu & (5.18) \\
&= \xi_\ell(\alpha r) \\
&\quad + 3\epsilon \left[\frac{-\ell(\ell-1)(\ell-2)}{(2\ell-3)(2\ell-1)} \xi_{\ell-2}(\alpha r) \right. \\
&\quad + \frac{\ell(\ell+1)}{(2\ell-1)(2\ell+3)} \xi_\ell(\alpha r) \\
&\quad \left. + \frac{(\ell+1)(\ell+2)(\ell+3)}{(2\ell+3)(2\ell+5)} \xi_{\ell+2}(\alpha r) \right] \\
&\quad + 2\epsilon \left[\frac{3\ell(\ell-1)}{2(2\ell-3)(2\ell-1)} \frac{d\xi_{\ell-2}(\alpha r)}{d \log(r)} \right. \\
&\quad + \frac{\ell(\ell+1)}{(2\ell-1)(2\ell+3)} \frac{d\xi_\ell(\alpha r)}{d \log(r)} \\
&\quad \left. + \frac{3(\ell+1)(\ell+2)}{2(2\ell+3)(2\ell+5)} \frac{d\xi_{\ell+2}(\alpha r)}{d \log(r)} \right], & (5.19)
\end{aligned}$$

where we have used the recursion relation for Legendre polynomials

$$(\ell+1)L_{\ell+1}(\mu) = (2\ell+1)\mu L_\ell(\mu) - \ell L_{\ell-1}(\mu), \quad (5.20)$$

the derivative relation

$$\frac{dL_\ell(\mu)}{d\mu} = \frac{(\ell+1)[\mu L_\ell(\mu) - L_{\ell+1}(\mu)]}{1-\mu^2} \quad (5.21)$$

and the orthonormality of Legendre polynomials

$$\int_{-1}^1 L_\ell(\mu) L_{\ell'}(\mu) d\mu = \delta_{\ell\ell'}. \quad (5.22)$$

Here, $\delta_{\ell\ell'}$ is the delta function. Since we measure the correlation function using our choice of fiducial cosmology, Equation (5.19) will form the basis of our fitting template for extracting the isotropic dilation (α) and the anisotropic warping (ϵ) signal from the data.

The same relations can be derived in Fourier space from the definitions (Padmanabhan & White, 2008)

$$k'_{\parallel} = \alpha^{-1}(1 + \epsilon)^{-2}k_{\parallel} \quad (5.23)$$

$$k'_{\perp} = \alpha^{-1}(1 + \epsilon)k_{\perp}. \quad (5.24)$$

The final equation for the measured multipole moments is identical to the configuration space case except $\xi_{\ell}(r) \rightarrow P_{\ell}(k)$ and the sign on each occurrence of ϵ is flipped.

5.2.3 The Anisotropic Signal

Although anisotropic information exists in all higher order multipoles, its magnitude decreases considerably. Hence, for the purposes of this study, we will only focus on the monopole ($\ell = 0$) and the quadrupole ($\ell = 2$). The monopole and quadrupole we expect to measure according to Equation (5.19) are

$$\xi_0(r) = \xi_0(\alpha r) + \frac{2}{5}\epsilon \left[3\xi_2(\alpha r) + \frac{d\xi_2(\alpha r)}{d \log(r)} \right] \quad (5.25)$$

$$\begin{aligned} \xi_2(r) = & 2\epsilon \frac{d\xi_0(\alpha r)}{d \log(r)} + \left(1 + \frac{6}{7}\epsilon \right) \xi_2(\alpha r) + \frac{4}{7}\epsilon \frac{d\xi_2(\alpha r)}{d \log(r)} \\ & + \frac{4}{7}\epsilon \left[5\xi_4(\alpha r) + \frac{d\xi_4(\alpha r)}{d \log(r)} \right], \end{aligned} \quad (5.26)$$

and will form the basis of our analysis. Here, $\xi_4(r)$ is the hexadecapole ($\ell = 4$).

Figure 5.1 shows variations of the expected monopole (Equation (5.25)), the transverse and radial correlation functions, and the quadrupole (Equation (5.26)) with ϵ for a linear theory based model. The transverse and radial correlation functions were calculated as $\xi_0 + L_2(\mu)\xi_2$ for $\mu = 1$ and 0 respectively. Note that taking the difference between these yields the quadrupole. We have included anisotropic large-scale redshift-space distortions (the Kaiser effect) so that the quadrupole becomes non-zero, but not the Finger-of-God effect. One can see that the sensitivity

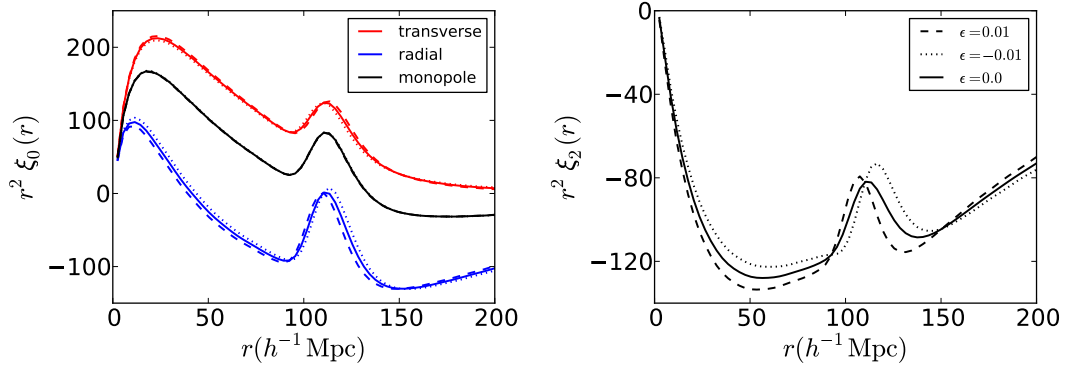


Figure 5.1: The monopole (left) and quadrupole (right) we expect to measure in the presence of anisotropic clustering for a linear theory based model including the Kaiser effect. The Kaiser effect gives rise to the BAO bump near $110h^{-1}\text{Mpc}$ in the quadrupole. ϵ parameterizes the amount of Alcock-Paczynski anisotropy, which, if there was none, would be equal to 0. The left panel shows the spherically-averaged monopole (black), the transverse correlation function (red) and the radial correlation function (blue), where the difference between these latter two yields a measurement of the quadrupole. Solid, dashed and dotted lines are defined as in the plot legend of the right panel which shows the spherically-averaged quadrupole. One can see that the spherically-averaged monopole is insensitive to ϵ . However, ϵ works to vary the position of the line-of-sight and transverse BAO features with the line-of-sight having a more prominent shift. The anisotropic nature of these shifts moves the BAO in the quadrupole. Hence, we expect the quadrupole to be sensitive to any anisotropic BAO signal.

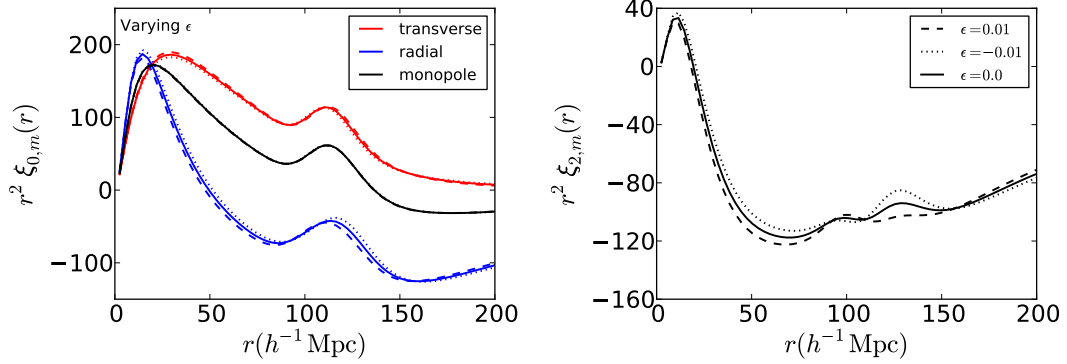


Figure 5.2: Variation of monopole and quadrupole models including the Kaiser effect and a full non-linear treatment of FoG and anisotropic Σ_{nl} . The solid black line in this and the similar plots following always corresponds to the fiducial model parameters $\Sigma_{\perp} = 6h^{-1}\text{Mpc}$, $\Sigma_{\parallel} = 10h^{-1}\text{Mpc}$ and $\Sigma_s = 4h^{-1}\text{Mpc}$ with $\beta = 0.35$ (center of the β prior in our fits). The monopole is again affected very little by ϵ . The fiducial quadrupole model picks up a crest-trough-crest structure at the BAO scale due to the differential broadening of the line-of-sight and transverse BAO signals the redshift-space distortions. We again see that ϵ works to shift the location of the quadrupole BAO. In addition, it can adjust the relative amplitude of the crests. This shifting of the BAO in the quadrupole but not in the monopole is only possible through changing ϵ . Note that the quadrupole BAO feature is much weaker in this more realistic non-linear model.

of the monopole to ϵ is quite low. However ϵ does cause slight shifts in the BAO position in the line-of-sight and transverse correlation functions. The shift in the radial direction is larger than that in the transverse direction which causes the BAO feature in the quadrupole at $\sim 110h^{-1}\text{Mpc}$ to shift with ϵ . Hence we see that the quadrupole can be used to obtain a measurement of the anisotropic BAO signal via ϵ .

5.2.4 A Non-linear Model

In Figure 5.1 discussed in the previous section, we have assumed linear theory including Kaiser effect models for $\xi_0(r)$ and $\xi_2(r)$. However, in order to model actual observations with fidelity, we must also account for the Finger-of-God (FoG) effect and non-linear structure growth. This section details a plausible model that includes all of these effects and will be used in our fitting procedure described in §5.3.3 to measure α and ϵ .

In Fourier space we can write the following template for the 2D non-linear power spectrum

$$P_t(k, \mu) = (1 + \beta\mu^2)^2 F(k, \mu, \Sigma_s) P_{dw}(k, \mu) \quad (5.27)$$

where

$$F(k, \mu, \Sigma_s) = \frac{1}{(1 + k^2\mu^2\Sigma_s^2)^2} \quad (5.28)$$

corresponds to a streaming model for the Finger-of-God effect and the $(1 + \beta\mu^2)^2$ term corresponds to the Kaiser model for large-scale redshift-space distortions. Here Σ_s is the streaming scale and is typically $\sim 3 - 4h^{-1}\text{Mpc}$.

The de-wiggled power spectrum $P_{dw}(k, \mu)$ is defined as

$$\begin{aligned} P_{dw}(k, \mu) &= [P_{lin}(k) - P_{nw}(k)] \\ &\cdot \exp \left[- \frac{k^2\mu^2\Sigma_{\parallel}^2 + k^2(1 - \mu^2)\Sigma_{\perp}^2}{2} \right] + P_{nw}(k) \end{aligned} \quad (5.29)$$

where $P_{lin}(k)$ is the linear theory power spectrum, $P_{nw}(k)$ is a power spectrum without an acoustic signature (Eisenstein & Hu, 1998) and $\Sigma_{nl}^2 = (\Sigma_{\parallel}^2 + \Sigma_{\perp}^2)/2$ is the standard Gaussian damping of the BAO used to model the degradation of the signal due to non-linear structure growth (Eisenstein, Seo & White, 2007). Here we have split this damping into transverse and line-of-sight components since it is anisotropic due to the Kaiser effect.

The multipoles of this template are then

$$P_{\ell,t}(k) = \frac{2\ell + 1}{2} \int_{-1}^1 P_t(k, \mu) L_{\ell}(\mu) d\mu, \quad (5.30)$$

which can be transformed to configuration space using

$$\xi_{\ell,t}(r) = i^{\ell} \int \frac{k^3 d \log(k)}{2\pi^2} P_{\ell,t}(k) j_{\ell}(kr). \quad (5.31)$$

Figure 5.2 shows the variation of our non-linear monopole and quadrupole models with ϵ while Figures 5.3, 5.4 & 5.5 shows the variations with other parameters. The variation with α is not shown as its role is well understood: α works to shift the BAO feature around equally in both the monopole and quadrupole. Figure 5.3 shows the variations with Σ_{\perp} and Σ_{\parallel} . Figure 5.4 shows the variations with Σ_s and Figure 5.5 shows the variations with β . In these plots, the solid black line always corresponds to the fiducial model parameters $\Sigma_{\perp} = 6h^{-1}\text{Mpc}$, $\Sigma_{\parallel} = 10h^{-1}\text{Mpc}$ and $\Sigma_s = 4h^{-1}\text{Mpc}$. β is set to the center of the prior, 0.35, unless indicated otherwise. These fiducial parameters will be discussed in more detail in §5.3.3.

We see that the spherically-averaged monopole model is only weakly affected by varying these parameters. Σ_{nl} has an immediately obvious effect on the BAO peak since it is designed to damp the BAO to model non-linear evolution. The change in the peak is only significant with a large change in Σ_{nl} . The $\Sigma_{\perp} = \Sigma_{\parallel} = 8h^{-1}\text{Mpc}$ case and the fiducial case have very similar Σ_{nl} values. Hence, we see little difference between the monopole models in these 2 cases. However, the $\Sigma_{\perp} = 4h^{-1}\text{Mpc}$,

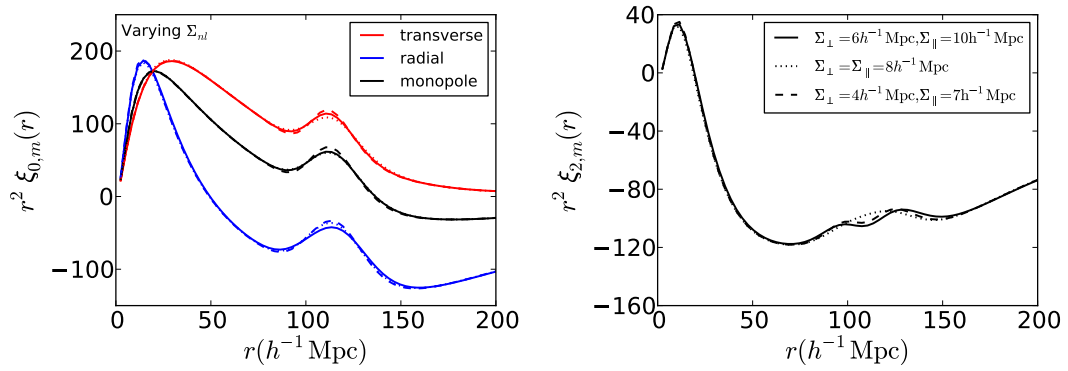


Figure 5.3: Variation of the monopole and quadrupole models with Σ_{\perp} and Σ_{\parallel} . The monopole BAO peak in can be affected by Σ_{nl} as expected since this parameter is used to model the smearing of the BAO due to non-linear structure growth. In these plots we have demonstrated the effects of going to an isotropic Σ_{nl} of roughly the same magnitude as the fiducial case (dotted line) and a smaller Σ_{nl} (dashed line). We see that going to an isotropic Σ_{nl} has little effect on the monopole, however, it completely eliminates the trough feature at the BAO scale in the quadrupole. Going to a smaller Σ_{nl} makes the peak appear sharper in the monopole as expected. In the quadrupole, it alters the structure of the peaks and reduces the crest-trough contrast.

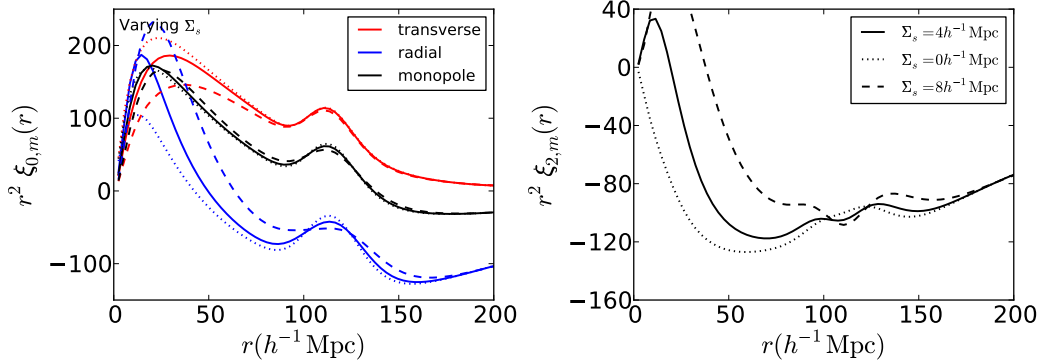


Figure 5.4: Variation of the monopole and quadrupole models with Σ_s . The BAO feature in the monopole can be slightly broadened by a large Σ_s . In the quadrupole, the effects of Σ_s are partially degenerate with Σ_{nl} in that it can alter the crest-trough contrast and can also completely eliminate the trough ($\Sigma_s = 0 h^{-1}$ Mpc). However, the effects of Σ_s are much stronger at small scales due to its large influence on the radial and transverse correlation functions, giving us leverage on this parameter. These variations are not surprising since the FoG effect is most pronounced at smaller scales.

$\Sigma_{\parallel} = 7 h^{-1}$ Mpc case corresponds to $\Sigma_{nl} \sim 6 h^{-1}$ Mpc which affords a weaker smearing of the peak. Large Σ_s values can also weakly damp the monopole BAO, causing slight modifications to its shape. β appears to have little affect on the monopole and ϵ has no affect. The only parameter that can shift the monopole BAO position is α , which also shifts the quadrupole BAO equally.

Looking at the quadrupole model in the fiducial case, we see that the BAO (at $r \sim 110 h^{-1}$ Mpc) looks different to the linear theory including Kaiser case presented in Figure 5.1. In that case, we saw a single bump at the acoustic scale due to the Kaiser anisotropy $(1 + \beta\mu^2)^2$. Including FoG and anisotropic Σ_{nl} introduces more structure at the BAO scale. We see that in the fiducial model, a dip has appeared at the center of the linear-theory peak, creating a crest-trough-crest structure. This is the result of anisotropic Σ_{nl} , Σ_s and β differentially broadening the BAO peak in the radial and line-of-sight directions. We see that the radial BAO is wider than

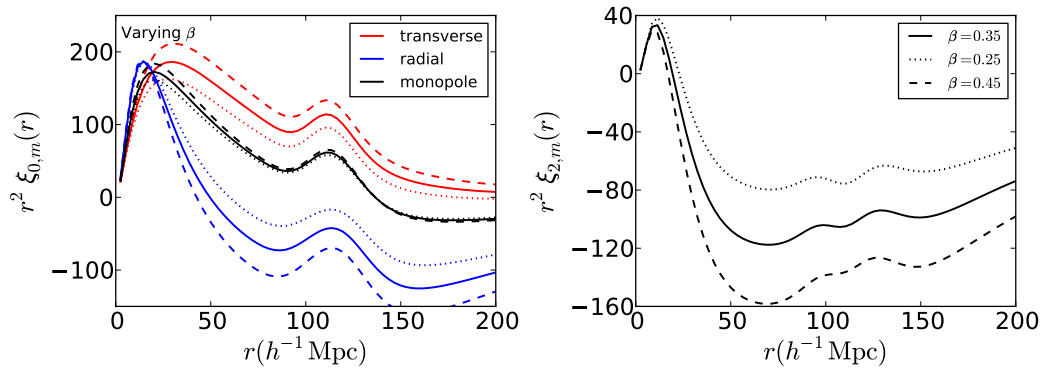


Figure 5.5: Variation of the monopole and quadrupole models with β . Again we see that the monopole is not significantly affected by β . The line-of-sight and transverse correlation functions experience large changes in amplitude leading to the quadrupole model having similarly large changes, especially near the acoustic scale. This is expected since β is used to model the large-scale redshift-space distortions. Such amplitude changes are not degenerate with any of the other parameters. Comparing the behaviour of Σ_{nl} , Σ_s and β to ϵ (Figure 5.2) indicates that these model parameters have mostly different effects on the quadrupole. While all of these parameters can affect the shape and/or magnitude of the quadrupole BAO, only ϵ can change its position separately from the monopole BAO (α changes both in lock-step). Hence we expect that the effects of ϵ should be detectable.

the transverse BAO, but the radial BAO peak has more contrast. Subtracting the two therefore yields the observed crest-trough-crest shape of the quadrupole near the BAO.

Varying Σ_{\perp} , Σ_{\parallel} , Σ_s and β all change the shape of the line-of-sight and transverse BAO signals but do not change their positions. Since the quadrupole is the difference between these two, we see that these parameters can only affect the shape of the quadrupole BAO. Figure 5.3 shows that changing Σ_{\perp} and Σ_{\parallel} gives rise to crests and troughs near the BAO scale. Taking Σ_{nl} to be isotropic and non-zero completely removes the trough, leaving a single peak that is broader than the linear-theory case. Changing the values of Σ_{\perp} and Σ_{\parallel} (but keeping their ratios roughly the same) alters the structure of the peaks and changes the crest-trough contrast.

Changing Σ_s has the most prominent effects at small scales as expected, since the FoG is strongest there. It also causes a noticeable change in the BAO signal which is partially degenerate with the effects of anisotropic Σ_{nl} , i.e. it can also adjust the crest-trough contrast and can eliminate the trough entirely ($\Sigma_s = 0h^{-1}\text{Mpc}$). Leverage on this parameter mostly comes from small scales, where Σ_s has a significant effect on the quadrupole shape.

Changing β is mostly a large-scale effect which is also not surprising since the Kaiser effect is a large-scale redshift-space distortion. This parameter shifts the overall magnitude of the quadrupole at large scales and is not degenerate with any of the other parameters.

Only ϵ and α can shift the location of the BAO. While α shifts the BAO position equally along all directions, Figure 5.2 shows that ϵ shifts the radial BAO position more than the transverse BAO position. Therefore changing ϵ will cause the quadrupole BAO position to change in addition to the shift induced by α . We see from 5.2 that ϵ can also adjust the BAO shape so it is not completely non-

degenerate with the other parameters. We emphasize that Σ_{\perp} , Σ_{\parallel} , Σ_s and β cannot shift the quadrupole BAO, they merely work to change the BAO shape. ϵ is the only parameter that can change the quadrupole BAO position without changing the monopole BAO position, so its effects should be detectable.

The above observations of the model quadrupole behaviour can be re-cast into Figure 5.6. The panels of this figure show the derivatives of the quadrupole model with respect to each parameter (Σ_{\perp} - top left, Σ_{\parallel} - top right, Σ_s - middle left, β - middle right, α - bottom left and ϵ - bottom right). The dashed line marks the acoustic scale. These derivatives show the variation of the model with these parameters and are especially interesting near the acoustic scale.

One can see that the behaviour of the Σ_{\perp} derivative near the BAO scale is exactly opposite to the Σ_{\parallel} case. In the former we see a down-up-down structure and in the latter we see an up-down-up structure. Hence these 2 modes are non-degenerate. The Σ_s derivative shows similar behaviour to the Σ_{\parallel} derivative near the acoustic scale and hence these 2 parameters are partially degenerate. However, its small-scale behaviour is much different. The β derivative shows only a single peak near the acoustic scale and is much different in magnitude than the previous three. Note that all of these derivatives show even parity around the acoustic peak.

The α and ϵ derivatives are different from the others in that they both show odd parity around the acoustic peak. This reflects their ability to shift the BAO feature. The difference between α and ϵ lies mainly in the monopole where α can significantly shift the BAO but ϵ cannot; ϵ only shifts the BAO in the quadrupole. Near the acoustic scale, the quadrupole α derivative shows a large amount of structure while the ϵ derivative shows a simple up-down structure. The crests and troughs of both of these will be partially degenerate with the other parameters despite their opposite parities near the acoustic scale. However, if we place well-informed priors on the

other parameters, we limit the model from exploring these degeneracies thereby obtaining reasonably robust measurements of ϵ .

A similar conclusion can be reached by noting that the first 3 cases look like the derivative of a Gaussian with respect to its width. The β case looks like the derivative of a Gaussian with respect to its height and the ϵ case looks like the derivative of a Gaussian with respect to its center. All of these behaviours are different.

5.2.5 Covariance Matrix Formalism

Assuming that the amplitude of primordial overdensities is drawn from a Gaussian random field, the covariance between two multipole moments ℓ and ℓ' is

$$C_{ij}(\xi_\ell(r_i), \xi_{\ell'}(r_j)) = \frac{2(2\ell + 1)(2\ell' + 1)}{V} \cdot \int \frac{k^3 d\log(k)}{2\pi^2} j_\ell(kr_i) j_{\ell'}(kr_j) P_{\ell\ell'}^2(k) \quad (5.32)$$

where V is the volume, the $j_\ell(kr)$ are the spherical Bessel functions of order ℓ and $P_{\ell\ell'}^2(k)$ is defined as

$$P_{\ell\ell'}^2(k) = \frac{1}{2} \int_{-1}^1 \left[P(k, \mu) + \frac{1}{\bar{n}} \right]^2 L_\ell(\mu) L_{\ell'}(\mu) d\mu. \quad (5.33)$$

Here, $P(k, \mu)$ is the 2D power spectrum and \bar{n} is the mean number density of galaxies. The $1/\bar{n}$ term corresponds to Poisson shot-noise expected in the linear theory regime, i.e. in the absence of non-linear structure growth and mode coupling. Typically the redshift dependence of \bar{n} is not taken into account, however, we will describe a method that allows its inclusion in §5.3.3.

In practice, the correlation functions we measure are binned and hence, if we are interested in using the Gaussian covariance matrix, we must also account for this binning. If we calculate the correlation function in bins with lower bounds r_1 and

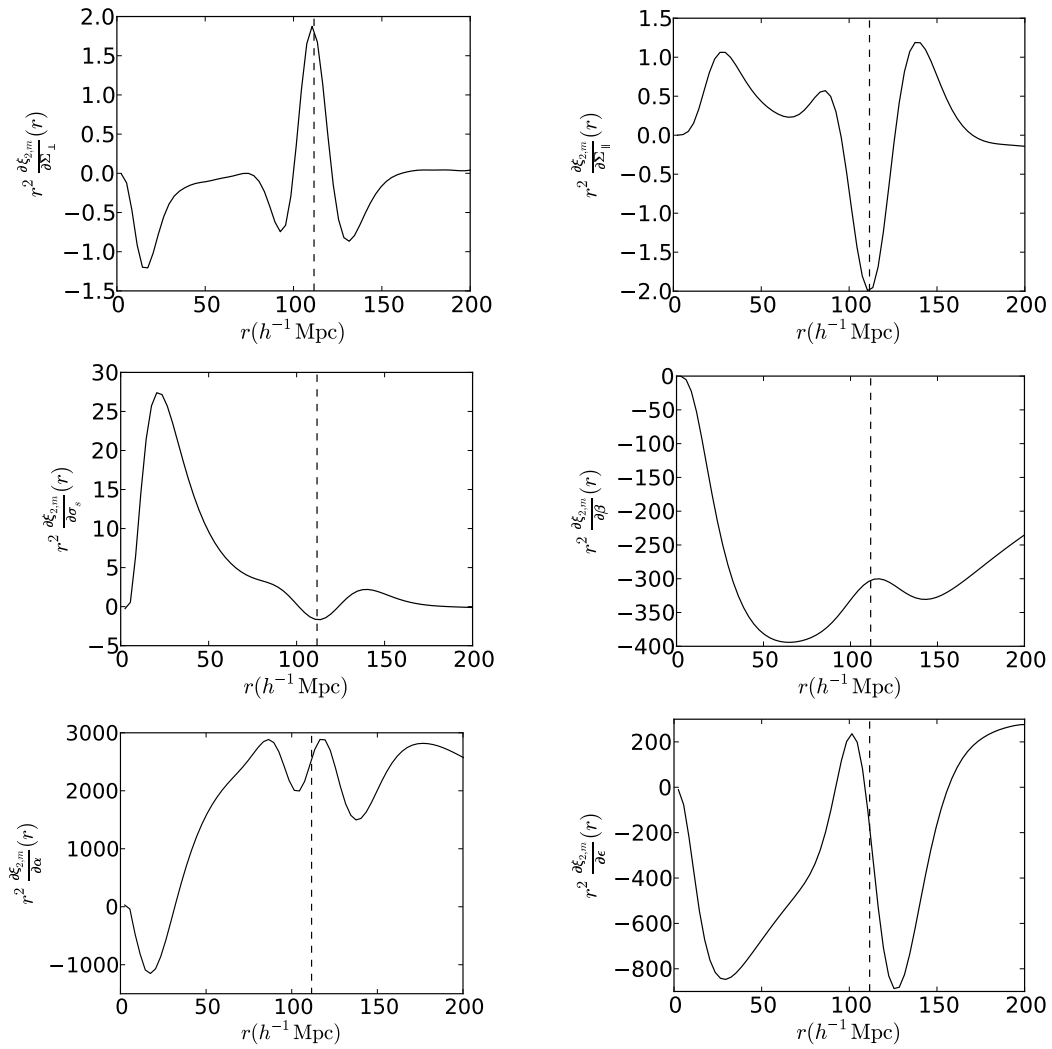


Figure 5.6

(Figure 5.6 caption on next page)

(Figure 5.6 continued)

Figure 5.6: Derivatives of the model quadrupole with respect to Σ_{\perp} (top left), Σ_{\parallel} (top right), Σ_s (middle left), β (middle right), α (bottom left) and ϵ (bottom right). These derivatives illustrate how the model changes with these various parameters and are especially interesting near the BAO scale marked by the dashed line. We see that the Σ_{\perp} and Σ_{\parallel} derivatives are similar in nature at the acoustic scale but opposite in sign, implying their non-degeneracy. The Σ_{\parallel} and Σ_s derivatives, however, are of the same sign and show the same up-down-up structure near the BAO scale. Therefore, these 2 parameters are partially degenerate, however, the behaviour of the Σ_s derivative is very different at small scales. The β derivative is much different in magnitude and also only shows a single peak near the acoustic scale. Note that the Σ_{\perp} , Σ_{\parallel} , Σ_s and β derivatives all show even parity near the acoustic scale while the α and ϵ derivatives show odd parity. The α derivative has the most structure near the acoustic scale. The ϵ derivative shows a simple up-down structure. Despite their opposite parities near the acoustic scale, the various crests and troughs of the α and ϵ derivatives will be partially degenerate with the other parameters. However, given reasonable priors on the other parameters, the model will not be allowed to explore these degeneracies and we will recover robust measurements of ϵ .

upper bounds r_2 , the binned covariance matrix is

$$\begin{aligned}
C_{ij}(\xi_\ell(r_i), \xi_{\ell'}(r_j)) &= \frac{2(2\ell + 1)(2\ell' + 1)}{V} \frac{3}{r_{i2}^3 - r_{i1}^3} \frac{3}{r_{j2}^3 - r_{j1}^3} \\
&\cdot \int_{r_{i2}}^{r_{i1}} r^2 dr \frac{d\Omega}{4\pi} \int_{r_{j2}}^{r_{j1}} r'^2 dr' \frac{d\Omega'}{4\pi} \\
&\cdot \int \frac{k^3 d \log(k)}{2\pi^2} j_\ell(kr) j_{\ell'}(kr') P_{\ell\ell'}^2(k).
\end{aligned} \tag{5.34}$$

We note that this assumes the correlation function is calculated by spherically averaging the 2D correlation function, which is slightly different to the correlation function calculated by spherically averaging over the paircounts (see §5.3.2). Here, we neglect the weighting specified by the random paircounts which encode the survey geometry and distribution of galaxies. In the case of the monopole and quadrupole relevant to this study, the above expression can be split into the $\ell = \ell' = 0$ case, the $\ell = 0$ and $\ell' = 2$ (or vice versa) case and the $\ell = \ell' = 2$. The first case was shown to have the form (Xu et al., 2012)

$$C_{ij}(\xi_0(r_i), \xi_0(r_j)) = \frac{2}{V} \int \frac{k^3 d \log(k)}{2\pi^2} \mathcal{J}_0(kr_i) \mathcal{J}_0(kr_j) P_{00}^2(k) \tag{5.35}$$

where

$$\mathcal{J}_0(kr) = \frac{3}{r_2^3 - r_1^3} \left[\frac{r^2 j_1(kr)}{k} \right]_{r_1}^{r_2} \tag{5.36}$$

and

$$j_1(kr) = \frac{\sin(kr)}{(kr)^2} - \frac{\cos(kr)}{kr}. \tag{5.37}$$

Here, $[f(x)]_b^a$ is standard notation for $f(a) - f(b)$ for any function f . The second case has the form

$$C_{ij}(\xi_0(r_i), \xi_2(r_j)) = \frac{10}{V} \int \frac{k^3 d \log(k)}{2\pi^2} \mathcal{J}_0(kr_i) \mathcal{J}_2(kr_j) P_{02}^2(k) \tag{5.38}$$

where

$$\mathcal{J}_2(kr) = \frac{3}{r_2^3 - r_1^3} \left[\frac{3\text{si}(kr)}{k^3} - \frac{1}{k} \left(\frac{3r}{k} j_0(kr) + r^2 j_1(kr) \right) \right]_{r_1}^{r_2}, \tag{5.39}$$

$$\text{si}(x) = \int_0^x \frac{\sin(x')}{x'} dx' \quad (5.40)$$

and

$$j_0(kr) = \frac{\sin(kr)}{kr}. \quad (5.41)$$

Note that due to symmetry, we have $C_{ij}(\xi_0(r_i), \xi_2(r_j)) = C_{ij}(\xi_2(r_i), \xi_0(r_j))$. Finally, the last case has the form

$$C_{ij}(\xi_2(r_i), \xi_2(r_j)) = \frac{50}{V} \int \frac{k^3 d \log(k)}{2\pi^2} \mathcal{J}_2(kr_i) \mathcal{J}_2(kr_j) P_{22}^2(k). \quad (5.42)$$

Collectively, we can then write

$$C_{ij}(\xi_\ell(r_i), \xi_{\ell'}(r_j)) = \frac{2(2\ell + 1)(2\ell' + 1)}{V} \cdot \int \frac{k^3 d \log(k)}{2\pi^2} \mathcal{J}_\ell(kr_i) \mathcal{J}_{\ell'}(kr_j) P_{\ell\ell'}^2(k). \quad (5.43)$$

These forms for the binned Gaussian covariance matrix form the basis for deriving a covariance matrix for our data. We extend the method for approximating the mock covariances using a modified form of the binned Gaussian covariance matrix as described in Xu et al. (2012). This will be outlined in §5.3.3.

5.3 Analysis

5.3.1 Reconstruction

Non-linear structure growth degrades and shifts the acoustic peak. Reconstruction was initially proposed to partially remove these effects (Eisenstein et al., 2007). In the linear theory description of structure growth, overdensities are small and hence remain largely in place as they accrete more matter and grow. However, at low redshifts, this description becomes increasingly less suitable as some overdensities grow to masses large enough that they begin exerting significant gravitational pulls

on each other. This gives rise to pairwise relative velocities between particles separated by $\sim 100h^{-1}\text{Mpc}$. These coherent flows that form large-scale structure are the dominant source of smearing of the BAO signal. The peculiar motions of particles within a gravitationally bound structure are subdominant. Reconstruction attempts to undo these coherent motions in the matter density field and arrive back at something that more closely resembles linear theory. This translates into a sharpening up of the acoustic peak in the correlation function which allows us to gain a better centroiding of its location and hence a more precise measure of the acoustic scale. It also removes some of the shifting of the BAO due to non-linear structure growth, which has been shown to be a $\sim 0.5\%$ effect at $z = 1$ (Seo et al., 2010; Mehta et al., 2011) and will be slightly larger at lower redshifts.

Our reconstruction algorithm is described in detail in Padmanabhan et al. (2012a). A more pedagogical discussion of reconstruction can also be found there. This method is extended from the original reconstruction algorithm proposed in Eisenstein et al. (2007) and its theoretical basis is established in Padmanabhan, White & Cohn (2009) and Noh et al. (2009). A basic outline is given below.

The ultimate goal of reconstruction is to infer the matter displacement field that arises due to non-linear structure growth from the observed galaxy density field. Then, we can shift the galaxies back along their inferred displacement vectors to place them where they would have been in linear theory. This is simple if we consider only the first order displacements Ψ . In this case

$$\nabla \cdot \Psi + \beta \nabla \cdot (\Psi_s \hat{\mathbf{s}}) = -\frac{\delta_{gal}}{b} \quad (5.44)$$

where $\Psi_s = \Psi \cdot \hat{\mathbf{s}}$ is the displacement in the line-of-sight direction (Nusser & Davis, 1994). δ_{gal} is the galaxy density field, b is the large-scale galaxy bias (which is roughly constant) and hence δ_{gal}/b is an approximation of the matter density field. The second term in this equation arises due to large-scale redshift-space distortions

caused by the coherent infall of galaxies towards overdense regions (the Kaiser effect, Kaiser (1987)). This implies that as an additional perk, reconstruction also corrects for Kaiser squashing. The β parameter governs the amount of anisotropy introduced by the Kaiser effect. It is defined as $\beta = f/b$ where $f = d \log D(a)/d \log(a) \sim \Omega_m(a)^{0.55}$ is the linear growth rate, $D(a)$ is the linear growth function and a is the scale factor (Caroll, Press & Turner, 1992; Linder, 2005). If we assume that Ψ is irrotational (i.e. curl-free), we can write $\Psi = \nabla\phi$. After selecting appropriate values of b and f , we can solve for the scalar field ϕ and then the displacement field Ψ using a finite difference approach.

Areas that do not fall within the survey or are masked out by the survey need to be accounted for as the gravitational potential (and hence the displacement field) is sensitive to these regions. Our algorithm fills in these external regions by embedding our survey into a volume that is sufficiently larger than the survey volume before the displacement field is calculated (we use $200h^{-1}\text{Mpc}$ padding). It then smooths over the density field using a Gaussian with a $15h^{-1}\text{Mpc}$ smoothing length and generates a constrained realization of a Gaussian density field that matches the observed density (Hoffman & Ribak, 1991; Zaroubi et al., 1995). This effectively fills in the masked and unobserved regions.

5.3.2 Computation

The computation of our correlation functions is tied to our reconstruction algorithm. We bin our correlation functions in $3h^{-1}\text{Mpc}$ bins starting at $2.5h^{-1}\text{Mpc}$ and going up to $197.5h^{-1}\text{Mpc}$. A list of the steps involved is given below.

- I) Obtain a set of randomly distributed points that have the same angular and radial selection function as the survey.
- II) Compute the unreconstructed monopole correlation function from the data

using the Landy-Szalay estimator (Landy & Szalay, 1993),

$$\xi_\ell(r, \mu) = \frac{DD - 2DR + RR}{RR} L_\ell(\mu) \quad (5.45)$$

where DD , DR and RR are the number of galaxy-galaxy, galaxy-random and random-random pairs that are separated by r and μ . We apply FKP weighting (Feldman et al., 1994) for each object as

$$w_i = \frac{1}{1 + \bar{n}(z_i)P(k_0)} \quad (5.46)$$

where $\bar{n}(z_i)$ is the number density at the redshift of the object z_i and $P(k_0) = 40000h^{-3} \text{ Mpc}^3$ is the approximate value of the power spectrum at the BAO scale. To obtain the spherically-averaged monopole and quadrupole ($\xi_0(r)$ and $\xi_2(r)$), we integrate over μ in the pair-counts themselves, but one could also choose to integrate over $\xi_\ell(r, \mu)$.

- III) Estimate the galaxy bias b and the anisotropy parameter β from the unreconstructed correlation function. We use fiducial values of $b = 2.2$ and $\beta = 0.3$.
- IV) Embed the survey in a larger volume and smooth the density field using a Gaussian (again, we use a smoothing length of $15h^{-1}\text{Mpc}$). Generate a constrained Gaussian realization matching the observed density to fill in the masked and unobserved regions.
- V) Estimate the displacement field Ψ using Equation (5.44) and shift the galaxies by $-\Psi - f(\Psi, \hat{s})$ to partially undo the effects of non-linear structure growth and large-scale redshift-space distortions. This is the essence of reconstruction.
- VI) Obtain another set of randomly generated particles with the same radial and angular selection function as the survey. Shift these by $-\Psi$ and denote as S .

VII) Compute the reconstructed correlation function using the Landy-Szalay estimator

$$\xi_\ell(r, \mu) = \frac{DD - 2DS + SS}{RR} L_\ell(\mu). \quad (5.47)$$

5.3.3 Fitting

We construct models of the monopole and quadrupole in a fiducial cosmology to measure the position of the BAO in the data relative to the model (parameterized by α) and the degree to which it is anisotropic in the data (parameterized by ϵ). We base our fitting templates for the monopole and quadrupole on Equations (5.25) & (5.26). That is, we define fitting models of the form

$$\xi_{0,m}(r) = B_0^2 \xi_{0,t}(\alpha r) + \frac{2}{5} \epsilon \left[3 \xi_{2,t}(\alpha r) + \frac{d\xi_{2,t}(\alpha r)}{d \log(r)} \right] + A_0(r) \quad (5.48)$$

$$\begin{aligned} \xi_{2,m}(r) = & 2B_0^2 \epsilon \frac{d\xi_{0,t}(\alpha r)}{d \log(r)} + \left(1 + \frac{6}{7} \epsilon \right) \xi_{2,t}(\alpha r) + \frac{4}{7} \epsilon \frac{d\xi_{2,t}(\alpha r)}{d \log(r)} \\ & + \frac{4}{7} \epsilon \left[5 \xi_{4,t}(\alpha r) + \frac{d\xi_{4,t}(\alpha r)}{d \log(r)} \right] + A_2(r) \end{aligned} \quad (5.49)$$

where

$$A_\ell(r) = \frac{a_{\ell,1}}{r^2} + \frac{a_{\ell,2}}{r} + a_{\ell,3}. \quad (5.50)$$

The $A_\ell(r)$ are composed of linear nuisance terms used to marginalize out broadband effects such as scale-dependent bias and redshift-space distortions as in Xu et al. (2012). The B_0^2 term adjusts the amplitude of the monopole template $\xi_{0,t}$. We infer the galaxy bias b from the multiplicative offset, b^2 , between this template and the measured correlation function at $r = 50h^{-1}\text{Mpc}$. We then use this offset to normalize the full models, $\xi_{0,m}$ and $\xi_{2,m}$ in Equations (5.48) & (5.49), to the data. This ensures that $B_0^2 \sim 1$ as it is primarily the monopole fit that sets this term and ϵ is very small. In practice we perform our fits in the non-linear parameter $\log(B_0^2)$ to prevent B_0^2 from going negative which would be unphysical. We adopt a Gaussian

prior on $\log(B_0^2)$ with standard deviation 0.4 and centered at 0 to prevent B_0^2 from wandering too far from 1 as described in Xu et al. (2012).

In addition, we apply a 10% Gaussian prior on $1 + \epsilon$ to limit the ability of noise in dragging ϵ to unrealistically large values. In fitting the mocks without the prior, only 2 have measured ϵ values > 0.1 , so this prior does not have a significant impact. To verify that this prior is not cosmologically informative, we take the results of a Markov Chain Monte Carlo simulation used to find the posterior distribution of various cosmological parameters. In particular, we use the CMB+allBAO ow_0w_a CDM chain from Mehta et al. (2012) which allows for a spatially curved universe and non-cosmological constant, time-varying dark energy. At each step in the chain, we calculate ϵ and plot up a histogram of these values. The distribution is nearly Gaussian with a standard deviation of ~ 0.026 which is much less than our 0.1 prior.

The monopole and quadrupole correlation function templates ($\xi_{0,t}(r)$ and $\xi_{2,t}(r)$) are derived from the 2D power spectrum $P_t(k, \mu)$ template (Equation (5.27)) as described in §5.2.4. We set $\Sigma_s = 4h^{-1}\text{Mpc}$. We let β vary in our fits as it affords us leverage on the amplitude of the quadrupole with which it is partially degenerate. We put a prior on β centered at $f/b \sim \Omega_m(z)^{0.55}/b = 0.35$ before reconstruction and 0 after reconstruction with 0.2 standard deviation in both cases. The choice of $\beta = 0$ as the center of the prior after reconstruction is because we expect the Kaiser effect to be mostly removed. We fix $\Sigma_{\perp} = 6h^{-1}\text{Mpc}$ and $\Sigma_{\parallel} = 10h^{-1}\text{Mpc}$ in our pre-reconstruction fits and $\Sigma_{\perp} = \Sigma_{\parallel} = 3h^{-1}\text{Mpc}$ in our post-reconstruction fits. These values are approximated from the fit results to the average correlation function of the mocks where we set $\Sigma_{\parallel} = (1 + f)\Sigma_{\perp}$ in the pre-reconstruction case due to the Kaiser effect and $\Sigma_{\parallel} = \Sigma_{\perp}$ in the post-reconstruction case due to the expected removal of Kaiser squashing by reconstruction. The pre-reconstruction fit results to the average mock correlation function are shown in Figure 5.7.

We simultaneously fit the monopole and the quadrupole for 4 non-linear parameters $\log(B_0^2)$, β , α and ϵ , in addition to the linear nuisance parameters in $A_\ell(r)$. The non-linear parameters are handled using a simplex algorithm and the linear parameters are obtained using a least-squares method nested within this simplex. That is, for each set of non-linear parameters, the least-squares algorithm returns the corresponding best-fit linear parameters. The simplex steps sequentially through the non-linear parameter space until the best-fit values are obtained. To determine the best-fit values, we minimize the χ^2 goodness-of-fit indicator given by

$$\chi^2 = (\vec{m} - \vec{d})^T C^{-1} (\vec{m} - \vec{d}) \quad (5.51)$$

where \vec{m} is a column vector of the model at each step in the simplex and \vec{d} is the data. Both of these must contain both the monopole and quadrupole values in sequence. C is the covariance matrix which is described below. We use a fiducial fitting range of $50 < r < 200h^{-1}\text{Mpc}$ which corresponds to fitting 50 points in both the monopole and the quadrupole. This gives $2 \times 50 - \#$ of fit parameters = $100 - 10 = 90$ degrees-of-freedom (dof) in the fit. Using this technique we can obtain best-fit values of our parameters of interest, the isotropic dilation α and the anisotropic warping ϵ of the BAO signal.

In addition, we can calculate the probability distribution $p(\alpha, \epsilon)$ by fitting for the other parameters at various grid values of these 2 parameters and measuring the best-fit χ^2 . This is feasible because $p(\vec{x}) \propto \exp(-\chi^2/2)$. The constant of proportionality corresponds to the normalization that makes the integral $\int p(\vec{x}) d\vec{x} = 1$. Then we can calculate $p(\alpha)$ and $p(\epsilon)$ as

$$p(\alpha) = \int p(\alpha, \epsilon) d\epsilon \quad (5.52)$$

$$p(\epsilon) = \int p(\alpha, \epsilon) d\alpha. \quad (5.53)$$

We can take the widths of these distributions (σ_α and σ_ϵ) as measurements of the

errors on α and ϵ if α and ϵ have Gaussian posteriors. In §5.4 we demonstrate using fit results to our mock catalogues that α and ϵ have finite probabilities of being drawn from Gaussian distributions. The covariance between α and ϵ ($C_{\alpha\epsilon}$) can also be calculated and converted into a correlation coefficient $\rho_{\alpha\epsilon}$. These are defined

$$\sigma_x^2 = \int p(x)(x - \langle x \rangle)^2 dx \quad (5.54)$$

$$C_{\alpha\epsilon} = \int p(\alpha, \epsilon)(\alpha - \langle \alpha \rangle)(\epsilon - \langle \epsilon \rangle) d\alpha d\epsilon \quad (5.55)$$

$$\rho_{\alpha\epsilon} = \frac{C_{\alpha\epsilon}}{\sigma_\alpha \sigma_\epsilon} \quad (5.56)$$

where $\langle x \rangle$ is the mean of the distribution $p(x)$. For our grids we pick the ranges $0.7 < \alpha < 1.3$ and $-0.3 < \epsilon < 0.3$ at spacings of 0.0025 and 0.005 respectively. We also apply an additional Gaussian prior on $\log(\alpha)$ with a width of 0.15 to suppress any unphysical downturns in the χ^2 distribution at small α . These α correspond to the acoustic peak in the model being pushed out to larger scales where the fitter has an easier time hiding the peak in the large errorbars. This procedure was scrutinized in detail in Xu et al. (2012). Note that our grids are only used to compute $p(\alpha)$ and $p(\epsilon)$. We do not use them to infer the best-fit values of these parameters, which are obtained through the non-linear simplex optimization described above.

We obtain a smooth estimate of the covariance matrix using the method described in Xu et al. (2012) extended here to include the quadrupole (see below). A detailed description of the method is given there. This method approximates the covariance matrix calculated directly from the mock correlation functions with a modified Gaussian covariance matrix. We use this method since the mock covariances show evidence of noise and ideally the covariance matrix should be smooth.

The method allows us to include the redshift dependence of the galaxy number density \bar{n} . This is anchored in the observation that the covariance in configuration space is just the transform of the variance in Fourier space $P_{\ell\ell'}^2(k)/V$. Hence, we

can imagine building up the inverse variance as

$$I^2(k) = \int \frac{dV}{P_{\ell\ell'}^2(k)} \quad (5.57)$$

where

$$dV = \frac{c}{H_0} \frac{r^2(z)}{\sqrt{\Omega_m(1+z)^3 + \Omega_\Lambda}} dz d\Omega \quad (5.58)$$

for a flat universe and defining $\mathfrak{P}_{\ell\ell'}^2(k) = [I^2(k)]^{-1}$. This allows us to include the redshift dependence of the number density which enters into the calculation of $P_{\ell\ell'}^2(k)$ (see Equation (5.33)), assuming $\bar{n}(z)$ has no angular dependence.

Since our correlation functions are computed via binning, we must use the binned Gaussian covariance given in Equation (5.43). Using the above observation, we can replace the $P_{\ell\ell'}^2(k)/V$ term in that equation with $\mathfrak{P}_{\ell\ell'}^2(k)$, i.e.

$$\begin{aligned} C_{ij}(\xi_\ell(r_i), \xi_{\ell'}(r_j)) &= 2(2\ell + 1)(2\ell' + 1) \\ &\cdot \int \frac{k^3 d \log(k)}{2\pi^2} \mathcal{J}_\ell(kr_i) \mathcal{J}_{\ell'}(kr_j) \mathfrak{P}_{\ell\ell'}^2(k). \end{aligned} \quad (5.59)$$

We can then insert the modification parameters c_0 , c_1 , c_2 and c_3 such that

$$\begin{aligned} C_{ij}(\xi_\ell(r_i), \xi_{\ell'}(r_j)) &= 2(2\ell + 1)(2\ell' + 1) \\ &\cdot \left[\int \frac{k^3 d \log(k)}{2\pi^2} \mathcal{J}_\ell(kr_i) \mathcal{J}_{\ell'}(kr_j) \right. \\ &\quad \left. \cdot \mathfrak{P}_{\ell\ell'}^2(k; c_0, c_1, c_2) \right] + c_3. \end{aligned} \quad (5.60)$$

Here, $\mathfrak{P}_{\ell\ell'}^2(k; c_0, c_1, c_2)$ corresponds to a $P_{\ell\ell'}^2(k)$, Equation (5.33), where we have made the substitution

$$\begin{aligned} P(k, \mu) + \frac{1}{\bar{n}} &\rightarrow \left[c_0 P_{dw}(k, \mu) + \frac{c_1}{\bar{n}(z)} \right] (1 + \beta\mu^2)^2 F(k, \mu, \Sigma_s) \\ &+ \frac{c_2}{\bar{n}(z)}. \end{aligned} \quad (5.61)$$

The c_0 term adjusts the magnitude of the sample variance. The c_1 term acts like a non-linear shot-noise component and the c_2 term adjusts the magnitude of the standard Poisson shot-noise contribution. The c_3 term can be associated with the integral constraint, which appears as an additive offset in the correlation function.

To derive values for these parameters, we maximize the likelihood function

$$\mathcal{L} = \prod_{i=0}^N (2\pi)^{-q/2} (\det C)^{-1/2} \exp(-\chi_i^2/2). \quad (5.62)$$

Here N is the total number of mocks and q is the number of points to fit. We derive the parameters using the mock covariances between $50 < r < 200h^{-1}\text{Mpc}$ (50 monopole points and 50 quadrupole points) and hence $q = 50 \times 2 = 100$. $\chi_i^2 = \vec{x}_i^T C^{-1} \vec{x}_i$ where \vec{x}_i is a column vector of dimension q containing the difference between the monopole and quadrupole of each mock and the average of all mocks.

Before reconstruction we set $\beta = f/b$. After reconstruction we set $\beta = 0$, again due to the expected removal of large-scale redshift-space distortions. We test several cases where we vary β from these fiducial values and find that changing β affects the relative amplitudes of the $C_{ij}(\xi_0(r_i), \xi_0(r_j))$ and $C_{ij}(\xi_2(r_i), \xi_2(r_j))$ terms. This can cause slight changes in the resulting σ_α and σ_ϵ at the 0.1% level, which is not significant at our current levels of statistical precision. The Σ_s streaming scale for the FoG is fixed at $4h^{-1}\text{Mpc}$. We find very little difference in the resulting modification parameters in cases where we allow Σ_s to vary. We fix Σ_\perp and Σ_\parallel to their fiducial model values (recapped below) in our covariance matrix calculations. With the modification parameters in hand, we can construct a smooth approximation to the mock covariances from the binned Gaussian covariance matrix using Equation (5.60).

Our fiducial model parameters are summarized as follows: we define our fiducial model before reconstruction to have $\Sigma_\perp = 6h^{-1}\text{Mpc}$, $\Sigma_\parallel = 10h^{-1}\text{Mpc}$, $\Sigma_s = 4h^{-1}\text{Mpc}$ and a prior on β centered on $\beta = 0.35$. After reconstruction, we set

$\Sigma_{\perp} = \Sigma_{\parallel} = 3h^{-1}\text{Mpc}$ and center our β prior on 0. Our fiducial fitting range is $50 < r < 200h^{-1}\text{Mpc}$.

In §5.4 and §5.5, we present our measured values of α and ϵ for the mocks (§3.2.1) and actual survey data (§3.2.2) using the fitting models defined in Equations (5.48) & (5.49) and the modified Gaussian covariance matrix described above.

5.4 Mock Catalogue Results

In this section we present the results of fits to the LasDamas mock correlation functions before and after reconstruction. These were computed and fit by taking the LasDamas cosmology as the fiducial cosmology. The LasDamas mocks are described in more detail in §3.2.1.

We plot the average monopole and quadrupole of the 160 mocks before reconstruction in Figure 5.7. The monopole and the quadrupole at large scales look very similar to the fiducial template plotted in Figure 5.2. The small scales in the quadrupole, however, show substantially different structure indicating that our model does not suit the data well at these scales. This motivated our choice for the fiducial fitting range: $50 < r < 200h^{-1}\text{Mpc}$. The best-fit model to the spherically-averaged monopole and quadrupole are overplotted as the red lines where the solid line corresponds to using the fiducial $A_{0,2}(r)$ and the dashed line corresponds to using $A_{0,2}(r) = 0$ (i.e. no broadband marginalization). The monopole fits look very similar; however the fiducial $A_{0,2}(r)$ does much better in the quadrupole near the acoustic scale with χ^2 decreasing by ~ 33 relative to the $A_{0,2}(r) = 0$ fit. We allow Σ_{\perp} and Σ_{\parallel} to vary in these fits and obtain best-fit values of $6.3h^{-1}\text{Mpc}$ and $10.4h^{-1}\text{Mpc}$, motivating our choices in the fiducial model. We keep Σ_s fixed at $4h^{-1}\text{Mpc}$.

A comparison of the monopole and quadrupole before and after reconstruction is

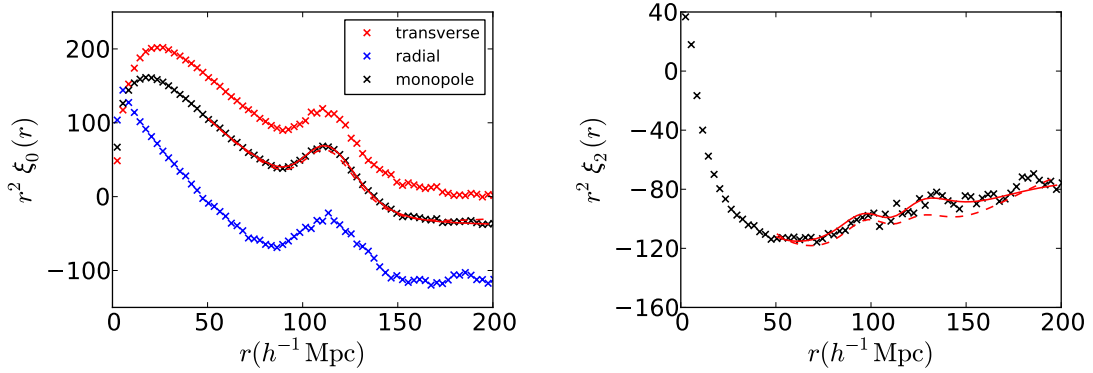


Figure 5.7: Average monopole (left) and quadrupole (right) of the 160 mock catalogues before reconstruction. One can see that the monopole and the quadrupole at large scales are very similar to the fiducial template (solid lines) plotted in Figure 5.2, however the quadrupole on small scales shows substantially different structure. The fit to the average of the spherically-averaged monopole and quadrupole from the mocks is overplotted in red. The solid line corresponds to a fit using the fiducial $A_{0,2}(r)$ (Equation (5.50)) and the dashed line corresponds to a fit using $A_{0,2}(r) = 0$. We allow Σ_{\perp} and Σ_{\parallel} to vary in these fits and obtain best-fit values of $6.3h^{-1}\text{Mpc}$ and $10.4h^{-1}\text{Mpc}$ respectively using the fiducial $A_{0,2}(r)$. In the monopole case, the fit using the fiducial $A_{0,2}(r)$ is very similar to the $A_{0,2}(r) = 0$ fit. In the quadrupole, the $A_{0,2}(r) = 0$ fit is much worse around the acoustic scale. Overall, χ^2 decreased by ~ 33 going from $A_{0,2}(r) = 0$ to the fiducial $A_{0,2}(r)$.

shown in Figure 5.8. As in Padmanabhan et al. (2012a), we see the acoustic peak in the monopole appears less smeared after reconstruction which indicates that our reconstruction technique was effective at partially undoing non-linear evolution. This is also reflected in the fact that after reconstruction, a fit to the average of the mocks gave a much smaller BAO smoothing scale of $\Sigma_{nl} = 2.9h^{-1}\text{Mpc}$ as opposed to the pre-reconstruction values of $\Sigma_{\perp} = 6.3h^{-1}\text{Mpc}$ and $\Sigma_{\parallel} = 10.4h^{-1}\text{Mpc}$. In addition, we see that the quadrupole is nearly zero on large scales after reconstruction, which implies that our reconstruction technique was also effective at partially removing the Kaiser effect. The fact that the quadrupole is positive and not exactly 0 is likely due to some slight anisotropy introduced by reconstruction. This is discussed in more detail below and shown not to significantly affect our measurements of α and ϵ .

By averaging the mocks we have effectively increased the survey volume by a factor of 160 and hence the variance should decrease by an equal amount. This means that the average of the mocks should have substantially less noise. In addition, we know that we are computing the correlation functions and fitting using the correct (LasDamas) cosmology. Hence, we expect that the α and ϵ values measured from the average of the mocks should be 1 and 0 respectively if our models are unbiased (i.e. there should be no shift in the location of the peak relative to the model and there should be no anisotropy). We find that fitting the pre-reconstruction mock average gives $\alpha = 1.005$ and $\epsilon = 0.003$ while post-reconstruction we measure $\alpha = 1.002$ and $\epsilon = 0.002$. The slight offset in α from 1 is not too concerning as we expect non-linear structure growth to shift the peak by $\lesssim 0.5\%$ (Padmanabhan & White, 2009; Mehta et al., 2011). The fact that α moves closer to 1 after reconstruction is encouraging as reconstruction is supposed to remove some effects of non-linear structure growth. The small bias in ϵ is not significant at our current levels of statistical precision and

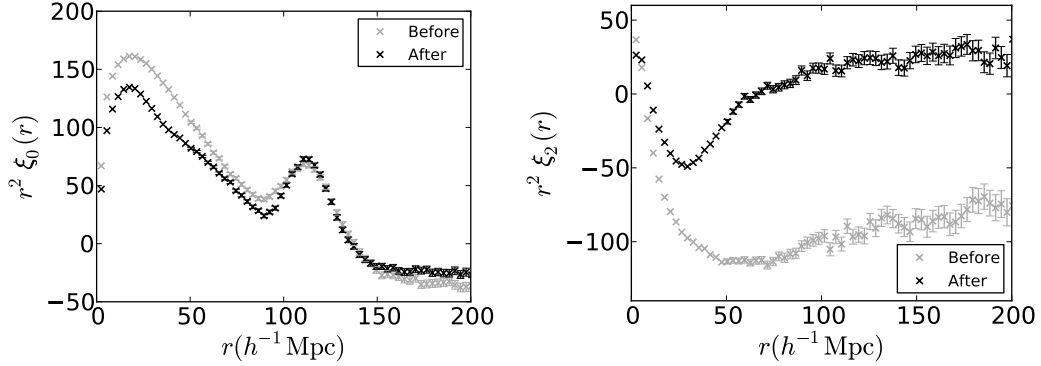


Figure 5.8: The average monopole (left) and quadrupole (right) of the 160 mocks before (gray crosses) and after (black crosses) reconstruction. One can see that after reconstruction, the acoustic peak in the monopole has sharpened up, indicating that reconstruction is effective at removing the degradation of the BAO caused by non-linear structure growth. In the quadrupole, the power at large-scales goes close to 0 which implies that reconstruction was effective at removing the Kaiser effect. It is not exactly zero due to some small anisotropy introduced by the reconstruction technique itself (see Figure 5.16). We note that the quadrupole is multiplied by r^2 in this figure and hence the magnitude of this anisotropy is exaggerated.

is likely the result of small mismatches between the broadband model and the data. This will be discussed in more detail shortly. We again emphasize that in these fits we have allowed Σ_{\parallel} and Σ_{\perp} to vary. When we fit the individual mocks, the signal-to-noise of the data is not sufficient for constraining any of these parameters and hence we fix them in the fiducial model to the values obtained in the averaged mock fits.

We measure α and ϵ for each mock using the fitting procedure and fiducial model outlined in §5.3.3. We also estimate the errors σ_{α} , σ_{ϵ} and the correlation coefficient $\rho_{\alpha\epsilon}$ for each mock using Equations (5.54) & (5.56). Before reconstruction, we measure a mean $\langle\alpha\rangle = 1.003 \pm 0.003$ with an rms scatter between the mocks of 0.034 and a median $\tilde{\alpha} = 1.008$ with 16th/84th percentiles of the mocks corresponding to ${}^{+0.030}_{-0.036}$ (these will henceforth be denoted the quantiles). For ϵ we measure a

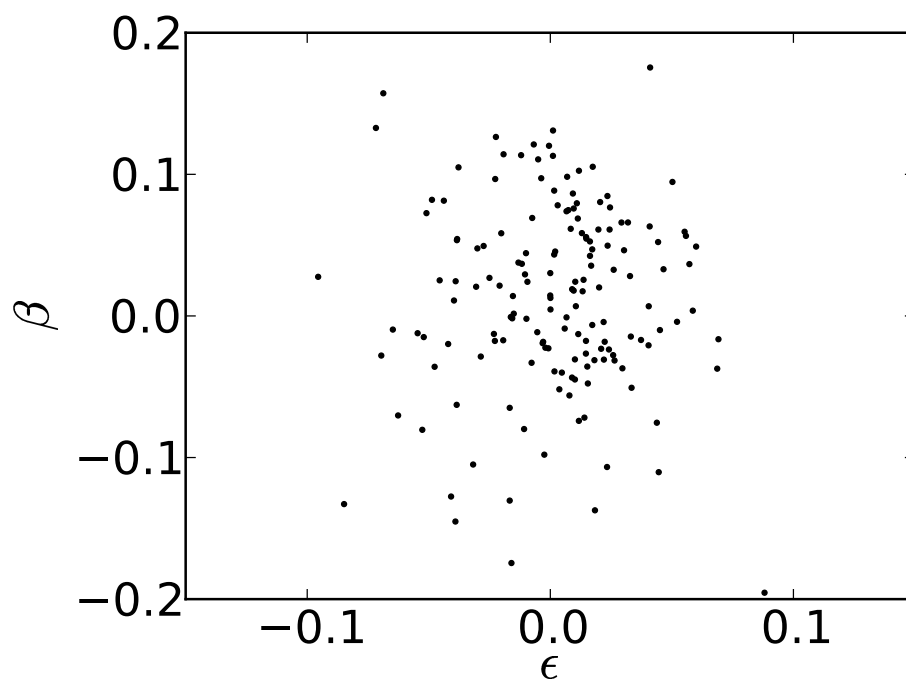


Figure 5.9: β versus ϵ measured from fits to the 160 mocks after reconstruction. One can see that these two parameters are uncorrelated as expected. We see similar results before reconstruction as well.

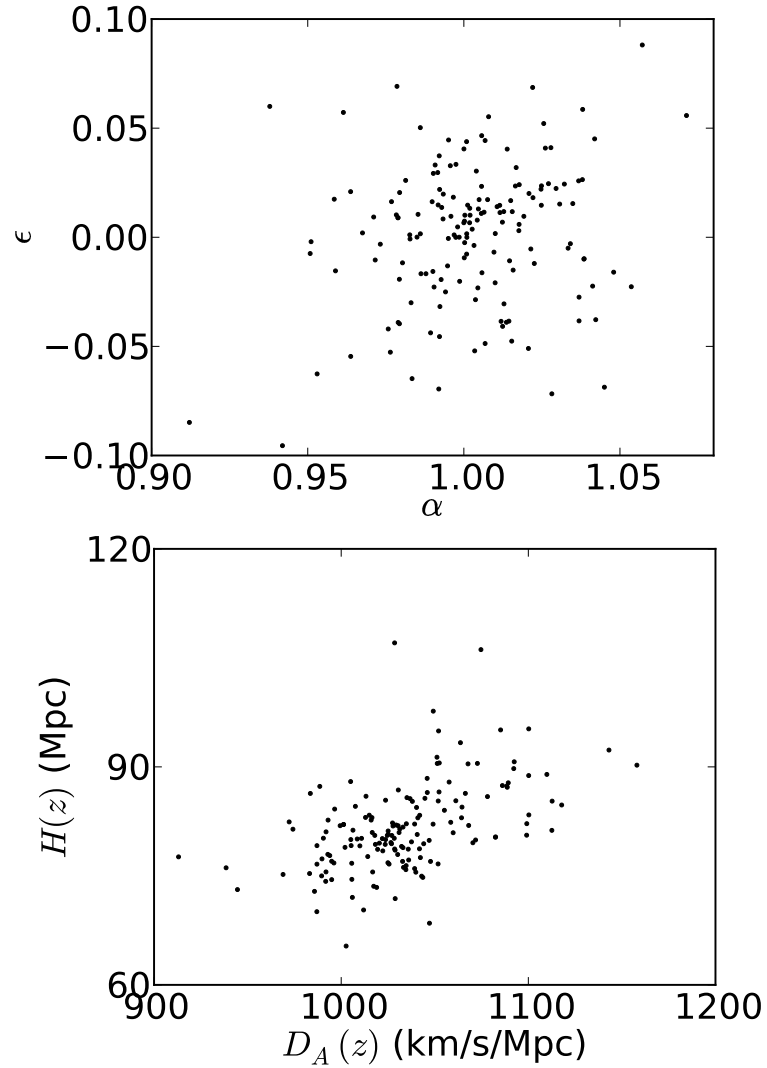


Figure 5.10: α versus ϵ (top) and $D_A(z)$ versus $H(z)$ (bottom) for the mocks after reconstruction. One can see that α and ϵ are not highly correlated. From the points plotted we measure a correlation coefficient of 0.27 and analogously in the pre-reconstruction case we measure 0.20. These are in excellent agreement with Fisher matrix predictions ($\rho_{\alpha\epsilon} \sim 0.21$). We see a stronger correlation between D_A and H which we obtained by combining α and ϵ as in Equations (5.5) & (5.6). We expect $\rho_{D_A H} \sim 0.4$ and we find correlation coefficients of 0.23 and 0.50 between our measured D_A and H values before and after reconstruction respectively.

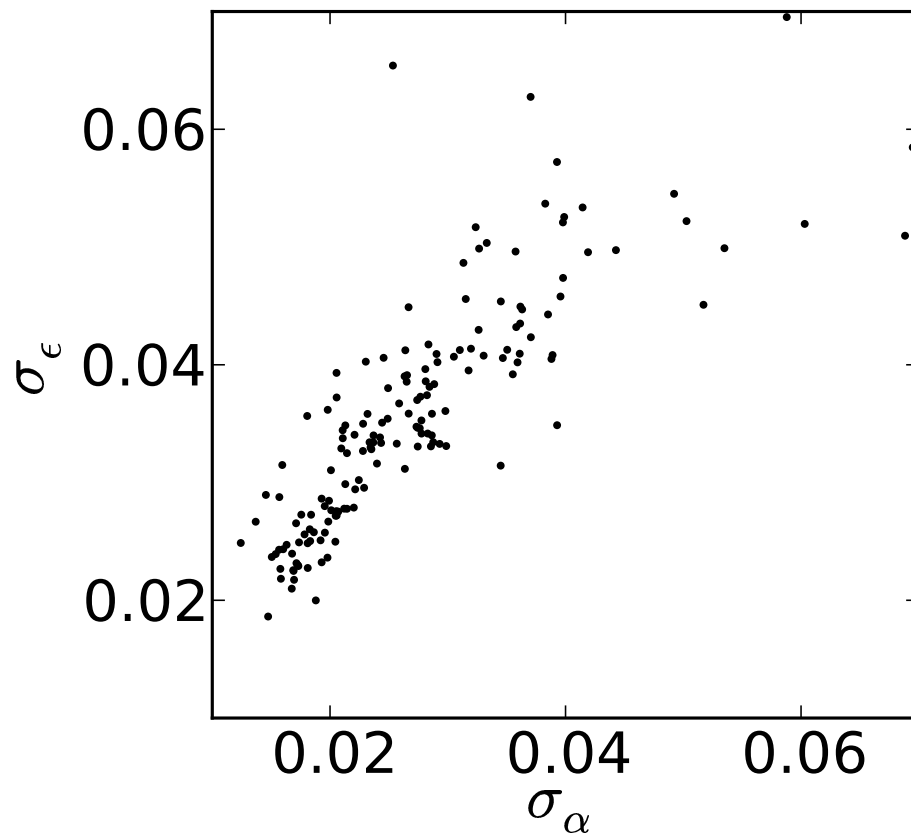


Figure 5.11: Post-reconstruction σ_α versus σ_ϵ for the mocks. We see that the errors on α and the errors on ϵ are directly correlated with each other. This indicates that mocks with poorer measurements of the acoustic scale α also have poorer measurements of the BAO anisotropy ϵ . A similar correlation exists in the pre-reconstruction case. The median ratios of $\sigma_\epsilon/(1 + \epsilon)$ -to- σ_α/α are ~ 1.3 and ~ 1.4 before and after reconstruction respectively. Fisher matrix arguments predict a ratio of ~ 1.2 .

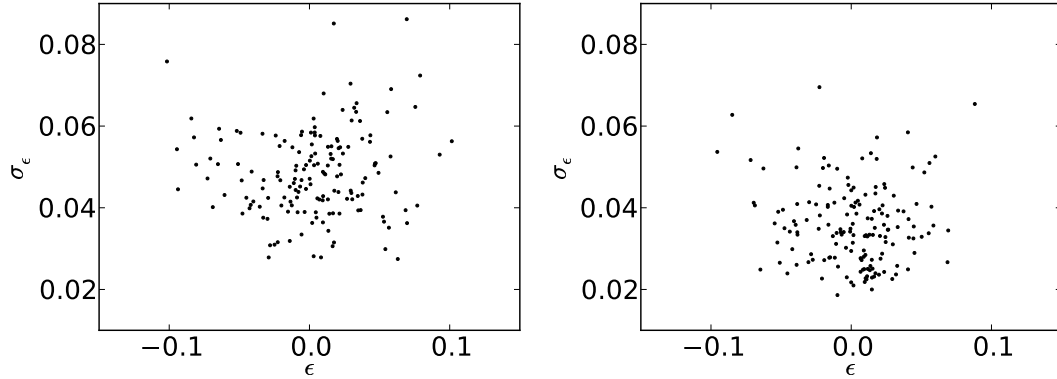


Figure 5.12: ϵ versus σ_ϵ before (left) and after (right) reconstruction for the 160 mocks. One can see that reconstruction decreases the scatter in the measured ϵ values (this is further highlighted in Figure 5.13). While reconstruction does decrease the average error on ϵ , we see that the errors we measure are still fairly large compared to the errors on α (see Figure 5.11). This suggests that our ability to detect ϵ with fidelity in current datasets such as the SDSS LRGs is marginal.

mean $\langle\epsilon\rangle = 0.001 \pm 0.003$ with an rms scatter between the mocks of 0.037 and a median $\tilde{\epsilon} = 0.004$ with quantiles ${}^{+0.032}_{-0.037}$. After reconstruction, we measure a mean $\langle\alpha\rangle = 1.002 \pm 0.002$ with an rms scatter between the mocks of 0.024 and a median $\tilde{\alpha} = 1.002$ with quantiles ${}^{+0.023}_{-0.022}$. For ϵ we measure a mean $\langle\epsilon\rangle = 0.002 \pm 0.003$ with an rms scatter between the mocks of 0.032 and a median $\tilde{\epsilon} = 0.007$ with quantiles ${}^{+0.023}_{-0.037}$. These values were calculated after rejecting the mocks where the acoustic signal is too weak to obtain an accurate centroiding of the BAO peak. This corresponds to making a cut in σ_α at 0.07 and discarding the mocks that lie above this cut as demonstrated in Xu et al. (2012). Before reconstruction, 9 mocks lie above this cut and after reconstruction, 0 lie above this cut.

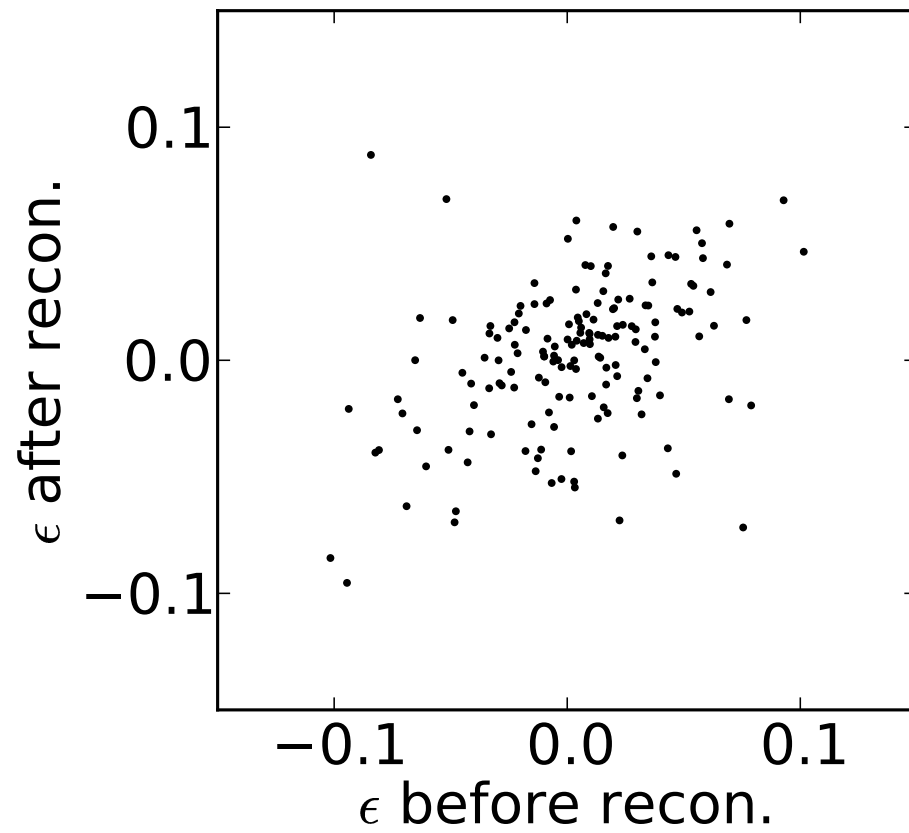


Figure 5.13: ϵ before reconstruction versus ϵ after reconstruction fit from the 160 mocks. The slope of a linear fit to these points is less than 1 implying that the post-reconstruction ϵ values have smaller scatter.

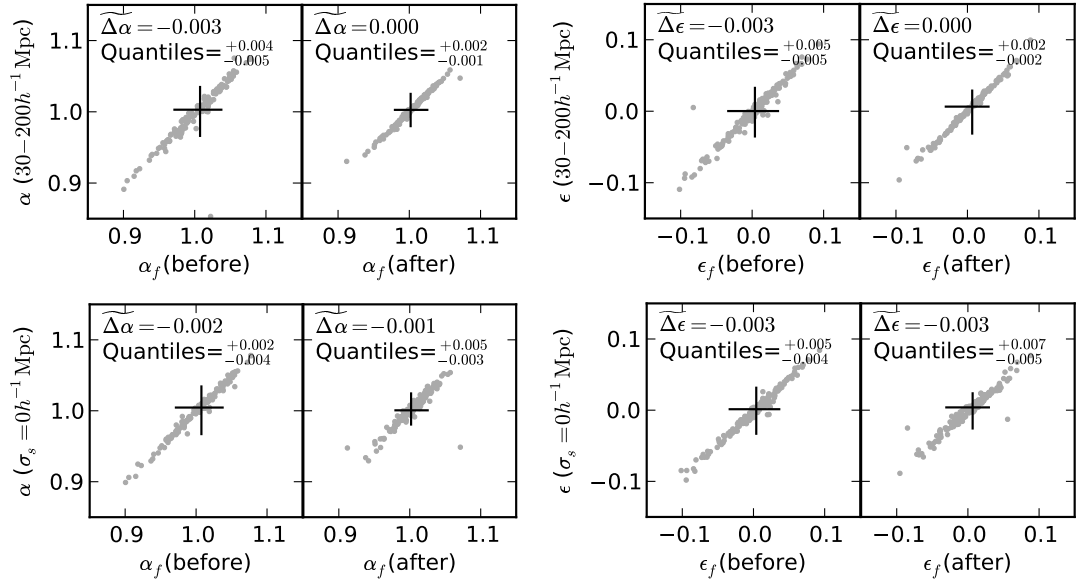


Figure 5.14: The robustness of our fitting model as demonstrated by α and ϵ scatter plots for some sample cases. Results for other tweaks to the fiducial model are given in Table 5.2. The plotted α and ϵ values were obtained through fitting the mock correlation functions before and after reconstruction. The plots are presented in pairs: α on the left and ϵ on the right. The first plot in each pair shows the pre-reconstruction results and the second plot shows the post-reconstruction results. If we obtain consistent measurements of α and ϵ , then we should see $\Delta\alpha$ and $\Delta\epsilon$ values that are ~ 0 . We see that this is true at the level of our current statistical precision. Therefore, our fitting model is reasonably robust against small changes to the fiducial model parameters. (top) Comparison of results obtained using a larger fitting range ($30 < r < 200 h^{-1} \text{Mpc}$) versus the fiducial fitting range. Here, we see an average $\Delta\alpha$ that is ~ -0.003 before reconstruction. The error on the mean is a factor of $\sim \sqrt{160}$ smaller than the scatter indicated by the quantiles, which makes this 0.003 shift statistically significant. This is caused by the templates being poor matches to the data at low r . While the $A_{0,2}(r)$ terms attempt to compensate for this, accurate fitting of the BAO scale is compromised. The significant $\Delta\epsilon$ in this case is rooted in the same cause. The fact that $\Delta\alpha$ and $\Delta\epsilon$ are both 0 after reconstruction suggests that the post-reconstruction model is better matched to the data. (bottom) Comparison of results obtained using $\Sigma_s = 0 h^{-1} \text{Mpc}$ versus the fiducial value of $\Sigma_s = 4 h^{-1} \text{Mpc}$. Here, we see that the average $\Delta\epsilon$ is different from 0 when considering the error on the mean. This is caused by the quadrupole model being a less optimal match to the data. We note that these small shifts in α and ϵ are certainly not detectable in each mock, which have much larger errors on α and ϵ than ~ 0.003 .

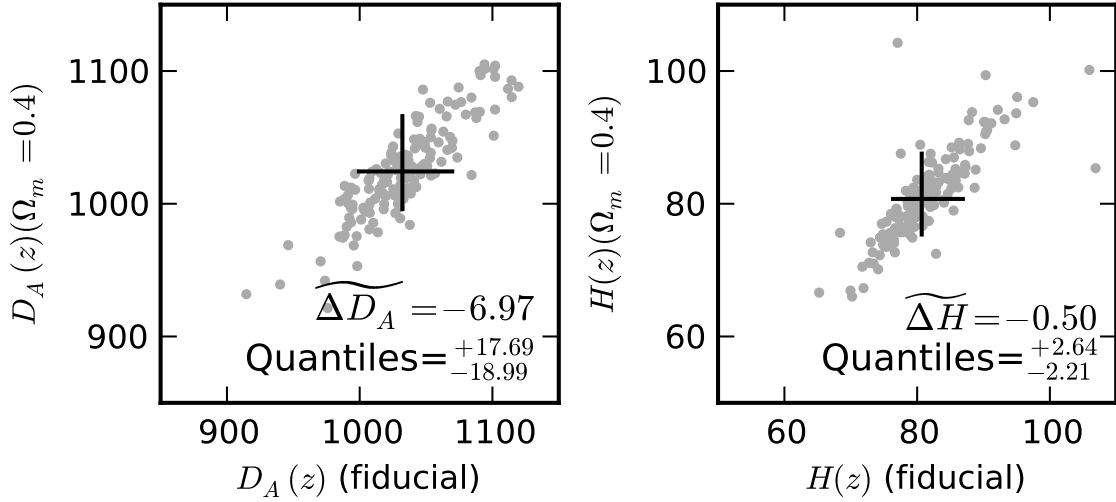


Figure 5.15: $D_A(z)$ and $H(z)$ scatter plots obtained by plotting those measured using an $\Omega_m = 0.4$ cosmology versus the true LasDamas cosmology. $D_A(z)$ is in units of Mpc and $H(z)$ is in units of km/s/Mpc. These values were calculated using Equations (5.5) & (5.6) and assuming $r_s = 159.71$ Mpc. The median ΔD_A and ΔH values are significantly different from 0 when approximating the error on the median as the scatter predicted by the quantiles divided by $\sqrt{160}$. Such a discrepancy may be due to our median redshift not being exactly $z = 0.35$ as assumed or the breakdown of the Taylor expansions around $\alpha = 1$ and $\epsilon = 0$ made in the derivation of our fitting model. In the $\Omega_m = 0.4$ cosmology, our measured α and ϵ deviate from 1 and 0 as shown in the last row of Table 5.2. We again emphasize that while this difference is detectable in the median α and ϵ of the mocks, it is not significant in each individual mock.

Table 5.1: ϵ statistics for various mock combinations. The first column indicates the number of mocks we have combined (m). The second column quotes the mean ϵ we measure with the standard error on the mean. The third column shows the rms of the mocks. The fourth column quotes the median ϵ and the fifth column quotes the quantiles.

m	$\langle\epsilon\rangle$	rms	$\tilde{\epsilon}$	Qtls
Redshift Space without Reconstruction				
1	0.001 ± 0.003	0.037	0.004	$+0.032$ -0.037
2	0.001 ± 0.003	0.029	0.006	$+0.023$ -0.030
4	0.001 ± 0.003	0.019	-0.001	$+0.017$ -0.010
8	0.002 ± 0.003	0.012	0.002	$+0.009$ -0.013
Redshift Space with Reconstruction				
1	0.002 ± 0.003	0.032	0.007	$+0.023$ -0.037
2	0.003 ± 0.002	0.018	0.006	$+0.012$ -0.020
4	0.003 ± 0.002	0.012	0.003	$+0.012$ -0.011
8	0.003 ± 0.002	0.008	0.006	$+0.004$ -0.007

Table 5.2: Fitting results from the mocks for various models. The model is given in column 1. The median α is given in column 2 with the 16th/84th percentiles from the mocks given in column 3 (these are denoted as the quantiles in the text, hence the label Qtls in the table). The median ϵ is given in column 6 with corresponding quantiles in column 7. The median difference in α on a mock-by-mock basis between the model listed in column 1 and the fiducial model is given in column 4 with corresponding quantiles in column 5. The analogues for ϵ are given in columns 8 and 9. The mean χ^2/dof is given in column 10.

Model	$\tilde{\alpha}$	Qtls	$\widetilde{\Delta\alpha}$	Qtls	$\tilde{\epsilon}$	Qtls	$\widetilde{\Delta\epsilon}$	Qtls	$\langle\chi^2\rangle/dof$
Redshift Space without Reconstruction									
Fiducial [f]	1.008	$^{+0.030}_{-0.036}$	–	–	0.004	$^{+0.032}_{-0.037}$	–	–	91.92/90
Fit w/ $(\Sigma_{\perp}, \Sigma_{\parallel}) \rightarrow (8, 8)h^{-1}\text{Mpc}$.	1.008	$^{+0.029}_{-0.039}$	0.001	$^{+0.003}_{-0.003}$	0.001	$^{+0.032}_{-0.037}$	–0.002	$^{+0.003}_{-0.003}$	91.97/90
Fit w/ $\Sigma_s \rightarrow 0h^{-1}\text{Mpc}$.	1.005	$^{+0.030}_{-0.037}$	–0.002	$^{+0.003}_{-0.004}$	0.000	$^{+0.031}_{-0.033}$	–0.003	$^{+0.005}_{-0.004}$	91.76/90
Fit w/ $A_2(r) = poly2$.	1.006	$^{+0.031}_{-0.036}$	0.000	$^{+0.002}_{-0.001}$	0.005	$^{+0.032}_{-0.036}$	0.001	$^{+0.005}_{-0.005}$	93.08/91
Fit w/ $A_2(r) = poly4$.	1.006	$^{+0.031}_{-0.035}$	0.000	$^{+0.001}_{-0.001}$	0.002	$^{+0.037}_{-0.033}$	–0.000	$^{+0.007}_{-0.007}$	90.98/89
Fit w/ $30 < r < 200h^{-1}\text{Mpc}$ range.	1.003	$^{+0.032}_{-0.037}$	–0.003	$^{+0.004}_{-0.005}$	0.000	$^{+0.032}_{-0.035}$	–0.003	$^{+0.005}_{-0.005}$	105.90/104
Fit w/ $70 < r < 200h^{-1}\text{Mpc}$ range.	1.007	$^{+0.030}_{-0.035}$	0.000	$^{+0.002}_{-0.002}$	0.004	$^{+0.032}_{-0.040}$	0.000	$^{+0.003}_{-0.003}$	79.33/76
Fit w/ $50 < r < 150h^{-1}\text{Mpc}$ range.	1.005	$^{+0.031}_{-0.040}$	–0.000	$^{+0.004}_{-0.006}$	0.004	$^{+0.036}_{-0.043}$	–0.001	$^{+0.008}_{-0.007}$	54.34/58
Redshift Space with Reconstruction									
Fiducial [f]	1.002	$^{+0.023}_{-0.022}$	–	–	0.007	$^{+0.023}_{-0.037}$	–	–	92.68/90
Fit w/ $(\Sigma_{\perp}, \Sigma_{\parallel}) \rightarrow (2, 4)h^{-1}\text{Mpc}$.	1.002	$^{+0.023}_{-0.021}$	–0.000	$^{+0.001}_{-0.001}$	0.008	$^{+0.022}_{-0.037}$	0.000	$^{+0.001}_{-0.001}$	92.73/90

Continued on next page

Table 5.2 – continued from previous page

Model	$\tilde{\alpha}$	Qtls	$\widetilde{\Delta\alpha}$	Qtls	$\tilde{\epsilon}$	Qtls	$\widetilde{\Delta\epsilon}$	Qtls	$\langle\chi^2\rangle/dof$
Fit w/ $\Sigma_s \rightarrow 0h^{-1}\text{Mpc}$.	1.001	$^{+0.024}_{-0.020}$	-0.001	$^{+0.005}_{-0.003}$	0.004	$^{+0.020}_{-0.030}$	-0.003	$^{+0.007}_{-0.005}$	92.27/90
Fit w/ $A_2(r) = poly2$.	1.002	$^{+0.024}_{-0.022}$	0.000	$^{+0.001}_{-0.000}$	0.008	$^{+0.023}_{-0.037}$	0.001	$^{+0.002}_{-0.002}$	94.23/91
Fit w/ $A_2(r) = poly4$.	1.002	$^{+0.023}_{-0.022}$	0.000	$^{+0.001}_{-0.001}$	0.005	$^{+0.025}_{-0.037}$	-0.001	$^{+0.004}_{-0.004}$	91.68/89
Fit w/ $30 < r < 200h^{-1}\text{Mpc}$ range.	1.003	$^{+0.022}_{-0.023}$	0.000	$^{+0.002}_{-0.001}$	0.006	$^{+0.022}_{-0.038}$	0.000	$^{+0.002}_{-0.002}$	106.12/104
Fit w/ $70 < r < 200h^{-1}\text{Mpc}$ range.	1.002	$^{+0.023}_{-0.021}$	0.000	$^{+0.001}_{-0.001}$	0.006	$^{+0.022}_{-0.036}$	-0.000	$^{+0.002}_{-0.002}$	79.99/76
Fit w/ $50 < r < 150h^{-1}\text{Mpc}$ range.	1.002	$^{+0.024}_{-0.023}$	-0.001	$^{+0.004}_{-0.004}$	0.008	$^{+0.022}_{-0.037}$	-0.001	$^{+0.005}_{-0.005}$	54.65/58
Recon. w/ $\beta \rightarrow 0.24$.	1.002	$^{+0.023}_{-0.022}$	-0.000	$^{+0.001}_{-0.001}$	0.005	$^{+0.023}_{-0.033}$	0.000	$^{+0.002}_{-0.003}$	92.49/90
Recon. w/ $\beta \rightarrow 0.36$.	1.002	$^{+0.022}_{-0.020}$	0.000	$^{+0.001}_{-0.002}$	0.005	$^{+0.024}_{-0.038}$	-0.000	$^{+0.002}_{-0.002}$	92.89/90
Recon. w/ $b \rightarrow 1.8$.	1.001	$^{+0.022}_{-0.021}$	-0.000	$^{+0.006}_{-0.005}$	0.006	$^{+0.025}_{-0.041}$	-0.000	$^{+0.006}_{-0.006}$	92.61/90
Recon. w/ $b \rightarrow 2.6$.	1.003	$^{+0.023}_{-0.023}$	0.001	$^{+0.004}_{-0.004}$	0.004	$^{+0.025}_{-0.036}$	-0.001	$^{+0.006}_{-0.005}$	92.65/90
Recon. w/ Wiener Filter.	1.004	$^{+0.020}_{-0.022}$	-0.000	$^{+0.004}_{-0.003}$	0.005	$^{+0.024}_{-0.035}$	-0.000	$^{+0.004}_{-0.004}$	92.69/90
Recon. on $\Omega_m = 0.4$ case. ¹	0.832	$^{+0.021}_{-0.019}$	-0.171	$^{+0.010}_{-0.010}$	0.020	$^{+0.028}_{-0.037}$	0.017	$^{+0.014}_{-0.014}$	92.61/90

¹ $\alpha = 1$ and $\epsilon = 0$ in the LasDamas cosmology correspond to $\alpha = 0.832$ and $\epsilon = 0.013$ in this $\Omega_m = 0.4$ cosmology according to Equations (5.5 & 5.6).

The median ϵ in the pre- and post-reconstruction cases are different from 0 and from the mean at $\gtrsim 1$ -2 times the error on the mean. In addition, the post-reconstruction quantiles are asymmetric, implying that the posterior ϵ distribution deviates from Gaussian. These appear to be in part due to the intrinsic noise in the data and in part due to a slight mismatch between the model and the data. To reduce noise, we combine our 160 mocks into groups of 2, 4 and 8, and re-perform our fits. In general, we see a better agreement between the mean and median ϵ . The quantiles remain mildly asymmetric in some cases but overall we see improved agreement. The rms scatter decreases by roughly the expected amount ($\sim \sqrt{m}$, where $m = 2, 4$ or 8) if we consider ϵ to be Gaussian. These results are summarized in Table 5.1.

We see that there is a persistent bias in ϵ towards non-zero values that is currently below our detection threshold. This bias is $\lesssim 1\sigma$ significant before reconstruction and only at the 1 - 1.5σ level after reconstruction. To further test this, we split the mocks into 2 groups of 80 which reduces the noise in the data. After re-performing the fits, we find $\langle \epsilon \rangle \sim 0.002$ both before and after reconstruction. These values agree with the fit results to the average of the 160 mocks described above. This suggests that the persistent bias in ϵ is not due to noise but is rather a result of some mismatch between the model and the data. In our fits we fix Σ_{\perp} , Σ_{\parallel} and Σ_s , and use the nuisance terms in $A_2(r)$ to account for any other mismatch in the broadband shape between the model and the data. However Σ_{\perp} , Σ_{\parallel} and Σ_s are partially degenerate with ϵ , so if they are fixed at non-optimal values that cannot be fully compensated by $A_2(r)$ (see bottom row of Figure 5.14), the fitter can resort to adjusting ϵ . We stress however, that such small biases in our redshift-space measurements of ϵ are below the current detection limit in a single DR7 realization as indicated by the rms of the mocks.

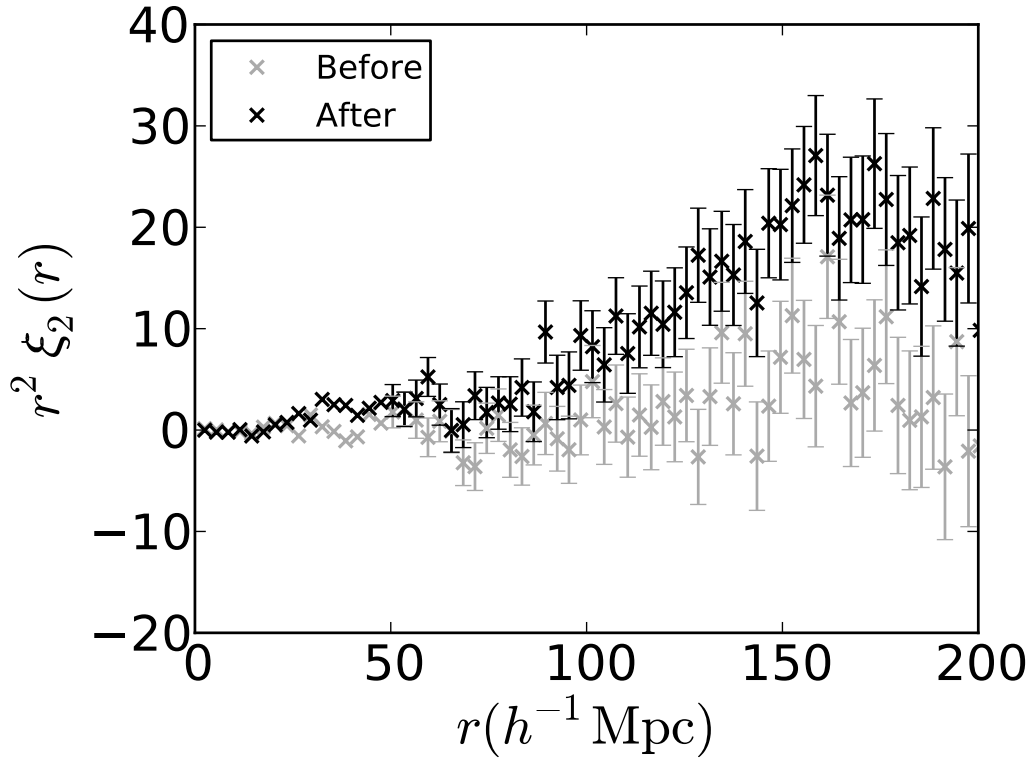


Figure 5.16: Average quadrupole from the mocks in real space before (grey) and after (black) reconstruction. The quadrupole before reconstruction is very close to 0 as we would expect in real space due to the lack of redshift-space distortions. Our ϵ measurements are unbiased in this case which suggests that the small biases we see in redshift space are due to slight mismatches between our redshift-space distortion models and the actual broadband in the data. After reconstruction, the quadrupole at large scales acquires some additional power likely due to the survey geometry and sample number density fluctuations as a function of redshift. Our post-reconstruction real space ϵ measurements remain unbiased which suggests that this anisotropy can be accounted for by our $A_2(r)$ nuisance terms.

We can gain additional insights by analyzing the real-space mocks which do not have redshift-space distortions and therefore do not require Σ_s or anisotropic Σ_{nl} in the model. We find that these give non-biased measures of ϵ in both the pre- and post-reconstruction cases. In the pre-reconstruction case we measure the mean ϵ to be $\langle\epsilon\rangle = 0.003 \pm 0.003$ with an rms between the mocks of 0.037. The median is $\tilde{\epsilon} = 0.002$ with quantiles ${}^{+0.040}_{-0.040}$. After reconstruction we measure $\langle\epsilon\rangle = 0.001 \pm 0.002$ with a mock rms of 0.027 and $\tilde{\epsilon} = -0.002$ with quantiles ${}^{+0.030}_{-0.023}$. One can see that the mean and median ϵ are consistent with each other and with 0. Fitting the average of the 160 mocks gives $\epsilon = 0.001$ and 0.000 before and after reconstruction respectively; again implying a largely unbiased measurement of ϵ in real space.

An interesting artifact we do find is that reconstruction appears to introduce some broadband anisotropy as shown in Figure 5.16. Here we have plotted the mean of the real-space quadrupoles before (grey) and after (black) reconstruction. We see that the quadrupole is nearly 0 before reconstruction as expected since there should not be any anisotropies in real space. However, after reconstruction, the quadrupole acquires some additional large-scale power. The reconstruction displacement vectors may take on a subtle anisotropy due to the variation of number density with redshift or the survey geometry (i.e. if it is wider than it is deep). Fortunately, this broadband anisotropy introduced by reconstruction is fairly smooth and can be removed by the $A_2(r)$ nuisance parameters as evidenced by our unbiased measures of ϵ in post-reconstruction real space.

To build more intuition for the parameters we fit in redshift space and to demonstrate their inter-dependencies, we show various scatter plots of these quantities in Figures 5.9, 5.10, 5.11, 5.12 & 5.13. Figure 5.9 shows the values of β and ϵ we obtain from our fits to the 160 mocks after reconstruction. Our pre-reconstruction results are similar. As expected, these two parameters are not degenerate with each other.

The top panel of Figure 5.10 shows the ϵ versus α values we measure from the mocks after reconstruction. Again we see that these two parameters are not highly correlated. The correlation coefficient between D_A and H is predicted to be $\rho_{D_A H} \sim 0.4$ (Seo & Eisenstein, 2007). This subsequently predicts a σ_H/H -to- σ_{D_A}/D_A ratio ~ 2 (i.e. the percentage error of the Hubble parameter is twice that of the angular diameter distance). Using these values, a Fisher matrix argument shows that we should expect $\rho_{\alpha\epsilon} \sim 0.21$ (see Appendix 8). The correlation coefficient between the α and ϵ values plotted in Figure 5.10 is 0.20 and the corresponding pre-reconstruction value is 0.27. Both are in excellent agreement with the Fisher matrix prediction. The bottom panel of Figure 5.10 shows our α and ϵ measurements translated into measurements of D_A and H using Equations (5.5) & (5.6). In the plotted post-reconstruction case, the correlation coefficient between D_A and H is ~ 0.50 and in the pre-reconstruction case it is ~ 0.23 , which are not too different from our assumed $\rho_{D_A H} = 0.4$.

Figure 5.11 shows σ_ϵ versus σ_α for the mocks after reconstruction. We see that the errors on α and ϵ are correlated which implies that mocks with poorer measurements of the acoustic scale (i.e. larger σ_α values) also have poorer measurements of the BAO anisotropy (i.e. larger σ_ϵ values). We see a similar correlation in the pre-reconstruction results. Taking the ratio of $\sigma_\epsilon/(1+\epsilon)$ -to- σ_α/α , we find a median ~ 1.3 before reconstruction and ~ 1.4 after reconstruction. Fisher matrix arguments predict a ratio of ~ 1.2 (Equation (8.16)), which is similar to what we see.

Figure 5.12 shows the values of ϵ we measure versus σ_ϵ before (left) and after (right) reconstruction. Reconstruction clearly decreases the scatter in ϵ which is again highlighted in Figure 5.13, showing the values of ϵ before and after reconstruction. While the two are correlated, the post-reconstruction values have smaller scatter as evidenced by the locus of points having a slope shallower than 1:1. From

Figure 5.12 we also see that reconstruction decreases σ_ϵ , our estimated error on ϵ . However, these σ_ϵ values are still large compared to σ_α (see Figure 5.11). This suggests that we are only able to obtain marginal detections of ϵ in current datasets such as the SDSS DR7 LRGs.

Next we test the robustness of our fitting model to changes in various model parameters. A full list of these results are found in Table 5.2 for changes of Σ_\perp , Σ_\parallel , Σ_s , fitting range and form of $A_2(r)$ both before and after reconstruction. In the table, *poly2* corresponds to an $A_2(r) = a_1/r^2 + a_2/r$ and *poly4* corresponds to an $A_2(r) = a_1/r^2 + a_2/r + a_3 + a_4r$. We see that the scatter in α between the mocks can show $\sim 10\%$ variations between the different cases; however, this is quite rare. For ϵ on the other hand, we see $\sim 10\%$ variations quite often. This again indicates the noisiness of our ϵ measurements.

Figure 5.14 shows scatter plots in α and ϵ for a few sample cases. Here, $\Delta\alpha$ and $\Delta\epsilon$ are the differences between the α and ϵ values measured using the slightly altered model and the fiducial model. We expect the average $\Delta\alpha$ and $\Delta\epsilon$ to be 0 within the errors if our measurements of α and ϵ are consistent between the two models. We see that in all cases, $\Delta\alpha = 0$ and $\Delta\epsilon = 0$ fall within the scatter predicted by the quantiles on a mock-by-mock basis. However, the errors on the average $\Delta\alpha$ and $\Delta\epsilon$ are on the order of $\sqrt{160}$ times smaller than the scatter implied by the mocks. This indicates that in a few cases, we detect a significant shift in the average value of α and ϵ measured.

In particular, this occurs in the pre-reconstruction cases where we have changed the fitting range. The α and ϵ scatter plots for the $30 < r < 200h^{-1}\text{Mpc}$ fitting range versus the fiducial fitting range cases are shown in the top row of Figure 5.14. The plots are shown in pairs with α on the left and ϵ on the right. The first plot in each pair corresponds to the pre-reconstruction case and the second plot to the post-

reconstruction case. We see that on average, the larger fitting range gives slightly smaller values of α and ϵ . If we begin fitting at $r = 30h^{-1}\text{Mpc}$ where the errorbars are smaller, the fitter forces the model to match the data at these small scales where we know the templates (especially the quadrupole) are not faithful representations of the data. The $A_{0,2}(r)$ marginalization terms compensate for this at the expense of accurately fitting the BAO scale. After reconstruction, $\Delta\alpha$ and $\Delta\epsilon$ are both 0 which suggests that the model is better matched to the data in this case.

We also see average $\Delta\epsilon$ values that are significantly different from zero in the $\Sigma_s = 0h^{-1}\text{Mpc}$ case both before and after reconstruction. This is illustrated in the bottom row of Figure 5.14. $\Sigma_s = 0h^{-1}\text{Mpc}$ implies that we exclude FoG from the model, which is unrealistic as it is implemented in the mocks. The likely culprit here is again the mismatch between the data and the model at small r especially in the quadrupole. In addition, if we compare the dotted line in Figure 5.4 (the $\Sigma_s = 0h^{-1}\text{Mpc}$ case) and the average quadrupole in Figure 5.7, we see that the quadrupole BAO feature in this model is a poorer fit to the data overall. The mocks show more of a crest-trough-crest structure near the BAO scale as in the fiducial parameter template (solid line in Figure 5.2) whereas the trough in the $\Sigma_s = 0h^{-1}\text{Mpc}$ case is much weaker. This is further affirmed by the fact that the dotted line in Figure 5.3 (isotropic Σ_{nl}) has a similar looking BAO feature and shows a similar discrepancy in ϵ relative to the fiducial model before reconstruction. The fitter can partially compensate for these differences through adjusting the value of ϵ which also gives rise to crests and troughs near the BAO scale, although with different structure than those introduced through Σ_{\perp} , Σ_{\parallel} and Σ_s . Hence one must pick a quadrupole model that has a BAO feature fairly well matched to the data to avoid biasing the ϵ values measured.

Despite these offsets in the median α and ϵ for different fitting models, we note

that at the statistical precision of current datasets, we would not be able to detect any of these changes. For the DR7 mocks, σ_α is ~ 0.04 before reconstruction and ~ 0.03 after reconstruction. The average σ_ϵ are even larger at ~ 0.05 before reconstruction and ~ 0.04 after reconstruction. Hence, assuming that σ_α and σ_ϵ characterize the error on α and ϵ , a 0.003 shift will fall entirely within the expected errors. Therefore, our fitting model is reasonably robust against small changes to model parameters and our measured α and ϵ values are largely unbiased.

We perform similar exercises for various different reconstruction parameters such as the bias and β values we input to the algorithm. The fiducial reconstruction parameters we use are $b = 2.2$ and $\beta = 0.3$. We also generate the constrained Gaussian realizations in a manner equivalent to Wiener filtering the data in the observed region. This is akin to setting the unconstrained Gaussian realization amplitudes (δ_U in Equation (3) of Padmanabhan et al. (2012a)) to 0, the expected mean amplitude from averaging over many constrained realizations. In our fiducial procedure, the δ_U are matched to the observed density field. The fitting results of these cases are also listed in Table 5.2. We see that in all cases we recover similar values of α and ϵ . This indicates that our fitting model effectively marginalizes away the broadband signal introduced by reconstruction when incorrect values of the fiducial parameters are used. The model is robust against small changes in reconstruction parameters and returns reliable measurements of α and ϵ .

Finally we calculate and perform our fits using a fiducial cosmology that is significantly different to the LasDamas cosmology. This forces a stronger anisotropic BAO signal to appear in the quadrupole. We pick a cosmology with $\Omega_m = 0.4$ that preserves the matter-to-baryon ratio of LasDamas. We also fix $\Omega_m h^2$ which implies $h = 0.553$. We convert the measured α and ϵ values to $D_A(z)$ and $H(z)$ using Equations (5.5) & (5.6) and compare these to the values measured using the fiducial

cosmology. This is illustrated in Figure 5.15. The equations listed above only allow us to infer $D_A(z)/r_s$ and $H(z)r_s$. We have assumed $r_s = 159.71$ Mpc, which is the sound horizon in the LasDamas cosmology, to obtain the $D_A(z)$ and $H(z)$ values plotted in the figure. In the LasDamas cosmology (which is the true cosmology in our mocks), $D_A(z) = 1032$ Mpc and $H(z) = 81.8$ km/s/Mpc at $z = 0.35$. Taking the ratio $\widetilde{\Delta D}_A/D_A(z)$ and $\widetilde{\Delta H}/H(z)$ implies that on average our measurements of $D_A(z)$ and $H(z)$ using the $\Omega_m = 0.4$ cosmology and the true LasDamas cosmology differ by $\sim 0.7\%$ and $\sim 0.6\%$ respectively. Dividing the scatter indicated by the quantiles by $\sqrt{160}$ suggests that these average offsets are significant, although again, in a single mock, we would not be able to detect these offsets. The fiducial $D_A(z)$ and $H(z)$ are calculated assuming a median redshift of $z = 0.35$; however, if the true median redshift were slightly different, such discrepancies would not be unexpected. In addition, our models for α and ϵ are based on Taylor expansions around 1 and 0 respectively. When the fitting model is constructed using a fiducial cosmology that is extremely wrong, the α and ϵ values we measure can deviate significantly from 1 and 0 as shown in the last row of Table 5.2. Our first-order Taylor assumption may be breaking down at this point, further affecting our measurements. In this case, one can iteratively change the fiducial cosmology and re-fit for α and ϵ until values closer to 1 and 0 are obtained.

We verify our assumption that the standard deviation of $p(\alpha)$ and $p(\epsilon)$ are good indicators of the errors on α and ϵ in Figure 5.17. The top panel of this figure shows a normalized histogram of $(\alpha - \langle\alpha\rangle)/\sigma_\alpha$ after reconstruction and the bottom panel shows the analogue for ϵ . The best-fit Gaussian is overplotted and the p-value from a K-S test is shown. This value gives the probability that the plotted distribution is drawn from a Gaussian. The pre-reconstruction p-values are 0.40 and 0.09 for α and ϵ respectively. These values indicate that there are finite probabilities that α and

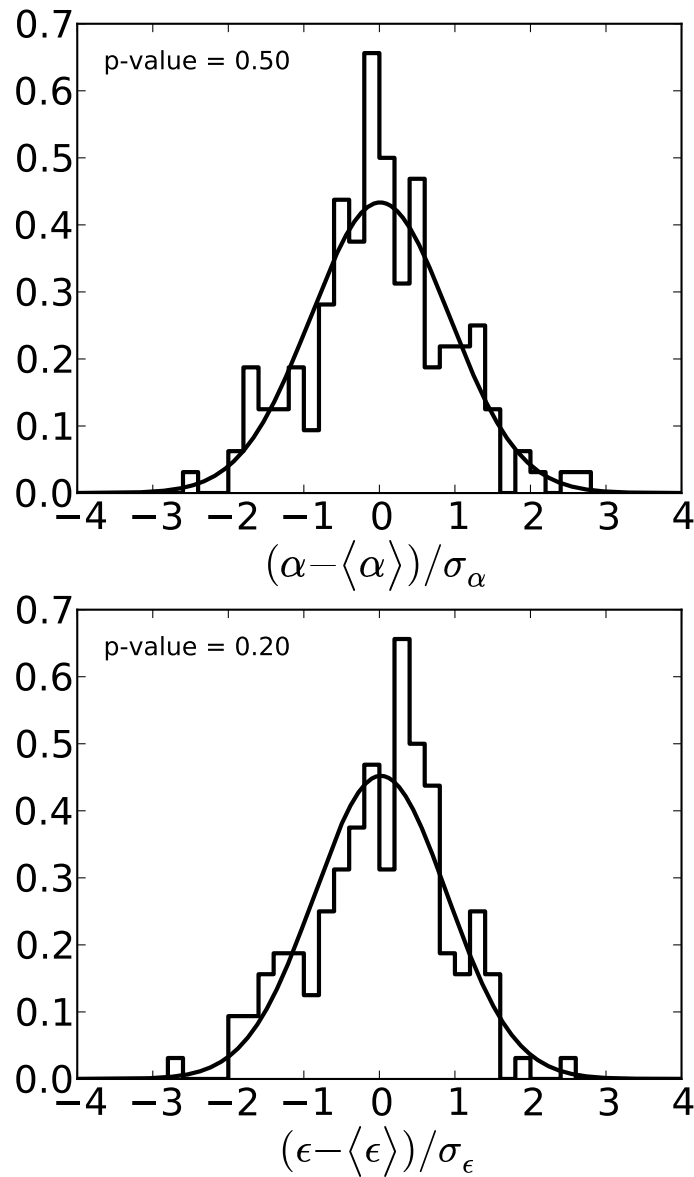


Figure 5.17: Histograms of $(\alpha - \langle \alpha \rangle) / \sigma_\alpha$ (top) and $(\epsilon - \langle \epsilon \rangle) / \sigma_\epsilon$ (bottom) after reconstruction. These are a measure of the signal-to-noise of our measured α and ϵ values. The best-fit Gaussians are overplotted as black lines. We perform a K-S test to see how likely these distributions are drawn from a normal distribution. The p-values or probabilities are indicated on the plots and imply that α and ϵ both have finite chances of being drawn from Gaussian distributions. This verifies that the standard deviations σ_α and σ_ϵ we calculate from $\chi^2(\alpha, \epsilon)$ characterize the errors on α and ϵ reasonably well. A similar conclusion holds for our α and ϵ values before reconstruction as well.

ϵ have Gaussian posteriors. Hence the standard deviations σ_α and σ_ϵ we calculate from $\chi^2(\alpha, \epsilon)$ characterize the errors on α and ϵ reasonably well.

5.5 DR7 Results

5.5.1 Anisotropic Results

Now that we have verified the robustness of our techniques and obtained a better understanding of the anisotropic signal from our mocks, we can proceed to the actual SDSS DR7 LRG data. This dataset is described in more detail in §3.2.2. To calculate our fitting model for the data, we use the flat Λ CDM cosmology predicted by WMAP7: $H_0 = 70.2 \pm 1.4$, $\Omega_b h^2 = 0.02255 \pm 0.054$, $\Omega_c h^2 = 0.1126 \pm 0.0036$, $n_s = 0.968 \pm 0.012$ and $\sigma_8 = 0.816 \pm 0.024$ (Komatsu et al., 2011). For the covariance matrix, we again use the modified Gaussian covariance matrix discussed in §5.3.3 with the modification parameters derived from the mocks and the WMAP7 cosmology.

The results of our fits are shown in Figure 5.18. The pre-reconstruction results are in the top row and the post-reconstruction results are in the bottom row. Our ϵ measurements have fairly large errors, again indicating that our detection of any anisotropy is only marginal. However, reconstruction does help in bringing down this error. The acoustic peak appears much sharper after reconstruction, again indicating the effectiveness of our technique in undoing non-linear evolution. This is reflected in the decrease in error on α and ϵ by factors of 1.8 and 1.3 respectively after reconstruction. The quadrupole near $100h^{-1}$ Mpc scales is much closer to 0 after reconstruction which implies that our partial removal of the Kaiser effect was also successful. The deviation from 0 at larger scales again indicates that reconstruction is introducing some additional anisotropy (see Figure 5.16).

Using our measured α , σ_α , ϵ , σ_ϵ and $C_{\alpha\epsilon}$ values from the DR7 data, we can use

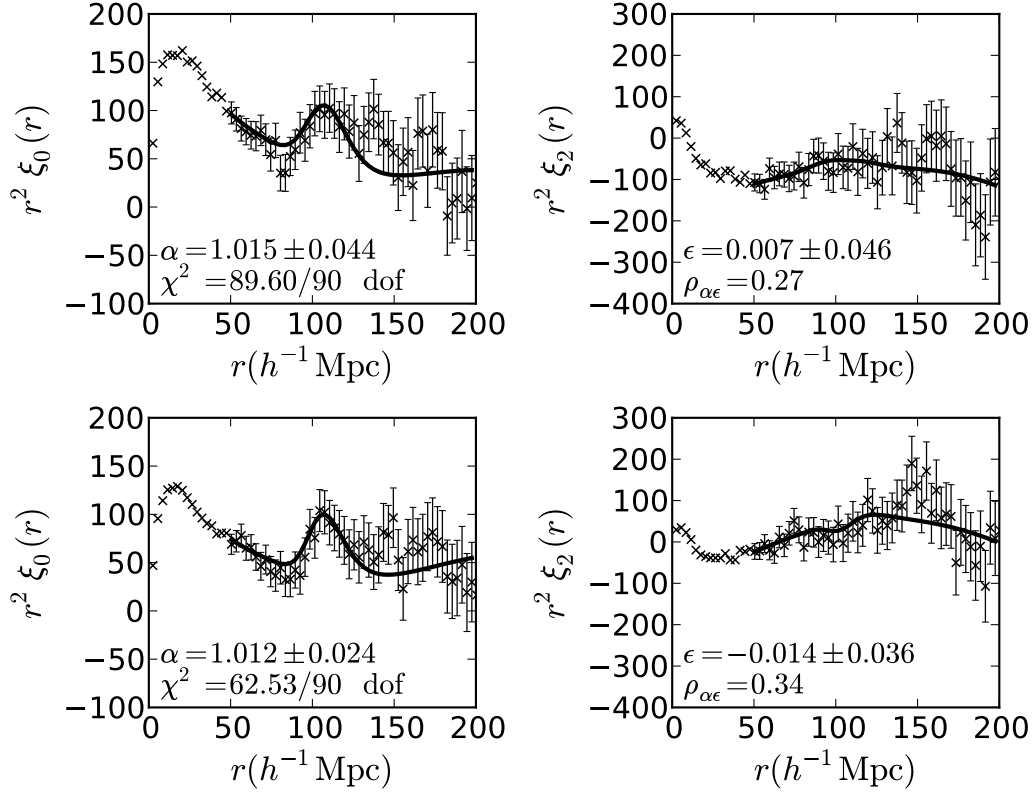


Figure 5.18: DR7 fit results before (top row) and after (bottom row) reconstruction. These values imply a 3.6% measurement of $D_A(z)$ and an 8.4% measurement of $H(z)$ after reconstruction. We see that the acoustic peak has sharpened up significantly after reconstruction as expected. The error on α decreases by a factor of 1.8 and the error on ϵ decreases by a factor of 1.3 as a result. The quadrupole is nearly 0 at $\sim 100h^{-1}\text{Mpc}$ after reconstruction, indicating the effectiveness of our Kaiser correction. The deviation from 0 at larger r is likely some anisotropy introduced by reconstruction.

Table 5.3: Summary of key measurements from DR7 data. Columns 2 and 3 list the α and ϵ values we measure. Column 4 lists the covariance between α and ϵ while column 5 lists their correlation coefficient. Column 6 and 7 list the distance constraints we obtain to $z = 0.35$ from our measured α and ϵ values. Columns 8 and 9 translate these relative distance measures into more tangible quantities assuming $r_s = 152.76$ Mpc as in the WMAP7 cosmology.

	α	ϵ	$C_{\alpha\epsilon}$	$\rho_{\alpha\epsilon}$	$D_A(z)/r_s$	$H(z)r_s$ (km/s)	$D_A(z)$ (Mpc)	$H(z)$ (km/s/Mpc)
Before recon.	1.015 ± 0.044	0.007 ± 0.046	0.00054	0.27	6.751 ± 0.363	12339 ± 1367	1031 ± 55	80.8 ± 9.0
After recon.	1.012 ± 0.024	-0.014 ± 0.036	0.00029	0.34	6.875 ± 0.249	12895 ± 1079	1050 ± 38	84.4 ± 7.1

Equations (5.5), (5.6), (5.8) & (5.9) to determine $D_A(z = 0.35)$ and $H(z = 0.35)$. These results are summarized in Table 5.3. The values in the table were obtained using the fiducial angular diameter distance and Hubble parameter in our WMAP7 cosmology: $D_{A,f} = 1022.7$ Mpc and $H_f = 83.1$ km/s/Mpc at $z = 0.35$. We see that post-reconstruction we have a $\sim 3.6\%$ measurement of $D_A(z)$ and $\sim 8.4\%$ measurement of $H(z)$ from SDSS DR7.

One can investigate whether DR7 is somehow an outlier with unusually large errors. We find that our DR7 measurements of σ_α and σ_ϵ are comparable to the scatter in α and ϵ from the mocks. Furthermore, we see that our DR7 σ_α and σ_ϵ measurements fall nicely within the locus of mock points as shown in Figure 5.19 for the post-reconstruction case. Note that the mock results shown in this figure are identical to Figure 5.11. Hence we have no reason to believe that our DR7 measurements have unusually large errors. The $\sigma_\epsilon/(1 + \epsilon)$ -to- σ_α/α ratio we obtain is ~ 1.1 before reconstruction and ~ 1.5 after reconstruction which is roughly consistent with the Fisher matrix prediction of ~ 1.2 . Lastly, we note that our σ_H/H -to- σ_{D_A}/D_A ratio is ~ 2 , consistent with the predictions of Seo & Eisenstein (2007) and the assumption that went into our Fisher matrix predictions (see Appendix 8).

The first column of Figure 5.20 shows the $\chi^2(\alpha, \epsilon)$ distribution measured at various grid points in α and ϵ . As described in §5.3.3, our α grid points are separated by 0.0025 in the range $0.7 < \alpha < 1.3$ and our ϵ grid points are separated by 0.005 in the range $-0.3 < \epsilon < 0.3$. The 1 through 6σ confidence levels for a 2D distribution are overplotted. The pre-reconstruction results are shown in the top row and the post-reconstruction results are shown in the bottom row. One can see that the contours in the central regions are fairly elliptical, indicating a nearly parabolic χ^2 distribution. As we go to smaller α , the acoustic peak in the model is being pushed out to larger scales where the errorbars are larger. Hence it is much easier

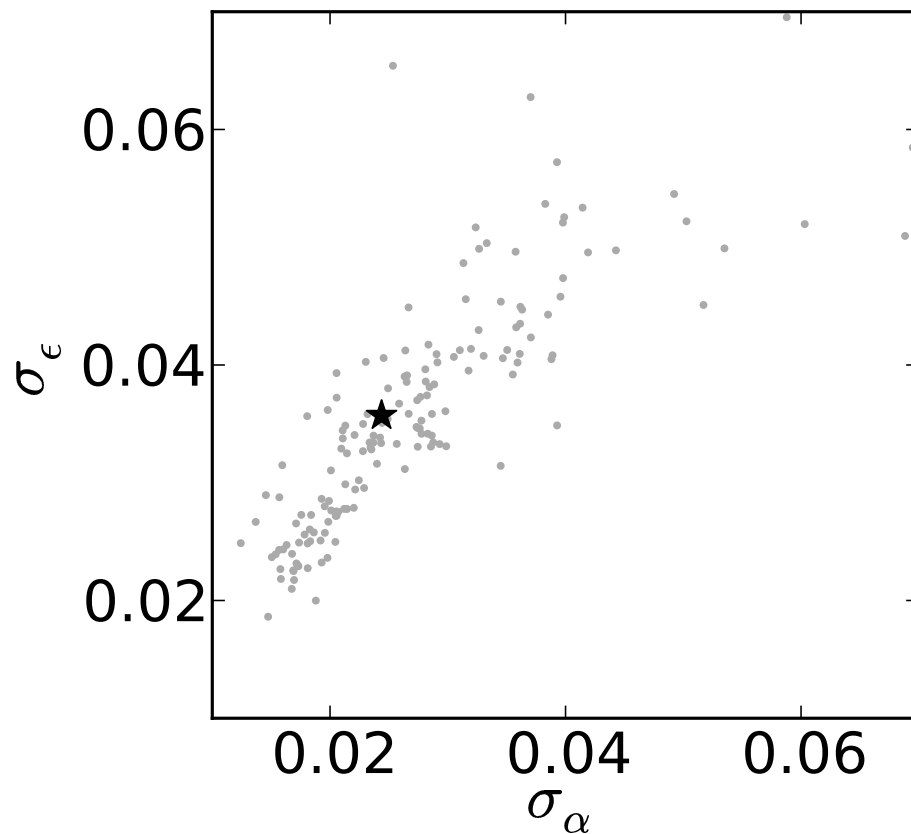


Figure 5.19: Post-reconstruction σ_α versus σ_ϵ for the mocks with the DR7 point overplotted as the black star. Note that the mock points are identical to Figure 5.11. We see that our DR7 measurement falls nicely within the locus of mock points which suggests that it is not unusual. The DR7 $\sigma_\epsilon/(1 + \epsilon)$ -to- σ_α/α ratio is ~ 1.1 before reconstruction and ~ 1.5 after reconstruction, roughly consistent with the Fisher matrix prediction of ~ 1.2 .

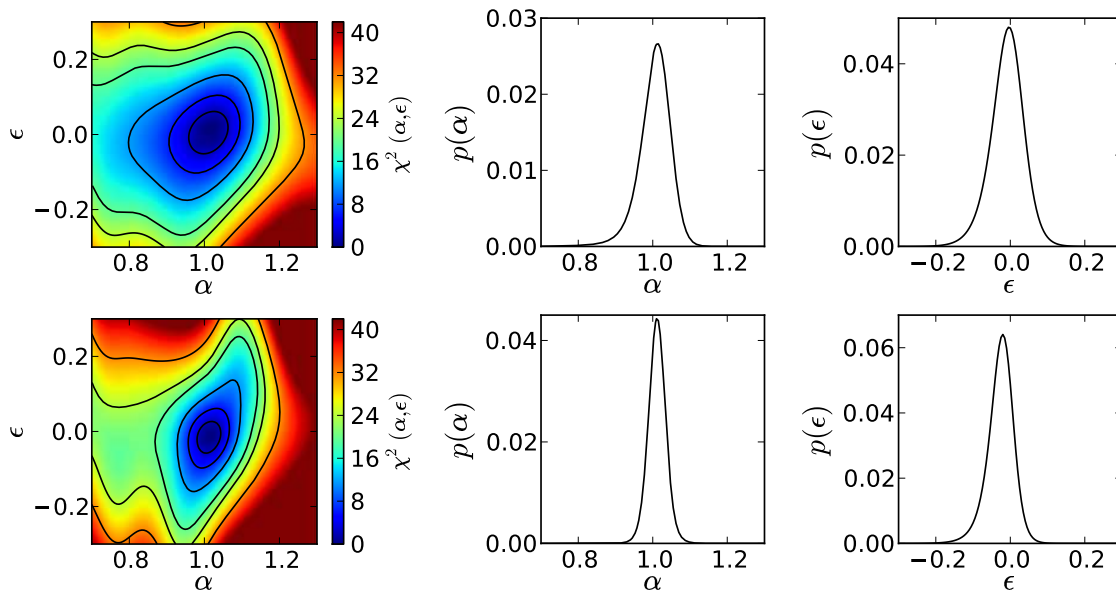


Figure 5.20: The $\chi^2(\alpha, \epsilon)$ distribution (column 1) and the derived $p(\alpha)$ and $p(\epsilon)$ distributions (columns 2 & 3) for DR7. The pre-reconstruction results are in the top row and the post-reconstruction results are in the bottom row. Contour levels corresponding to $1-6\sigma$ for a 2D distribution are overplotted. The central regions of the χ^2 distributions are fairly elliptical which indicates their parabolic natures. We apply a 0.15 prior in $\log(\alpha)$ to suppress the unphysical downturn at low α which corresponds to the acoustic peak being pushed out to large r . The errorbars are much larger here and the fitter has an easier time hiding the peak inside the errors. The plateauing of the distribution at small α is a result of this. We also see that after reconstruction, the contours become much tighter. This corresponds to the tightening of $p(\alpha)$ and $p(\epsilon)$ after reconstruction seen in columns 2 & 3 due to the sharpening up of the acoustic peak. We see that $p(\alpha)$ and $p(\epsilon)$ are nearly Gaussian and hence the standard deviations σ_α and σ_ϵ characterize the errors on α and ϵ well.

for the fitter to hide the peak within the errors. Although we have applied a 0.15 prior in $\log(\alpha)$ to suppress this unphysical downturn in χ^2 , the distribution still plateaus in this region. One can also see that after reconstruction, the $\chi^2(\alpha, \epsilon)$ distribution is much tighter at the center, indicating that the best-fit values are much better measured. This corresponds to the smaller errorbars we see in α and ϵ after reconstruction.

The second and third columns of Figure 5.20 show the α and ϵ probability distributions derived from the χ^2 grid. One can see that both of these are fairly Gaussian so we can quantify the errors on α and ϵ as the standard deviations of these distributions, σ_α and σ_ϵ . The smaller standard deviations after reconstruction accompany the sharpening up of the acoustic peak. This corresponds to the tightening of the contours in the χ^2 distribution shown in column 1.

Our measured $C_{\alpha\epsilon}$, σ_α and σ_ϵ imply correlation coefficients of $\rho_{\alpha\epsilon} = 0.27$ and 0.34 before and after reconstruction. These values are slightly larger than the expected $\rho_{\alpha\epsilon} \sim 0.21$ from Fisher matrix arguments. However, given the large rms of $\rho_{\alpha\epsilon}$ from the mocks of ~ 0.35 both before and after reconstruction, our DR7 results are not significantly different from the Fisher matrix prediction.

Table 5.4: DR7 fitting results for various models. The model is given in column 1. The measured α values are given in column 2 and the measured ϵ values are given in column 3. The χ^2/dof is given in column 4.

Model	α	ϵ	χ^2/dof
Redshift Space without Reconstruction			
Fiducial [f]	1.015 ± 0.044	0.007 ± 0.046	89.60/90
Fit w/ $(\Sigma_{\perp}, \Sigma_{\parallel}) \rightarrow (8, 8)h^{-1}\text{Mpc}$.	1.012 ± 0.045	0.009 ± 0.044	89.77/90
Fit w/ $\Sigma_s \rightarrow 0h^{-1}\text{Mpc}$.	1.018 ± 0.040	0.007 ± 0.040	89.60/90
Fit w/ $A_2(r) = poly2$.	1.018 ± 0.043	0.013 ± 0.046	91.42/91
Fit w/ $A_2(r) = poly4$.	1.015 ± 0.044	0.006 ± 0.047	89.58/89
Fit w/ $30 < r < 200h^{-1}\text{Mpc}$ range.	1.018 ± 0.039	0.004 ± 0.043	105.03/104
Fit w/ $70 < r < 200h^{-1}\text{Mpc}$ range.	1.016 ± 0.050	0.008 ± 0.050	82.43/76
Fit w/ $50 < r < 150h^{-1}\text{Mpc}$ range.	1.019 ± 0.042	0.001 ± 0.049	47.10/58
Redshift Space with Reconstruction			
Fiducial [f]	1.012 ± 0.024	-0.014 ± 0.036	62.53/90
Fit w/ $(\Sigma_{\perp}, \Sigma_{\parallel}) \rightarrow (2, 4)h^{-1}\text{Mpc}$.	1.012 ± 0.025	-0.014 ± 0.036	62.48/90
Fit w/ $\Sigma_s \rightarrow 0h^{-1}\text{Mpc}$.	1.013 ± 0.021	-0.013 ± 0.029	61.83/90
Fit w/ $A_2(r) = poly2$.	1.013 ± 0.025	-0.011 ± 0.036	65.61/91

Continued on next page

Table 5.4 – continued from previous page

Model	α	ϵ	χ^2/dof
Fit w/ $A_2(r) = poly4$.	1.013 ± 0.025	-0.011 ± 0.036	61.92/89
Fit w/ $30 < r < 200h^{-1}\text{Mpc}$ range.	1.014 ± 0.023	-0.013 ± 0.033	68.39/104
Fit w/ $70 < r < 200h^{-1}\text{Mpc}$ range.	1.012 ± 0.027	-0.016 ± 0.040	54.50/76
Fit w/ $50 < r < 150h^{-1}\text{Mpc}$ range.	1.017 ± 0.023	-0.009 ± 0.034	31.95/58
Recon. w/ $\beta \rightarrow 0.24$.	1.014 ± 0.024	-0.016 ± 0.035	68.77/90
Recon. w/ $\beta \rightarrow 0.36$.	1.013 ± 0.024	-0.013 ± 0.036	67.05/90
Recon. w/ $b \rightarrow 1.8$.	1.014 ± 0.025	-0.017 ± 0.036	66.75/90
Recon. w/ $b \rightarrow 2.6$.	1.015 ± 0.024	-0.012 ± 0.035	77.09/90
Recon. w/ Wiener Filter.	1.012 ± 0.025	-0.014 ± 0.035	61.23/90
Recon. w/ $\ell = 20h^{-1}\text{Mpc}$.	1.010 ± 0.024	-0.014 ± 0.035	79.12/90

We again test the robustness of our α and ϵ measurements to our fitting model. The results are listed in Table 5.4. We see that our α and ϵ measurements are always consistent with the results obtained using the fiducial fitting parameters. Our σ_α and σ_ϵ measurements show $\sim 10\%$ variations which are consistent with the differences in scatter between the various cases seen in the mocks.

We also test the robustness of our reconstruction technique by varying the input parameters and then re-performing our fits. The α and ϵ values we measure from these tests are also listed in Table 5.4. Again we see very consistent α , ϵ , σ_α and σ_ϵ values between the various cases. This indicates that our measurements of the acoustic scale and anisotropy are robust against reconstruction parameters.

5.5.2 Comparison with Past Works

Our measurements are consistent with those of Chuang & Wang (2011) who measure $D_A(z) = 1048_{-58}^{+60}$ Mpc and $H(z) = 82.1_{-4.9}^{+4.8}$ km/s/Mpc at $z = 0.35$ using the same DR7 data. Their analysis fits the 2D correlation function of the LRGs before reconstruction whereas we fit the monopole and quadrupole. One can see that their derived errors on D_A are similar to our pre-reconstruction value, however, their derived errors on H are about a factor of 2 smaller than ours. The correlation function model they use is similar to ours, except they do not take Σ_{nl} to be anisotropic. Their covariance matrix is also derived from the LasDamas mocks. The only significant difference is that they use a Markov Chain Monte Carlo approach over the parameter space $\{D_A(z), H(z), \beta, \Omega_m h^2, \Omega_b h^2, n_s, \Sigma_s, \Sigma_{nl}\}$ to derive their D_A and H measurements at $z = 0.35$. The inclusion of β and Σ_s in their parameter estimation without any other marginalization (such as $A(r)$) to allow for inaccuracies in their model indicates that their method also attempts to extract anisotropic information in the broadband shape of the correlation function. In particular, their method hinges on being able to correctly distinguish between anisotropy caused by redshift-

space distortions (β and Σ_s) and those induced by assuming the wrong cosmology (i.e. the Alcock-Paczynski effect). The latter of course, is what allows direct and separate constraints of D_A and H . This differs from the method we present which *only* utilizes the anisotropy of the BAO signal.

Reid & White (2011) show that accurately modeling redshift-space distortions is a challenging theory problem and requires going beyond simple Σ_s and β models. They demonstrate that neglecting bispectrum and higher order terms from the real to redshift space transformation results in models that are not accurate enough at our current levels of observational precision. Since the observed anisotropic signal in the correlation function is due to a combination of redshift-space distortions and the Alcock-Paczynski effect, the difficulty in accurately modeling redshift-space distortions makes isolating Alcock-Paczynski information challenging. This means that although Chuang & Wang (2011) obtain a better measurement of $H(z)$ by also utilizing shape information from the correlation function, it is unclear whether the Alcock-Paczynski signal they detect by doing this is fully separated from redshift-space distortions.

Our method uses only the anisotropy in the BAO signal through fixing Σ_s and allowing broadband marginalization terms, $A_{0,2}(r)$, to account for any residual mismatch between the model and the data. This represents a more conservative approach since we do not attempt to utilize Alcock-Paczynski information in the broadband by disentangling it from redshift-space distortions in our measurement of $H(z)$. The loss of shape information in our method makes it unsurprising that our errorbar on $H(z)$ is larger. However, we believe that the large uncertainty in redshift-space distortion modeling warrants an Alcock-Paczynski method that only uses the BAO signal such as that presented here.

Our DR7 α measurements are consistent with the monopole-only measurements

of Xu et al. (2012), however, our errorbars on α are a factor of 1.25 larger both before and after reconstruction. Although this is a very small change in absolute terms, it is still worthy of some investigation. The top left panel of Figure 5.21 shows the σ_α values we measure for our full monopole+quadrupole fits as described in §5.3.3 from the post-reconstruction mocks versus the monopole-only results of Xu et al. (2012). The DR7 results are overplotted as the black star. We see that, in general, the mocks have larger σ_α values in our full monopole+quadrupole fits. The scatter at large σ_α where the acoustic scale is not well measured is also significantly bigger. Our DR7 σ_α measurement lies within the locus of mock points and hence the increase we see is consistent with the mocks.

Our monopole+quadrupole full fits have several differences relative to the monopole-only fits of Xu et al. (2012). First, the covariance matrix is expanded to include the quadrupole-quadrupole and monopole-quadrupole covariances. Second, we introduce β as a fitting parameter. Third, we include FoG (i.e. $\Sigma_s = 4h^{-1}\text{Mpc}$) in our fitting model; Xu et al. (2012) have Σ_s implicitly set to $0h^{-1}\text{Mpc}$. Since Σ_s can induce some smearing of the BAO, the Σ_{nl} value we use in the full fits is correspondingly smaller ($3h^{-1}\text{Mpc}$ versus $4h^{-1}\text{Mpc}$ in the monopole-only case). In addition, in our pre-reconstruction fitting model, we introduce a non-isotropic Σ_{nl} . To understand which of these steps induces the greatest change in σ_α , we start by fitting the monopole+quadrupole using the new covariance matrix and gradually add in the other changes. Before we describe our results, we again stress that the changes in σ_α we see are very small and require probing some subtleties in our models to understand. Our measurements of α and σ_α are still reasonably robust against fitting parameters in a single DR7 realization as shown in Tables 5.2 & 5.4.

The median changes in σ_α as we add in more elements of the fitting are listed in Table 5.5 for the pre- and post-reconstruction mocks. The total change between

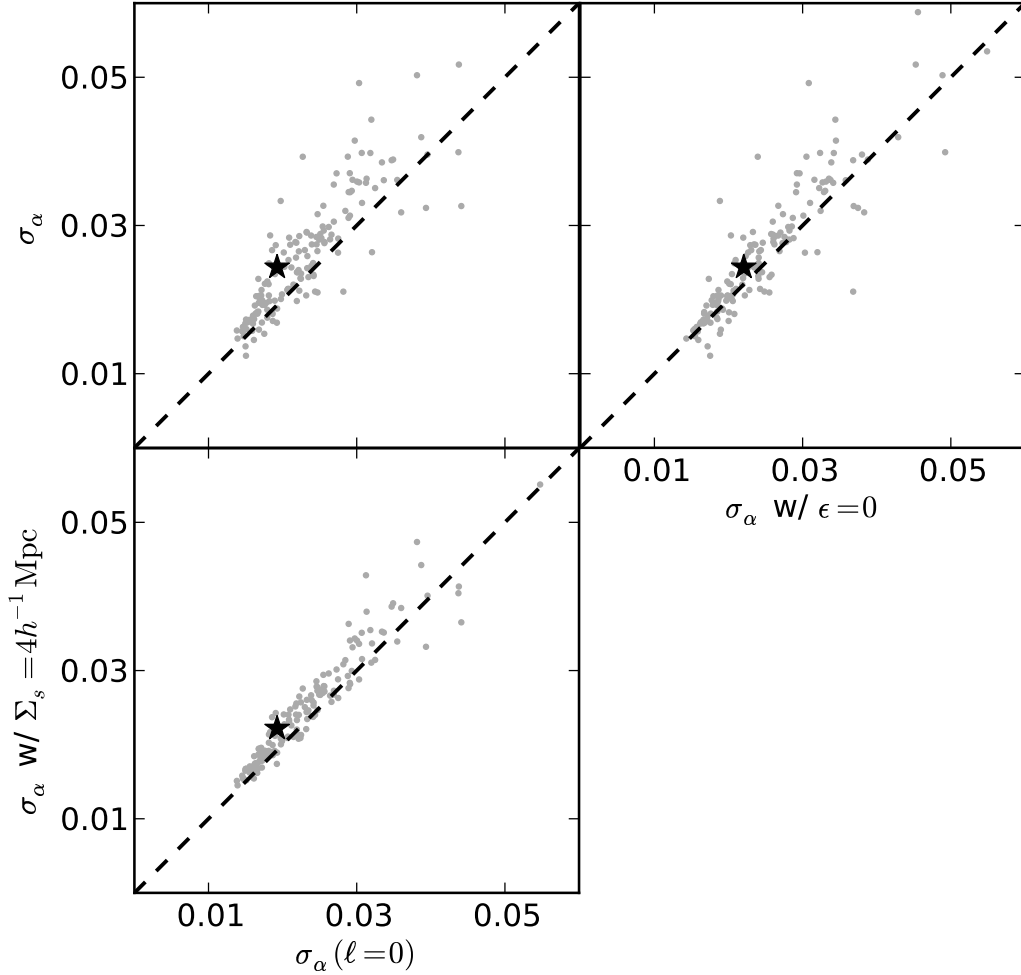


Figure 5.21: The σ_α values measured from the post-reconstruction mocks for various fitting models. The DR7 results are overplotted as the black stars and fall within the locus of mock points. (top left) The σ_α values measured through the full monopole+quadrupole fits versus the monopole-only results of Xu et al. (2012). One can see that the full fits have σ_α that are larger on average. There is also considerable scatter at large σ_α where the acoustic scale is not as well measured. We emphasize however, that these variations in σ_α are incredibly small and do not significantly affect our results. (bottom left) σ_α from monopole+quadrupole fits with $\Sigma_s = 4h^{-1}\text{Mpc}$ and $\Sigma_{nl} = 3h^{-1}\text{Mpc}$ versus those from the original monopole-only fits with $\Sigma_s = 0h^{-1}\text{Mpc}$ and $\Sigma_{nl} = 4h^{-1}\text{Mpc}$. The degradation in σ_α is obvious and again suggests that there is some mismatch between our fitting model and the data. (top right) σ_α from full monopole+quadrupole fits including ϵ versus those from the monopole+quadrupole fit with $\epsilon = 0$. The introduction of ϵ appears to cause most of the scatter in σ_α and also further degrades σ_α . ϵ is known to have some correlation with α so this is not surprising.

Table 5.5: Effects on σ_α of introducing various new elements to the monopole-only fits of Xu et al. (2012). In the first row we introduce the quadrupole fitting with the new combined monopole+quadrupole covariance matrix. The second row introduces our β fitting in addition to the new covariance matrix while the third row introduces changes in Σ_s and Σ_{nl} instead. The fourth row combines the previous two and corresponds to fitting with the fiducial model while forcing $\epsilon = 0$. The last row introduces ϵ fitting and corresponds to our fiducial model results.

Parameters	Before Recon.		After Recon.	
	$\widetilde{\Delta\sigma}_\alpha$	Qtls	$\widetilde{\Delta\sigma}_\alpha$	Qtls
New C_{ij}	0.0007	$\begin{smallmatrix} +0.0014 \\ -0.0015 \end{smallmatrix}$	0.0005	$\begin{smallmatrix} +0.0020 \\ -0.0016 \end{smallmatrix}$
New C_{ij} , adding β fit	0.0007	$\begin{smallmatrix} +0.0030 \\ -0.0016 \end{smallmatrix}$	0.0006	$\begin{smallmatrix} +0.0018 \\ -0.0019 \end{smallmatrix}$
New C_{ij} , $\sigma_s = 4h^{-1}\text{Mpc}$, new Σ_{nl}	0.0015	$\begin{smallmatrix} +0.0017 \\ -0.0016 \end{smallmatrix}$	0.0013	$\begin{smallmatrix} +0.0021 \\ -0.0016 \end{smallmatrix}$
New C_{ij} , adding β fit, $\Sigma_s = 4h^{-1}\text{Mpc}$, new Σ_{nl} (fiducial model w/ $\epsilon = 0$)	0.0018	$\begin{smallmatrix} +0.0024 \\ -0.0017 \end{smallmatrix}$	0.0014	$\begin{smallmatrix} +0.0014 \\ -0.0016 \end{smallmatrix}$
New C_{ij} , adding β & ϵ fits, $\Sigma_s = 4h^{-1}\text{Mpc}$, new Σ_{nl} (fiducial model)	0.0036	$\begin{smallmatrix} +0.0040 \\ -0.0044 \end{smallmatrix}$	0.0022	$\begin{smallmatrix} +0.0039 \\ -0.0027 \end{smallmatrix}$

the monopole-only fits and the full monopole+quadrupole fits is listed in the last row of this table. We find that changing the covariance matrix (first row) increases σ_α by a small amount and adding β (second row) does not further degrade the errors. Introducing Σ_s and the accompanying change in Σ_{nl} (third row) appears to be a major contributor to the degradation of σ_α . This increases the median σ_α by about half the total. Combining the β fitting and the changes in Σ_s and Σ_{nl} (fourth row) shows little additional degradation above the previous case. Note that this corresponds to using the fiducial model with ϵ fixed at 0. Finally, as mentioned above, the last row adds in ϵ fitting and corresponds to the fiducial model. We see that this step causes the other half of the total increase in σ_α . It also introduces a significant amount of scatter in σ_α .

The steps that contribute the most to the σ_α increase are shown in the bottom left and top right panels of Figure 5.21 for the post-reconstruction case. In the bottom left we have plotted the σ_α values measured from monopole+quadrupole fits with $\Sigma_s = 4h^{-1}\text{Mpc}$ and $\Sigma_{nl} = 3h^{-1}\text{Mpc}$ versus those measured from the monopole-only fits with $\Sigma_s = 0h^{-1}\text{Mpc}$ and $\Sigma_{nl} = 4h^{-1}\text{Mpc}$. The offset between the two is obvious and again suggests that our FoG model is not perfectly matched to the data.

The top right panel shows the σ_α values measured from the mocks through the full monopole+quadrupole fits versus the monopole+quadrupole fits with ϵ fixed at 0. In addition to the obvious offset, we also see the appearance of significant scatter. ϵ has small but non-zero correlation with α , implying a slight degeneracy between these 2 parameters. It is not surprising that this extra covariance may increase σ_α and its scatter. Again, this small degradation is not of great concern at our current levels of statistical precision.

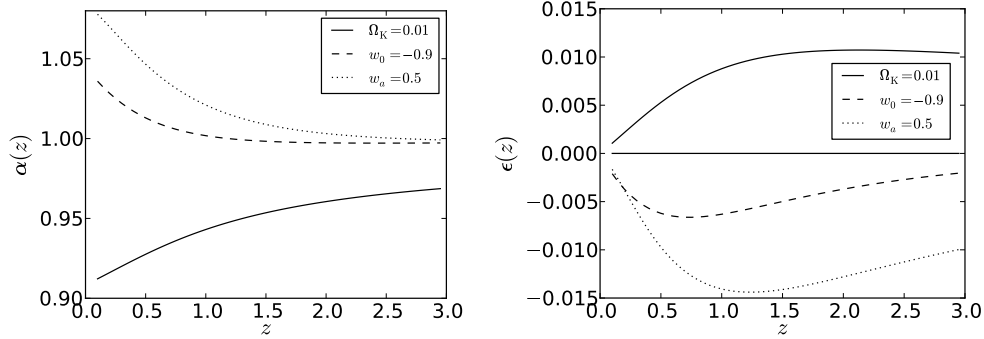


Figure 5.22: The expected variation in $\alpha(z)$ (left) and $\epsilon(z)$ (right) as we open up curvature or allow non-cosmological constant or time-varying dark energy. We have taken the fiducial cosmology to be the flat, Λ CDM cosmology predicted by WMAP7 as usual. One can see that curvature and dark energy properties affect α more at low z . At high z it becomes increasingly difficult to distinguish between non-cosmological constant and time-varying dark energy models using measurements of α . However, we see that ϵ is affected by curvature and dark energy the most at higher z , peaking at $z \sim 1$. This suggests that the anisotropic BAO signal is stronger and therefore offers more constraining power at higher redshifts.

5.6 Cosmological Implications

In this section we will place our measurement of ϵ within the context of current cosmological constraints. To build more intuition for how $\alpha(z)$ and $\epsilon(z)$ vary as we change the amount of curvature or the nature of dark energy, we look to Figure 5.22. The left panel shows α as a function of redshift for a cosmology that has positive curvature ($\Omega_K = 0.1$), dark energy that is not a cosmological constant ($w_0 = -0.9$) and time-varying dark energy ($w_a = 0.5$). The analogous plot for ϵ is shown in the right panel. Here we have again taken the fiducial cosmology to be the flat Λ CDM cosmology predicted by WMAP7. As we vary the cosmology, we fix $\Omega_m h^2$ and the distance to the last scattering surface (i.e. the distance to $z = 1089$, the redshift of recombination). This guarantees that the sound horizon will be the same in all the plotted cosmologies.

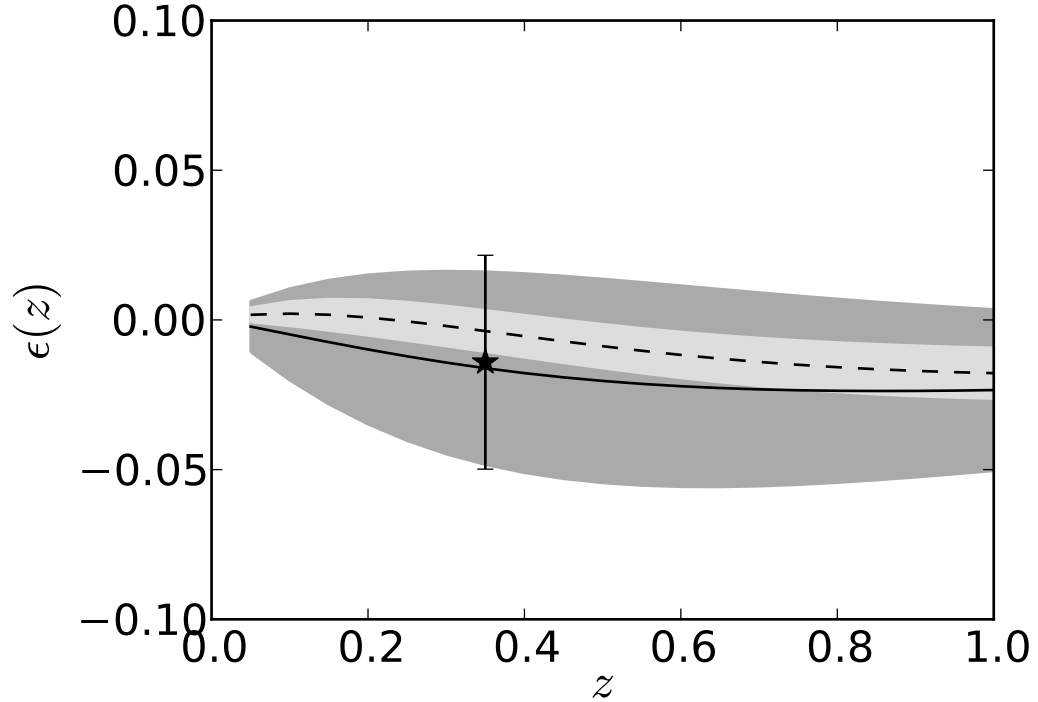


Figure 5.23: Our DR7 ϵ measurement at $z = 0.35$ overplotted on the 1σ regions predicted by MCMC chains. Here we have assumed a WMAP7 fiducial cosmology. We have used chains for the most generalized cosmology in which the universe is allowed to be curved. Dark energy is not forced to be a cosmological constant and it is allowed to vary in time. The chains were computed using the most recent CMB+BAO (dark grey) and CMB+BAO+SN (light grey) distance measures. The solid black line corresponds to the mean $\epsilon(z)$ from the CMB+BAO chain and the dashed black line is the analogue for the CMB+BAO+SN chain. One can see that our DR7 point overlaps these predicted regions very well. The fact that our errorbar is larger than the 1σ regions is not surprising since these regions were predicted by combining different datasets whereas our measurement is only based on 1 dataset. However, the largeness of our errorbar suggests that even if we were to include our anisotropic distance measure in the MCMC chains, we would not be able to substantially improve the constraints on cosmological parameters.

Recall that if the fiducial cosmology matches the true cosmology of the universe, then we would expect $\alpha = 1$ and $\epsilon = 0$. We see that introducing curvature and altering the nature of dark energy both perturb α away from 1 the most at low redshift. However, at higher redshift, it becomes increasingly difficult to distinguish between non-cosmological constant models and time-varying dark energy models using measurements of α . The opposite is true for ϵ . We see that the effects of adding curvature or changing the properties of dark energy are most prominent at larger redshifts, peaking at $z \sim 1$. This suggests that to exploit the anisotropic BAO signal, we gain more leverage by going to higher z . However, we also see that even the maximum difference in ϵ between the $w_a = 0.5$ and $\Omega_K = 0.1$ cosmologies is smaller than our current error on ϵ which indicates that we are not able to distinguish between these cosmologies using our DR7 measurement.

Figure 5.23 shows our DR7 measurement of ϵ overplotted on constraints derived from cosmological Markov Chain Monte Carlo (MCMC) sampling. The MCMC method computes the likelihood that a set of input cosmological parameters fits distance measures from Cosmic Microwave Background (CMB) observations at high redshift, and Type Ia supernova and BAO observations at low redshift. The number of steps in the chain spent exploring a certain region in the cosmological parameter space is proportional to the likelihood of that region representing the true cosmology. Hence, we can infer $D_A(z)$ and $H(z)$ at each step in the chain to compute $\epsilon(z)$ relative to some fiducial cosmology (WMAP7 in our case). At each z , we can measure the mean and rms of the ϵ distribution which gives us an estimate of what we should measure ϵ to be and how well current measurements can constrain ϵ .

The grey regions in Figure 5.23 are derived from MCMC chains exploring a cosmology which is allowed to have curvature and varying dark energy with equation of state $w(a) = w_0 + (1 - a)w_a$ where a is the scale factor. Note that this is the most

generalized and least-constraining cosmology that is typically tested. These chains were computed using CosmoMC, a standard MCMC sampler (Lewis & Bridle, 2002) and were originally analyzed in Anderson et al. (2012). More detailed descriptions of the MCMC algorithm and the specific chains can be found in these two papers. The dark grey region (CMB+BAO) corresponds to the 1σ limits calculated from a chain where we have used CMB data from WMAP7 (Komatsu et al., 2011) and spherically-averaged BAO distance measures from the 6 Degree Field Galaxy Survey at $z = 0.1$ (Beutler et al., 2011), SDSS DR7 at $z = 0.35$ (Padmanabhan et al., 2012a) and SDSS DR9 at $z = 0.57$ (Anderson et al., 2012). The light grey region (CMB+BAO+SN) includes additional distance constraints from the Supernova Legacy Survey 3 (Conley et al., 2011).

One can see that our DR7 measurement of ϵ is consistent with the CMB+BAO and CMB+BAO+SN constraints at $z = 0.35$. It is not surprising that our 1σ errorbar is larger than the grey regions as our datapoint represents the constraints from only a single dataset. However, the fact that this is true suggests that including our measurement will not significantly improve our constraints on cosmological parameters. This again, is not surprising given that our measurement of the BAO anisotropy is only marginal in the DR7 data.

The future is nonetheless bright with the SDSS DR9 CMASS sample (Anderson et al., 2012) now in hand. The galaxies in this dataset are denser and more abundant than DR7, and also at higher redshift ($z = 0.57$). Therefore, the DR9 CMASS anisotropic BAO signal should be less noisy and more prominent, implying a much tighter constraint on ϵ .

5.7 Conclusions

The differential clustering along the line-of-sight and transverse directions that arise from assuming the wrong fiducial cosmology can be used to directly constrain the angular diameter distance $D_A(z)$ and the Hubble parameter $H(z)$. This anisotropy can be measured from the BAO signal in the monopole and quadrupole moments of 2-point statistics such as the correlation function studied in this work.

We have presented measurements of the anisotropic BAO signal (ϵ) from the SDSS DR7 LRG sample. We measured $\alpha = 1.012 \pm 0.024$ and $\epsilon = -0.014 \pm 0.036$ after density field reconstruction which translate into $D_A(z = 0.35) = 1050 \pm 38$ Mpc and $H(z = 0.35) = 84.4 \pm 7.1$ km/s/Mpc assuming $r_s = 152.76$ Mpc. The relatively large error on ϵ suggests that our detection of the anisotropic signal is only marginal in DR7 and results in the large 8.4% uncertainty in $H(z)$. However, we have demonstrated that the methods for extracting ϵ outlined in this chapter are robust and nonetheless applicable to future anisotropic BAO studies.

We have given a detailed account of the theoretical background motivating the origin of the anisotropic signal and a parameter, ϵ , for measuring it. An in-depth look at the fitting model and method we use to extract the anisotropic signal is also given. We find that our model parameters have different morphological structures in their derivatives from ϵ , although they can still be partially degenerate with each other. These minor degeneracies appear to introduce a small bias in ϵ at the 0.2% level, far below our current level of statistical precision.

We apply density field reconstruction and test the robustness of our measured α and ϵ against changes in the reconstruction parameters using 160 LasDamas mock catalogues. We find that reconstruction appears to introduce some anisotropy into the quadrupole, however this is adequately accounted for by our $A_2(r)$ nuisance parameters. We then perform the same robustness checks on our fitting model

using the mock catalogues. Similar tests were also performed on the DR7 data returning consistently robust results. We demonstrate that α and ϵ have near-Gaussian posteriors. Hence estimating their errors as the standard deviations σ_α and σ_ϵ from their respective probability distributions is reasonable. The σ_α , σ_ϵ and $\rho_{\alpha\epsilon}$ values obtained from the mocks and the DR7 data are mostly consistent with Fisher matrix predictions.

We find that in the mocks and the DR7 data, our α error estimates are slightly larger than those obtained when only the monopole is fit. This small increase does not detract significantly from the overall robustness of our measurements which we verify as discussed above. About half of this increase is a result of including a Finger-of-God model in our full monopole+quadrupole fits while the other half arises from fitting for ϵ . This first point suggests that our FoG model does not match the data perfectly and may induce slight biases into our measurements. Given the non-zero covariance between ϵ and α the second point is not surprising. The behaviour of DR7 falls completely within the locus of mock points and is therefore not unusual.

Our DR7 measurements of D_A and H before reconstruction are consistent with those obtained by Chuang & Wang (2011) using the same dataset. The errors we predict for D_A are also consistent, however, our H error is about a factor of 2 larger. This is likely a result of differing methodology and more conservative assumptions on our part. The errors on α and ϵ we measure from the DR7 data are consistent with the scatter from the mocks as well as their average σ_α and σ_ϵ values. In addition, our $\sigma_\epsilon/(1+\epsilon)$ -to- σ_α/α ratio agrees reasonably well with Fisher matrix predictions and our σ_H/H -to- σ_{D_A}/D_A ratio is ~ 2 and in good agreement with the predictions of Seo & Eisenstein (2007). Hence we have no reason to suspect that our DR7 measurement is unusual in the magnitude of its errors.

Our post-reconstruction DR7 ϵ measurement agrees well with the predictions

from current datasets. However, its large error suggests that it will not offer much leverage in obtaining cosmological constraints. We find that the anisotropic signal is stronger at higher redshifts which suggests that we should be able to obtain a more robust measurement of ϵ at higher z . The recently obtained SDSS DR9 CMASS dataset has a higher number density than the DR7 LRG sample, contains more galaxies and is at higher redshift ($z = 0.57$). The basic theory and methodology presented in this work should serve as a foundation for obtaining a much better detection of ϵ , and subsequently D_A , H and other cosmological parameters from CMASS.

CHAPTER 6

CONCLUSIONS

The baryon acoustic oscillations (BAO) method is a very promising technique for probing the properties of dark energy. Its geometric nature frees it from the many systematics that plague the other major dark energy probes allowing statically-limited measurements of the cosmic expansion history. I have presented detailed techniques for obtaining precision measurements of the BAO scale and demonstrated how these translate into improved constraints on cosmological parameters. The main results of this thesis are summarized below.

In Chapter 2 we presented a new statistic designed to further limit the already small systematics in BAO analyses. The new statistic, $\omega_\ell(r_s)$, corresponds to band-filtering the correlation function or the power spectrum using a filter matched to the BAO signal. As a result of this matching, the BAO signal is localized in $\omega_\ell(r_s)$. The filter has steep drop-offs at large and small k in Fourier space, limiting the sensitivity of the statistic to both large and small scales in the survey. Both of these are poorly constrained, the former because galaxy surveys simply do not probe extremely small scales and the latter because our surveys are finite in size. In addition, the filter is compensated which means that it integrates to 0. This eliminates effects due to the integral constraint which manifests itself as an additive offset in the correlation function. The integral constraint is a statement that we do not know the true cosmic number density of galaxies. These properties of the filter make $\omega_\ell(r_s)$ calculated in different subvolumes of a survey more independent and hence improves the robustness of error estimates from bootstrap and jackknife approaches. The statistic is sensitive to anisotropic clustering because it can be computed via paircounting. This accurately records the clustering distribution along all directions. Finally, the

computation of $\omega_\ell(r_s)$ does not require us to bin the data as $\xi(r)$ and $P(k)$ do. Binning, if not treated correctly, can introduce additional noise into our clustering measurements.

We demonstrated the computation of $\omega_\ell(r_s)$ on 44 N-body simulations. We presented a method for measuring the acoustic scale from $\omega_\ell(r_s)$ and showed that our results were consistent with measurements from $P(k)$. In addition, We demonstrated that the error we expect to measure on the acoustic scale from $\omega_\ell(r_s)$, $\xi(r)$ and $P(k)$ are all consistent with each other. Hence $\omega_\ell(r_s)$ represents a robust new statistic for BAO analysis.

In Chapter 3 we presented the first application of density-field reconstruction to a galaxy redshift survey. The SDSS DR7 LRG sample lent itself nicely to this exercise due to the large cosmological volume it probes. The LRG sample covers $\sim 10,000 \text{ deg}^2$ on the sky, spans a redshift range of $0.16 < z < 0.47$ and has a number density of $\sim 10^{-4} h^3 \text{ Mpc}^{-3}$. The median redshift is $z = 0.35$.

Reconstruction is designed to partially remove the effects of non-linear structure growth on the BAO scale. It also corrects for large-scale redshift-space distortions which introduce anisotropies into our clustering measures. Non-linear evolution causes the BAO signal to be smeared and shifted relative to its linear theory position. The smearing makes the BAO more difficult to centroid and hence reduces the statistical precision with which we can measure the acoustic scale. The shifting affects the accuracy with which we can calibrate our BAO distance scale. Hence it is clear that undoing these effects will allow us to obtain more precise distance measurements.

We measured the spherically-averaged correlation function before and after reconstruction from the DR7 data and from 160 mock catalogues constructed from the LasDamas simulations. We parameterize the acoustic scale as α , which measures the

position of the acoustic peak in our data relative to some fiducial cosmology. We fit for α using a simple χ^2 minimization technique. The covariance matrix we employ is constructed using a new method we introduce that involves approximating the covariance matrix calculated from the mock catalogues with a modified Gaussian covariance matrix. The modification parameters are obtained through a maximum likelihood fit. We perform detailed robustness tests of this matrix as well as our acoustic scale fitting model on the mock catalogues as well as the DR7 data itself. To do this, we vary the model parameters and confirm that we obtain consistent measurements of α . We perform similar robustness checks on the reconstruction parameters and also find consistent results. Since we are only interested in the BAO information, we must separate it from broadband effects such as redshift-space distortions and scale-dependent bias. We find that this is adequately accomplished through including a few nuisance parameters in our fits.

Most importantly, we find that reconstruction is able to significantly improve our measurement of the acoustic scale through sharpening up the acoustic peak. We find that in the mocks, the rms scatter in α drops from 3.3% to 2.1% after reconstruction. In the DR7 data, the error on α we estimate from its probability distribution drops from 3.5% to 1.9%. This is a factor of 1.8 decrease which is equivalent to the effects of tripling the survey volume. In addition, the significance of our BAO detection increases from 3 to 4σ after reconstruction. The level at which the data prefers the best-fit α increases from 3 to 5σ . Our α measurements translate into a spherically-averaged distance $D_V(z)/r_s = 8.88 \pm 0.17$ to $z = 0.35$ after reconstruction.

In Chapter 4 we employ similar techniques to those described in Chapter 3 to obtain a BAO distance measure from the SDSS DR9 CMASS sample. CMASS covers 3275 deg^2 on the sky, spans a redshift range of $0.43 < z < 0.7$ and has a

number density of $3 \times 10^{-4} h^3 \text{Mpc}^{-3}$.

We find that reconstruction does not appear to improve our acoustic scale measurement in CMASS. This is likely a result of CMASS having a highly irregular (donut-shaped) survey geometry. It is unclear how well the large central gap of the survey can be filled in via constrained Gaussian realizations as our reconstruction technique employs. While we use the correlation function for our BAO measurement, a parallel study using the power spectrum was also performed. We combine the results from these two statistics by averaging their α measurements and adopting the rms of the mocks as the error. This gave a spherically-averaged distance of $D_V(z)/r_s = 13.67 \pm 0.22$ to $z = 0.57$ after reconstruction, a 1.7% measurement. We detect the CMASS BAO signal at 5σ confidence and the data prefers the best-fit α at 6σ confidence. Our CMASS distance measurement is consistent in the context of past BAO and supernova distance measures.

We find that the BAO detection significance in the DR7+DR9 combined dataset is greater than 6.5σ with a $\sim 8\sigma$ preference for the best-fit α . Hence it is clear that we have measured the BAO. Further combining with other BAO, supernova and cosmic microwave background observations, Markov Chain Monte Carlo sampling predicts cosmological parameters consistent with standard Λ CDM. We find that BAO distance measures are better for measuring the curvature of the universe while supernovae distance measures are better for constraining the equation of state of dark energy. This is because the BAO distance scale is inverted. It is calibrated by CMB measurements of the sound horizon at the redshift of recombination and extends down to lower redshifts. Curvature is more important at high z and hence BAO is more sensitive to it. The supernova distance scale is calibrated on H_0 measurements in the local universe and extends up to higher redshifts. The transition from matter to dark energy domination occurred in the low redshift universe and

hence supernovae are more sensitive to it.

In Chapter 5 we used the anisotropic BAO signal in SDSS DR7 to obtain separate and direct constraints of D_A and H at $z = 0.35$ from the monopole and quadrupole correlation functions. As $H(z)$ maps the cosmic expansion history, being able to directly measure it is key to understanding the acceleration of our universe. The anisotropic BAO method relies on using slight differences in the BAO position along the line-of-sight and transverse directions that arise when we assume the wrong cosmology in calculating the correlation function. Only recently did we acquire large enough datasets to begin probing this small anisotropic signal. In addition, our work marks the first application of reconstruction to the anisotropic BAO analysis of a galaxy redshift survey.

We measured the anisotropic warping, ϵ , and the isotropic dilation, α , of the BAO signal by fitting correlation function models to our data in a manner similar to what was described in Chapter 3. We presented the theoretical background behind the anisotropic BAO technique and performed a detailed investigation of our models. We also conducted thorough robustness checks of our fitting and reconstruction methods on the LasDamas mock catalogues and the data itself. We saw that our simple redshift-space distortion models did not perfectly match the data and resulted in slight biases in our measurements of ϵ . However, these were far below our current levels of statistical precision. We also saw that reconstruction introduces additional anisotropy into the quadrupole broadband. Fortunately the use of nuisance parameters in our fitting model was able to account for this excess power so it did not affect our measurements of ϵ .

We find that our measurement of ϵ in a single DR7 realization is only marginal due to the noisiness of the quadrupole. From the DR7 data we measure $D_A(z) = 1050 \pm 38$ Mpc and $H(z) = 84.4 \pm 7.1$ at $z = 0.35$ after reconstruction. This

corresponds to a 3.6% measurement of D_A and an 8.4% measurement of H . Our results agree with Chuang & Wang (2011) who use the same pre-reconstruction DR7 dataset, however, our errorbar on H is about a factor of 2 larger due to our more conservative approach. The ϵ values we measure are consistent within the context of current cosmological constraints. Although the uncertainty of our DR7 measurement is large, this work outlines the necessary techniques for exploiting the anisotropic BAO signal. With the improved DR9 CMASS dataset currently in-hand and many others to come, we will be able to use these same techniques to obtain more precise measurements of ϵ (and hence D_A and H) in the future.

I have presented in this thesis a number of techniques for obtaining precision distance measures using the BAO method. As we continue in this era of precision cosmology, BAO will be a major focus of future galaxy surveys such as LSST and BigBOSS for probing the cosmic expansion history. It is my hope that the methods outlined in this thesis will remain core elements of future BAO analyses.

CHAPTER 7

EVALUATING $\widetilde{W}_\ell(k)$

The expressions for $\widetilde{W}_\ell(k)$, in terms of polynomials of k times trigonometric functions, involve a lot of cancellation. This makes them unstable to direct evaluation. However if we define

$$K_n(k) = \frac{2+n}{(kr_s)^{2+n}} \int_0^{kr_s} x^n \sin x \, dx \quad (7.1)$$

then

$$\widetilde{W}_0(k) = \frac{8\pi}{3} \left[\frac{1}{3} (K_7 - K_{16}) - (K_{10} - K_{13}) \right] \quad (7.2)$$

while

$$\widetilde{W}_2(k) = -\frac{24\pi}{5k^2} [3K_5 - 16K_8 + 25K_{11} - 12K_{14}]. \quad (7.3)$$

It is straightforward to evaluate $K_n(x)$, the limits are

$$K_n(x) = 1 - \frac{n+2}{3!(n+4)}x^2 + \frac{n+2}{5!(n+6)}x^4 + \dots \quad (7.4)$$

as $x \rightarrow 0$ and

$$K_n(x) = -(n+2)\frac{\cos x}{x^2} + n(n+2)\frac{\sin x}{x^3} + \dots \quad (7.5)$$

as $x \rightarrow \infty$. The K_n also satisfy a simple recurrence relation

$$K_n(x) = \frac{n+2}{x^3} [n \sin x - x \cos x - (n-1)xK_{n-2}]. \quad (7.6)$$

Use of this recurrence relation for high k and the power-series expansion for low k results in stable evaluation of the \widetilde{W}_ℓ .

CHAPTER 8

FISHER MATRIX PREDICTIONS

To derive the expected relationships between σ_α and σ_ϵ , we begin with the matrix equation

$$\begin{pmatrix} \sigma_\alpha^2 & \sigma_{\alpha\epsilon} \\ \sigma_{\alpha\epsilon} & \sigma_\epsilon^2 \end{pmatrix} = \begin{pmatrix} \frac{\partial\alpha}{\partial D_A} & \frac{\partial\alpha}{\partial H} \\ \frac{\partial\epsilon}{\partial D_A} & \frac{\partial\epsilon}{\partial H} \end{pmatrix} \begin{pmatrix} \sigma_{D_A}^2 & \sigma_{D_A H} \\ \sigma_{D_A H} & \sigma_H^2 \end{pmatrix} \begin{pmatrix} \frac{\partial\alpha}{\partial D_A} & \frac{\partial\alpha}{\partial H} \\ \frac{\partial\epsilon}{\partial D_A} & \frac{\partial\epsilon}{\partial H} \end{pmatrix}^T. \quad (8.1)$$

Note that this is essentially the inverse process to Equation (5.7). Expanding we get

$$\sigma_\alpha^2 = \sigma_{D_A}^2 \left(\frac{\partial\alpha}{\partial D_A} \right)^2 + \sigma_H^2 \left(\frac{\partial\alpha}{\partial H} \right)^2 + 2\sigma_{D_A H} \frac{\partial\alpha}{\partial D_A} \frac{\partial\alpha}{\partial H} \quad (8.2)$$

$$\sigma_\epsilon^2 = \sigma_{D_A}^2 \left(\frac{\partial\epsilon}{\partial D_A} \right)^2 + \sigma_H^2 \left(\frac{\partial\epsilon}{\partial H} \right)^2 + 2\sigma_{D_A H} \frac{\partial\epsilon}{\partial D_A} \frac{\partial\epsilon}{\partial H}. \quad (8.3)$$

$$\begin{aligned} \sigma_{\alpha\epsilon} &= \sigma_{D_A}^2 \frac{\partial\alpha}{\partial D_A} \frac{\partial\epsilon}{\partial D_A} + \sigma_{D_A H} \left(\frac{\partial\alpha}{\partial H} \frac{\partial\epsilon}{\partial D_A} + \frac{\partial\alpha}{\partial D_A} \frac{\partial\epsilon}{\partial H} \right) \\ &\quad + \sigma_H^2 \frac{\partial\alpha}{\partial H} \frac{\partial\epsilon}{\partial H} \end{aligned} \quad (8.4)$$

Plugging in the relevant derivatives from Equations (5.3) & (5.4) we get

$$\frac{\sigma_\alpha^2}{\alpha^2} = \frac{4}{9}\sigma_{\log D_A}^2 + \frac{1}{9}\sigma_{\log H}^2 - \frac{4}{9} \left(\frac{\sigma_{D_A H}}{D_A H} \right) \quad (8.5)$$

$$\frac{\sigma_\epsilon^2}{(1+\epsilon)^2} = \frac{1}{9}\sigma_{\log D_A}^2 + \frac{1}{9}\sigma_{\log H}^2 + \frac{2}{9} \left(\frac{\sigma_{D_A H}}{D_A H} \right) \quad (8.6)$$

$$\frac{\sigma_{\alpha\epsilon}}{\alpha(1+\epsilon)} = -\frac{2}{9}\sigma_{\log D_A}^2 + \frac{1}{9}\sigma_{\log H}^2 - \frac{1}{9} \left(\frac{\sigma_{D_A H}}{D_A H} \right) \quad (8.7)$$

where $\sigma_{\log y}^2 = \frac{\sigma_y^2}{y^2}$.

The correlation coefficient between D_A and H is $\rho_{D_A H} = \sigma_{D_A H} / \sigma_{D_A} \sigma_H$. If we

write $f = \sigma_{\log H} / \sigma_{\log D_A}$, then we have

$$\frac{\sigma_\alpha^2}{\alpha^2} = \frac{1}{9} \sigma_{\log D_A}^2 (4 + f^2 - 4\rho_{D_A H} f) \quad (8.8)$$

$$\frac{\sigma_\epsilon^2}{(1 + \epsilon)^2} = \frac{1}{9} \sigma_{\log D_A}^2 (1 + f^2 + 2\rho_{D_A H} f) \quad (8.9)$$

$$\frac{\sigma_{\alpha\epsilon}}{\alpha(1 + \epsilon)} = \frac{1}{9} \sigma_{\log D_A}^2 (-2 + f^2 - \rho_{D_A H} f). \quad (8.10)$$

Note that f is just the ratio of σ_H/H -to- σ_{D_A}/D_A which is typically ~ 2 (Seo & Eisenstein, 2007). The correlation coefficient $\rho_{D_A H}$ is predicted to be ~ 0.4 . Hence, we have

$$\frac{\sigma_\alpha}{\alpha} = \sigma_{\log \alpha} = 0.73 \sigma_{\log D_A} \quad (8.11)$$

$$\frac{\sigma_\epsilon}{1 + \epsilon} = \sigma_{\log(1+\epsilon)} = 0.86 \sigma_{\log D_A}, \quad (8.12)$$

which implies the ratio

$$\frac{\sigma_\epsilon}{1 + \epsilon} \text{ to } \frac{\sigma_\alpha}{\alpha} \sim 1.2. \quad (8.13)$$

The correlation coefficient between α and ϵ is

$$\rho_{\alpha\epsilon} = \frac{\sigma_{\alpha\epsilon}}{\sigma_\alpha \sigma_\epsilon} \quad (8.14)$$

$$= \frac{\alpha}{\sigma_\alpha} \frac{(1 + \epsilon)}{\sigma_\epsilon} \left(\frac{1}{9} \sigma_{\log D_A}^2 \right) (-2 + f^2 - \rho_{D_A H} f). \quad (8.15)$$

Using Equations (8.11) & (8.12) and plugging in the assumed values of f and $\rho_{D_A H}$ gives

$$\rho_{\alpha\epsilon} \sim 0.21. \quad (8.16)$$

REFERENCES

- Abazajian, K. N., et al., 2009, ApJS, 182, 543
- Abdalla, F. B., & Rawlings, S., 2005, MNRAS, 360, 27
- Aguirre, A. N. 1999, ApJ, 525, 583
- Aihara, H., et al. 2011, ApJS, 193, 29
- Albrecht, A., et al. 2006, [[arXiv:astro-ph/0609591]]
- Alcock, C., & Paczynski, B. 1979, Nature, 281, 358
- Amendola, L., Quercellini, C., & Giallongo, E. 2005, MNRAS, 357, 429
- Anderson, L., et al. 2012, MNRAS, submitted
- Angulo, R., et al., 2005, MNRAS, 362, L25
- Angulo, R., et al. 2008, MNRAS, 383, 755
- Bahcall, N. A., & Fan, X. 1998, ApJ, 504, 1
- Barnard, M., et al. 2008, Phys. Rev. D, 78, 043528
- Baumgart, D. J., & Fry, J. N. 1991, ApJ, 375, 25
- Becker, M. R., & Kravtsov, A. V. 2011, ApJ, 740, article id. 25
- Bennett, C. L., et al. 2003, ApJ, 583, 1
- Berlind, A. A., et al. 2003, ApJ, 593, 1
- Bernardeau, F., et al. 2002, Phys. Rep., 367, 1

- Bernstein, G. M. 1994, ApJ, 424, 569
- Beutler, F., et al., 2011, MNRAS, 416, 3017
- Blake, C., & Glazebrook, K. 2003, ApJ, 594, 665
- Blake C., Collister A., Bridle S., Lahav O., 2007, MNRAS, 374, 1527
- Blake, C., et al. 2011, MNRAS, 415, 2892
- Blake, C., et al. 2011, MNRAS, 418, 1707
- Blake, C., et al. 2011, MNRAS, 418, 1725
- Blanchard, A., & Alimini, J.-M. 1998, A&A, 203, L1
- Blanchard, A., & Bartlett, J. G. 1998, A&A, 332, L49
- Blanton, M., et al. 2003, AJ, 125, 2276
- Bond, J. R., & Efstathiou, G. 1984, ApJ, 594, 665
- Bridle, S., & King, L. 2000, New Jour. of Phys., 9, 444
- Cabré, A., & Gaztañaga, E., 2011, MNRAS, 412, L98
- Carroll, S. M., Press, W. H., & Turner, E. L. 1992, ARA&A, 30, 499
- Catelan, P., Kamionkowski, M., & Blandford, R. D. 2001, MNRAS, 320, L7
- Chevallier, M., & Polarski, D. 2001, Int. J. Mod. Phys. D, 10, 213
- Chotard, N., et al., 2011, 529, L4
- Chuang, C.-H., & Wang, Y., 2011, arXiv:1102.2251
- Cole, S., Fisher, K. B., Weinberg, D. H. 1994, MNRAS, 267, 785

- Cole, S., Fisher, K. B., Weinberg, D. H. 1995, MNRAS, 275, 515
- Cole S., et al., 2005, MNRAS, 362, 505
- Coleman, S. R. 1988, Nucl. Phys. B, 310, 643
- Colgate, S. A. 1979, ApJ, 232, 404
- Colless M., et al., 2003, [[astro-ph/0306581]]
- Conley, A., et al. 2011, ApJS, 192, 1
- Cremmer, E., Ferrara, C., Kounnas, C., & Nanopoulos D. V. 1983, Phys. Lett. B, 133, 61
- Crocce, M., & Scoccimarro, R. 2006, Phys. Rev. D, 73, 063520
- Crocce, M., & Scoccimarro, R. 2008, Phys. Rev. D, 77, 023533
- Davis, M., & Peebles, P. J. E. 1983, ApJ, 267, 465
- Davis, M., Efstathiou, G., Frenk, C. S., White, S. D. M. 1985, ApJ, 292, 371
- Dawson, K., et al. 2012, in prep
- de Lapparent, V., Geller, M. J., Huchra, J. P. 1988, ApJ, 332, 44
- de Putter, R., et al. 2012, JCAP, accepted, [[arxiv:1111.6596]]
- Doi, M., et al. 2010, AJ, 139, 1628
- Dolney, D., Jain, B., & Takada, M., 2006, MNRAS, 366, 884
- Drell, P. S., Lored, T. J., & Wasserman, I. 2000, ApJ, 580, 593
- Drinkwater M., et al., 2010, MNRAS, 401, 1429

- Efstathiou, G., et al. 2002, MNRAS, 330, L29
- Einstein, A. 1917, Sitzungsber. Preuss. Akad. Wiss. Berlin (Math. Phys.), 142
- Eisenstein, D. J., & Hu, W. 1998, ApJ, 496, 605
- Eisenstein, D. J., Hu, W., Tegmark, M. 1998, ApJL, 504, L57
- Eisenstein, D. J., et al. 2001, AJ, 122, 2267
- Eisenstein, D. J. 2002, Astr. Soc. of the Pacific Conf. Series, 280, 35
- Eisenstein, D.J., 2003, in ASP Conference Series, volume 280, Next Generation Wide Field Multi-Object Spectroscopy, ed. M.J.I. Brown & A. Dey (ASP: San Francisco) pp. 35-43; astro-ph/0301623
- Eisenstein, D. J., & White, M. 2004, Phys. Rev. D, 70, 103523
- Eisenstein, D. J., et al. 2005, ApJ, 633, 560
- Eisenstein, D. J., Seo, H.-J., & White, M., 2007, ApJ, 664, 660
- Eisenstein, D. J., Seo, H.-J., Sirko, E., & Spergel, D. N., 2007, ApJ, 664, 675
- Eisenstein, D. J., & Bennett, C. L. 2008, Physics Today, 61 (4), 040000
- Eisenstein, D. J., et al. 2011, AJ, 142, 72
- Feldman, H. A., Kaiser, N., Peacock, J. A. 1994, ApJ, 426, 23
- Frieman, J. A., Hill, C. T., Stebbins, A., & Waga, I. 1995, Phys. Rev. Lett., 75, 2077
- Fukugita, M., et al., 1996, AJ, 111, 1748
- Gaztanaga E., Cabre A., Hui L., 2009, MNRAS, 399, 1663

- Glazebrook, K., & Blake, C., 2005, ApJ, 631, 1
- Golfand, Y. A., & Likhtman, E. P. 1971, JETP Lett., 13, 323
- Gunn, J. E., et al., 1998, AJ, 116, 3040
- Gunn, J. E., et al., 2006, AJ, 131, 2332
- Guo, H., Zehavi, I., & Zheng, Z., ApJ, submitted, [[arXiv:1111.6598]]
- Guzik, J., & Seljak, U. 2002, MNRAS, 335, 311
- Guzik, J., Bernstein, G., & Smith, R. E., 2007, MNRAS, 375, 1329
- Haiman, Z., Mohr, J., & Holder, G. P. 2001, ApJ, 553, 545
- Hallman, E. J., Motl, P. M., Burns, J. O., & Norman M. L. 2006, ApJ, 648, 852
- Hamilton, A. J. S. 1992, ApJ, 385, L5
- Hamilton, A. J. S. 1993, ApJ, 417, 19
- Hamilton, A. J. S. 1998, in The Evolving Universe, ed. D. Hamilton (Dordrecht: Kluwer), 185
- Hamilton, A. J. S., Rimes, C. D., & Scoccimarro, R., 2006, MNRAS, 371, 1188
- Hawkins, E., et al. 2003, MNRAS, 346, 78
- Heavens, A. F., & Taylor, A. N. 1995, MNRAS, 275, 483
- Hewett, P. C. 1982, MNRAS, 201, 867
- Hinshaw, G., et al., 2003, ApJS, 148, 135
- Hinshaw, G., et al., 2007, ApJS, 170, 288

- Hoffman, Y., & Ribak, E., 1991, ApJ, 380, L5
- Hogg, D. W., Finkbeiner, D. P., Schlegel, D. J., & Gunn, J. E., 2001, AJ, 122, 2129
- Holtzman, J. A. 1989, ApJS, 71, 1
- Howell, D. A, Sullivan, M., Conley, A., & Carlberg, R., 2007, ApJ, 667, L37
- Hu, W. 1999, ApJ, 522, L21
- Hu, W., & Haiman, Z. 2003, Phys. Rev. D, 68, 063004
- Hu, W., & Sugiyama, N. 1996, ApJ, 471, 542
- Hu, W., & White, M. 1996, ApJ, 471, 30
- Hubble, E. 1929, Proc. Nat. Acad. Sci. 15, 168
- Huff, E., et al. 2007, Astroparticle Physics, 26, 351
- Hütsi, G., 2006, A&A, 449, 891
- Iben, I. & Tutukov, A. V. 1984, ApJS, 54, 335
- Ivezić, Ž., et al., 2004, Astronomische Nachrichten, 325, 583
- Jain, B., & Bertschinger, E. 1994, ApJ, 431, 495
- Jarosik, N., et al. 2011, ApJS, 192, 14
- Jeong, D., & Komatsu, E. 2006, ApJ, 651, 619
- Jeong, D., & Komatsu, E. 2009, ApJ, 691, 569
- Jones D. H., et al., 2009, MNRAS, 399, 683
- Kachru, S., Kumar, J., & Silverstein, E. 1999, Phys. Rev. D, 59, 106004

- Kaiser, N. 1986, MNRAS, 219, 785
- Kaiser, N. 1987, MNRAS, 227, 1
- Kaiser, N. 1992, ApJ388, 272
- Kaiser, N. 1998, ApJ, 498, 26
- Kaiser, N., & Peacock, J. A. 1991, ApJ, 379, 482
- Kazin, E., et al., 2010, ApJ, 710, 1444
- Kazin, E., Sánchez, A. G., Blanton, M. R. 2012, MNRAS, 419, 3223
- Kitching, T. D., Taylor, A. N., & Heavens, A. F. 2008, MNRAS, 389, 173
- Komatsu, E., et al. 2009, ApJS, 180, 330
- Komatsu E., et al., 2011, ApJS, 192, 18
- Kravtsov, A. V., et al. 2004, ApJ, 609, 35
- Kravtsov, A. V., Vikhlinin, A., & Nagai, D. 2006, ApJ, 650, 128
- Landy, S. D., & Szalay, A. S. 1993, ApJ, 412, 64
- Larson, D., et al., 2011, ApJS, 192, 16
- Lemaître, G. 1927, Annales de la Société Scientifique de Bruxelles, 47, 49
- Lewis, A., & Bridle, S. 2002, Phys. Rev. D, 66, 103511
- Linden, S., Virey, J.-M., & Tilquin, A., 2009, A&A, 506, 1095
- Linder, E. V. 2003, Phys. Rev. D, 68, 083504
- Linder, E. V., 2005, Phys. Rev. D, 72, 043529

- Lupton R., et al. 2001, “Astronomical Data Analysis Software and Systems X”, 238, 269.
- Ma, Z. 2007, ApJ, 665, 887
- Manera M., et al., 2012, MNRAS, submitted
- Maraston, C., et al. 2009, MNRAS, 394, 107
- Maraston, C., et al. 2012, in prep
- Masters, K. L., et al. 2011, MNRAS, 418, 1055
- Matsubara, T. 2004, ApJ, 615, 573
- Matsubara, T. 2007, Phys. Rev. D, 77, 063530
- Matsubara, T. 2007, Phys. Rev. D, 78, 083519
- McBride, C., et al., 2012, in prep
- McQuinn, M., et al. 2006, ApJ, 653, 815
- Mehta, K., et al. 2011, ApJ, 734, 94
- Metha, K., et al. 2012, MNRAS, submitted, [[arXiv:1202.0092]]
- Meiskin, A., & White, M. 1999, MNRAS, 308, 1179
- Meiksin, A., White, M., Peacock, J. A. 1999, MNRAS, 304, 851
- Metchnik, M., & Pinto, P. 2010, in prep
- Miller, C. J., Nichol, R. C., & Batuski, D. J. 2001, ApJ, 555, 68
- Nobili, S., & Goobar, A., 2008, A&A, 487, 19

- Noh, Y., White, M., & Padmanabhan, N., 2009, Phys. Rev. D, 80, 123501
- Nolta, M., et al., 2009, ApJS, 180, 296
- Nuza, S. E., et al. 2012, MNRAS, submitted
- Nusser, A., & Davis, M., 1994, ApJ, 421, L1
- Okumura, T., et al. 2008, ApJ, 676, 889
- Padmanabhan, N., White, M., Eisenstein D. J. 2007, MNRAS, 376, 1702
- Padmanabhan, N., & White, M. 2008, Phys. Rev. D, 77, 123540
- Padmanabhan, N., et al., 2008, ApJ, 674, 1217
- Padmanabhan, N., White, M., & Cohn, J. D., 2009, Phys. Rev. D, 79, 063523
- Padmanabhan, N., & White, M. 2009, Phys. Rev. D, 80, 063508
- Padmanabhan, N., et al. 2009, MNRAS, 397, 1862
- Padmanabhan, N., et al. 2012, MNRAS, submitted, [[arXiv:1202.0090]]
- Padmanabhan, N., et al. 2012, in prep
- Park, C., Gott, J. R., da Costa, L. N. 1992, ApJL, 392, L51
- Peacock, J. A., & Nicholson, D. 1991, MNRAS, 253, 307
- Peacock, J. A., & Dodds, S. J. 1994, MNRAS, 267, 1020
- Peacock, J. A., et al. 2001, Nature, 410, 169
- Peebles, P. J. E., & Yu, J. T. 1970, ApJ, 162, 815
- Peebles, P. J. E. 1973, ApJ, 185, 413

- Peebles, P. J. E. 1980, *The Large-Scale Structure of the Universe* (Princeton: Princeton University Press)
- Percival W. J., et al., 2001, *MNRAS*, 327, 1297
- Percival, W. J., et al. 2002, *MNRAS*, 337, 1068
- Percival, W. J., et al. 2004, *MNRAS*, 353, 1201
- Percival W. J., et al., 2007, *MNRAS*, 381, 1053
- Percival, W. J., et al., 2010, *MNRAS*, 401, 2148
- Percival, W. J., & White, M. 2009, *MNRAS*, 393, 29
- Perlmutter, S., et al. 1999, *ApJ*, 517, 565
- Phillips, M. M. 1993, *ApJ*, 413, L105
- Phillips, M. M., et al., 1993, *AJ*, 118, 1766
- Pier, J. R., et al., 2003, *AJ*, 125, 1559
- Ratra, B., & Peebles, P. J. E. 1988, *Phys. Rev. D*, 37, 3406
- Reid, B. A., et al. 2010, *MNRAS*, 404, 60
- Reid, B. A., & White, M., 2011, *MNRAS*, 417, 1913
- Reindl, B., Tammann, G. A., Sandage A., & Saha, A., 2005, *ApJ*, 624, 532
- Riess, A. G., et al. 1998, *AJ*, 116, 1009
- Riess, A. G., Filippenko, A. V., Li, W., & Schmidt, B. P. 1999, *AJ*, 118, 2668
- Riess, A. G., et al. 2011, *ApJ*, 730, 119

- Ross, A. J., et al. 2012, MNRAS, submitted
- Sakharov, A. D. 1966, Soviet Journ. of Exp. and Theor. Phys., 22, 241
- Sanchez, A. G., Baugh, C. M., Angulo, R. 2008, 390, 1470
- Sanchez, A. G., et al., 2009, MNRAS, 400, 1643
- Schlegel, D. J., Finkbeiner, D. P., & Davis M. 1998, ApJ, 500, 525
- Schlegel D., White M., Eisenstein D., 2009, The Astronomy and Astrophysics Decadal Survey, Science White Papers #314 [arxiv:0902.4680]
- Schmidt, B. P. 1998, ApJ, 507, 46
- Scoccamarro, R., Zaldarriaga, M., Hui, L. 1999, ApJ, 527, 1
- Scoccamarro, R., & Sheth, R. K., 2002, MNRAS, 329, 629
- Seo, H.-J., & Eisenstein, D. J. 2003, ApJ, 598, 720
- Seo, H.-J., & Eisenstein, D. J. 2005, ApJ, 633, 575
- Seo, H.-J., & Eisenstein, D. J., 2007, ApJ, 665, 14
- Seo, H.-J., Siegel, E. R., Eisenstein, D. J., White, M. 2008, ApJ, 686, 13
- Seo, H.-J., et al. 2010, ApJ, 720, 1650
- Seo, H.-J., et al. 2012, ApJ, submitted, [[arXiv:1201:2172]]
- Sharp, N. A. 1979, A&A, 74, 308
- Silk, J. 1968, ApJ, 151, 459
- Sirko, E. 2005, ApJ, 634, 728

- Slipher, V. M. 1913, Lowell Observatory Bulletin, 1, 56
- Slosar, A., Ho, S., White, M., & Louis, T. 2009, Journal of Cosmology and Astroparticle Physics, 10, 19
- Smith, J. A., 2002, AJ, 123, 2121
- Smith, R. E., Scoccimarro, R., Sheth, R. K. 2008, Phys. Rev. D, 77, 043525
- Song, Y.-S. & Percival, W. J. 2008, Phys. Rev. D, in press (astro-ph/0807.0810)
- Spergel, D. N., et al. 2003, ApJS, 148, 175
- Springel, V., et al. 2005, Nature, 435, 629
- Strauss, M. A., 2002, AJ, 124, 1810
- Sunyaev, R. A., & Zeldovich, Y. B. 1970, Ap&SS, 7, 3
- Szalay, A. S., Matsubara, T., Landy, S. D. 1998, ApJL, 498, L1
- Szapudi, I. 2004, ApJ, 614, 51
- Takahashi, R., et al., 2009, ApJ, 696, 93
- Taruya, A., Saito, S., & Nishimichi, T., 2012, Phys. Rev. D, 83, 103527
- Tegmark, M., et al. 2004, Phys. Rev. D, 69, 103501
- Tegmark, M., et al. 2006, Phys. Rev. D, 74, 123507
- Tegmark, M., Hamilton, A. J. S., Xu, Y. 2002, MNRAS, 335, 887
- Thomas, D., et al. 2012, in prep
- Tucker, D. L., et al., 2006, Astronomische Nachrichten, 327, 821

- Viana, P. T. P., & Liddle, A. R. 1999, MNRAS, 303, 535
- Wagner, C., Müller, V., & Steinmetz, M. 2008, A&A, 487, 63
- Webbink, R. F. 1984, ApJ, 277, 355
- Weinberg, D. H., et al. 2012, arXiv:1201.2434
- Whelan, J., & Iben, I. 1973, ApJ, 186, 1007
- White, M. 2001, MNRAS, 321, 1
- White, M., Song, Y.-S., Percival, W. J. 2009, MNRAS, 397, 1348
- White M., et al., 2011, ApJ, 728, 126
- Xu, X., et al., 2010, ApJ, 718, 1224
- Xu. X., et al., 2012, MNRAS, submitted, [[arXiv:1202.0091]]
- York, D. G., et al., 2000, AJ, 120, 1579
- Zaroubi, S., Hoffman, Y., Fisher, K. B., & Lahav, O., 1995, ApJ, 449, 446
- Zehavi, I., et al. 2002, ApJ, 571, 172
- Zehavi, I., et al. 2005, ApJ, 621, 22
- Zel'dovich, Y. B. 1970, A&A, 5, 84
- Zheng, Z., et al. 2005, ApJ, 633, 791
- Zheng, Z., Coil, A., & Zehavi, I. 2007, ApJ, 667, 760